https://doi.org/10.15388/vu.thesis.453
https://orcid.org/0000-0001-8427-1219

VILNIUS UNIVERSITY

CENTER FOR PHYSICAL SCIENCE AND TECHNOLOGY

Justina Jovaišaitė

Control of Singlet and Triplet States in Organic Intramolecular Charge Transfer Compounds

DOCTORAL DISSERTATION

Natural Sciences,

Physics (N 002)

VILNIUS 2023

The dissertation was prepared between 2016 & 2020 and between 2022 & 2023 at Institute of Photonics and Nanotechnology, Vilnius University.

The research and internships were supported by the Research Council of Lithuania and Erasmus+ (scholarship for academical accomplishments project no. P-DAP-18-208, scientific internship project no. 09.3.3.-LMT-K-712-07-0004, scientific events project no. 09.3.3.-LMT-K-712-13-0305 and 09.3.3.-LMT-K-712-06-0014). The experimental activities were partially financed by European Social Funds (project no. 09.3.3-LMT-K-718-01-0026 and 09.3.3-LMT-K-712-01-0084).

Academic supervisor – Prof. Habil. Dr. Saulius Juršėnas (Vilnius University, Natural Sciences, Physics – N 002)

Dissertation defense panel:

Chairman – Dr. Renata Butkutė (Center for Physical Sciences and Technology, Technological Sciences, Materials Engineering – T 008).

Members:
Prof. Habil. Dr. Przemyslaw Data (Lodz University of Technology, Natural Sciences, Chemistry – N 002),
Prof. Habil. Dr. Saulius Grigalevičius (Kaunas University of Technology, Natural Sciences, Chemistry – N 002),
Dr. Vytautas Klimavičius (Vilnius University, Natural Sciences, Physics – N 002),
Prof. Dr. Mikas Vengris (Vilnius University, Natural Sciences, Physics – N 002).

The dissertation shall be defended at a public meeting of the Dissertation Defense Panel at 3 PM on 5 April 2023 in conference room A101 of the Center for Physical Sciences and Technology.
Address: Saulėtekis av. 3, NFTMC, A101, Vilnius, Lithuania
Tel. +37052649211; e-mail: office@ftmc.lt

The text of this dissertation can be accessed at the libraries of Vilnius University, as well as on the website of Vilnius University:
www.vu.lt/lt/naujienos/ivykiu-kalendorius

https://doi.org/10.15388/vu.thesis.453
https://orcid.org/0000-0001-8427-1219

VILNIAUS UNIVERSITETAS

FIZINIŲ IR TECHNOLOGIJŲ MOKSLŲ CENTRAS

Justina Jovaišaitė

Singletinių ir tripletinių būsenų valdymas vidumolekulinės krūvio pernašos molekulėse

DAKTARO DISERTACIJA

Gamtos mokslai,

Fizika (N 002)

VILNIUS 2023

Disertacija rengta 2016–2020 ir 2022–2023 metais Vilniaus universiteto Fizikos fakulteto Fotonikos ir nanotechnologijų institute.

Mokslinius tyrimus ir doktorantūros stažuotes rėmė Lietuvos mokslų taryba ir Erasmus+ (stipendijos už akademinius pasiekimus registracijos Nr. P-DAP-18-208, kompetencijos kėlimas mokslinėje stažuotėje projekto Nr. 09.3.3.-LMT-K-712-07-0004, kompetencijos kėlimas mokslo renginiuose projekto Nr. 09.3.3.-LMT-K-712-13-0305 ir 09.3.3.-LMT-K-712-06-0014). Atlikta eksperimentinė veikla iš dalies finansuota Europos socialinio fondo lėšomis pagal projektus Nr. 09.3.3-LMT-K-718-01-0026 ir 09.3.3-LMT-K-712-01-0084.

Mokslinis vadovas – prof. habil. dr. Saulius Juršėnas (Vilniaus universitetas, gamtos mokslai, fizika – N 002).

Gynimo taryba:

Pirmininkė – dr. Renata Butkutė (Fizinių ir technologijos mokslų centras, technologijos mokslai, medžiagų inžinerija – T 008).

Nariai:
prof. habil. dr. Przemyslaw Data (Lodzės technologijos universitetas, gamtos mokslai, chemija – N 003),
prof. habil. dr. Saulius Grigalevičius (Kauno technologijų universitetas, gamtos mokslai, chemija – N 003),
dr. Vytautas Klimavičius (Vilniaus universitetas, gamtos mokslai, fizika – N 002),
prof. dr. Mikas Vengris (Vilniaus universitetas, gamtos mokslai, fizika – N 002).

Disertacija ginama viešame Gynimo tarybos posėdyje 2023 m. balandžio mėn. 5 d. 15 val. Nacionalinio fizinių ir technologijų mokslo centro auditorijoje A101. Adresas: Saulėtekio al. 3, Vilnius 10257, Lietuva, tel. +37052649211; el. paštas: office@ftmc.lt

Disertaciją galima peržiūrėti Vilniaus universiteto bibliotekoje ir VU interneto svetainėje adresu:
https://www.vu.lt/naujienos/ivykiu-kalendorius

ACKNOWLEGMENTS/PADĖKA

Disertaciją skiriu savo dviem aukseliams ir mylimam vyrui.

Stodama į doktorantūros studijas tikėjausi iš arti pažinti mokslininko gyvenimą bei jo darbo specifiką, kurios iki tol būnant bakalauro ar magistro studente, turiu pripažinti, negalėjau iki galo perprasti. Ir iš tiesų, doktorantūros studijų metu šis tikslas išsipildė su kaupu: pamačiau, koks žavus, tačiau kartais nenuspėjamas ir sunkus yra mokslininko darbas, iš arti pamačiau kaip gimsta idėjos, tyrimai ir galiausiai mokslas. Koks kartais būna ilgas kelias nuo pirmųjų eksperimentų iki išspausdintų straipsnių arba laimėtų projektų. Doktorantūros metu mane supo daug žmonių, naujų pažinčių ir užsimezgusių draugysčių, kelionių bei ilgų ilgų valandų laboratorijoje. Apibendrindama galiu pasakyti, kad metai buvo puikūs, nors ir kupini iššūkių.

Na, o toliau – labai svarbi dalis – padėkos. Visų pirma, noriu padėkoti savo vyrui Šarūnui. Už tai, kad mane pastūmėjo, įkvėpė ir nei karto nesuabejojo. Už tai, kad buvo šalia visų nuopuolių ir pakilimų metu, kad kantriai mane išklausydavo ir visada paskatindavo. Ačiū tau! Tu buvai neatsiejama šios kelionės dalis.

Be abejo, didelis ačiū visai mane supusiai mokslo bendruomenei. Dėkoju savo vadovui prof. Sauliui Juršėnui, įkalbėjusiam mane imtis doktorantūros studijų. Ačiū jam už kantrybę, pasitikėjimą ir laisvę, kuri man padėjo užaugti ir kaip mokslininkei, ir kaip asmenybei. Taip pat noriu padėkoti dr. Gediminui Jonušauskui, kuris priėmė į praktiką Bordo universitete, už tai, kad visada mane laikė lygiaverte kolege ir už tai, kad visada noriai dalinosi savo idėjomis, daug padėjo bei prisidėjo prie bendrų projektų. Taip pat noriu padėkoti dr. Karoliui Kazlauskui, kad patikėjo man atlikti eksperimentus savo projektams, o tai man suteikė galimybę iš arčiau pažinti naujas mokslo sritis. Toliau – neapsakomo dydžio padėka visiems buvusiems ir esamiems kolegoms. Iš tiesų, turiu labai pasidžiaugti savo kolektyvu: nesutikau nei vieno žmogaus, kuris būtų atsisakęs padėti, patarti, padiskutuoti, pasidalinti žiniomis ar savo įdirbiu. Ačiū jums visiems!

TABLE OF CONTENTS

LIST OF ABBREVIATIONS

A	Electron acceptor
CT	Charge transfer
D	Electron donor
DF	Delayed fluorescence
EQE	External quantum efficiency
HOMO	Highest occupied molecular orbital
IC	Internal conversion
ISC	Intersystem crossing
LE	Locally excited
LUMO	Lowest unoccupied molecular orbital
OLED	Organic light emitting diode
OURTP	Organic ultralong room temperature phosphorescence
PET	Photoinduced electron transfer
PH	Phosphorescence
PL	Photoluminescence
QY	Quantum efficiency
RIC	Reverse internal conversion
RISC	Reverse intersystem crossing
RT	Room temperature
RTP	Room temperature phosphorescence
SOC	Spin-orbit coupling
TADF	Thermally activated delayed fluorescence
TICT	Twisted intramolecular charge transfer

INTRODUCTION

Organic compounds are the main building material of all living organisms, including human beings. Besides their indispensable role in biology, organic materials have penetrated into our everyday life as organic light emitting diodes (OLEDs) used for a top-notch display technology. Apart from the extensively growing OLED market, which is forecasted to reach $214 billion by 2030,[1] organic materials remain very attractive for applications in many other fields: photovoltaics, wearable technologies, integrated sensors or intelligent labels.[2–5] The popularity and extensive research of organic optoelectronic field is mainly driven by the possibility to easily manufacture devices on a rigid or flexible substrates (for example, by printing), that would allow to reduce production cost and to obtain easily integrated gadgets.[6,7] Also, the employment of organic compounds is often considered as a more green technological approach allowing reducing energy consumption due to optimized low-temperature manufacturing processes and the possibility to employ easily recyclable materials for both active layers and substrates.[3] Finally, yet importantly, the properties of organic molecules and thus the device functionality can be synthetically tailored with endless prospect.

Many of organic molecules are fluorescent materials that emit light from excited singlet states and thus the phenomenon of fluorescence has been investigated for almost a century. The emission from triplet states (i.e. phosphorescence) is usually not observable at room temperature due to spin-forbidden $T_1 \rightarrow S_0$ transition and pronounced competition from nonradiative deactivation pathways.[8] Consequently, *triplets* were long considered as "dark" undesirable states. This changed significantly upon improvement of detection techniques and introduction of organometallic complexes, that made triplet states more easily accessible for research as well as for applications.[9–11] However, the limitations related to precious metal complexes, such as high cost or biological incompatibility, encourage the development of novel pure organic room temperature phosphorescent materials, where the phenomenon of long-lived phosphorescence is realized due to sophisticated molecular design and deep understanding of photophysical processes.[12]

The precise manipulation of energy level alignment, (reverse) intersystem crossing ((R)ISC) constants and (non)radiative excitation decay rates (of both fluorescence and phosphorescence) is imperative to purposively control processes between singlet and triplet states that allow to cover a wide excited state lifetime range: from nanoseconds to seconds. The different lifetimes of excited organic molecules are essential while considering the

possible application. For example, the employment of lone singlet states will result in relatively short transient fluorescence lifetimes of ~ 10^{-9} s, that would be beneficial for probes, sensors or even light emitting devices.[13–15] The mixing of singlet and triplet states may produce such processes as thermally activated delayed fluorescence (TADF) or triplet-triplet annihilation with intermediate delayed fluorescence lifetimes of ~10^{-6} s that may be of extreme importance while creating new generation OLED devices[16,17] or applying materials for imaging, photodynamic therapy or even photocatalysis.[18,19] The ultralong excited state lifetimes at room temperature resulting from excited triplet to ground singlet state emission may reach several seconds and can be applied for security systems, information storage, digital encryption, or optical recording devices.[20]

One of the most fundamental factors that governs processes between states of different multiplicities is the nature of electronic transition upon excitation, or, in other words, electronic configuration of ground and excited states. According to charge distribution before and after excitation, the electronic configuration of states can be roughly divided into locally excited (LE) and charge transfer (CT). The intramolecular CT-type molecules typically contain electron donating (D) and electron accepting (A) fragments that are usually connected through π-conjugated linkers.[21] CT-type organic molecules have been extensively studied throughout the years[22,23] and are often considered as the key design strategy for many different application fields due to the possibility to control their properties by synthetic approach or by environmental parameters.[21,24–26] Recently, organic D-A compounds experienced a major revival owing to its importance in developing the 3rd generation OLED devices, based on TADF concept.[27–31] The phenomenon of TADF relies on a on a small energy difference between excited singlet and triplet states (ΔE_{ST}), that is essential to facilitate efficient reverse intersystem crossing.[32] The employment of D-A structural combination appeared to be a highly effective strategy towards creation of TADF active emitters as the spatial separation between highest occupied molecular orbital (HOMO) and lowest unoccupied molecular orbital (LUMO) orbitals results in minimized ΔE_{ST}, more pronounced spin-orbit coupling (SOC), and thus, the increased possibility for (R)ISC to occur.[16,29,30] On the other hand, this approach faces a serious contradiction as the small orbital overlap will determine small radiative rates of singlet states, that will result in decreased fluorescence (and delayed fluorescence) quantum yields. Consequently, the overlap between HOMO and LUMO states needs to be precisely balanced.[27]

Clearly, the development of high-performance organic-based devices requires a careful selection of molecular structures as well as detailed understanding of the fundamental mechanisms and processes behind. The employment of CT-type materials offers an extensive possibility to manipulate singlet and triplet excited states both through environmental and molecular-structure related parameters. The control of singlet or singlet and triplet states, on the other hand, is an optimal tool to achieve the desired excited state lifetimes for targeted applications.

Aim, tasks and novelty

As the understanding and the ability to purposefully manipulate photophysical properties remain critical for intended development of organic functional materials, this dissertation will be devoted to photophysical study of different molecular series that possess intramolecular charge transfer. The idea of this thesis is to reveal the conducted research in a manner representing the complexity of molecular structures and (photo) excited state dynamics as well as means to control it: going from employing only singlet states to combining both singlet and triplet states for more advanced photophysical processes. The first two series of novel CT-type materials employ only singlet states and related photophysical processes, such as twisted intramolecular charge transfer (TICT), dual-CT transitions in a single molecule or intermolecular photoinduced electron transfer (PET). The third and fourth D-A molecular series are created to realize TADF process, which requires the employment of both singlet and triplet states with their careful energy manipulation for small ΔE_{ST}. The final molecular series are complex compounds with extremely important higher-lying excited singlet and triplet states for long and efficient afterglow demonstration.

Thus, the aim of the work is to study different CT-type molecular series by combining different electron donating and accepting fragments in order to understand and optimize their photophysical properties related to singlet and/or triplet excited states and to provide a perspective towards applications.

In order to reach the main goal of this dissertation, several tasks were set:

1. To determine excited state properties (including singlet & triplet states) with relevant processes and parameters by employing steady-state and time-resolved experimental techniques in combination with theoretical modelling in different sets of solvents and/or films, for both oxygen saturated and degassed environments.

2. To evaluate the control possibilities of photophysical properties by comparing experimental results and to select the optimal molecular structure as well as most appropriate molecular surroundings, including solvents for samples in solutions or polymer matrix, dopants, and the concentration for samples in films, for enhanced performance of relevant processes.
3. To demonstrate the studied organic compounds for specific possible applications, such polarity probes, cation or temperature sensors, TADF-based OLEDs and information recording tags.

The novelty of the dissertation is based on newly synthesised organic compounds and their characterization. All presented dissertation topics were originally published in scientific journals, where new CT-type molecular structures, processes and control possibilities were analysed and presented. The dissertation is presented as a collection of articles based on five publications with summarized results in Chapter 3.

Statements of the dissertation

1. The TICT state formation in 1,8-naphthalimide (electron acceptor) – dimethylaniline (electron donor) compounds, connected through two types of linkers, determines the excited singlet state properties dependence on the environmental factors. The variation of solvent's and polymer matrix's polarity allows to differentiate competing excited singlet state processes, i.e. dynamic solvation and twist reaction.
2. Combination of two asymmetric electron donating branches to purine core through triazole linkers allows to create D-A-D' type molecule with independent dual-band CT fluorescence, which can be further controlled by the strength of electron donors, polarity of the environment and by complexation with metal ions.
3. The TADF properties in materials with benzophenone-derived electron acceptor linked with multiple carbazolyl units are determined by non-radiative decay of triplet excitons which can be suppressed through chemical substitution of loose phenyl moiety with methoxy group.
4. The TADF properties in carbazole-naphthyridine-carbazole (D-A-D) compounds are determined by the strength of charge transfer character between D and A units, which can be sterically controlled by an additional methyl substitution.
5. The lateral substitution of polycyclic diboraanthracene scaffold (electron acceptor), together with weak transversal electron-donating mesityl groups, ensures the optimal molecular properties for (reverse) intersystem crossing and long-lived triplet states in a rigid polymer matrix for organic ultralong room temperature phosphorescence and persistent TADF (i.e. emission afterglow) with properties tuneable by molecular structure, sample concentration, rigidity, and temperature of the environment.

Author's contribution

The author has carried on the majority of steady-state & time-resolved photoluminescence spectroscopy experiments and prepared solutions or most of the solid-state samples that were further used for the experimental study. Also, the author performed photophysical characterization of compounds, processed and analysed obtained data. The author actively participated in scientific discussions and significantly contributed to idea generation, international collaboration, was responsible for manuscript preparation & writing and the coordination of submission process (Papers 1, 2 and 5). For Papers 3 and 4, the authors mostly contributed by performing photophysical measurements and characterization of compounds.

The studied naphthalimide compounds were synthesized by dr. Dalius Gudeika and prof. Juozas V. Gražulevičius (Kaunas University of Technology); the purine-based organic derivatives were synthesized by Latvian organic chemistry group led by prof. Maris Turks (Riga Technical University); the naphthyridines and benzophenone-carbazoles were prepared by the organic chemistry group led by dr. Edvinas Orientas (Vilnius University) and diboraanthracenes were synthesized by dr. Sven Kirschner and prof. Matthias Wagner (Goethe-University Frankfurt).

DFT modelling was performed by dr. Alytis Gruodis, dr. Regimantas Komskis and dr. Gediminas Kreiza (Vilnius University). NMR spectroscopy experiments for complexation mode determination were done by prof. Maris Turks group. Time-resolved emission spectra (and emission lifetimes) in a picosecond time domain were recorded by dr. Gediminas Jonušauskas (Bordeaux University) or by dr. Paulius Baronas (Vilnius University). Transient absorption experiments were carried on by dr. Paulius Baronas with the assistance of the author. Solid-state encapsulated samples and diboraanthracene-based tags for data recording were prepared by dr. Steponas Raišys (Vilnius University). OLED devices were prepared and characterized by dr. Dovydas Banevičius (Vilnius University). The technical equipment improvement for time-resolved measurements of long-lived systems were introduced by dr. Rokas Skaisgiris (Vilnius University).

The author is grateful to all co-authors for the contribution to this work.

LIST OF PUBLICATIONS

On the topic of dissertation

Paper I. **J. Jovaišaitė**, P. Baronas, G. Jonusauskas, D. Gudeika, A. Gruodis, J. V. Gražulevičius and S. Juršėnas, TICT compounds by design: comparison of two naphthalimide-p-dimethylaniline conjugates of different lengths and ground state geometries, *Phys. Chem. Chem. Phys.*, **25**, 2411-2419 (2023).

Paper II. **J. Jovaisaite**, D. Cirule, A. Jeminejs, I. Novosjolova, M. Turks, P. Baronas, R. Komskis, S. Tumkevicius, G. Jonusauskas and S. Jursenas, Proof of principle of a purine D–A–D' ligand based ratiometric chemical sensor harnessing complexation induced intermolecular PET, *Phys. Chem. Chem. Phys.*, **22**, 26502-26508 (2020).

Paper III. G. Kreiza, D. Banevičius, **J. Jovaišaitė**, K. Maleckaitė, D. Gudeika, D. Volyniuk, J. V. Gražulevičius, S. Juršėnas and K. Kazlauskas, Suppression of benzophenone-induced triplet quenching for enhanced TADF performance, *J. Mater. Chem. C.*, **7**, 11522 (2019).

Paper IV. G. Kreiza, D. Banevičius, **J. Jovaišaitė**, S. Juršėnas, T. Javorskis, V. Vaitkevičius, E. Orentas and K. Kazlauskas, Realization of deep-blue TADF in sterically controlled naphthyridines for vacuum- and solution-processed OLEDs, *J. Mater. Chem. C.*, **8**, 8560 (2020).

Paper V. **J. Jovaišaitė**, S. Kirschner, S. Raišys, G. Kreiza, P. Baronas, S. Juršėnas and M. Wagner, Diboraanthracene-Doped Polymer Systems for Colour-Tuneable Room-Temperature Organic Afterglow, *Angew. Chem. Int. Ed.*, **62**, e202215071 (2023).

Other publications

VI. B. Simon, **J. Jovaišaitė**, C.-Y. Huang, P. Baronas, K. Tulaite, S. Juršėnas, D. Jacquemin and S. Hecht, Mechanistic Insights into the Photoisomerization of N,N′-Disubstituted Indigos, *Chem. Eur. J.*, **28**, e202200496 (2022).

VII. L Martinez-Fernandez, AJ Pepino, J Segarra-Martí, **J Jovaisaite**, I Vayá, A Nenov, D Markovitsi, T Gustavsson, A Banyasz, M. Garavelli and R Improta, Photophysics of Deoxycytidine and 5-Methyldeoxycytidine in Solution: A Comprehensive Picture by Quantum Mechanical Calculations and Femtosecond Fluorescence Spectroscopy, *J. Am. Chem. Soc.*, **139**, 23, 7780–7791 (2017).

VIII. L. Skardziute, J. Dodonova, A. Voitechovicius, **J. Jovaisaite**, R. Komskis, A. Voitechoviciute, J. Bucevicius, K. Kazlauskas, S. Jursenas and S. Tumkevicius, Synthesis and optical properties of the isomeric pyrimidine and carbazole derivatives: Effects of polar substituents and linking topology, *Dye. Pigment.*, **118**, 118–128 (2015).

Conferences

1. Justina Jovaišaitė, Erika Bizdena, Maris Turks and Saulius Juršėnas "Control of optical properties and sensing application of purin e derivative", 60th International Conference for Students of Physics and Natural Sciences – Open Readings 2017 (Vilnius, Lithuania, March 14-17, 2017).

2. Justina Jovaišaitė, Tomas Serevičius, Tadas Bučiūnas, Jelena Dodonova, Jonas Bucevičius, Sigitas Tumkevičius and Saulius Juršėnas "Pirimidine based metal ion sensing, assisted by thermally activated delayed fluorescence",42th National Physics Conference of Lithuania (Vilnius, Lithuania, October 4-6, 2017).

3. Justina Jovaisaite, Gediminas Jonusauskas, Jelena Dodonova, Jonas Bucevicius, Sigitas Tumkevicius and Saulius Jursenas "A comprehensive photophysical study of pyrimidine dyes containing carbazoles and aniline: the interplay between singlets and triplets", 24th International Conference on Science and Technology of Synthetic Metals 2018 (ICSM 2018) (Busan, South Korea, July 1-6, 2018).

4. Justina Jovaisaite, Gediminas Jonusauskas, Jelena Dodonova, Jonas Bucevicius, Sigitas Tumkevicius and Saulius Jursenas "A comprehensive photophysical study of TADF pyrimidine compound decorated with aniline: the interplay between singlets and triplets", 7th EuCheMS Chemistry Congress (Liverpool, UK, August 26-30, 2018).

5. Justina Jovaišaitė, Gediminas Jonusauskas, Dace Cirule, Irina Novosjolova, Maris Turks and Saulius Jursenas "Photophysical study of bis-triazolyl-purine nucleoside push-pull molecular systems and their applicability as self-calibrating transition metal ion sensors", 13th International Conference on Optical Probes of Oranic and Hybrid Optoelectronic Materilas and Applications (OP2019) (Vilnius, Lietuva, July 7-12, 2019).

6. Justina Jovaisaite, Gediminas Jonusauskas, Dace Cirule, Irina Novosjolova, Maris Turks and Saulius Jursenas "Photophysical evaluation of bis-triazolyl-purine nucleoside derivatives and their potential application as self-calibrating

transition metal ion sensors," SPIE Organic Photonics + Electronics 2019 (San Diego, United States. August 11-15, 2019).

7. Justina Jovaišaitė, Sven Kirshner, Steponas Raišys, Gediminas Kreiza, Paulius Baronas, Matthias Wagner and Saulius Juršėnas "Diboraanthracene and polymer-based systems for room temperature organic afterglow" Advanced Properties and Processes in Optoelectronic Materials and Systems (APROPOS 18) (Vilnius, Lithuania, October 5-7, 2022).

1. LITERATURE REVIEW

The literature review starts from the discussion on fundamentals of molecular spectroscopy that is essential to understand and employ more advanced photophysical processes. Then, a brief introduction representing different electronic nature of excited states is provided. The further discussion continues on presenting the possibility to employ and control singlet and triplet excited states in CT-type molecules by considering several different photophysical processes, related to the thesis.

1.1 Most important parameters of photophysical processes

The control of spectroscopic molecular properties is mostly related to the control of the key photophysical parameters, that are well reflected in an iconic Jablonski diagram.[8,33] The extended version of Jablonski diagram in terms of photophysical processes is given in Figure 1 as an energy level diagram.[8,34] The most important controlled parameters of spectroscopic molecular properties are listed in Table 1.

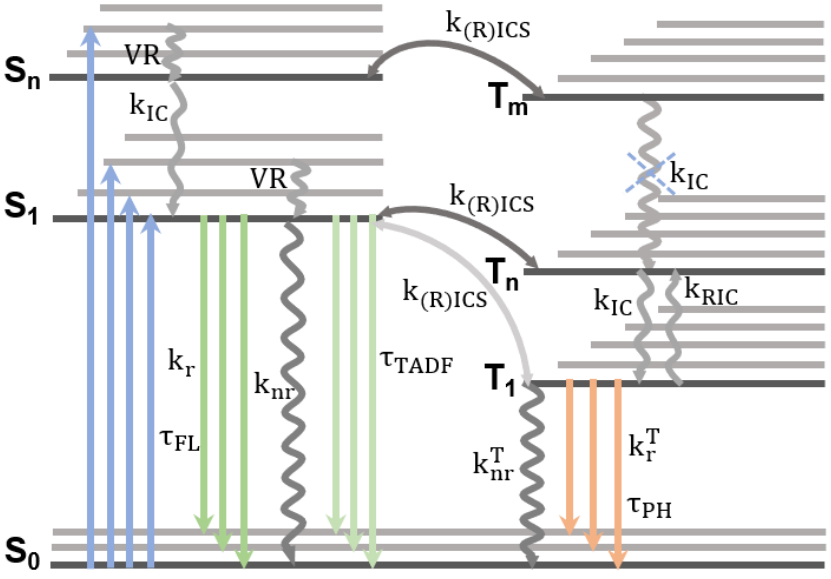

Figure 1. Energy level diagram depicting main photophysical processes in organic molecules.

Once molecule absorbs light, it is excited to the vibrational level of a singlet state S_1 or S_n. The absorption takes place almost instantaneously in 10^{-15} s, that, according to Franck-Condon principle, is too fast for the displacement of the nuclei. Subsequently, the molecule will relax from a higher vibrational level to the lowest vibrational level of S_n and subsequently, the internal conversion (IC) to S_1 will take place. The S_1 de-activation channels can be radiative (fluorescence) or non-radiative: IC to S_0 or intersystem crossing (ISC) to triplet states.[8] One has to note that there are alternative quenching mechanisms that may determine the efficient non-radiative excitation relaxation, such as conical intersection, isomerization, electron and proton transfer or additional mechanism involving interactions with other molecules (triplet-triplet or singlet-triplet annihilation, energy transfer, excimer or exciplex formation, quenching by oxygen or humidity etc.).[34] However, in this section IC to S_0 and ISC will be mostly referred.

According to the Kasha's rule, photon emission occurs only from the lowest excited state of a given multiplicity.[35] The physical background of this rule is the close alignment between S_1 and S_n states (that is also applicable for triplet states, as discussed below). However, even if this rule describes the majority of fluorescent materials, it is worth mentioning that there have been many examples of observable emission from higher-laying excited states (the classic example is an azulene molecule).[36]

The emission of a photon from S_1 takes place in a similar time scale as absorption (~10^{-15} s). However, the excited molecule stays in S_1 for a certain period of time before emitting a photon, which is defined as a lifetime of S_1, or more often as fluorescence lifetime τ_{FL}. The fluorescence lifetime, in fact, reflect both, radiative and non-radiative excitation de-activation processes as per 1.1 expression:[8,34]

$$\tau_{FL} = \frac{1}{k_r + k_{nr}}, \tag{1.1}$$

where k_r and k_{nr} are radiative and non-radiative excitation deactivation rates for singlet state, respectively.

The non-radiative rate for $S_1 \rightarrow S_0$ transitions, if other quenching factors are absent or insignificant, is:[8]

$$k_{nr} = k_{IC} + k_{ISC}, \tag{1.2}$$

where k_{IC} and k_{ISC} represent rates of internal conversion and intersystem crossing, respectively.

The quantum yield (QY) of a process (e.g., fluorescence) as well as lifetimes (and consequently, the radiative and non-radiative rates) are usually the most important characteristics to describe a fluorophore. Specifically, the fluorescence quantum yield is a ratio of the emitted photons to absorbed photons or the fraction of molecules that decay radiatively, as expressed below:

$$\phi_{FL} = \frac{k_r}{k_r + k_{nr}}. \quad (1.3)$$

As already mentioned, one of the possible non-radiative transitions for singlet states is ISC to triplet states, that requires the spin change and results in the excited orbital having the same spin orientation as the ground state. Due to this reason, the ISC from S_1 to T_n, as well as ISC from T_1 to S_0 (i.e., phosphorescence) are considered to be forbidden.[9] It is well known that ISC can be promoted by incorporating heavy atoms (I, Br, etc.) or metal ions (e.g., Ir^{3+} or Ru^{2+} complexes) in the molecular structure.[37,38] In fact, it was shown that ISC may occur in (sub)picosecond time scale even for molecules composed only of light elements, including heteroatoms.[39,40] Thus, ISC can efficiently compete with fluorescence or even IC, meaning that ISC can take place from higher excited singlet states. The mechanism responsible for crossing between states of different multiplicities is coupling between the orbital magnetic moment and the spin magnetic moment, i.e. spin-orbit coupling (SOC). The extended discussion on the SOC and its importance will be provided in the upcoming sections.

When T_n is populated, again, the IC to the lowest vibrational level of T_1 is expected, that would ultimately result in phosphorescence ($T_1 \rightarrow S_0$ transition) or thermal energy losses. Phosphorescence itself has a very low radiative rate and is usually not observable in solutions due to numerous possible collisions with solvent molecules during the lifetime of lowest triplet state and thus, the promoted vibrational relaxation to S_0.[8] On the other hand, the rigid environment or low temperature reduces the non-radiative phosphorescence deactivation rate and if external quenchers are absent, such as oxygen or humidity, the phosphorescence may be observed and can last up to seconds and more.[9] The phosphorescence lifetime as well as its quantum yield can be expressed analogous to fluorescence:

$$\tau_{PH} = \frac{1}{k_r^T + k_{nr}^T} \quad (1.4)$$

and

$$\phi_{PH} = \phi_{ISC} \times \frac{k_r^T}{k_r^T + k_{nr}^T}, \quad (1.5)$$

where k_r^T and k_{nr}^T are radiative and non-radiative phosphorescence decay rates, respectively, and ϕ_{ISC} is a quantum efficiency of intersystem crossing from singlet to triplet states.

The efficiency of ϕ_{ISC} can be defined as:[41]

$$\phi_{ISC} = k_{ISC} \times \tau_{PH}. \quad (1.6)$$

In the case of reasonable SOC between S_n and T_n as well as a small energy gap (ΔE_{ST}) between these two states (usually ≤200 meV), the internal conversion may start to compete with intersystem crossing from triplet states back to singlet states, which is referred to as reverse intersystem crossing (RISC).[42] It is now well understood that RISC will occur between states with different molecular orbitals as per El-Sayed's rule,[43] meaning that if S_1 and T_1 are both of the same electronic nature, the intermediate state of different nature close to S_1 and T_1 will be required.[44] Thus, reverse internal conversion (RIC) prior to RISC will then take place. The definition of RISC efficiency, again, can be expressed through respective rate constants:[41]

$$\phi_{RISC} = \frac{k_{RISC}}{k_{RISC}+k_r^T+k_{nr}^T}. \quad (1.7)$$

Once singlet states are thermally populated from triplet states, the delayed fluorescence, known as thermally activated delayed fluorescence (TADF), may be expected with lifetime between hundreds of nanoseconds to hundreds of microseconds. The QY of TADF will be defined by all included processes:

$$\phi_{TADF} = \phi_{RISC} \times \phi_{FL} \times \phi_{ISC}. \quad (1.8)$$

If energy gap between T_n ($n \geq 1$) and T_m ($m > 1$) is large enough, the IC from T_m to T_n can start to compete with RISC from T_m back to singlet states. In the case IC for $T_m \rightarrow T_n$ transition is fully forbidden, and RISC is fast enough, the immediate transition back to higher lying S_n ($n \geq 1$) states may be observed. This kind of process is referred to as hot exciton mechanism.[45]

Up to now, the reader may have already noticed that the photophysical processes are mostly defined by the competition between their rates, that mainly depend on the energy level alignment and their electronic nature as will be discussed in the upcoming section.

Table 1. Main tuneable parameters that define spectroscopic properties of organic molecules.

Absorption wavelength	λ_{ABS}	Phosphorescence lifetime	τ_{PH}
Molar extinction coefficient	ε	Phosphorescence radiative/non-radiative rates	k_r^T, k_{nr}^T,
Fluorescence wavelength	λ_{Fl}	Phosphorescence quantum yields	ϕ_{PH}
Fluorescence lifetime	τ_{FL}	Spin-orbit coupling matrix element	SOCME
Fluorescence radiative/non-radiative rates	k_r, k_{nr}	Singlet-Triplet energy difference	ΔE_{ST}
Fluorescence quantum yield	ϕ_{Fl}	Lifetime of delayed fluorescence	τ_{DF}
Intersystem crossing rate	k_{ISC}	Delayed fluorescence quantum efficiency	ϕ_{DF}
Reverse intersystem crossing rate	k_{RISC}		
Phosphorescence wavelength	λ_{PH}		

1.2 Molecular orbital distribution: LE & CT states

One of the most important factors affecting spectroscopic properties of organic molecules, which is not reflected in a Jablonski diagram, is the nature of electronic transition. According to the charge distribution in the highest occupied molecular orbital (HOMO) and the lowest unoccupied molecular orbital (LUMO), the excited states can be denoted as locally excited (LE) or the intramolecular charge transfer (CT) states. In the case of LE states, the distribution of electrons and holes before and after electronic transition are roughly the same. The LE type transitions are characteristic to conjugated rigid molecules, such as naphthalene,[46] perylene,[47] anthracene,[48] etc. In contrast, for CT states the motion of electron charge from one molecular orbital to another will be induced upon photoexcitation so that the initial and final orbitals will be separated in space. Typically, CT states appear for molecules bearing electron donating (D) and electron accepting (A) fragments that are usually connected through π-conjugated linkers.[21] Figure 2 provides several examples of most common D and A units and linkers.[8,21,24,49,50] Nevertheless, some of molecules (or fragments) may act both as electron donors and electron acceptors in different molecular combinations. The most

important factor is their oxidation-reduction potentials in a combined molecular structure.[51]

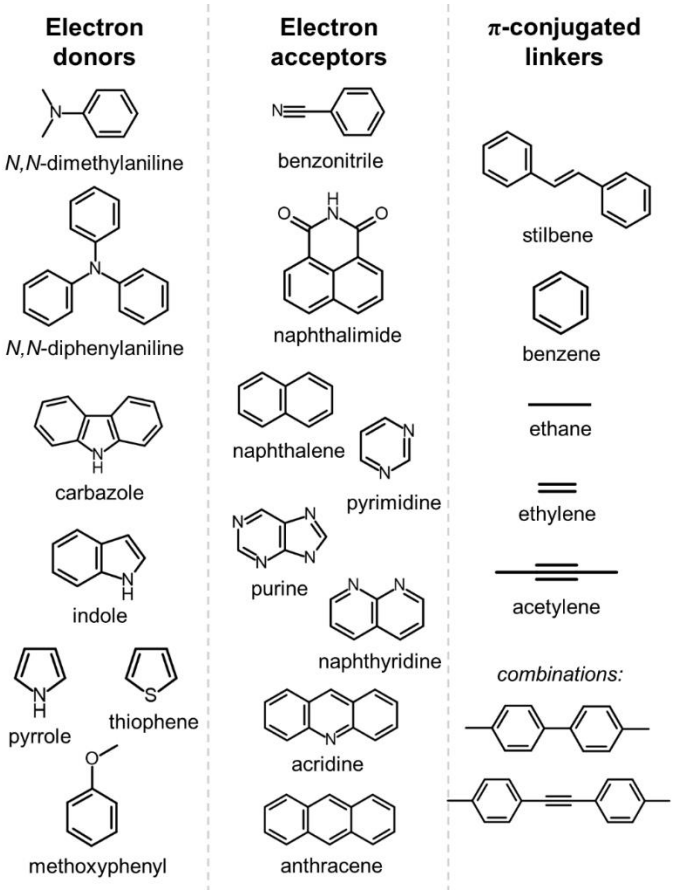

Figure 2. Examples of most widely used electron donors, electron acceptors and π-conjugated linkers in intramolecular charge transfer compounds.

The higher overlap of HOMO and LUMO wavefunctions will determine the higher oscillator strength of the transition and thus, high fluorescence quantum yields up to 100% can be expected for LE-type molecules in the absence of other non-radiative de-excitation channels. The separation of HOMO and LUMO orbitals will typically determine the reduced oscillator strength, lower fluorescence quantum yields and prolonged fluorescence lifetimes due to pronounced k_{nr}.[34,52] However, the CT-type molecules remain of an extreme importance in organic optoelectronics and are often the key design strategy for many different application fields due the possibility to control their properties by both molecular structure and environment

parameters.[21,24–26] Figure 3 summarizes the most popular approaches to control properties of intramolecular CT molecules.

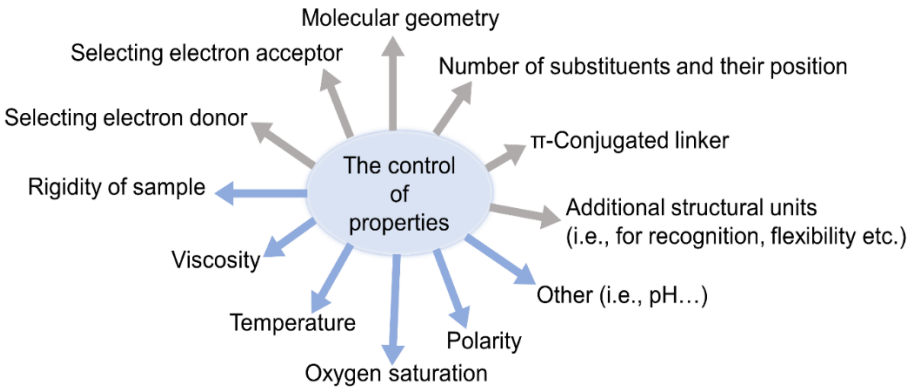

Figure 3. The illustration of possibilities to control photophysical properties of CT-type molecules mainly through molecular structure (grey arrows) or through environmental parameters (blue arrows).

Many different configurations of electron donating and electron accepting subunits can be realized in a molecular structure, such as D-A, D-A-D, D-A-D', A-D-A, A-A-D, etc.[21] In some cases, the unusual combinations can result in unexpected, though, advantageous properties. The dual emission from two CT states in D–A–D' systems was demonstrated for 3rd generation OLED emitter caused by intramolecular and intermolecular CT due to exciplex formation[53] or due to different conformers.[54] Also, it was shown that two independent CT emitting states can exist in one molecular system and can be attributed to D–A and A–D' moieties and are controlled by conformations and stabilized by the polarity of the surroundings.[55]

It should be mentioned that recent research (especially 3rd generation OLED devices) has broadened the classic knowledge and understanding about CT states by introducing molecular structures for hybridized local and charge transfer (HLCT) states, where the lowest excited state possesses LE and CT characters simultaneously due to strong state mixing.[56] Furthermore, HOMO-LUMO separation may result from multiple resonance effect, without a conventional electron donor-acceptor structure, that is also extremely beneficial in terms of TADF emitters as high photoluminescence (PL) quantum yields in combination with narrow PL spectra can be obtained.[57]

1.3 The employment of singlet states in D-A type molecules

So far it was discussed that the most crucial part to create the molecular system with desired properties is to select the appropriate electron donating and electron accepting substituents, π-conjugated linker, and the substitution position. These selections will determine molecular geometry, or more generally, molecular orbital distribution and their interaction. Additionally, the recognition groups that would be able to complex with desired analytes may be chemically introduced into molecular structure.

In the context of this thesis, two completely different photophysical processes will be introduced that may be used as a tool or design principal to control properties of singlet states: twisted intramolecular charge transfer and photoinduced electron transfer. Finally, the most common applications of CT molecules by employing their singlet states will be shortly reviewed.

1.3.1 Twisted intramolecular charge transfer (TICT)

The perpendicular configuration of D and A fragments against each other may be classified as twisted intermolecular charge transfer state (TICT). TICT states undergo the full charge separation as twisting around the single bond leads to the deconjugation of electron donor and acceptor excited states. Originally, TICT was first proposed and rationalized by Grobowski *et al*. to explain the extraordinary photophysical behaviour of 4-(dimethylamino)benzonitrile (DMABN) compound resulting in the dual emission, discovered by Lippert *et al.*[22,49] According to authors, the dual emission originates from both, LE and TICT states, where dimethylamino group is perpendicularly twisted against phenyl ring (see Figure 4 for the illustration). The topic concerning the photophysical processes of DMABN upon excitation gained the tremendous interest among scientific community which lasts to this day.[58] It was concluded that the excited state dynamics of DMABN is rather complex and cannot be rationalized by a single time constant and, consequently, the simplified two-state model needs to be clarified. Specifically, it was shown that within few hundred femtoseconds after the photoexcitation, the CT state with small twist angle is formed from LE state and directly from S_2. Then this partially twisted CT state undergoes further relaxation to reach the TICT state, which additionally can be accessed directly from LE state.[59]

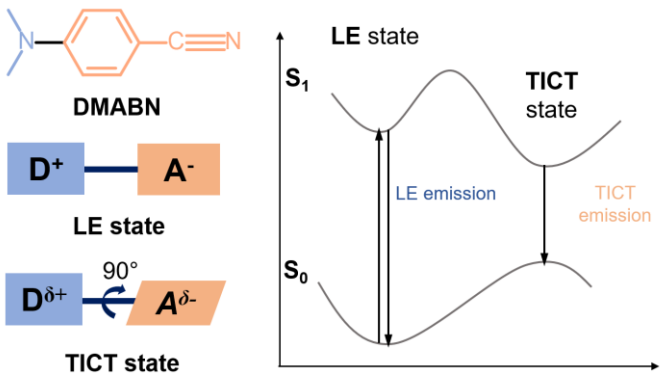

Figure 4. The schematic illustration of LE and TICT states formed in classic TICT molecule DMABN. Adapted from [22].

Considering other molecules with a TICT character and this process in general, there has been several attempts to rationalize the twisting dynamics and to predict whether TICT reaction will take place in a given molecular design.[60] It is generally accepted that TICT can occur due to dipole solute-solvent interactions as the TICT state is better stabilized by a polar solvent. Intuitively, the TICT can be predicted by selecting electron donor with a low ionization potential and electron acceptor with a high electron affinity and the appropriate linker between these two groups.[60] If TICT is favourable in the molecular system, it is more likely to occur in non-viscous, polar solvents due to unrestricted molecular motions and better stabilization of polar charge transfer states.[61] In addition, some of the literature points towards the pre-twisted molecular geometry as it may promote more efficient TICT formation.[62] In many cases the prediction of TICT is sophisticated and many molecules with D-A groups will not necessary show TICT character. Theoretically, the transition from LE or CT state to TICT state can be modelled by evaluating the potential energy surface of S_1 as a function of the twist angle by employing appropriate computational methods.[60,63,64]

Besides of before mentioned classification of CT states as PICT and TICT, more categories can be found in the literature, such as partially twisted charge transfer states (pTICT) or, less popular, rehybridized charge transfer states (WICT) and others, mostly related to the historical discussion on the photophysics of DMABN.[65] Recently, the new charge transfer and separation process was discovered, named as twisted intramolecular charge shuttle (TICS).[66] In TICS compounds, the dialkylated amino group (or aniline) acts as an electron withdrawing group upon light absorption, however, after rotating by approximately 90° it starts to act as an electron-donor. Apparently,

this concept is applicable to several families of well-known fluorophores, such as coumarin, BODIPY and rhodamine.[66,67]

1.3.2 Photoinduced electron transfer (PET)

Photoinduced electron transfer (PET) is one of the most fundamental processes in physics, chemistry, and biology and has been extensively studied throughout the years. The main contribution to electron transfer theory has been introduced by R. A. Marcus, first formulated as early as in 1956.[68] However, here only very basic aspects of PET mechanism will be mentioned, avoiding deeper explanations of the mentioned Marcus theory.

PET occurring from an electron donor (D) to an electron acceptor (A) determines the charge separation as donor radical cation and the acceptor radical anion are formed. PET itself can be an intramolecular process, meaning that D and A coexists in the same molecule, or intermolecular process between different molecules. The appearance and properties of PET are regulated by the electrochemical and excited state properties of the acceptor and donor moieties, including their energy level alignment.[69,70] Importantly, the proximity of D and A is needed, meaning that in the case of intramolecular process, the short spacer/bridge would be preferable, while in terms of intermolecular PET, high concentrations are essential. The presence of intra- or intermolecular PET usually determines the fluorescence quenching as fluorescence quantum yields and fluorescence lifetimes are decreased. As it is typical for many photophysical and/or photochemical processes, PET occurrence is competing with radiative and non-radiative deactivation channels, including IC, ISC, quenching through dark states or other energy transfer processes.[69]

PET mechanism can be oxidative or reductive, depending on whether the transfer of electron occurs between LUMO or HOMO levels. In the case of oxidative PET, the electron donor is excited and subsequently electron is transferred from the LUMO of D unit to the LUMO of A unit (Figure 5 a). During the reductive PET, the excited electron acceptor leads to an electron transfer from the HOMO level of D to HOMO of A (see Figure 5 b).[8,70,71]

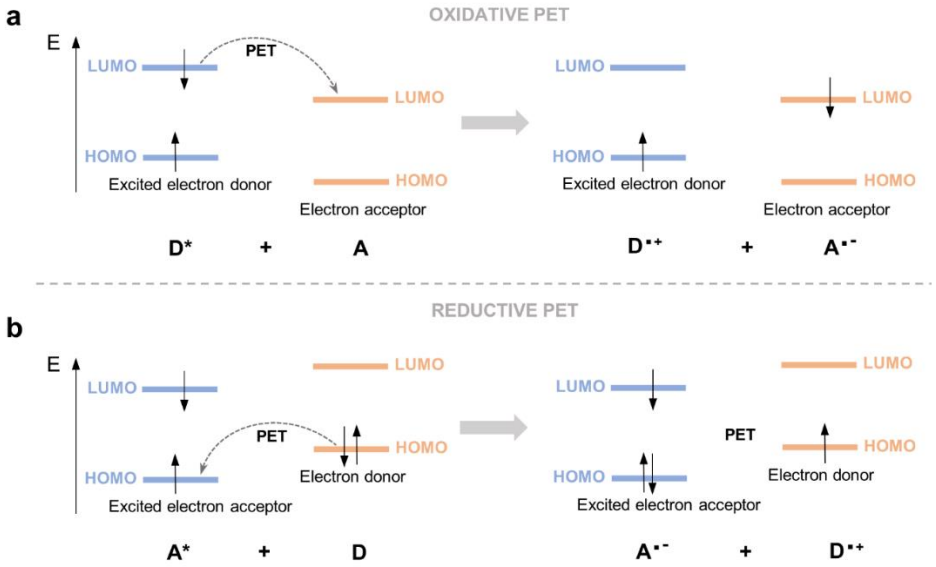

Figure 5. Oxidative (a) and reductive (b) photoinduced electron transfer and its energetical alignment requirements. Adapted from [8].

The possibility to control the presence or absence of PET in the same molecular system through structural, conformational, or environmental factors, such as complexation with targeted analytes, led to the unprecedented popularity of PET-based fluorescence sensors and switches.[72–75] In terms of fluorescence sensors, the fluorophore is often an electron acceptor, while electron donating subunit may act as receptor, capable of binding the selected analytes.[76] The typical scheme for PET-based fluorescence sensor with its ON and OFF states along with respective energy diagrams are given in Figure 6. Even though the innumerable quantity of PET driven applications have been presented (see the next section for more examples), the attribution of latter mechanism is often based on fluorescence quenching and the feasible D and A energetical alignment. However, for the precise proof of PET existence and for the determination of its rate, the time-resolved spectroscopy analysis is required, which allows to determine the radical ion spectra.[69]

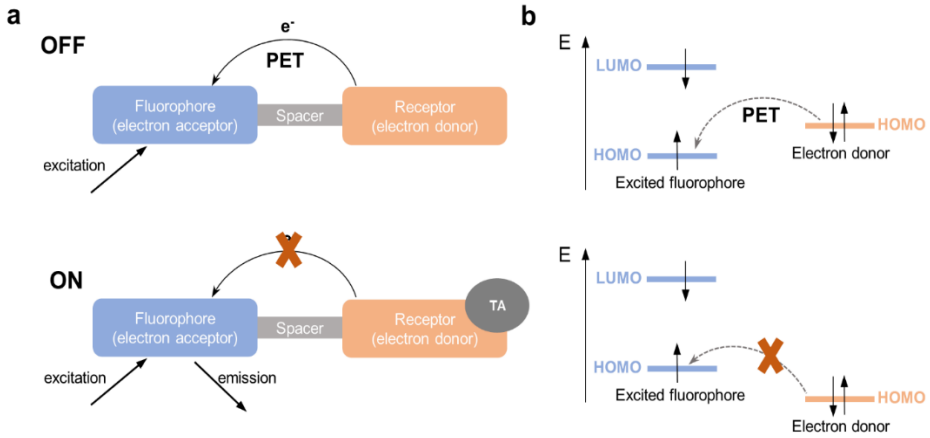

Figure 6. The scheme of PET-based fluorescence sensor, containing fluorophore (electron acceptor) -spacer – receptor (electron donor) design, in OFF and ON states (a). The binding of targeted analyte (TA) with the receptor may cause the decrease of its HOMO energy and thus, the prohibition of PET. The respective frontier molecular orbitals to OFF and ON states (b). Adapted from [69,77].

1.3.3 Applications

The relatively simple concept that governs CT (and TICT) processes, especially considering the singlet states, determined the creation of the countless number of new functional materials. The explicit dependence of such kind of compounds to the environment properties (polarity, viscosity, etc.) encourage for the straightforward applications, such as probing and sensing the targeted parameters or analytes, and labelling (fluorescence imaging).

The dependence of CT properties on environment's polarity, which is usually expressed in a red shift of fluorescence spectra as well as in the alterations of its intensity, is employed to probe the polarity in vitro (for example, solvent, material or protein polarity) and in live systems (mitochondrial, lysosomal, endoplasmic reticulum polarity).[78] The wide chemical possibilities to incorporate the recognition group into D-A structure as well as the complexation ability of some atoms (for example, nitrogen and/or oxygen) with metal ions resulted in an explicit research on chemo- and bio-sensors of various analytes. For example, numerous organic structures are constructed to selectively detect cations, anions, small neutral molecules and other biologically important species, such as reactive oxygen or reactive nitrogen species (that plays a vital role in terms of many physiological and

pathological processes), etc.[79,80] Two types of fluorescence "turn-on" ratiometric chemosensors for metal ion detection, based on the enhancement or suppression of intramolecular CT character, are shown in Figure 7.[81] The sensor L_1 in Figure 7 a is composed of quinoline backbone with tetrahydrofuran carboxamide (C-8 position) and phenylethynyl (C-5 position) groups. Upon complexation with Zn^{2+}, the fluorescence intensity at 430 nm decreases, while the band at 525 nm increases, that is related to the enhancement of charge transfer from the amide nitrogen.[82] The sensor E3 that has a naphthalimide core, exhibits fluorescence at 528 nm upon excitation at 440 nm (Figure 7 b). Once Co^{2+} ions are added to the solution, they bind to four nitrogen atoms in two aminomethyl pyridine arms. Apparently, the coordination causes the decrease of CT fluorescence band, while the LE band increases.[83]

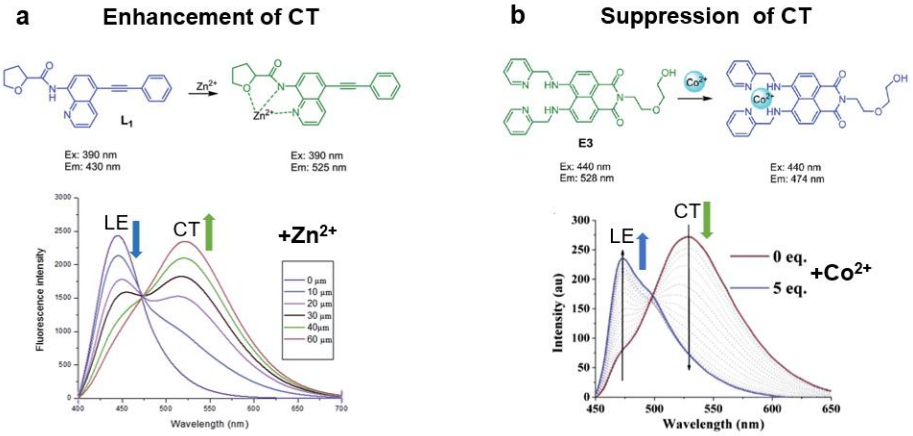

Figure 7. The example of two types of fluorescence "turn-on" chemosensors for metal ion detection based on the enhancement (a) and the suppression (b) of intramolecular CT character. Adapted from [82,83].

The possible water solubility and biocompatibility as well as the combination of multiple reaction sites also determined the use of organic CT molecules to label biological systems for fluorescence imaging, to distinguish and trace the metabolism of substances in vivo.[78,84] Even more, the TICT character expanded the applicability of organic compounds for molecular rotors and for luminogens with aggregation induced emission characteristics. The charge transfer-based molecules found its place in nonlinear optics and solar energy harvesting techniques.[85,86]

In terms of PET-favourable molecules, the possible application fields are similar to the discussed above. PET probes are extensively designed for metal

ion sensing, for microenvironment parameter sensing in living cells, such as reactive biological species, intracellular pH, intracellular polarity.[87,88] In addition, PET enzyme-targeting probes have been created, where receptor bind to enzymes which may affect the folded or unfolded conformations and thus, control the PET process. Such strategy was demonstrated to be suitable for cancer diagnosis and even therapy.[88] Also, molecules with PET are used as fluorescent molecular logic gates responsive to acids and oxidants. For example, redox potential PET sensors are primarily used for cell viability and cytotoxicity studies.[89] Furthermore, PET was applied in a two-colour single molecule PET fluorescence microscopy for multiple conformational motions detection within single protein molecule.[90]

1.4 Triplet states in CT molecules

Up to this point, mainly singlet states of CT-type molecules were considered. The non-radiative ISC to triplet states is a common excitation deactivation channel and is often undesirable process in terms of previously discussed applications. However, the sophisticated molecular design alongside with subtle knowledge may allow to proficiently enable both singlet and triplet states for more advanced applications. Thus, this section will be devoted to two selected processes that require to use the excited states with different multiplicities: thermally activated delayed emission and even more sophisticated ultralong room temperature phosphorescence/afterglow. The summary of possible applications related to mentioned processes will be also introduced.

1.4.1 Thermally activated delayed fluorescence (TADF)

One of the most common examples of delicately employed singlet and triplet states in D-A type compounds is a concept of so called thermally activated delayed fluorescence, which is the basis of the 3rd generation OLED devices.[27,91] Generally, TADF is a mechanism that relies on the thermally promoted RISC between triplet and singlet states that need to lie close in energy (usually, $\Delta E_{ST} \leq 200$ meV). In reality, the mechanism is more complex and not only energy gap, but also a sufficient spin-orbit coupling (SOC) between states of different multiplicity, spin-vibronic coupling between triplet states, as well as minimized lifetimes of triplet states (or enhanced reverse intersystem crossing rates) are needed for an efficient process. Furthermore, even if molecular structure is favourable for TADF to take place, more things need to be considered to satisfy the requirements for OLEDs. To name a few,

the suitable colour according to CIE, the sufficiently short delayed fluorescence (DF) (preferably, several hundred nanoseconds), the narrow DF spectra and high stability of compounds.[13,92]

One of the most important TADF parameters that needs to be considered and appropriately controlled is a reverse intersystem crossing rate (k_{RISC}). According to Boltzmann distribution equation (1.9), k_{RISC} is inversely proportional to the energy gap between singlet and triplet states (ΔE_{ST}), thus it is critical to minimize ΔE_{ST} in order to maximize k_{RISC}, which is essential for an efficient TADF emitter.[41]

$$k_{RISC} = Aexp\left(-\frac{\Delta E_{ST}}{kT}\right), \tag{1.9}$$

where A is a pre-exponential factor, k is Boltzmann constant and T is an absolute temperature.

A general strategy to minimize ΔE_{ST} is to design the relevant molecular structure: the HOMO and LUMO frontier orbital overlap needs to be minimized. This rule can be understood considering the state energies and expressing the energy difference via exchange energy. The energies of the lowest excited singlet and triplet states with the same electronic configuration can be expressed by using orbital energy (E_{orb}), the electron repulsion energy (K) and the exchange energy (J). The latter term is the first order quantum mechanical correction that involves electron-electron repulsion due to Pauli principle, which affects one electron in HOMO and one in LUMO states (upon excitation). Due to the different spin arrangements of singlet and triplet excited states, the exchange energy increases energy for singlet state and decreases for the triplet state:[41]

$$E_{S1} = E_{orb} + K + J, \tag{1.10}$$

$$E_{T1} = E_{orb} + K - J, \tag{1.11}$$

Thus, ΔE_{ST} is then expressed by:[41]

$$\Delta E_{ST} = E_{S1} - E_{T1} = 2J. \tag{1.12}$$

The exchange energy is given as per equation below:[41]

$$J = \iint \Psi_a(r_1)\Psi_b(r_2)\left(\frac{e^2}{r_1 - r_2}\right)\Psi_a(r_2)\Psi_b(r_1)dr_1dr_2. \tag{1.13}$$

In the latter equation, Ψ_a and Ψ_b are the wavefunctions of HOMO and LUMO, e is electron charge and r_1 and r_2 are electron coordinates.

From equation (1.12) it is obvious that ΔE_{ST} is minimized by reducing exchange energy. The exchange energy itself can be reduced by decreasing the overlap between HOMO and LUMO orbitals which is realized by spatially separating the frontier orbitals. Indeed, this is the main reason, why CT type molecules achieved the tremendous attention in terms of molecular structures for TADF active emitters. Additional to the pronounced CT character of a D-A molecule, the singlet-triplet energy splitting can be further reduced by obtaining a near-orthogonality of D-A units or by increasing the D-A distance through a molecular bridge.[41,93] On the other hand, this approach faces a serious contradiction: the small orbital overlap will determine low absorption and emission oscillator strengths and thus the small radiative rates of singlet state will reduce fluorescence (and delayed fluorescence) quantum yields. Hence, the TADF emitter design is very sophisticated, and the scientific research is dedicated to find a balance between k_{RISC} and k_r rates.

The introduced approach to minimize ΔE_{ST} which should increase k_{RISC} is just a rough simplification. In fact, more factors directly affecting intersystem and reverse intersystem crossing need to be carefully evaluated. Some studies have revealed that molecules with similar ΔE_{ST} have significantly different reverse intersystem crossing rates.[94] These observations along with more experimental and theoretical research helped to conclude that intermediate states play a critical role in terms of TADF.[44,95] Indeed, the straightforward understanding that RISC takes place directly between lowest singlet and lowest triplet CT states is conceptually wrong due to some fundamental aspects of spin-orbit coupling, i.e. process that allows the transition between states of different multiplicity. Note that in the context of present thesis, the molecules with light atoms will only be considered and discussed.

SOC operator acts on both, the spin and angular momentum, meaning that the change of spin will determine the change of angular momentum, that will be only possible if the charge distribution of two interacting states is different.[43,96] Thus, it was proposed that an efficient RISC is determined by mixing the triplet CT with triplet LE states, that need to lie close in energy. Consequently, the spin-vibronic coupling between multiple excited states of the same multiplicity was also introduced as a key element for the efficient RISC.[95,97,98] It is now widely accepted and understood that RISC is a two-step process, governed by the vibronic coupling of ^{3}CT and ^{3}LE states and the SOC between ^{3}LE and ^{1}CT.[97] The relative terms to express the RISC process in D-A TADF emitter can be expressed as follows:[92,97]

$$k_{RIC} = \frac{2\pi}{\hbar}\left|\langle {}^3\Psi_{CT}\left|\hat{\mathcal{H}}_{vib}\right|{}^3\Psi_{LE}\rangle\right|^2 \delta\left({}^3E_{CT} - {}^3E_{LE}\right), \quad (1.14)$$

$$k_{RISC} = \frac{2\pi}{\hbar}\left|\frac{\langle {}^1\Psi_{CT}|\hat{\mathcal{H}}_{SOC}|{}^3\Psi_{LE}\rangle\langle {}^3\Psi_{LE}|\hat{\mathcal{H}}_{vib}|{}^3\Psi_{CT}\rangle}{{}^3E_{CT} - {}^3E_{LE}}\right|^2 \delta\left({}^1E_{CT} - {}^3E_{CT}\right). \quad (1.15)$$

Where k_{RIC} denotes the rate of reverse internal conversion, $\hbar$ is a Planck constant; ${}^1\Psi_{CT}$, ${}^3\Psi_{CT}$, ${}^3\Psi_{LE}$ are the wavefunctions of charge transfer singlet state, charge transfer and locally excited triplet states, respectively; $\hat{\mathcal{H}}_{vib}$ and $\hat{\mathcal{H}}_{SOC}$ are vibronic coupling and spin-orbit coupling Hamiltonians. The δ functions ensure the conservation of the molecular energy for the nonradiative transitions between indicated states.

First, the vibronic coupling between ^{3}LE (initial state) and ^{3}CT (final state) promotes the equilibrium (or mixing) between these two states. The time scale of reverse internal conversion (RIC) is much faster that RISC. The second term (1.15) couples ^{3}CT (initial) and the ^{1}CT (final state) using ^{3}LE as an intermediate state. The simplified scheme of discussed TADF mechanism, also denoted as model Hamiltonian, is given in Figure 8. The indicated non-discussed term $\hat{\mathcal{H}}_{\mathrm{HFL}}$, defines the hyperfine coupling between CT states of different multiplicities. However, it was showed that this term has a negligible effect in terms of (reverse) intersystem crossing and thus, was negleted.[95] Note, that three configurations of state energy arrangements are possible, where ^{3}CT>^{3}LE, ^{3}CT=^{3}LE or ^{3}CT<^{3}LE. The most prominent configuration is where all three states are degenerate, and thus mixing is most effective.[97]

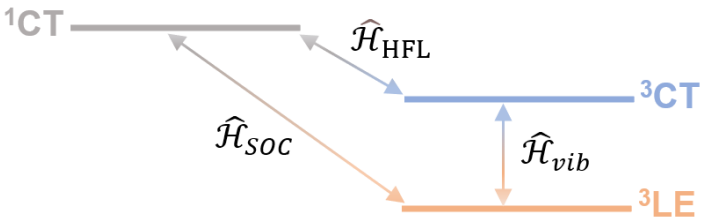

Figure 8. The simplified model Hamiltonian scheme representing the most important states for TADF and coupling between them. Adapted from [95].

If a CT TADF system possesses a sufficient SOC between triplet and singlet states as well as the sufficient spin-vibronic coupling between states of the same multiplicity, then, again, the most important factor which will define the efficiency of TADF is the energy gap between singlet and triplet states, as briefly discussed in the beginning of the section. Thus, while studying TADF type emitters, it is crucial to correctly determine ΔE_{ST}. There are two most

widely adopted experimental methods for the latter task. The first and the most straightforward approach to define the energy difference is to identify the optical gap from the onsets of fluorescence and phosphorescence spectra, though, in some cases this strategy may provide inaccurate results. The second approach relies on the Arrhenius equation and is obtained as an activation energy by plotting and fitting the integral of delayed fluorescence spectra (or the k_{RISC} constant) versus reciprocal temperature.[99]

The obtained ΔE_{ST} values by different approaches does not necessarily match, as repeatedly reported by several groups.[100,101] Indeed, due to nonadiabatic coupling, the equilibrium between T_1 and T_2 of different characters (^{3}LE and ^{3}CT) can be formed. It leads to a significant population transfer and thus, the energy gap S_1-T_2 starts to dominate over S_1-T_1, meaning that activation barrier for TADF is lowered and thus does not correspond to the optical gap.[102] Importantly, the TADF model is not necessarily limited to three excited (LE or CT) singlet and triplet state levels and, depending on the molecular system, can additionally include intermediate ππ* or nπ* triplet or higher lying nπ* singlet states.[98,103] However, even if excellent TADF properties have been demonstrated in such kind of system, their analysis and understanding remains very complex as the intermediate states are spectroscopically invisible and thus, only high-level quantum chemistry calculations can help to gain knowledge on the mechanism.

So far, the discussed TADF parameters and processes are mainly dependent on the molecular structure and its geometrical arrangement. However, the involvement of multiple excited states with different characters (both, LE and CT) as well as the presence of labile fragments means that the environment parameters, such as polarity, rigidity and disorder, especially in terms of solid matrices, are also of a great importance and can significantly change TADF efficiency. Thus the evaluation of environmental effects is critical.[104,105]

As already briefly mentioned in previous sections, TADF can be realized by even more complex approaches, such as hot excitons, based on HLCT type materials,[45,56,106,107] multiple resonance type molecules,[57,108] heterocycles utilizing the n–π* excited state[103] and excited-state intramolecular proton transfer (ESIPT).[109] However, due to successful examples of TADF type emitters, based on sterically hindered spiro-structures or D-A separation via large and twisted spacers, the CT molecules still remain attractive for scientific research.[110–112] Some iconic D-A type TADF active materials are depicted in Figure 9.

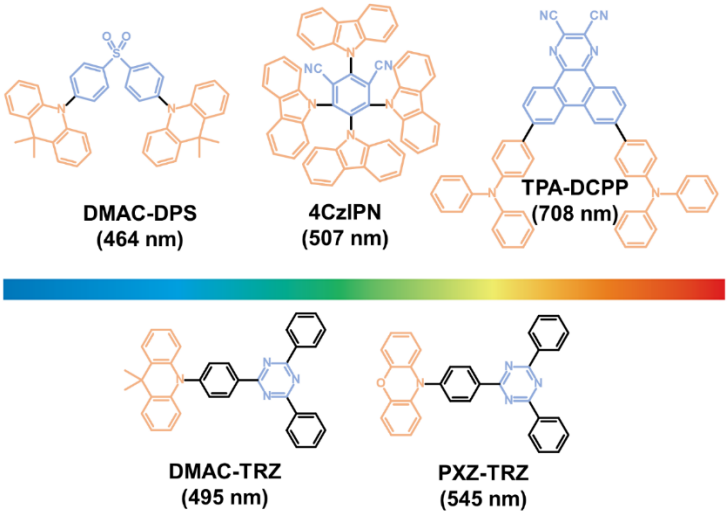

Figure 9. Examples of classic TADF materials containing electron accepting (light blue) and electron donating (orange) units. The colour bar represents the emission wavelength of molecules, also indicated in parentheses. Adapted from [113].

1.4.2 Ultralong RT phosphorescence/afterglow

Phosphorescence, as briefly introduced previously, is a radiative relaxation from T_1 to S_0. If compared to the spin-allowed fluorescence with short emission lifetimes and high quantum yields, the room temperature phosphorescence (RTP) in purely organic compounds demonstrate a relatively long lifetimes and low quantum yields, mainly due to spin-forbidden transition of triplet excitons. Furthermore, triplet excitons are efficiently de-activated by collisions with solvent molecules or quenched by oxygen, moisture, or impurities. Consequently, phosphorescence is usually observed at low temperatures and/or in a rigid environment, well-protected from oxygen.[8,20,114] If observed at room temperature, phosphorescence lifetimes are usually in a range from several hundred microseconds to several milliseconds. Phosphorescence is considered to be ultralong, if its lifetime is longer than 100 ms at room temperature.[115] Organic ultralong RT phosphorescence (OURTP) is also referred to as organic afterglow, however, this term is sometimes used to describe persistent luminescence, caused by charge separation and recombination.[116] In this work the term organic afterglow will only be used as a synonym for ultralong phosphorescence (and persistent TADF, *vide infra*).

Due to long-lived excited triplet states and large Stokes shift, the OURTP phenomenon found its applicability in sensing, imaging, data encryption,[51] etc. (see 1.4.3 Applications for more examples), and thus, became of a particular interest among scientific community. For the successful application, phosphorescence should be not only long, but also, an efficient (>5%). These two tasks are in principle a conflicting design goal. Thus, the exploitation of this phenomenon became interesting not only because of expanded application possibilities for organic molecules, but also because of the fundamental interest. The reader has to note that long-lived triplet states are not necessarily related to CT-type molecules (as it is exclusively suitable for TADF). However, the CT-type molecules or more concretely, CT states can find its applicability due to pronounced SOC enhancement or even due to persistent TADF that would help to enhance afterglow QYs. The RTP mechanism and fundamental design principles as well as possibilities to control properties of OURTP materials will be discussed as follows.

Upon optical excitation, the lowest triplet state T_1 is populated via intersystem crossing through the $S_n \rightarrow T_m$ (where m, n≥1) with subsequent $T_m \rightarrow T_1$ internal conversion. Usually, ISC occurs via $S_1 \rightarrow T_m$ due to the fast $S_n \rightarrow S_1$ IC.[117] The equation of phosphorescence efficiency (ϕ_{PH}) (1.5) can be further expressed as follows:[117,118 20]

$$\phi_{PH} = \phi_{ISC} \times \frac{k_r^T}{k_r^T + k_{nr}^T} = \phi_{ISC} \times k_r^T \times \tau_{PH}. \qquad (1.16)$$

In the given expression other non-radiative phosphorescence deactivation channels, such as energy transfer, quenching by oxygen, etc., are neglected. According to the equations $\tau_{PH} = \frac{1}{k_r^T + k_{nr}^T}$ (1.4) and (1.16), it becomes obvious that long and efficient phosphorescence are in principle incompatible: the increase of k_r^T will increase ϕ_{PH} (Eq. 1.16), however, it will simultaneously decrease τ_{PH} (Eq. 1.4). Nevertheless, some general rules how to achieve long and efficient RTP can be introduced.

First, the population of T_1 will be determined mainly by the ISC of $S_1 \rightarrow T_m$ transition, which is governed by SOC. The rate constant of ISC, k_{ISC}, can be expressed as first-order perturbation and short-term approximation:[117]

$$k_{ISC} \propto \left|\langle S|\hat{\mathcal{H}}_{SOC}|T\rangle\right|^2 exp\left(-\Delta {E_{ST}}^2\right). \qquad (1.17)$$

To achieve high phosphorescence quantum yields, the following guidelines may be needed:[117]

(i) Promoting ϕ_{ISC} by increasing k_{ISC} of $S_1 \rightarrow T_m$. The strategy to increase k_{ISC} includes the enhancement of $\langle S_1|\hat{\mathcal{H}}_{SOC}|T_m\rangle$ and

reorganization energy (which describes the contribution of nuclear change during ISC) or the decrease of ΔE_{ST} between S_1 and T_m.

(ii) Decreasing k_{nr}^T by diminishing the nuclear reorganization energy, $\langle T_1 | \widehat{\mathcal{H}}_{SOC} | S_0 \rangle$ and by increasing ΔE_{ST} of $T_1 \rightarrow S_0$.

(iii) Increasing k_r^T by rising ΔE_{ST} and transition dipole moment μ of $T_1 \rightarrow S_0$ transition.

For a long phosphorescence lifetime the reduction of both, k_r^T and k_{nr}^T is required, as per equation (1.4). The latter is strictly in conflict with condition (iii). The condition (i) is the most important for the phosphorescence to take place and be efficient, leaving k_r^T(as well as k_{nr}^T) unaffected. In terms of condition (ii), if the ΔE_{ST} of $T_1 \rightarrow S_0$ is increased, the k_{nr}^T will be reduced, however, the k_r^T would be promoted and vice versa, thus it is again in conflict with long and efficient phosphorescence. In fact, due to the balance of ΔE_{ST} of $T_1 \rightarrow S_0$ and radiative and non-radiative phosphorescence rates, most of the RTP materials demonstrate green to yellow emission afterglow, while the blue or red afterglow colour is hardly reachable.[117] To sum up, a generalized and simplified rule to obtain long and efficient RTP can be defined as follows: (i) the enhancement of ISC between $S_1 \rightarrow T_n$ that dominates ϕ_{ISC} and (ii) suppression of k_{nr}^T that determines τ_{PH}.[118] The efficiency of ISC, again, can be increased by heavy atom effect, heteroatoms or halogen bond incorporation.[119] However, the simplest approach would be to rely on different nature of electronic excited states, thus, molecules with CT states may become of a particular interest. The reduction of k_{nr}^T is mainly achieved through a rigid environment, protected from external factors (e.g. oxygen). A set of strategies, how to supress non-radiative triplet exciton relaxation, has been proposed: crystallization,[120,121] co-crystals,[122] aggregation,[123,124] host-guest doping,[20 12] self-assembly,[125] π-π stacking,[126] hydrogen bond formation with polymers[127] and deuteration.[128] In addition, it is preferable that the lowest excited triplet state would possess a π-π* nature in order to reduce SOC of $T_1 \rightarrow S_0$ transition and thus prolong τ_{PH}.[118] Even more, several studies has demonstrated that persistent TADF may be extremely advantageous for the increased afterglow quantum yield.[129–131] Several examples of recent best results of OURTP phenomenon in chromophore-polymer systems are provided in Figure 10.[127,131–133]

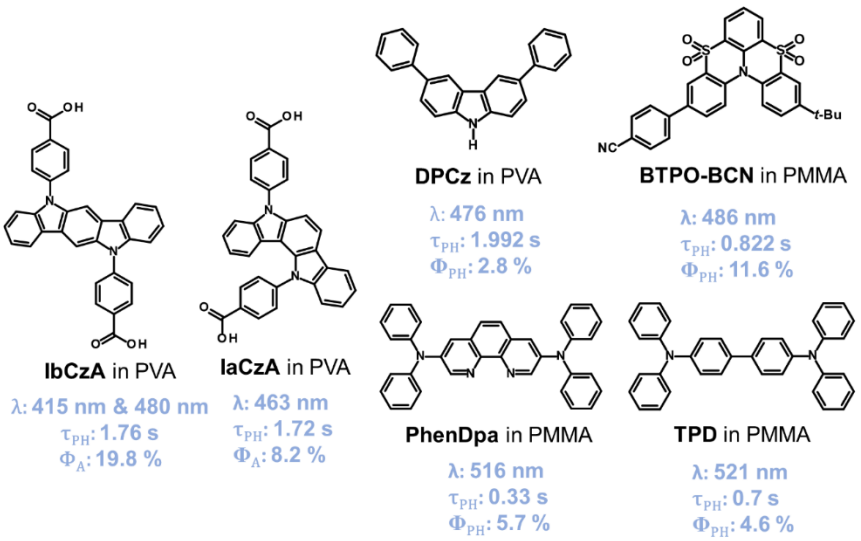

Figure 10. The organic materials demonstrating afterglow emission in chromophore-polymer systems. PVA and PMMA denotes polyvinyl alcohol and poly methyl(methacrylate), respectively. The afterglow emission wavelength, lifetime and efficiency are indicated below each molecular structure.

1.4.3 Applications

The TADF type materials are a hot spot in OLEDs field and remain the most promising approach to harvest excitons in OLED devices. Indeed, stunning results have been achieved in terms of external quantum efficiencies (EQEs): EQE~39% of sky-blue OLED,[134] EQE~39% of green OLED,[135] EQE~28% of deep-red OLED.[136] Nevertheless, some fundamental aspects, such as the lack of device stability and the non-sufficient colour purity, hinder the commercialization of pure TADF emitters, especially for red and blue OLEDs. However, the introduction of hyperfluorescence mechanism, which combines both fluorescent and TADF-type emitters, provides the unprecedented properties of organic molecules for 4th generation OLEDs.[137] The green hyperfluorescence materials are planned to be commercialized in 2023, while red and blue will follow in 2024.[138]

Besides the promising TADF future in commercialization for OLEDS, more potential application fields have been demonstrated that do not necessarily require such high-quality properties as recently discussed. For example, the relatively long TADF lifetimes, compared to prompt fluorescence, as well as the possibility to tune emission colour are the great

advantages to exploit TADF molecules for time-resolved imaging and bio-imaging.[139] Recently, the efficient organic X-ray scintillators have been demonstrated based on classic TADF molecules (DMAC-TRZ, 4CzIPN and 4CzTPN-Bu, see Figure 9 for some of the structures) that provided highly resolved X-ray images. TADF materials in this context are extremely advantageous due to high conversion efficiency, large Stokes shift and full spectral availability.[140] Furthermore, it has been proposed to apply TADF materials for photodynamic therapy (PDT) as it does not need to contain heavy metals.[141] The relatively high triplet quantum yields and long lifetimes are two beneficial features for an efficient triplet to triplet energy transfer activation for the photocatalysis process.[19,139]

Therefore, as from the discussion above, the short lifetimes of delayed fluorescence are of extreme importance for applications in OLEDs, while molecules with longer τ_{DF} lifetimes may find their niche in imaging, PDT or photocatalysis. The phenomenon of OURTP or organic afterglow allows to increase the lifetime of triplet excited states up to tens of seconds (while the afterglow duration can last up to minutes) and more, which in turn extends the field of applications for organic optoelectronic materials. As expected, since long-lived phosphorescence can be effectively differentiated from the background fluorescence, the OURTP compounds have been demonstrated for bio-imaging with high resolution and contrast.[142,143] Although, due to its sensitivity to oxygen, special treatment and preparation of such molecules may be needed.[119] As OURTP compounds have greater excited triplet state lifetimes compared to typical photosensitizers (microseconds to milliseconds), these materials are potentially favourable to greatly extend the collision time and energy transfer for the purpose of singlet oxygen generation. Thus, the properties of OURTP molecules can be applied for PDT.[144] Furthermore, long-lived excited states can be employed for security systems (e.g., anti-counterfeiting),[145,146] information and optical storage,[147] digital encryption and optical recording devices.[148] In the light of exclusive external-stimuli responsiveness, the materials can be successfully applied for oxygen, pH, solvent and temperature sensing.[149]

2. EXPERIMENTAL DETAILS

2.1 Sample preparation

Solutions

The concentration of studied compounds for steady-state absorption and fluorescence and time-resolved fluorescence spectra measurements was selected in a concentration range of 10^{-6}-10^{-5} M. Only spectroscopic grade solvents were used to prepare solutions. All measurements of solutions were carried on using 1 cm quartz cuvettes, except transient absorption measurement, where quartz cuvettes of 1 mm thickness were used. To obtain oxygen free environment for solutions, the freeze–pump–thaw method was employed.

Solid-state films

Solid-state samples were prepared with polymer matrixes (polystyrene (PS) or poly (methyl methacrylate) (PMMA)) or non-polymer hosts (mCP or DPEPO) by choosing the relevant solvent to dissolve sample molecules and polymers/host (toluene or chromophore) and by selecting the specific concentrations (percentage by weight wt%). Films were prepared by spin-coating or by drop-casting the solutions (solvent, sample molecule and polymer/host) on the quartz or glass substrates. If the polarity of solid-state samples needed to be variated, the specific amount of camphoric anhydrite was added to solvent-sample-polymer mixture.

In case photophysical experiments needed to be carried on in oxygen-free environment, two approaches were used:

1) Films made in ambient conditions were placed in a vacuum cryostat equipped with a turbo-molecular pump that served as a vacuum chamber;
2) Samples were prepared and encapsulated inside the nitrogen-filled glovebox. Encapsulation was realized by sealing the edges of the glass substrates with epoxy resin prior to conducting various photophysical measurements at ambient conditions.

If needed, the heat-treatment was used to remove residual solvent or to increase the film rigidity. The low-temperature measurements were only performed for solid-state samples in a closed-cycle helium cryostat 204N (Cryo Industries).

Solid-state samples for information recording

Films for information recording were based on the concept presented elsewhere.[150] Stock solutions of 1 mg/mL and 50 mg/mL concentrations in toluene were prepared and mixed with the ration of 1:10 to get the concentration of 0.2 wt% of sample compounds in PMMA. The sample/PMMA mixture was drop-casted (in an amount of 350 μL) on pre-cleaned microscope cover glass slides (24 x 40 mm). The films were left at room temperature for 72 h for the solvent to evaporate. Next, poly(vinyl alcohol) (PVA) was dissolved in distilled water at 5 mg/mL concentration and drop-casted (in an amount of 350 μL) on top of sample (0.2 wt%)/PMMA film to form oxygen barrier layer and left to dry at least for 24 h prior measurements. Films for data encryption were prepared at ambient conditions.

2.2 Photophysical measurements

Steady-state absorption spectroscopy

The absorption spectra were taken on UV-vis-NIR Lambda 950 (Perkin Elmer) or Varian-Cary 5G spectrophotometers using a pure solvent (or empty polymer matrix or non-polymer hosts on a glass for solid-state samples) as a reference. The obtained absorbance (A) is in optical density (OD) units and can be expressed as per equation below:

$$A = -lg\left(\frac{I}{I_0}\right), \tag{2.1}$$

where I_0 and I are intensities of incident and transmitted light, respectively.

The molar extinction coefficient (ε) is expressed as:

$$\varepsilon = \frac{A}{cl}, \tag{2.2}$$

where c is molar concentration of sample molecules in a solvent and l is the pathlength.

Steady-state photoluminescence spectroscopy

Steady-state emission spectra was measured with a CCD spectrometer PMA-12 (Hamamatsu). Samples were excited using a CW xenon lamp coupled to a monochromator. Alternatively, spectrofluorometer FluoroMax-3 was used.

Photoluminescence quantum yields

Fluorescence quantum yields for solutions were determined by the comparative method or by using integrating sphere. Emission quantum yields for solid state samples were determined by integrating sphere.

In case the comparative method was employed, the relative standard was selected according to the expected fluorescence quantum yields as well as the absorption and fluorescence wavelengths: 9,10-diphenylanthracene in cyclohexane (ϕ_{Fl}=0.97),[151] $Ru(bpy)_3^{2+}$ in H_2O (ϕ_{Fl}=0.04)[151] or quinine sulfate in 0.1 M H_2SO_4 (ϕ_{Fl}=0.54)

The concentrations of studied compounds in solvents and relative standard were selected so that OD would be around 0.05. The fluorescence quantum yields were calculated using:

$$\phi_S = \phi_0 \frac{S_S A_0 n_S^2}{S_0 A_S n_0^2}. \quad (2.3)$$

Where ϕ_S and ϕ_0 are the fluorescence quantum yields of the studied samples in solvents and the standard compound as reference, respectively; A_s and A_0 are the absorptions of samples and standard reference compounds, respectively; S_s and S_0 denotes areas underneath the curves of the fluorescence spectra of the sample solution and the standard reference, respectively; and n_s and $n_0$are the refraction indices of solvents for the substance under study and the standard compound.

If higher sample concentration (OD up to 0.1) was used due to low fluorescence quantum yields, the following formula for quantum yield determination was employed:

$$\phi_S = \phi_0 \frac{S_S(1-10^{-A_0})n_S^2}{S_0(1-10^{-A_S})n_0^2}. \quad (2.4)$$

The measurements with integrating sphere (Sphere Optics) were carried on according to the further procedure. Two spectra of different configuration were recorded with PMA-12 (Hamamatsu) spectrometer connected via optical fibre to integrating sphere. The configuration A contains a reference sample inside integrating sphere. The configuration C is measured with the sample of interest in the same position as A. The recorded spectra are divided into two regions: L (the excitation light region) and P (emission region). The observed emission quantum yield can be calculated by integrating regions in both configurations and further using the expression below:[152]

$$\phi^{obs} = \frac{P_C - P_A}{L_A - L_C}. \quad (2.5)$$

To obtain correct quantum yields, the re-absorption needs to be corrected. First, the "true" emission spectrum needs to be recorded outside the integrating sphere. The long tail of this spectra is matched with the tail of emission spectra from integrating sphere. The difference of two integrated spectral areas corresponds to re-absorbed area a_{reab}. The correct quantum yield is then described according to FLS980 Series Reference Guide (by Edinburg Instruments):[153]

$$\phi_{FL} = \frac{\phi^{obs}}{1-a_{reab}+a_{reab}\times\phi^{obs}}. \quad (2.6)$$

The phosphorescence (or afterglow) quantum yields were determined by peak-differentiation-imitating method.

Time-resolved photoluminescence spectroscopy

Time-resolved emission spectra and its decay transients were recorded by selecting the measurement equipment suitable for the required time range.

Picosecond to nanosecond range. Time-resolved emission measurements in a picosecond time domain were performed with Streak Scope C10627 detector (Hamamatsu) coupled with femtosecond laser Pharos-SP (Light Conversion, 190 fs, 10 kHz) and wavelength-tunable optical parametric amplifier Orpheus (Light Conversion).

Alternatively, a Ti:sapphire laser system emitting pulses of 0.6 mJ and 30 fs at 800 nm and 1 kHz pulse repetition rate (Femtopower Compact Pro) with Light Conversion Topas-C optical parametric generator and frequency mixers was used to excite the samples at chosen wavelength. The fluorescence was collected by reflective optics and focused with a spherical mirror onto the input slit of a spectrograph (Chromex 250) coupled to a streak camera (Hamamatsu 568).

Nanosecond range. The fluorescence lifetimes were estimated by time-correlated single photon counting (TCSPC) system PicoHarp 300 (PicoQuant). Pulsed semiconductor laser diode (PicoQuant, repetition rate 1 MHz, pulse duration 70 ps, emission wavelength 375 nm) or pulsed light emitting diode (PicoQuant, repetition rate 1 MHz, pulse duration 500 ps, emission wavelength 330 nm) were used to excite the samples.

Nanosecond to millisecond range. Time-resolved emission spectra, fluorescence decay transients and phosphorescence spectra in this time range were recorded with time-gated intensified CCD camera iStar DH340T (Andor) with a spectrograph SR-303i (Shamrock). For sample excitation, the camera is synchronized with nanosecond YAG:Nd^{3+} laser NT 242 with an

optical parametric generator (Ekspla, pulse duration 7 ns, repetition rate 10 Hz – 1 kHz). The setup allows to exponentially increase the delay and integration time of gated iCCD camera.

Millisecond to second range. To measure decay transients in seconds, the Andor camera setup was upgraded with a synchronized shutter. The shutter hardware was composed of repurposed HDD Head Stack Assembly (HSA) wrapped in 3D-printed case paired with ATmega32U4 microprocessor with home-written firmware to synchronize it with Andor software. This allowed to control the excitation and spectral integration times from 25 ms to tenths of seconds and more.

Transient absorption spectroscopy

Femtosecond time-resolved differential absorption (TA) measurements were performed using a Harpia pump-probe spectrometer (Light Conversion) pumped with a 10 kHz pulsed laser Pharos-SP (Light Conversion). The probe source was white light continuum generated by focusing 190 fs 1030 nm laser pulses onto a sapphire crystal or onto the quartz cuvette with purified water coupled to home-built flow system. Pump wavelength was set in accordance with sample absorbance using an optical parametric amplifier Orpheus (Light Conversion). Global analysis of TA data was performed by data analysis software "CarpetView" (Light Conversion).

2.3 DFT modelling

Quantum chemical calculations of studied derivatives were performed using DFT and TD-DFT implemented in the Gaussian 16,[154] Gaussian 09W or ORCA 5.0.3[155,156] software packages. Ground state optimization, ground- to excited state transition energies, oscillator strengths, emission energies and HOMO and LUMO orbitals were calculated with one of the selected functionals: BMK functional at a 6-31g (d,p) basis set level, B3LYP functional at 6-31G(d) basis set or CAM-B3LYP method at 6-31g(d,p) or 6-311G(d) theory level. Spin-orbit coupling matrix values of triplet and singlet states were evaluated with CAM-B3LYP/6-311G(d) using ORCA 5.0.3 software. Multiwfn 3.8 software was used to generate natural transition orbitals (NTOs).[157] The solvent surrounding was simulated using linear response polarized continuum model (LR-PCM).

3. RESULTS AND DISCUSSION

The research presented in this thesis is devoted to the photophysical study of intramolecular charge transfer materials. Each section is related to specific Paper and can be sub-categorized in accordance with the acquired excited states of different multiplicity – singlet states (sections 3.1 and 3.2) or singlet and triplet states altogether (sections 3.3, 3.4 and 3.5).

Five different series of molecules are presented that comprise different ways to control the excited state dynamics. In the first Paper, the singlet states are controlled through introducing twisted intramolecular charge transfer states by appropriate combination of electron A and D units through π-conjugated linkers. The second Paper presents unique molecular structures with asymmetrically attached identical electron donating branches, that ensured the dual-band fluorescence and the presence of intermolecular PET upon complexation with metal ions. The rest of the papers represent the sophisticated interplay between triplet and singlet states. Papers 3 and 4 contain the photophysical study of TADF active materials, where the specific control of targeted parameter was realized by minor changes in molecular structures. In Paper 5, complex systems with weak electron donors are presented, where delicate arrangement of higher-lying CT excited states of different manifolds ensured the possibility to manipulate processes between singlet and triplet states for efficient afterglow emission in single molecules.

Each presented section contains a brief introduction of studied organic compounds, the description on how singlet or triplet state properties, and, consequently, the present photophysical processes were controlled, the representation of electron accepting or donating groups used to design molecular structures and key findings of a relevant Paper. The perspective to possible applications as well as conclusions are also provided.

3.1 D-A compounds with TICT character by design: the study of twisting and dynamic solvation (dimethylaniline-naphthalimides)

According to Paper I, a comprehensive study of two new A-π-D fluorophores specially designed to realize twisted intramolecular charge transfer character was performed. Both molecules contain electron acceptor 1,8-naphthalimide (NI) and electron donor dimethylaniline (DMA) units connected through two types of linkers at 4th position of NI core: single bond (NA1) or acetylene-like junction (NA2) (Figure 11). The molecular design of NA1 and NA2 ensures the different pre-requisites of compounds for the photophysical study: pre-twisted (NA1) or planar (NA2) ground state

geometries, different conjugation length and different molecular dipolar moments in the excited state. In this Paper, singlet state properties are controlled through molecular geometry which may possess TICT character upon excitation, as well as by environmental factors (the polarity or rigidity). The manipulation of excited state properties in such way together with steady-state and time-resolved experiments allowed to comprehensively study the excited state dynamics, or more precisely, to differentiate the spectral effects produced by dynamic solvation or by geometry changes in the excited state, and to reveal TICT formation pathways.

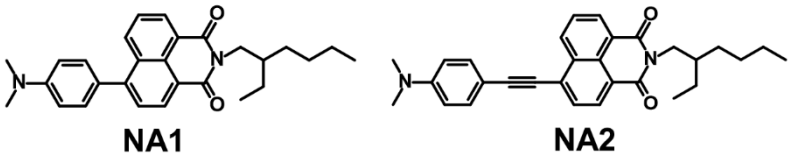

Figure 11. Molecular structures of studied NA1 and NA2 compounds.

Selected materials

1,8-Naphthalimides (NIs) are well-known electron acceptors and are considered among the most important building blocks of efficient fluorescent materials.[158] Due to relative simplicity of synthetic operations for targeted modification,[159,160] tunable photophysical properties,[161] photo[162] and thermostability[161,163] and biocompatibility,[164] NI materials have gained a tremendous attention among scientific community and became a highly adaptable scaffold with a huge diversity of proposed real life applications:[165] from optoelectronic devices to bio and chemosensors[166,167] or fluorescent cell imaging agents.[168] Having in mind a redox potential of 1,8-naphthalimide core (~-1.8 V, vs Ag/Ag^+)[169], many of strategies for the mentioned applications cover the simple design of adding electron donating substituent to NI core at its 4th position to create the donor-acceptor (D-A) type compounds with a CT character. One of the classic electron-donating substituents is N,N-dimethylaniline (DMA) with a redox potential of at least 0.65 V (vs Ag/AgCl)[170] may serve as a perfect charge donor with a high driving force for the intramolecular charge transfer upon combination with NI core through selected linkers.

Key findings and potential application

Both molecules demonstrate a charge transfer character whether in partially planar (NA1)/planar (NA2) or twisted excited state geometries, that significantly depend on parameters of the environment. The molecules are pre-twisted or planar in non-polar solvents and thus, high fluorescence quantum yields up to 70 % are observed. However, the increase of solvent polarity determines the competition between CT and TICT states. Once the TICT state is dominant in solvents with $\varepsilon>6$, the efficient non-radiative decay channel is enabled which determines up to three orders of magnitude drop of fluorescence quantum yields (down to 0.1% for NA1 and to 0.03% for NA2 in acetonitrile with $\varepsilon=37.5$) and the decreased fluorescence lifetimes (from 3.4 ns and 6.3 ns in cyclohexane with $\varepsilon=2.02$ to 70 ps and 40 ps in acetonitrile for NA1 and NA2, respectively). Contrary, in the polymer matrix with $\varepsilon=8.31$, where TICT reaction is restricted, fluorescence quantum yields remain comparatively high (ca. 30 % - 40 %) along with increased fluorescence lifetimes (9.5 ns for NA1 and 5.5 ns for NA2) due to more stabilized CT states. The transient absorption spectroscopy confirmed the results obtained by steady-state and time-resolved fluorescence measurements and revealed that different channels exist to reach TICT states: whether from CT states in Franck-Condon region or from solvated CT states. In the case TICT is formed directly from FC region, its reaction rate outcompetes the dynamic solvation. The pre-twisted geometry of compound has no influence in terms of excited state reaction rates. On the other hand, the higher excited state dipole moment determines the faster excited state processes. Figure 12 illustrates time-resolved transient absorption maps of both compounds in ethyl acetate ($\varepsilon=6.02$) reflecting pre-twisted or planar molecular geometries at the early-time scale (up to 1 ps) and the formation of TICT states (from 1 ps) upon excitation. The TICT reaction rates are also indicated in the picture.

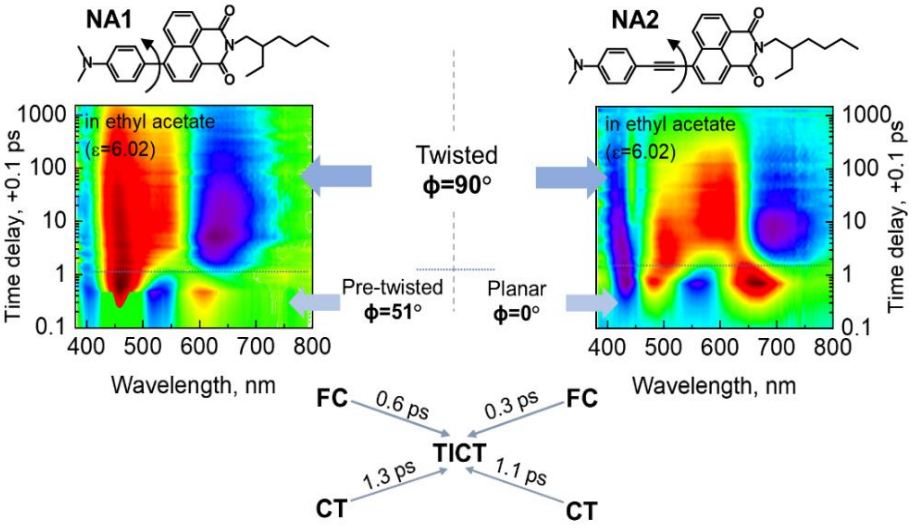

Figure 12. Transient absorption maps of NA1 (left) and NA2 (right) in ethyl acetate. The time constants for TICT state formation either from Franck-Condon region (FC) or from CT states are indicated in the picture.

Although not discussed in the referred Paper, NA1 and NA2 materials may serve as perfect polarity probes. The sensing could be realized by relying on the extreme Stokes shift (through all the visible wavelength range up to 8601 cm^{-1}), the decreased fluorescence quantum yields or lifetimes upon the environment's polarity increase. Figure 13 illustrates the fluorescence color changes of NA1 in solvents of different polarity.

Figure 13. The photograph of NA1 in solvents of different polarity upon excitation.

Conclusions

(i) The TICT state formation in A-π-D type naphthalimide-π-dimethylaniline compounds in polar solvents (ε>6) determines the efficient non-radiative decay channel, which in turn causes the drop of fluorescence quantum yields up to three orders of magnitude and the decreased fluorescence lifetimes. The significant red-shift of fluorescence spectra may be beneficial for the creation of polarity probes.
(ii) The rigid environment created by doping compounds in polymer matrix and the possibility to change its polarity allowed to identify TICT reaction and to distinguish between the competing excited state processes in the early-time scale.
(iii) TICT state can be formed either from solvated CT state (after the dynamic solvation is completed) or directly from Franck-Condon state with the reaction rate outcompeting the dynamic solvation.

3.2 Dual branch D-A-D' systems with complexation induced intermolecular PET (purine-based compounds)

According to Paper II, the photophysical study was performed for four 2,6-bis-(1,2,3-triazol-1-yl)purine derivatives (**1**-**4**), asymmetrically decorated with two identical fragments at C2 and C6 positions: electron accepting methyl carboxylate (**1**) or electron donating phenyl ring (**2**), 4-methoxyphenyl (**3**) or 4-N,N-dimethylaminophenyl (**4**) (see Figure 14). The asymmetrical substitution of identical electron donating subunits ensured the possibility to create D-A-D' type molecules possessing two independent electronic charge transfer (CT) systems resulting in dual-band fluorescence (molecules **3** and **4**). In this Paper, the control of singlet states is realized through different substituents that cause the appearance of intramolecular CT character in case electron donating units are attached to triazolyl-purine core. The properties of singlet CT states were further altered by the polarity of solvent. Finally, the selected molecular design with triazole fragments used as linkers for electron donating branches, ensured the possibility for molecule **3** to form complexes with metal ions, which further assisted in the control of singlet state properties, or more precisely, the blue side fluorescence band quenching caused by intermolecular PET.

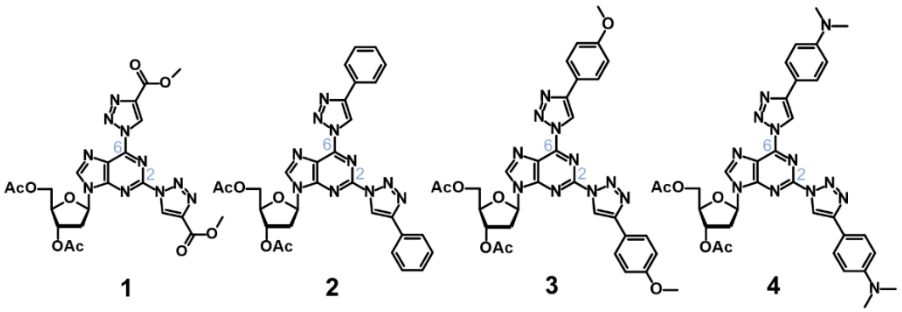

Figure 14. Chemical structure of bis-triazolyl-purine nucleoside derivatives with electron accepting (**1**) and electron donating (**2**, **3**, **4**) substituents.

Selected materials

The development and research of fluorescent nucleobase (purine or pyrimidine) analogues have been a subject of high interest for decades due to their biological and medical importance.[171] Purines as nitrogen heterocycles are starting materials widely available in natural product pool and are readily accessible for chemical modifications that can alter their photophysical properties dramatically. The electron donating functional groups may be coupled at C2, C6 or C8 positions of purine core. Some of the desired optical properties of purine push-pull derivatives have been achieved due to the progress of synthetic methods and their integrity.[172,173] Purine derivatives have already been demonstrated as emitters in OLEDs,[174–176] as pH sensors[177] or even as imaging tools of cell compartments[178] and its environment.[179] Additionally, purine derivatives are natural-like molecules that can be easier recognized by cells.[180]

The electron donating parts such as anisole and dimethylaniline are considered to be general for push-pull systems[24] and may be selected based on its strength. Purines, on the other hand, are known to be ambipolar,[181] however, using them as electron accepting units may provide with several advantages.

Key findings and potential application

The steady-state and time-resolved experimental results, and theoretical calculations of **3** and **4**, as well as the comparison with other molecules bearing electron accepting or weak electron donating substituent (**1** and **2**, respectively), allowed to determine and confirm the nature of two bands in the emission spectra both corresponding to CT states. Apparently, the blue band

of fluorescence spectrum emission is related to the transition within the C2 branch (referred to as the “blue” branch), while the red side band of emission is caused by charge transfer in the C6 branch (the “red” branch). See Figure 15 for the fluorescence spectral composition according to spatial distribution of molecular orbitals of compound **3** in acetonitrile.

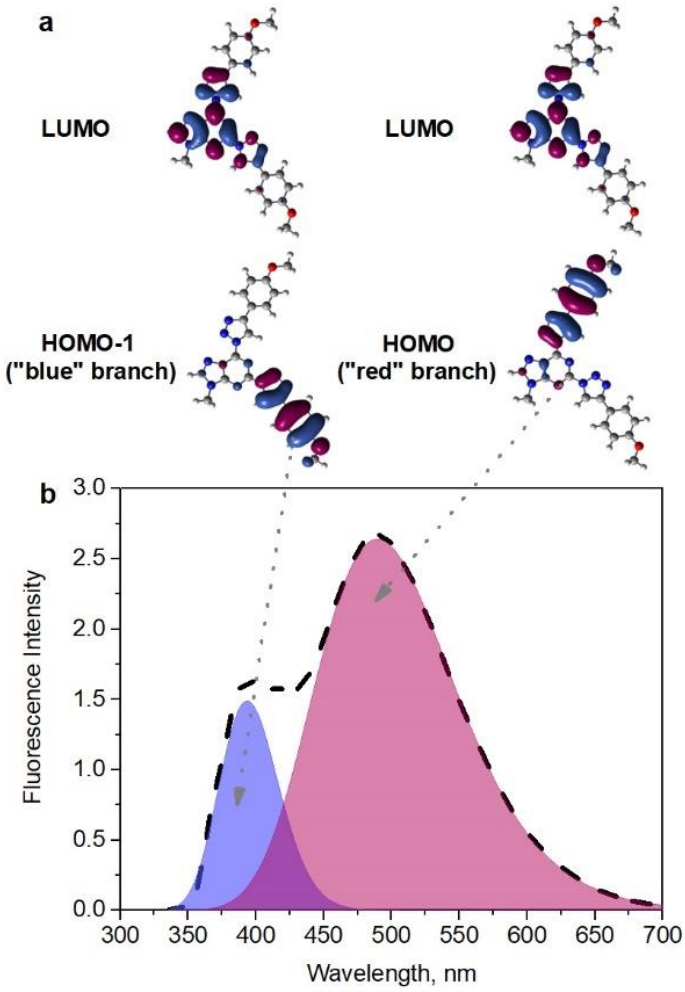

Figure 15. Spatial distribution of HOMO – LUMO and HOMO-1 – LUMO molecular orbitals of compound **3** (a) and the composition of fluorescence spectra, consisting of distinct charge transfer states within “blue” or “red” branches (b) of **3** in acetonitrile.

The different strength of electron donating substituents determined the absorption and fluorescence spectra positions, the fluorescence spectral separation between different states, and fluorescence quantum yields with lifetimes. The strong electron donating 4-N,N-dimethylaminophenyl substituents (referred to as dimethylaniline in previous sub-section) determined the most expressed spectral separation between two CT states related to different branches (recorded fluorescence maxima at 513 nm and 653 nm). However, at the same time the drastic fluorescence quenching is observed as the fluorescence quantum yield of compound **4** is only 0.1% in most polar acetonitrile. On the other hand, electron donating 4-methoxyphenyl groups in compound **3** contribute to comparatively high fluorescence quantum yield (QY=20% in acetonitrile) along with sufficient spectral separation between two fluorescence bands (fluorescence maxima at 393 nm and 490 nm). Based on these properties, compound **3** was selected to demonstrate the ratiometric fluorescence chemosensor.

The presence of nearby triazoles used as spacers for electron donating and accepting fragments further assisted in the complexation with metal ions. Compound **3** revealed a bidentate coordination mode: Ca^{2+} is coordinated between both triazoles, while Zn^{2+} forms a complex between the triazole at C6 and N7 of the purine. The complexation with both metal ions occurs with the equivalence point of one metal ion with three purine molecules. The coordination resulted in the gradual decrease of blue fluorescence band intensity, while the red one remained almost unchanged. In was concluded, that the assembly of materials around metal ion as well as small energy difference between HOMO and HOMO-1 of each branch ensure favourable conditions for PET to take place between “blue” and “red” branches of different molecule. Thus, a proof-of-a concept of ratiometric chemical sensor for Ca^{2+} and Zn^{2+} ions with intermolecular PET was demonstrated. The changes of fluorescence spectra in the presence of different Zn^{2+} concentrations in acetonitrile, the complexation mode with Ca^{2+} and Zn^{2+} as well as illustration of PET along with its scheme are illustrated in Figure 16.

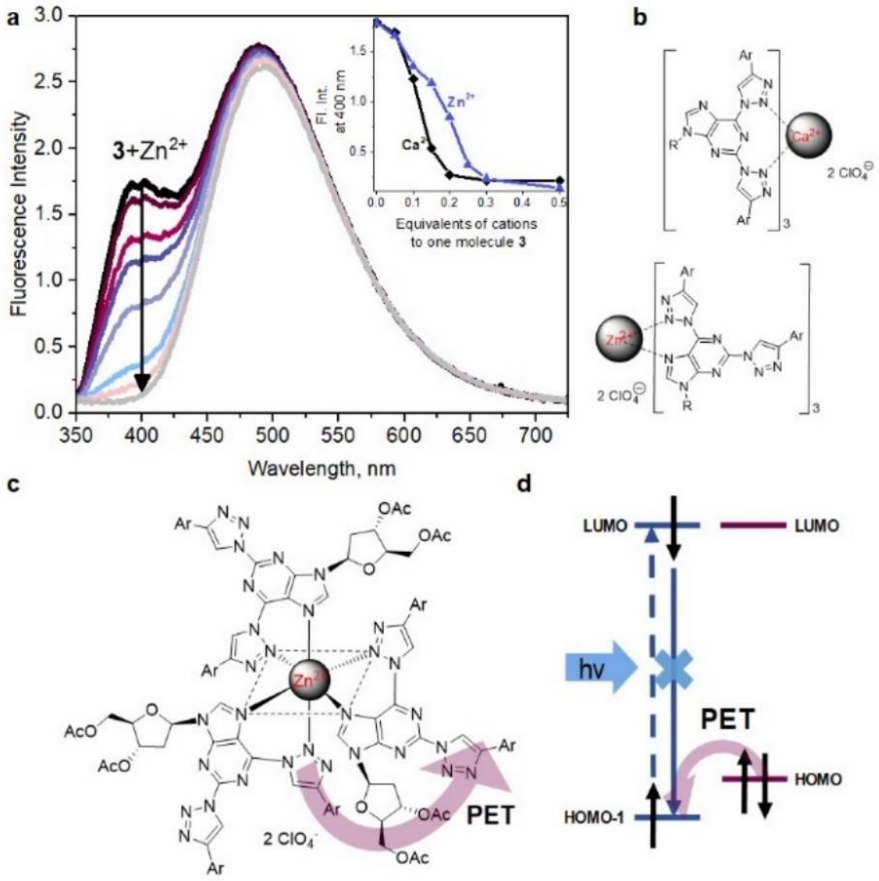

Figure 16. The illustration of intermolecular PET ratiometric chemical sensor based on D-A-D' compound **3**. The fluorescence spectra upon addition of Zn^{2+} of **3** in acetonitrile (a), the coordination mode of **3** with Ca^{2+} and Zn^{2+} (b) and the illustration of PET process (c) along with energy level arrangement of HOMO (HOMO-1) – LUMO levels of different branches (d).

Conclusions

(i) D-A-D' asymmetric structure of purine-based compounds ensured dual band fluorescence from two distinct CT states related to each of the electron donating branches.

(ii) The strong electron donor 4-N,N-dimethylaminophenyl determined pronounced fluorescence intensity quenching in most polar solvent, while weaker electron donor 4-methoxyphenyl ensured relatively high fluorescence quantum yield and the sufficient separation between spectral bands.

(iii) PET occurs between D and D' fragments of neighbouring ligands assembled upon complexation with metal ions and is responsible for the quenching of the blue fluorescence band. Based on this process, a proof-of-a-concept of ratiometric fluorescence cation senor is demonstrated.

3.3 Electron A and multiple D derivatives for efficient control of triplet quenching to enhance TADF performance (benzophenone-carbazoles)

In Paper III, the selected CT-type molecular structures demonstrate the delayed fluorescence attributed to an efficient TADF process. Both compounds contain five electron donating carbazolyl groups and an electron accepting benzophenone (5tCzBP) or methyl benzoate (5tCzMeB) and are decorated with *tert*-butyl groups at C3 and C6 positions of carbazole moieties to reduce concentration quenching and enhance morphological stability as well as solubility (Figure 17). In this Paper, the control of singlet and triplet state properties and thus, the performance of TADF, is realized through controlling k_{nr}^{T}, as the experimental study revealed that the main non-radiative deexcitation channel is related to the decay of long-lived triplet states. The non-radiative triplet decay rate itself can be manipulated via structural changes: the replacement of loose phenyl moiety by the methoxy group in electron accepting benzophenone fragment ensured the significant suppression of triplet quenching.

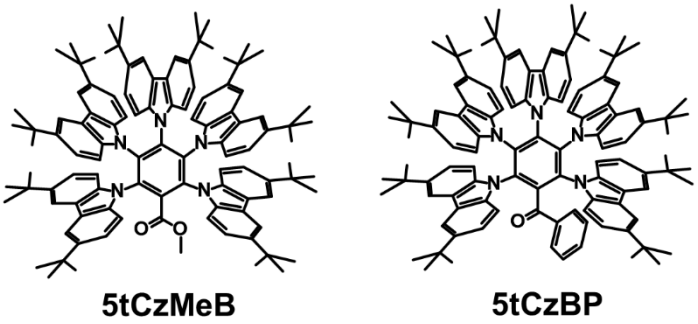

Figure 17. Molecular structures of TADF-type emitters 5tCzMeB and 5tCzBP.

Selected materials

Carbazole units demonstrate great stability, easily accessible functionalization, and excellent hole transport properties.[182] The combination of carbazoles with appropriate electron acceptors, such as benzonitrile or phthalonitrile, leads to the creation of organic systems for TADF with

increased excited state delocalization and thus enhanced k_{RISC}.[183] It was shown that k_{RISC} can be further improved by decorating carbazolyl units with phenyl or methoxy groups at 3rd and 6th positions.[184] The bulky *tert*-butyl groups at the same positions may assist in increasing device lifetime.[185]

Benzophenone is a widely used building block for blue TADF emitter with good electron accepting properties.[186,187] However, it is known that benzophenones with loose phenyl moieties are responsible for non-radiative decay of long-lived excited states in TADF emitters, which cannot be completely suppressed even in solid state matrix.[188,189]

Key findings and potential application

By the means of theoretical calculations, it was determined that carbazole groups in each molecule are sterically twisted by 60° -70° towards central phenyl fragment. Such molecular geometry ensured strong spatial separation between HOMO and LUMO orbital distribution and thus, the sufficiently small ΔE_{ST} (0.08 eV for 5tCzMeB and 0.10 eV for 5tCzBP). On the other hand, the maintained small orbital overlap determined moderate oscillator strengths and thus decent k_r values (3.30×10^6 s^{-1} for 5tCzBP and 1.02×10^7 s^{-1} for 5tCzMeB). The existence of TADF was identified by time-resolved experiments in oxygen saturated and oxygen deficient environments and further confirmed by the measurements of photoluminescence intensity as a function of excitation power density.

High k_{RISC} is considered to be the main parameter to achieve efficient TADF. Both compounds examined in this study possess similarly high k_{RISC} values (3.81×10^6 s^{-1} and 4.44×10^6 s^{-1} for 5tCzBP and 5tCzMeB, respectively). However, it was estimated that ϕ_{RISC} differs almost twice: 53% for 5tCzBP and 93% for 5tCzMeB, meaning that *triplets* are quenched more efficiently in the case of 5tCzBP. The substitution of loose phenyl moiety in the benzophenone by a methoxy group enabled to sufficiently suppress non-radiative triplet quenching, mainly caused by the torsional/rotational displacement of loose phenyl moiety, that is reflected in one order of magnitude lower k_{nr}^T value in terms of 5tCzMeB (0.33×10^6 s^{-1}) if compared to 5tCzBP (3.32×10^6 s^{-1}). These structural modifications benefitted in complete harvesting of triplet excitons via RISC resulting in almost unity photoluminescence quantum efficiency of 5tCzMeB. The energy level diagram with energy transfer routes and most important parameters for TADF performance is provided in Figure 18 along with the contribution of prompt fluorescence and delayed fluorescence to overall emission transients.

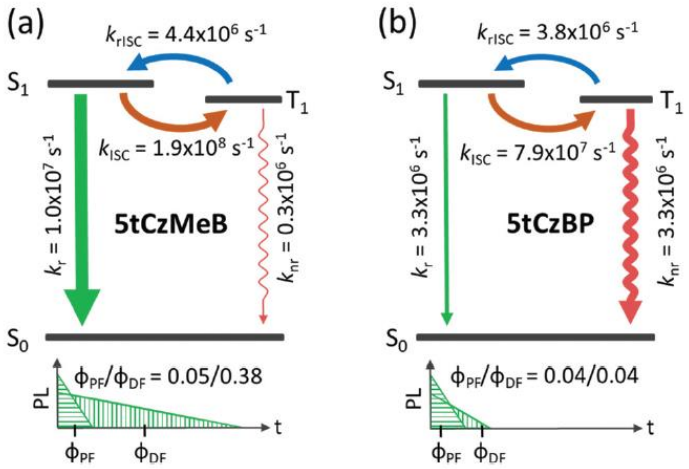

Figure 18. Energy level diagrams representing energy transfer routes with rates of relevant processes for compounds 5tCzMeB (a) and 5tCzBP (b) in toluene. Schematic representations of prompt and delayed fluorescence to emission transients for each compound are shown below.

The efficient RISC and large k_r value of 5tCzMeB is extremely advantageous in terms of creating TADF-type materials for application in TADF-based OLEDs. Thus, compound 5tCzMeB was further employed as emitting layer in doped or non-doped OLED device. The 5tCzMeB-based OLED device demonstrated electroluminescence maximum at 481 nm, corresponding to sky-blue emission. The best OLED properties were demonstrated for doped TADF OLED, fabricated by vacuum evaporation technique, as the achieved external quantum efficiency was extraordinarily high with EQE=24.6 %.

Conclusions

(i) The combination of five carbazoles as electron donors with an electron accepting benzophenone or methyl benzoate units resulted in the creation of CT-type molecules possessing efficient TADF.
(ii) The chemical modification of benzophenone by substituting loose phenyl moiety with a methoxy group allowed to significantly suppress triplet quenching as k_{nr}^T was reduced by one order of magnitude.
(iii) The controlled non-radiative triplet decay channel and maintained high k_{RISC} values in carbazole-methyl benzoate compound resulted in near unity

PL quantum yield which allowed to demonstrate TADF-based OLED with sky-blue electroluminescence and high EQE (up to 24.6 %).

3.4 Sterically controlled D-A-D compounds for realization of deep-blue TADF emitters (carbazole-naphthyridine-carbazoles)

In Paper IV, two organic D-A-D materials were designed as blue TADF emitters, containing 1,8-naphthyridine (ND) as electron acceptors and *tert*-butyl-carbazoles (*t*Cz) as electron donors (*t*Cz-ND and Me*t*Cz-ND, see Figure 19). The additional methyl units (Me) were introduced at the first positions of *t*Cz donors in the case of Me*t*Cz-ND. The TADF properties in this case are controlled through H-bonding and CT interaction between D and A units. The involvement of intramolecular H-bonding interactions may increase the rigidity of investigated compounds and thus, reduce the conformational disorder (which usually results in unwanted broadening and/or red-shifting of emission spectra). The D-A interaction and hence the CT character determines the TADF performance, the emission wavelength and a band-width. The CT strength can be further controlled by additionally introducing methyl substituents at the first linking position of *tert*-butyl-carbazole units that alter steric hindrance and thus, twisting of the D an A fragments.

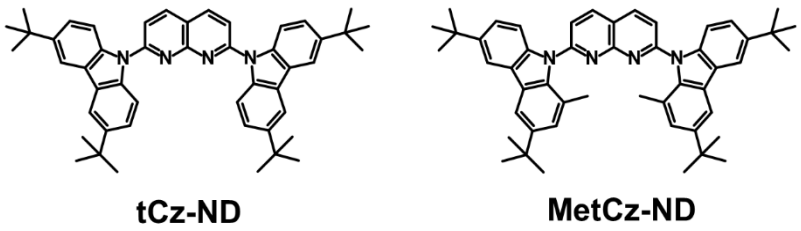

Figure 19. Chemical structures of studied 1,8-naphthyridine derivatives.

Selected materials

1,8-Naphthyridines have been known for a long time and widely explored in a field of medical chemistry.[190,191] Only recently, naphthyridines were successfully used as electron acceptors in the construction of TADF emitters.[192,193] The combination of naphthyridine with a variety of donors, such as acridane, carbazole, phenoxazine and phenothiazine that are regularly employed for designing efficient TADF compounds, produced yellow/green/blue emitters with peak wavelength above 460 nm.[164] Meanwhile, implementing them in efficient OLEDs produced surprisingly low EQE roll-offs.[166]

The unmodified *t*Cz-ND demonstrated a rather weak CT character due to relatively small dihedral angle between *t*Cz donors and ND acceptor, which was calculated to be 31°. Due to additional Me units in the case of Me*t*Cz-ND, the larger steric hindrance and thus dihedral angles of 51° were estimated. This resulted in more pronounced CT character of the compound and thus, the reduced oscillator strength, reduced ΔE_{ST} and slightly more red-shifted and broaden emission spectra (Figure 20 a). The proximity between N atoms of ND acceptor and H atoms of D groups resulted in possible H-bonding interactions. The presence of TADF character in both compounds was confirmed by the oxygen-sensitive fluorescence in solutions with two distinct decay components, corresponding to prompt and delayed fluorescence. Both compounds were found to express small ΔE_{ST} (0.18 eV and 0.09 eV, for *t*Cz-ND and Me*t*Cz-ND, respectively), high photoluminescence QY (76 % and 86 %) and rather short TADF lifetimes (8.8 μs and 3.1 μs) resulting in high RISC rates (0.34×10^6 s^{-1} and 1.06×10^6 s^{-1}). All the mentioned properties were demonstrated in a rigid mCP host (7 wt%). Obviously, the pronounced CT character in the case of Me*t*Cz-ND determined better TADF performance (Figure 20 b). However, the deep blue emission peaking at 452 nm and the narrow emission spectra with FWHM=66 nm in terms of *t*Cz-ND, makes it a perfect candidate for a pure blue TADF OLED. Contrarily, even though Me*t*Cz-ND demonstrate better TADF properties, the sky-blue emission peaking at 480 nm would not meet the requirements for a deep-blue TADF-based OLED.

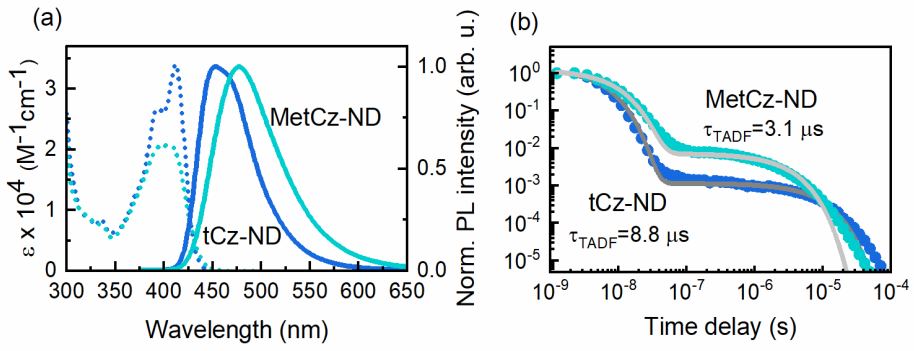

Figure 20. Absorbance in toluene (dotted line) and normalized photoluminescence spectra (solid line) of tCz-ND (blue) and MetCz-ND (cyan) in 7 wt% mCP (a). Photoluminescence decay transients of tCz-ND (blue) and MetCz-ND (cyan) in 7 wt% mCP at room temperature with double

exponential fits (grey) (b). Measurements in solid state were carried on in oxygen-free environment at room temperature.

The studied ND compounds were further demonstrated as TADF emitters for vacuum- and solution-processed TADF OLEDs with low efficiency roll-off in the deep-blue (*t*Cz-ND) or sky-blue spectral ranges (Me*t*Cz-ND). The optimized devices with 7 wt% ND emitters in mCP host delivered up to 17.6 % (Me*t*Cz-ND) and up to 13.5 % (*t*Cz-ND) EQEs for the vacuum- and solution-processed OLEDs, respectively.

Conclusions

(i) The designed D-A-D type carbazole-naphthyridine-carbazole compounds demonstrated deep-blue/blue TADF due to an effective HOMO-LUMO separation by steric hindrance.
(ii) The TADF properties can be altered by changing the CT strength of D-A interaction: the additional substitution by methyl units determines higher dihedral angle between carbazoles and naphthyridine resulting in three-fold higher RISC rate, though, more red-shifted, and broadened emission spectra.
(iii) High photoluminescence quantum yields, blue spectral range of photoluminescence spectra and rather short TADF lifetimes ensured the possibility to employ studied materials for deep-blue or sky-blue OLEDs with EQEs up to 17.6 %.

3.5 Strong A – weak D systems for persistent TADF and RT phosphorescence (diboraanthracenes)

In Paper V, two molecular systems are presented as novel RT afterglow materials. The strong electron accepting diboraanthracene group is combined with weak electron donating mesityl groups to form 9,10-dimesityl-9,10-diboraanthracene (DBA) compounds. The DBA core is laterally expanded by acenaphthylene (anDBA) or phenanthrene units with by *tert*-butyl groups (phenDBA) (see Figure 21). The studied DBA derivatives are not conventional CT-type materials as the lowest singlet and triplet states are of LE excitonic nature. However, the weak electron donating mesityl groups ensured the presence of upper-lying CT excited states. This allowed to fulfil the El-Sayed's rule and thus, the sufficient ISC and RISC between S_n and T_n states ensured long and efficient afterglow emission, comprised of persistent TADF and ultralong RT phosphorescence. The lateral expansion of DBA scaffold by acenaphthylene or phenanthrene units with tert-butyl groups

governed the excited state energies. For example, acenaphthylene units result in more extended conjugation in the polycyclic scaffold of anDBA if compared to phenDBA. The extended conjugation itself determines the lower energies of excited states of anDBA resulting in more red shifted fluorescence and phosphorescence spectra. The afterglow properties can be further tuned by using various concentrations of compounds in a polymer matrix, by annealing the samples or by changing the temperature.

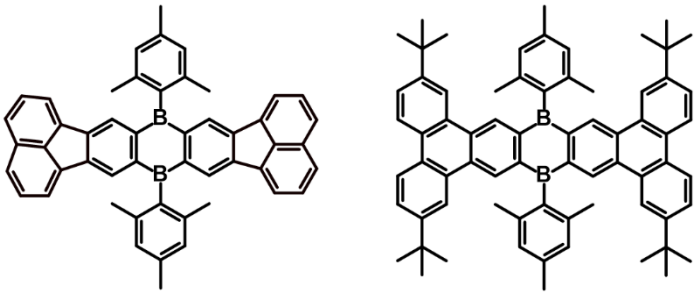

Figure 21. Molecular structures of 9,10-dimesityl-9,10-diboraanthracenes anDBA and phenDBA.

Selected materials

The incorporation of three-coordinating boron into polycyclic aromatic hydrocarbons, such as acenes, creates an electron-deficient system with appealing optoelectronic properties.[195] For instance, 9,10-dihydro-9,10-diboraanthracenes (DBAs) have low energy LUMOs and relatively small HOMO-LUMO gaps that determine their potential applicability as electron-transporting or light-emitting materials in organic optoelectronic devices.[195,196] The functionalization of boron atoms by mesityl groups (9,10-dimesityl-9,10-dihydro-9,10-diboraanthracene (DBA(Mes)$_2$) was found as a good choice in order to overcome several drawbacks of its parent DBA. The mesityl groups sterically hinders the vacant p_z orbitals on boron atoms and protects the B-C bond, thus ensuring the compound stability towards ambient conditions and moisture.[196,197] In addition, the undesired aggregation of molecules is reduced. Recently, it has been shown that further functionalization of mesityl groups by electron donating moieties resulted in green[198] or red[199] TADF emitters with excellent properties.

The presence of long-lived delayed emission in DBA compounds was attributed to ultralong RT phosphorescence and persistent TADF, that in combination are referred to as emission afterglow. The synthetic approach as well as the rigid oxygen-free poly(methyl methacrylate) environment allowed to demonstrate explicit afterglow properties attributed to single molecules: afterglow quantum yields of up to 3 % and 15 %, afterglow lifetimes up to 0.8 s and 3.2 s and afterglow durations up to 5 s and 25 s, for red (anDBA) and blue-green (phenDBA) emitters, respectively. The presence of persistent TADF not only enhances the afterglow quantum yields, but also allows to tune the afterglow colour by simply changing the temperature. The afterglow mechanism is a combination of i) the multiple available channels for an efficient ISC between excited singlet and triplet states of different nature; ii) the lowest excited LE triplet states (T_1) with very low radiative and non-radiative decay rates; and finally, iii) closely lying triplet and singlet states as well as long-lived population of T_1 that both create the possibility for reverse intersystem crossing, causing the appearance of TADF component through intermediate states. Figure 22 illustrates the afterglow spectra of anDBA and phenDBA compounds with main afterglow parameters.

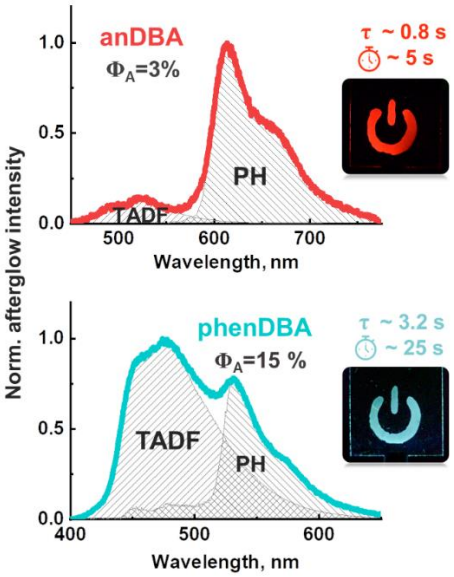

Figure 22. The afterglow spectra of anDBA (top) and phenDBA (bottom) with key afterglow parameters: quantum yield, lifetime, and duration. The photographs of tags with recorded information after the excitation is turned off are also depicted.

The properties of the studied compounds were further tested for information recording. Two tags of different colours with encrypted information were prepared (photographs are given in Figure 22). The tags demonstrate red and cyan afterglow emission up to 2 s and 8 s, for anDBA and phenDBA, respectively. The idea of information recording was based on coating thin DBA layers of 0.2 wt% in PMMA on a glass and covering them with poly(vinyl alcohol) (PVA) layers that serve as an oxygen barrier. The data into these layers can be written by intense laser light and further read by changing the irradiation intensity to a low level (alternatively, a CW light source can be used), as only regions that were previously strongly irradiated are glowing.

Conclusions

(i) A new class of purely organic room temperature afterglow materials are demonstrated based on laterally expanded diboraanthracene scaffold with transversal weak electron donating mesityl groups, determining the appearance of higher-lying CT singlet and triplet excited states.
(ii) The bi-component afterglow emission, combined of persistent TADF and ultralong RT phosphorescence, can be tuned by structural changes and environmental parameters: rigidity and oxygen saturation of samples, concentration of compounds in polymer matrix and temperature.
(iii) The afterglow properties can be successfully applied to create emissive layers (tags) for information recording.

SANTRAUKA

Įvadas

Organinės medžiagos yra ne tik nepakeičiama biologinių sistemų dalis, bet tampa vis labiau neatsiejamos ir nuo mūsų kasdienio technologinio gyvenimo. Cheminės sintezės metu suformuotos organinės molekulės sėkmingai taikomos organinių šviestukų (OLED) gamyboje, kurie, savo ruožtu, jau plačiai ir sėkmingai naudojami pažangiose ekranų gamybos technologijose. Be jau minėtos sparčiai augančios OLED rinkos, organiniai puslaidininkiniai junginiai išlieka patrauklūs ir kitiems potencialiems taikymams. Pavyzdžiui, organinėse saulės celėse; kuriant lengvus nešiojamus prietaisus, įskaitant ir biomedicininius jutiklius su sportu ar sveikata susijusiems rodikliams sekti; taip pat, įvairių temperatūros, drėgmės, slėgio, dujų ir pan. jutiklių vystymui, kurie galėtų būti integruoti į aplinkoje esančius daiktus; ar išmaniųjų etikečių gamybai, kurios pasitarnautų tiek valgomų produktų kokybės kontrolei, tiek įvairaus klastojimo prevencijai.[2–5] Organinių junginių populiarumų bei nenutrūkstamus tyrimus pagrinde lemia jų pranašumai prieš tradicinius neorganinius puslaidininkius: galimybė sumažinti gamybos kaštus dėl paprastos prietaisų gamybos, galimybė kurti aplinkai draugiškas technologijas dėl mažesnių gamybai reikalingų energijos sąnaudų bei lengvai perdirbamų ar biologiškai skaidomų medžiagų panaudojimo.[3,6,7] Galų gale, organinių molekulių panaudojimas kuriant prietaisus leistų išgauti norimą jų funkcionalumą dėl sąlyginai lengvai keičiamų medžiagų savybių cheminės sintezės metodais.

Apskritai, didelė dalis potencialių organinių junginių taikymų yra susiję su molekulių liuminescencinėmis savybėmis. Sužadinus organinius junginius šviesa, liuminescencija gali būti dvejopos prigimties – iš šviesa sužadintų singletinių būsenų (fluorescencija) arba iš sužadintųjų tripletinių būsenų (fosforescencija). Kadangi didžioji organinių junginių dalis pasižymi fluorescencinėmis savybėmis, šis fenomenas buvo aktyviai tyrinėjamas daugiau nei šimtmetį. Tuo tarpu savo prigimtimi draustos tripletinės būsenos ilgai buvo laikomos *tamsiomis* ir nepageidaujamomis, mat fosforescencija retai pasireiškia kambario temperatūroje, o tuo tarpu tripletinių eksitoninių būsenų sukūrimas lemia prastesnes junginių fluorescencines savybes. Šis požiūris į *tripletus* smarkiai pasikeitė atsiradus geresnėms detektavimo galimybėms bei sukūrus organinius metalų kompleksus su našia kambario temperatūros fosforescencija, siekiančia 100 %.[9–11] Įdomu tai, kad tikslingai realizuojant bei išnaudojant singletų ir tripletų būsenas bei procesus, vykstančius tarp šių būsenų, galima gauti labai plačią laikų skalę dengiančias

organaninių molekulių gyvavimo trukmes, kurios toliau gali apspręsti junginių panaudojimo galimybes. Pavyzdžiui, pasitelkiant tik *singletus*, fluorescencijos gyvavimo trukmės realizuojamos nanosekundžių ($\sim 10^{-9}$ s) laikinėje skalėje. Tokios trukmės yra naudingos medžiagas taikant jutiklių ar šviesą emituojančių prietaisų (pavyzdžiui, lazerių ar šviestukų) kūrimui.[13–15] Išnaudojant tiek singletines, tiek tripletines būsenas, galima realizuoti tokius procesus kaip termiškai aktyvuota uždelstoji fluorescencija (TADF) arba tripletų anihiliacija, dėl kurių atsiradusios uždelstosios fluorescencijos trukmės gali siekti mikrosekundes ($\sim 10^{-6}$ s). Tokios trukmės naudingos organinius junginius pasitelkiant OLED kūrimui[16,17] ar taikymams vaizdinimui, fotodinaminei vėžio terapijai bei fotokatalizei.[18,19] Tuo tarpu tripletinių būsenų panaudojimas, o ypač naujų visiškai organinių kambario temperatūros fosforescencijos medžiagų sukūrimas, gali lemti labai ilgai gyvuojančių sužadintų būsenų egzistavimą, kurių gyvavimo trukmės gali siekti nuo mikrosekundžių iki keliolikos sekundžių (10^{-6} s ~ 10^{1} s). Tokios ilgos gyvavimo trukmės atveria visiškai naujas organinių medžiagų taikymo galimybes kuriant saugumo sistemas, informacijos įrašymo, laikymo ir jos kodavimo/šifravimo metodus,[20] o tai, savo ruožtu, lemia dar didesnę konkurenciją su įprastais neorganiniais puslaidininkiniais šviesą emituojančiais diodais.

Vienas pagrindinių veiksnių, lemiančių procesus tarp (šviesa) sužadintųjų būsenų, turinčių skirtingus elektronų sukinius, yra elektroninio šuolio prigimtis. Šio darbo kontekste bei atsižvelgiant į krūvio persiskirstymą prieš ir po molekulės sužadinimo, galima išskirti krūvio pernašos (CT) bei lokaliai sužadintas (LE) būsenas. Vidumolekulinės CT tipo molekulės įprastai kuriamos π-kunjuguotomis jungtimis sujungiant elektronų donorinius (D) ir akceptorinius (A) fragmentus.[21] Šioms molekulėms būdingas jautrumas aplinkos parametrams bei galimybė lengvai keisti funkcines savybes modifikuojant struktūras,[21,24–26] lėmė beprecedentį organinių singletinių CT būsenų panaudojimą kuriant katijonų, anijonų, mažų neutralių molekulių, biologijoje svarbių junginių, aplinkos ar ląstelių poliškumo, pH ar klampos jutiklius, taip pat, kuriant ir pademonstruojant molekulinius rotorius, tyrinėjant netiesinės optikos efektus ar tobulinant fluorescencinės mikroskopijos metodus.[78–80,85,86,88,90] CT molekulių tyrimai tęsėsi ilgus metus ir buvo beprarandantys savo aktualumą, tačiau visiškai neseniai pademonstruotos CT tipo molekulės su labai efektyviu TADF procesu, kuriuo paremtas 3-čiosios kartos OLED prietaisų kūrimas, lėmė minėtų molekulių populiarumo atgimimą.[27–31] Verta paminėti, kad TADF proceso atsiradimas yra daugiausiai nulemtas mažo energijos tarpo tarp singletinių ir tripletinių būsenų (ΔE_{ST}), kuris svarbus efektyviai atgalinei interkombinacinei

konversijai vykti.[32] Pasirodo, kad D-A tipo struktūros yra itin patraukli strategija šiems procesams realizuoti, mat šioms molekulėms būdingas viršutinės užpildytos molekulinės orbitalės (HOMO) bei žemiausios neužpildytos molekulinės orbitalės (LUMO) erdvinis atskyrimas, kuris ir nulems nedidelį ΔE_{ST}.[16,29,30] Turbūt jau įprasta organinėje elektronikoje, kad vienų palankesnių savybių gavimas neigiamai paveikia kitas savybes: minėtas HOMO ir LUMO orbitalių atskyrimas, t.y. maža šių orbitalių sanklota, dažniausiai nulems ir mažesnius fluorescencijos bei uždelstosios fluorescencijos kvantinius našumus.[27] Tad D-A tipo struktūros kūrimas TADF procesui realizuoti – pakankamai sudėtingas uždavinys.

Taigi, akivaizdu, kad norint kurti organinės elektronikos prietaisus, paremtus funkcinėmis organinėmis medžiagomis, labai svarbu gerai suprasti fundamentinius vyksmus sužadintose CT molekulėse ir gebėti tiksliai bei sistemingai valdyti tiek singletines, tiek tripletines būsenas bei tarp šių būsenų vykstančių procesų parametrus.

Darbo tikslas, uždaviniai ir naujumas

Šios disertacijos tikslas – sistemingai ištirti 5 skirtingų vidumolekulinės krūvio pernašos organinių junginių serijų fotofizikines savybes, siekiant suprasti ir gebėti valdyti sužadintose molekulėse vykstančius reiškinius bei numatyti šių junginių galimus taikymus. Atlikti darbai pagal tiriamų molekulinių struktūrų ir juose vykstančių reiškinių sudėtingumą gali būti skirstomi, atsižvelgiant, kokį sukinį turinčios būsenos yra panaudojamos: singletinės ar singletinės kartu su tripletinėmis. Pirmuose dvejuose darbuose bus nagrinėjamos CT junginių serijų singletinės būsenos ir jų valdymo galimybės, realizuojant susisukusią vidumolekulinę krūvio pernašą (TICT) arba dvigubą CT šuolį viename junginyje bei papildomai realizuojant tarpmolekulinę fotoindukuotą krūvio pernašą (PET). Trečiame ir ketvirtame darbe tiriamos CT molekulinės sistemos yra sukurtos taip, kad būtų realizuota termiškai aktyvuojama uždelstoji fluorescencija (TADF), reikalaujanti tiek singletinių, tiek tripletinių būsenų įtraukimo bei preciziško jų valdymo mažam energijos tarpui tarp šių būsenų gauti bei gebėti pagerinti TADF proceso parametrus. Galiausiai, penktame darbe pristatomi naujos klasės junginiai pasižymi labai kompleksiniu tiek singletinių, tiek tripletinių būsenų išsidėstymu, kai svarbu valdyti ne tik žemiausias sužadintąsias, bet ir aukštesniąsias būsenas našios ir ilgos vėlyvosios emisijos (*angl.* afterglow) gavimui.

Norint pasiekti pagrindinį disertacijos tikslą, buvo išsikelti šie uždaviniai, tinkami kiekvienai molekulių serijai:

1. Pasitelkiant laike nuostoviosios ir kintančios emisijos spektroskopijos metodus bei teorinį modeliavimą, nustatyti tiriamų molekulinių serijų sužadintųjų būsenų savybes, dominuojančius procesus bei susijusius parametrus, bandinius ruošiant skirtingose tirpikliuose ir/ar kietoje terpėje, paliekant arba pašalinant deguonį.
2. Palyginti gautus eksperimentinius duomenis ir įvertinti fotofizikinių savybių valdymo galimybes; atsirinkti optimalias molekulines struktūras bei terpes, kuriose paruošti bandiniai, įskaitant tinkamo poliškumo tirpiklį arba tinkamą polimerą sluoksniams ruošti, kitas molekules kietai aplinkai suformuoti ir reikiamą bandinių koncentraciją, kad būtų optimizuotos ir maksimaliai pagerintos vyraujančio proceso savybės.
3. Pademonstruoti tiriamų molekulių tinkamumą potencialiems taikymams poliškumo, katijonų ar temperatūros jutikliams kurti, taip pat OLED prietaisams ar informacijos įrašymo sluoksniams gaminti.

Disertacija parengta kaip 5 mokslinių straipsnių rinkinys. Disertacijos naujumas paremtas naujai susintetintų molekulių moksliniais tyrimais bei iš to sekančiomis išvadomis. Visos disertacijoje nagrinėjamos temos buvo publikuotos moksliniuose straipsniuose, kuriuose pristatomos ne tik naujos organinės medžiagos, bet ir jose vykstantys procesai bei galimybės juos valdyti.

Ginamieji teiginiai

1. TICT būsenos susidarymas 1,8-naftalimido (elektronų akceptorius) – dimetilanilino (elektronų donoras) junginiuose, sujungtuose dvejais skirtingais būdais, nulemia stiprią singletinių būsenų savybių priklausomybę nuo aplinkos parametrų. Tirpiklio bei kietos polimero matricos poliškumo keitimas leidžia atskirti dinaminės solvatacijos ir sąsukos reakcijos nulemtus procesus.
2. Dvejų asimetrinių, tačiau identiškų, elektronų donorų prijungimas prie purino kamieno per triazolų fragmentus leidžia sukurti D-A-D‘ tipo molekules, kurios demonstruoja dvigubą fluorescenciją, priskiriamą krūvio pernašos būsenoms. Spektroskopinės tokių molekulių savybės toliau gali būti valdomos pasitelkiant skirtingo stiprumo donorus, keičiant aplinkos poliškumą ar pasitelkiant kompleksaciją su metalų jonais.

3. Organiniuose junginiuose su elektronų akceptoriniu benzofenono fragmentu sujungtu su penkiais elektronų donoriniais karbazolų pakaitais pasireiškiančio TADF proceso efektyvumą riboja nespindulinis tripletinių sužadintų būsenų gesinimas. Šis gesinimas gali būti nuslopintas struktūriniais molekulės pokyčiais, kai fenilo žiedas yra pakeičiamas metoksi grupe.
4. Karbazolo-naftiridino-karbazolo (D-A-D) tipo junginiuose TADF proceso savybes pagrinde nulemia krūvio pernašos būsenos tarp D ir A fragmentų stiprumas. CT būsena gali būti valdoma pasitelkus donorinių pakaitų geometriją, kuri pasikeis cheminės sintezės metu įterpus papildomas metilų grupes.
5. Šoninių pakaitų prijungimas prie stipraus elektronų akceptoriaus policiklinio diboraantraceno kamieno bei silpnų elektronų donorinių mesitilo grupių įvedimas užtikrina optimalias sąlygas (atgalinei) interkombinacinei konversijai vykti bei ilgai gyvuojančioms tripletinių eksitonų būsenoms egzistuoti. Tokios molekulės dėl savo savybių bei atitinkamo aplinkos parinkimo (kieta, *bedeguonė* polimero matrica) nulemia labai ilgos uždelstosios fluorescencijos bei kambario temperatūros fosforescencijos arba, vėlyvosios emisijos, atsiradimą, kurių savybės gali būti papildomai valdomos molekulinių struktūrų, bandinių koncentracijos, bandinių kietumo ar aplinkos temperatūros pagalba.

Autorės indėlis

Disertacijos autorė atliko didžiąją dalį disertacijoje pateiktų organinių junginių spektroskopijos eksperimentų, ruošė bandinius skirtingais metodais, taip pat apdorojo bei analizavo gautus rezultatus. Daug dėmesio ir laiko autorė skyrė bendroms diskusijoms su disertacijos vadovu bei bendraautoriais, skirtoms rezultatams aptarti bei numatyti tolimesnius reikalingus tyrimus. Taip pat, rengė kai kurias mokslines publikacijas bei koordinavo straipsnių publikavimo procesą. Doktorantūros metais autorė aktyviai užmezgė naujus bendradarbiavimo ryšius su užsienio partneriais bei palaikė kontaktą jau su esamais.

Organinių junginių sintezę atliko Lietuvos ir užsienio partneriai. Naftalimidų junginiai buvo susintetinti dr. Daliaus Gudeikos ir prof. Juozo V. Gražulevičiaus (KTU). Purinų junginių serija buvo susintetinta Latvijos organinės chemijos grupės, vadovaujamos prof. Maris Turks (Rygos technikos universitetas). TADF aktyvūs junginiai buvo susintetinti dr. Edvino Oriento organinės chemijos grupės (VU). Diboraantracenų junginius susintetino Vokietijos mokslininkai dr. Sven Kirschner ir prof. Matthias Wagner (Getės universitetas, Frankfurtas).

Teorinį modeliavimą atliko dr. Alytis Gruodis, dr. Regimantas Komskis ir dr. Gediminas Kreiza (VU). Branduolių magnetinio rezonanso spektroskopijos tyrimus, skirtus metalų jonų-junginių kompleksacijai nustatyti, atliko prof. Maris Turks grupė. Laike kintančios fluorescencijos matavimus pikosekundžių laikiniame ruože atliko dr. Gediminas Jonušauskas (Bordo universitetas) ir dr. Paulius Baronas (VU). Dr. Paulius Baronas taip pat atliko skirtuminės sugerties eksperimentus. Įkapsuliuotus diboraantraceno bandinius, o taip pat ir šiais junginiais paremtus informacijos įrašymo sluoksnius paruošė dr. Steponas Raišys (VU). Disertacijoje minimus organinius šviestukus pagamino bei elektroliuminescencines jų savybes ištyrė dr. Dovydas Banevičius (VU). Dr. Rokas Skaisgiris (VU) patobulino laike kintančios emisijos matavimo įrangą ilgoms gyvavimo trukmėms (>50 ms) nustatyti.

Autorė dėkoja kolegoms už įsitraukimą bei galimybę bendradarbiauti.

Rezultatai ir jų aptarimas

Šioje disertacijoje pristatomi moksliniai darbai apima organinių vidumolekulinių krūvio pernašos junginių fotofizikinius tyrimus. Kiekvienas žemiau aptartas rezultatų skyrius yra susijęs su atitinkama moksline publikacija. Atlikti darbai toliau gali būti kategorizuojami priklausomai nuo to, ar buvo tiriamos tik singletinių būsenų (skyriai 1 ir 2) ar singletinių ir tripletinių būsenų (skyriai 3, 4 ir 5) savybės bei jų valdymo galimybės.

Pirmame skyriuje (ir pirmoje mokslinėje publikacijoje) singletinės eksitonų būsenos yra valdomos pasitelkiant statmena elektronų donorinio ir akceptorinio fragmentų sąsuka vienas kito atžvilgiu, arba, taip vadinamos TICT būsenos realizavimu. Antrame skyriuje pristatomos molekulinės struktūros su dviem nesimetriniais, tačiau vienodais, elektronų donorais, kurie lemia dvigubos fluorescencijos atsiradimą ir tarpmolekulinę fotoindukuotą elektrono pernašą, atsirandančią molekulėms suformavus kompleksus su metalų jonais. 3 ir 4 skyriai apima TADF medžiagų fotofizikinius tyrimus, kai yra pasitelkiamos ir valdomos tiek singletinės, tiek tripletinės būsenos. TADF proceso parametrai gali būti efektyviai valdomi nežymiai koreguojant molekulines struktūras. Galiausiai, 5 skyriuje pristatomos kompleksinės sistemos su silpnais elektronų donorais, kurie nulemia ne žemiausių, kaip įprasta CT tipo molekulėms, tačiau aukštesniųjų sužadintųjų CT būsenų atsiradimą. Šios, savo ruožtu, nulemia tam tikrų procesų tarp singletinių ir tripletinių būsenų atsiradimą, reikalingą ilgai vėlyvajai emisijai realizuoti.

1 skyrius. TICT būsena D-A junginiuose: dinaminės solvatacijos ir sąsukos tyrimas

Pirmoje publikacijoje atlikta išsami dviejų naujai susintetintų A-π-D fluoroforų, kuriuose vyksta TICT reakcija, fotofizikė studija. Abu junginius sudaro elektronų akceptorinis 1,8-naftalimido fragmentas sujungtas su dimetilanilino grupe, panaudojant skirtingas π-konjuguotas jungtis: viengubą jungtį NA1 molekulės atveju ir acetileno-tipo jungtį NA2 molekulės atveju (žr. 1 paveikslą). Pasirinkti molekuliniai fragmentai ir jų tinkamas sujungimas lemia skirtumus tarp molekulių, kuriuos svarbu įvertinti atliekant fotofizikinius tyrimus: NA1 molekulė yra šiek tiek susisukusi savo pagrindinėje būsenoje, kai tuo tarpu, NA2 yra visiškai plokščia; skiriasi molekulių konjugacijos ilgis bei dipolinių momentų pokyčiai sužadintoje būsenoje. Šio tyrimo metu singletinių būsenų savybės yra valdomos pasitelkiant molekulių geometriją, kuri tam tikruose poliniuose tirpikliuose

gali būti nulemta statmenai vienas kito atžvilgiu pasisukusių fragmentų. Taip pat, sužadintųjų būsenų savybes lemia aplinkos parametrai: poliškumas arba kietumas. Tokiais būdais keičiant molekulių savybes bei išnaudojant nuostoviosios bei laike kintančios spektroskopijos metodus, galima atskirti konkuruojančius procesus: dinaminę solvataciją nuo TICT reakcijos bei įvertinti TICT atsiradimo kelius.

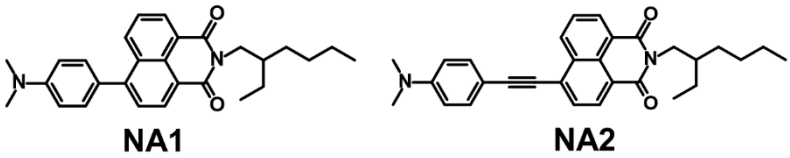

1 paveikslas. Organinių junginių NA1 ir NA2 molekulinės struktūros.

Abu junginiai demonstruoja CT būsenoms būdingas savybes. Nepoliniuose ar mažai poliniuose tirpikliuose molekulių geometrija tik šiek tiek susisukusi (NA1) arba plokščia (NA2). Todėl tokiuose tirpikliuose stebimi aukšti fluorescencijos kvantiniai našumai. Tirpiklio poliškumo didinimas nulemia konkurenciją tarp CT ir TICT būsenų. TICT būsena ima dominuoti tirpikliuose, kurių dielektrinė konstanta (ε) didesnė nei 6. Tuomet atsiranda labai efektyvus nespindulinis sužadinimo gesinimo kanalas, kurio buvimas pasireiškia stipriu fluorescencijos kvantinio našumu sumažėjimu (iki 0.1 % NA1 atveju ir iki 0.03 % NA2 atveju poliškiausiame acetonitrilo tirpiklyje, kurio ε=37.5) bei ženkliai sutrumpėjusiomis fluorescencijos gyvavimo trukmėmis (nuo 3.4 ns ir 6.3 ns cikloheksano tirpiklyje, kurio ε=2.02, iki 70 ps ir 40 ps acetonitrilo tirpiklyje, atitinkamai NA1 ir NA2 molekulėms). Priešingai aptartiems vyksmams tirpaluose, patalpinus medžiagas į kietus sąlyginai aukšto poliškumo polimerinius sluoksnius (ε=8.31) ir taip uždraudus sąsukos reakcijas, fluorescencijos kvantiniai našumai išlieka gana aukšti (apie 30 % - 40 %), o fluorescencijos gyvavimo trukmės pailgėjo (iki 9.5 ns NA1 atveju ir iki 5.5 ns NA2 atveju) dėl labiau stabilizuotų CT būsenų. Skirtuminės sugerties spektroskopijos eksperimentai papildomai leido įvertinti skirtingus TICT formavimosi būdus: tiesiai iš Franko-Kondono būsenos (kai dinaminė tirpiklio solvatacija dar nėra pilnai įvykusi) ir/arba iš CT būsenos (kai dinaminė solvatacija jau yra pilnai įvykusi). Taip pat, šio tyrimo metu paaiškėjo, kad šiek tiek susisukusi molekulės geometrija pagrindinėje būsenoje neturėjo įtakos greitesnei sąsukos reakcijai sužadintoje būsenoje. Tačiau didesnis sužadintosios būsenos

dipolinis momentas (NA2 atveju) lemia greičiau vykstančius fotofizikinius procesus.

Nors ir nepristatyta mokslinėje publikacijoje, atitinkančioje šį tyrimą, NA1 ir NA2 medžiagos galėtų būti taikomas aplinkos poliškumo nustatymui. Aplinkos poliškumo jutimas galėtų būti realizuojamas pasitelkiant ekstremalius Stokso poslinkius per visą regimą spektro dalį (iki 8601 cm^{-1}), sumažėjusios fluorescencijos kvantinius našumus ar gyvavimo trukmes, didėjant aplinkos/tirpalo dielektrinei konstantai.

Apibendrinant tyrimo rezultatus, padarytos šios išvados:

a) TICT būsenos susiformavimas A-π-D tipo naftalimido-π-dimetilanilino junginiuose poliniame tirpiklyje ($\varepsilon>6$) nulemia efektyvaus nespindulinio sužadinimo gesinimo kanalo susidarymą, kuris, savo ruožtu, sumažina fluorescencijos kvantinius našumus ir fluorescencijos gesimo trukmes.
b) Junginių patalpinimas kietuose polimeriniuose sluoksniuose ir galimybė keisti šių sluoksnių poliškumą leido identifikuoti TICT reakciją bei atskirti konkuruojančius sužadintų singletinių būsenų procesus: dinaminę solvataciją nuo sąsukos reakcijos, vykstančius ankstyvuose laikuose.
c) TICT būsena gali susidaryti dviem būdais: iš Franko-Kondono būsenos, kai dinaminė solvatacija dar nėra pasibaigusi, arba iš CT būsenos, kai dinaminė solvatacija jau pasibaigusi.

2 skyrius. D-A-D' molekulinės sistemos su kompleksacijos nulemta fotoindukuota elektrono pernaša (purino junginiai)

Remiantis antrąja publikacija, fotofizikiniai tyrimai buvo atlikti keturiems 2,6-bis-(1,2,3-triazol-1-yl)purino junginiams (**1**-**4**), kuriuose papildomi fragmentai prie purino kamieno prijungti asimetriškai C2 ir C6 pozicijose. Prijungti pakaitai pasižymi elektronų akceptorinėmis (metil karboksilatas, **1** junginys) arba skirtingo stiprumo elektronų donorinėmis savybėmis (fenilo žiedas **2**-oje molekulėje, 4-metoksifenilas **3**-čioje molekulėje arba 4-N,N-dimetilaminofenilas **4**-oje molekulėje). Junginių molekulinės struktūros pateiktos 2 paveiksle. Asimetrinių tačiau identiškų pakaitų įvedimas leidžia sukurti D-A-D‘ tipo molekules, kuriose krūvio pernaša gali vykti nepriklausomai tarp abiejų šakų ir purino žiedo. Šis vyksmas nulemia dvigubos fluorescencijos atsiradimą stipresnius donorus turinčiose **3** ir **4** molekulėse. Šiame darbe singletinės būsenos valdomos

pasitelkiant skirtingus pakaitus. Kaip įprastai būdinga CT būsenoms, savybės toliau gali būti paveiktos skirtingu tirpiklių poliškumu. Be to, pasirinkta molekulių struktūra užtikrino galimybę junginiams suformuoti kompleksus su metalų jonais, kas leido realizuoti tarp molekulių vykstančią fotoindukuotą krūvio pernašą (PET). Šis procesas gali būti papildomai naudojamas manipuliuoti sužadintų singletinių būsenų savybes užgesinant mėlynąją fluorescencijos juostą.

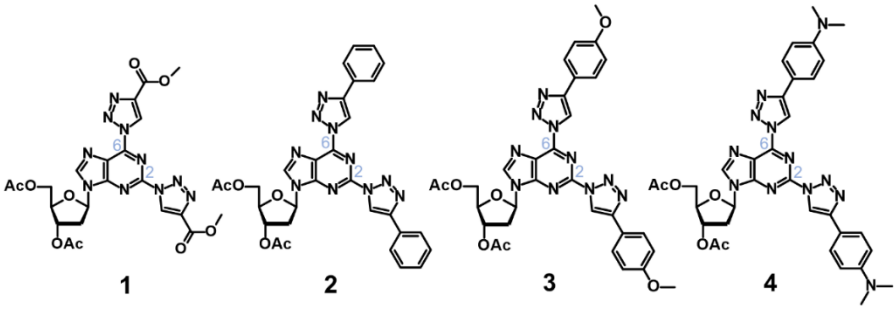

2 paveikslas. Molekulinės bis-triazolyl-purinų junginių struktūros su prijungtu elektronų akceptoriniu fragmentu (**1**) ir prijungtais elektronų donoriniais fragmentais (**2**, **3**, **4**).

Laike nuostoviosios ir laike kintančios spektroskopijos metodai bei teorinis modeliavimas leido palyginti tirtų junginių savybes bei nustatyti dvigubos fluorescencijos prigimtį junginiuose **3** ir **4**. Įvertinus gautus rezultatus tapo akivaizdu, kad mėlynoji fluorescencijos juosta atsiranda dėl krūvio pernašos, vykstančios C2 pozicijoje prijungtoje šakoje („mėlynoji“ šaka), kai tuo tarpu, raudonoji fluorescencijos juosta yra susijusi su krūvio pernaša C6 šakoje (“raudonoji” šaka). Taigi, dvigubos fluorescencijos prigimtis donorinius pakaitus turinčiose molekulėse – nepriklausomi krūvio pernašos šuoliai tarp šviesa sužadintų ir pagrindinių singletinių būsenų.

Skirtingo stiprumo elektronų donoriniai pakaitai lemia į raudonąją pusę besislenkančius sugerties ir fluorescencijos spektrus, taip pat skirtingą emituojančių būsenų atsiskyrimą fluorescencijos spektruose, fluorescencijos kvantinius našumus ir gyvavimo trukmes. 4-N,N-dimetilaminofenilo pakaitai (**4** junginys) nulėmė geriausiai matomą dviejų CT būsenų atsiskyrimą fluorescencijos spektre (spektro intensyviausių verčių padėtys ties 513 nm ir 653 nm). Tačiau stiprūs elektronų donoriniai pakaitai taip pat sąlygojo žymų fluorescencijos gesinimą: **4** junginio fluorescencijos kvantinis našumas siekia vos 0.1% acetonitrilo tirpiklyje. Tuo tarpu kiek silpnesnės elektronų donorinės

4-metoksi fenilų grupės junginyje **3** leido realizuoti sąlyginai aukštus fluorescencijos kvantinius našumus (iki 20% acetonitrilo tirpiklyje) ir pakankamą atskyrimą tarp fluorescencijos spektrinių juostų (spektro intensyviausių verčių padėtys ties 393 nm ir 490 nm). Remiantis šiomis savybėmis, junginys **3** toliau buvo naudojamas pademonstruoti naują ratiometrinio fluorescencijos jutiklio koncepciją.

Triazolo grupių panaudojimas jungtimis tarp purino ir dimetilfenilų užtikrino tirtų junginių kompleksacijos galimybę su metalų jonais. Branduolių magnetinio rezonanso metodu buvo nustatyta, kad Ca^{2+} jungiasi prie dvejų triazolų, o Zn^{2+} formuoja kompleksą tarp triazolo C6 pozicijos ir purino N7 pozicijos. Kompleksacija su minėtais metalų jonais įvyksta santykiu 1:3 (vienas metalo jonas ir trys purino molekulės). Kompleksų susidarymas nulemia mėlynosios fluorescencijos juostos gesinimą, kai, tuo tarpu, raudonoji fluorescencijos juosta yra beveik nepaveikta. Papildomi skirtuminės sugerties tyrimai leido patvirtinti, kad dėl molekulių pakavimosi aplink metalų joną įvyksta PET procesas tarp „mėlynosios“ ir „raudonosios“ šakų, priklausančių skirtingoms molekulėms. Taigi, tokiu būdu pademonstruotas ratiometrinis Ca^{2+} ir Zn^{2+} fluorescencinis jutiklis.

Darbo metu suformuluotos šios išvados:

a) Asimetrinė D-A-D‘ purino junginių struktūra užtikrino dvigubos fluorescencijos atsiradimą dėl dviejų nepriklausomų krūvio pernašos vyksmų, susijusių su skirtingomis elektronų donorinėmis šakomis.
b) Stipriausias molekulinėse struktūrose naudotas 4-N,N-dimetilaminofenilo fragmentas nulėmė fluorescencijos gesinimą poliškiausiame tirpiklyje, tuo tarpu kiek silpnesnės elektronų donorinės 4-metoksi fenilų grupės užtikrino pakankamą fluorescencijos kvantinį našumą ir spektrinį fluorescencijos juostų atsiskyrimą.
c) PET įvyksta tarp D ir D‘ fragmentų, priklausančių skirtingoms molekulėms, kurios dėl kompleksacijos su metalų jonais atsiduria šalia viena kitos. Vykstantis tarpmolekulinis PET procesas lemia mėlynosios fluorescencijos juostos intensyvumo mažėjimą. Šie vyksmai buvo panaudoti ratiometrinio fluorescencinio metalų jonų jutiklio pademonstravimui.

3 skyrius. Tripletų gesinimo valdymas TADF aktyviuose D-A junginiuose su penkiomis elektronų donorinėmis šakomis (benzofenono/metilbenzoato-karbazolai)

Penktame straipsnyje pristatomos CT medžiagos, pasižyminčios TADF procesu. Du junginius sudaro 5 elektronų donoriniai karbazolyl fragmentai, papildomai dekoruoti *tert*-butilo grupėmis, ir elektronų akceptorinės grupės benzofenonas (5tCzBP) arba metilbenzoatas (5tCzMeB) (žr. 3 paveikslą). Šiame darbe singletinių ir tripletinių sužadintųjų būsenų valdymas, kuris nulemia ir TADF proceso savybes, realizuojamas kontroliuojant nespindulinio tripletų eksitonų gesinimo konstantą k_{nr}^{T}. Pastaroji konstanta, savo ruožtu, gali būti veikiama įvedant molekulių struktūrinius pokyčius: benzofenono akceptoriniame fragmente laisvąjį fenilo žiedą pakeitus metoksi grupe stipriai sumažėja nespindulinis tripletų gesinimas.

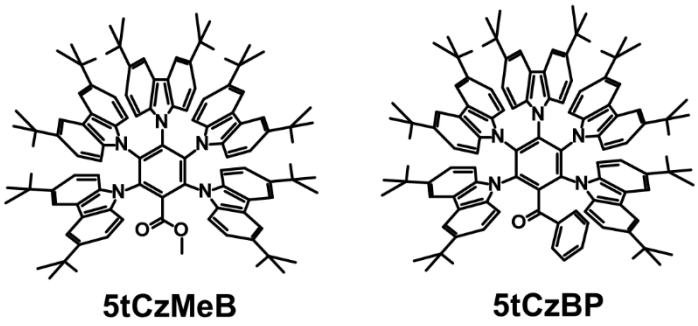

3 paveikslas. TADF aktyvių molekulių 5tCzMeB ir 5tCzBP struktūros.

Pasitelkiant teorinio modeliavimo metodus, buvo nustatyta, kad abejose molekulėse karbazolų grupės yra pasisukusios apytiksliai 60° -70° kampu centrinio fenilo fragmento atžvilgiu. Tokia molekulių geometrija užtikrino pakankamą HOMO ir LUMO molekulinių orbitalių erdvinį atsiskyrimą, lemiantį pakankamai mažą ΔE_{ST} (0.08 eV molekulei 5tCzMeB ir 0.10 eV molekulei 5tCzBP). Maža orbitalių sanklota nulėmė vidutinio dydžio osciliatoriaus stiprius bei pakankamas k_r vertes (3.30×10^6 s^{-1} molekulei 5tCzBP ir 1.02×10^7 s^{-1} molekulei 5tCzMeB). TADF procesas nustatytas laike kintančios emisijos eksperimentų pagalba, kurie atlikti tiek deguonimi prisotintoje, tiek *bedeguonėje* aplinkoje. TADF patvirtinimui papildomai matuotos fotoliuminescencijos intensyvumo priklausomybės nuo sužadinimo galios.

Efektyviam TADF procesui pasiekti būtinos aukštos atgalinės interkombinacinės konversijos (RISC) spartos (k_{RISC}). Abu šiame darbe tirti junginiai demonstruoja pakankamai aukštas k_{RISC} vertes: 3.81x10^6 s^{-1} ir 4.44x10^6 s^{-1} atitinkamai molekulėms 5tCzBP ir 5tCzMeB. Nepaisant to, buvo nustatyta, kad RISC proceso našumas skiriasi beveik du kartus: 53% molekulei 5tCzBP ir 93% molekulei 5tCzMeB. Šis skirtumas galėtų reikšti, kad tripletų eksitoninės būsenos žymiai efektyviau gesinamos mažesniu RISC našumu pasižyminčiame 5tCzBP junginyje. Vadinasi, laisvojo fenilo žiedo pakeitimas metoksi grupe leidžia efektyviai sumažinti nespindulinį sužadintųjų tripletų būsenų gesinimą, mat apskaičiuotos 10 kartų mažesnės k_{nr}^T vertės molekulės 5tCzMeB atveju (0.33x10^6 s^{-1}), lyginant su 5tCzBP (3.32x10^6 s^{-1}). Efektyvus sužadintųjų tripletinių būsenų gesinimas junginyje 5tCzMeB gali būti susijęs su laisvais fenilo žiedo judesiais, pavyzdžiui pasisukimu. Įvesti struktūriniai pokyčiai, t.y. metoksi grupė, leido realizuoti beveik maksimaliai aukštą fotoliuminescencijos kvantinį našumą 5tCzMeB medžiagoje.

Našus RISC procesas ir aukštos k_r vertės ypatingai svarbūs siekiant pritaikyti TADF aktyvias medžiagas 3-čiosios kartos organinių šviestukų (OLED) kūrimui. Taigi, junginys 5tCzMeB buvo panaudotas šviesą spinduliuojančio OLED sluoksnio gamybai. Toks prietaisas pasižymėjo aukštu išoriniu kvantiniu našumu, siekiančiu 24.6 % bei žalsvai mėlyna elektroliuminescencija, kurios intensyviausia vertė atitinka 481 nm.

Išvados:

a) Penkių karbazolų fragmentų, veikiančių kaip elektronų donorai, prijungimas prie elektronų akceptorinių benzofenono ar metilbenzoato grupių užtikrino CT tipo medžiagų sukūrimą, demonstruojančių našų TADF procesą.
b) Cheminė benzofenono akceptorinio fragmento modifikacija, laisvąjį fenilo žiedą pakeičiant metoksi grupe, leidžia stipriai sumažinti nespindulinį tripletų gesinimą, pasireiškiantį 10 kartų sumažėjusia k_{nr}^T konstanta.
c) Sumažintas nespindulinis tripletinių eksitonų gesinimas ir aukštos k_{RISC} vertės karbazolo-metilbenzoato junginyje lėmė beveik vienetui lygų fotoliuminescencijos kvantinį našumą. Tai savo ruožtu leido sukurti itin našų organinį mėlynos spalvos šviestuką, kurio išorinis kvantinis našumas siekia 24.6 %.

4. Sterine sąveika pasižymintys D-A-D junginiai mėlynai TADF emisijai (karbazolas-naftiridinas-karbazolas)

4-oje mokslinėje publikacijoje pristatomos D-A-D organinės medžiagos mėlynai TADF emisijai realizuoti. Junginius sudaro elektronų akceptorius 1,8-naftiridinas (ND) ir du elektronų donorai *tert*-butil-karbazolai (*t*Cz). Junginių *t*Cz-ND ir Me*t*Cz-ND, su papildomai įterptomis metilų grupėmis, molekulinės struktūros pateiktos 4-tame paveiksle. Šio darbo kontekste TADF savybės valdomos pasitelkiant vandenilinius ryšius bei CT sąveiką tarp D ir A grupių. Vandenilinių ryšių atsiradimas tarp N naftiridino atomų ir arčiausiai esančių H atomų padidina junginių *kietumą*, taip sumažinant nepageidaujamus konformacinės netvarkos efektus. Elektronų akceptoriaus ir donoro tarpusavio sąveika, t.y. CT būsenos, lemia TADF proceso atsiradimą bei šio proceso savybes, taip pat emisijos spektro padėtį bei spektro plotį (*angl. trumpinys* FWHM). CT būsenos stiprumas gali būti valdomas papildomai prijungiant metilo grupes prie karbazolų fragmentų, mat dėl sterinės sąveikos pasikeičia donorinių fragmentų pasisukimo kampas.

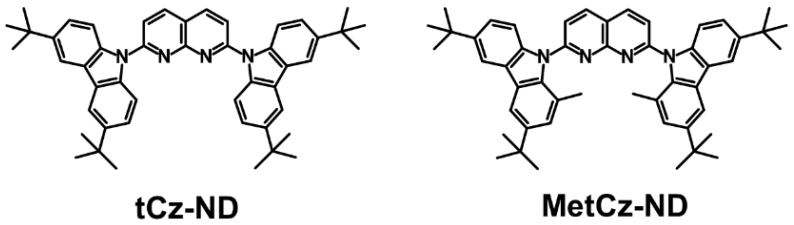

4 paveikslas. Molekulinės 1,8-naftiridino junginių struktūros.

Nemodifikuotas *t*Cz-ND junginys demonstruoja pakankamai silpnas CT būsenos savybes, kadangi elektronų donorai yra pasisukę pakankamai mažu 31° kampu akceptoriaus atžvilgiu. Tuo tarpu metilų grupės Me*t*Cz-ND junginyje lemia minėtų fragmentų pasisukimą 51° laipsnio kampu, o tai lemia geriau išreikštas CT būsenos savybes: sumažėjusį osciliatoriaus stiprį, sumažėjusį ΔE_{ST} ir labiau pasislinkusį bei išplatėjusį emisijos spektrą. Abiejų junginių demonstruojama uždelstoji fluorescencija buvo priskirta TADF procesui. Nustatyti pakankamai maži energijos tarpai tarp singletinių ir tripletinių būsenų (ΔE_{ST} = 0.18 eV junginiui *t*Cz-ND ir ΔE_{ST} = 0.09 eV junginiui Me*t*Cz-ND), aukšti fotoliuminescencijos kvantiniai našumai (76 % ir 86 %) bei sąlyginai trumpos TADF gyvavimo trukmės (8.8 μs ir 3.1 μs), lemiančios aukštas RISC spartas (0.34×10^6 s^{-1} ir 1.06×10^6 s^{-1}). Minėtos savybės nustatytos kietuose sluoksniuose (7 wt%), mCP aplinkoje. Iš pateiktų

verčių matyti, kad stipriau pasireiškianti CT būsena Me*t*Cz-ND molekulėje nulemia geresnes TADF savybes. Kita vertus, junginio *t*Cz-ND tamsiai mėlynos spalvos emisija (452 nm) ir pakankamai siauras spektras (FWHM=66 nm) suteikia didelį pranašumą medžiagos taikymams mėlyno OLED kūrimui.

Pagaminti OLED prietaisai minėtų medžiagų pagrindu pasižymėjo pakankamai geru išoriniu kvantiniu našumu: iki 17.6 % (Me*t*Cz-ND) panaudojant vakuuminio garinimo gamybos metodą arba iki 13.5 % (*t*Cz-ND) panaudojant liejimo iš tirpalo metodą. Elektroliuminescencija pasižymėjo tamsiai mėlyna spalva *t*Cz-ND atveju arba žalsvai-mėlyna spalva Me*t*Cz-ND atveju.

Išvados:

a) D-A-D tipo karbazolo-naftiridino-karbazolo junginiai demonstruoja tamsiai mėlyną/žalsvai mėlyną TADF emisiją dėl efektyvaus HOMO-LUMO atskyrimo panaudojant sterinę sąveiką.
b) TADF proceso savybės gali būti valdomos keičiant D-A sąveiką, t.y. pasireiškiančios CT būsenos stiprumą. CT būsena, savo ruožtu, yra valdoma prijungus papildomas metilo grupes prie karbazolų fragmentų, taip pakeičiant donorinių fragmentų geometriją. Šie struktūriniai pokyčiai lemia 3 kartus išaugusių RISC spartą, tačiau ir labiau į raudonąją pusę pasislinkusį emisijos spektrą.
c) Aukšti fotoliuminescencijos kvantiniai našumai, mėlyna emisijos spektro sritis ir pakankamai trumpos TADF proceso gyvavimo trukmės leidžia toliau taikyti tirtus junginius OLED prietaisų gamyboje. Gauti mėlynų ir žaliai mėlynų organinių šviestukų išoriniai kvantiniai našumai siekia 17.6 %.

5. Stipraus akceptoriaus – silpnų donorų vėlyvosios emisijos junginiai (diboraantracenai)

5-tame disertacijos straipsnyje pristatomos dvi naujos molekulės, demonstruojančios labai ilgą vėlyvąją emisiją kambario temperatūroje. Organinių junginių 9,10-dimesitil-9,10-diboraantraceno (DBA) struktūra sudaryta naudojant stiprų elektronų akceptorių diboraantraceną kartu su silpnomis elektronų donorinės mesitil grupėmis. Skirtingose molekulėse prie DBA fragmento yra prijungti skirtingi šoniniai pakaitai: acenaftilenas (anDBA) arba fenantrenas su *tert*-butil grupėmis (phenDBA), žr. 5 paveikslą. Verta paminėti, kad šiame darbe tirtos medžiagos nėra standartiniai CT tipo junginiai, mat žemiausios sužadintosios singletinės ir tripletinės būsenos

pasižymi lokaliu sužadinimu (t.y., LE būsena). Tačiau silpni elektronų donoriniai pakaitai lemia aukštesniųjų CT būsenų atsiradimą, kurios yra svarbios ISC ir RISC realizavimui. Šie efektai kartu su labai ilgai gyvuojančiomis tripletinėmis būsenomis dėl itin mažų k_{nr}^{T} verčių leido realizuoti vėlyvąją emisiją, kurią sudaro ilgai išliekantis TADF ir fosforescencija. Minėti šoniniai DBA kamieno pakaitai leido keisti sužadintųjų būsenų energijas: anDBA fluorescencijos ir fosforescencijos spektrai raudonesni nei phenDBA. Be to, šių junginių savybės papildomai gali būti valdomos keičiant junginių koncentraciją sluoksniuose, keičiant sluoksnių kietumą, panaudojant atkaitinimą, ar keičiant temperatūrą.

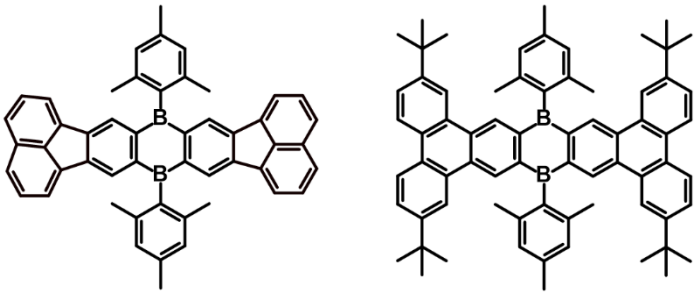

5 paveikslas. Molekulių anDBA ir phenDBA struktūros.

Ilgai gyvuojanti emisija aptinkama bandinius patalpinus į *bedeguonę* poli(metil metakrilato) (PMMA) matricą. Darbo metu buvo nustatyti šie vėlyvosios emisijos parametrai: kvantiniai našumai iki 3 % ir iki 15 %, gyvavimo trukmės iki 0.8 s ir iki 3.2 s, kurios tęsiasi iki 5 s ir iki 25 s atitinkamai anDBA ir phenDBA junginiams. TADF proceso indėlis į bendrą emisijos spektrą leidžia ne tik pagerinti vėlyvosios emisijos našumą, bet ir suteikia galimybę keisti šios emisijos spalvą, keičiant temperatūrą. Labai ilgai gyvuojančios emisijos atsiradimą lemia: i) keli skirtingi kanalai interkombinacinės konversijos procesui vykti tarp skirtingos elektroninės prigimties singletinių ir tripletinių būsenų; ii) lokaliu sužadinimu pasižyminti žemiausia sužadinto tripleto būsena, su labai mažomis k_r^T ir k_{nr}^{T} spartomis; iii) energetiniu atžvilgiu arti tarpusavyje esančios singletinės ir tripletinės būsenos bei ilgai gyvuojanti žemiausio sužadinto tripletų būsena, kurie kartu užtikrina optimalias sąlygas RISC procesui vykti, kuris ir lemia TADF atsiradimą.

Toliau šių junginių savybės buvo panaudotos specialių sluoksnių kūrimui, kuriuose galima įrašyti informaciją. Šių sluoksnių kūrimo idėja paremta tuo, kad PMMA sluoksniai, paruošti deguonimi prisotintoje aplinkoje, papildomai padengiami polivinilo acetato (PVA) sluoksniu, kuris vėliau veiks kaip barjeras deguoniui. Informacija į sluoksnį įrašoma intensyvia lazerio šviesa, kuri nulemia didelę tripletinių būsenų generaciją DBA junginiuose. *Tripletai* iš pradžių gesinami deguonies molekulių, esančių polimero matricoje, pagalba. Taip sugeneruojamas singletinis deguonis, kuris, savo ruožtu, reaguoja su aplink esančiu polimeru. Taip tam tikrose apšviestose vietose sumažinama deguonies koncentracija. Todėl bandinį vėliau apšvietus mažiau intensyvia šviesa, skirta sužadinti molekules, šviesą emituoja tik tos vietos, kurios prieš tai buvo apšviestos intensyvia lazerio spinduliuote.

Šio darbo išvados:

a) Pristatyta nauja organinių medžiagų klasė kambario temperatūroje demonstruoja vėlyvąją emisiją. Organiniai junginiai sudaryti iš šoniniais pakaitais dekoruoto diboraantraceno kamieno ir silpnų elektronų donorinių mesitilo grupių, lemiančių aukštesniųjų sužadintųjų CT tipo singletinių ir tripletinių būsenų atsiradimą.
b) Bi-komponentė vėlyvoji emisija sudaryta iš ilgai išliekančio TADF ir ilgai gyvuojančios kambario temperatūros fosforescencijos. Šių procesų savybės gali būti valdomos struktūriniais molekulių pokyčiais ir aplinkos parametrais: bandinių koncentracija sluoksnyje, sluoksnio kietumu, deguonies buvimu arba temperatūra.
c) Šios medžiagos dėl savo savybių gali būti taikomos šviesą emituojančių sluoksnių kūrimui, skirtų informacijos įrašymui.

BIBLIOGRAPHY

1. OLED Market Size to Worth Around USD 214.8 Billion by 2030. https://www.precedenceresearch.com/oled-market.
2. Basiricò, L., Mattana, G. & Mas-Torrent, M. Editorial: Organic Electronics: Future Trends in Materials, Fabrication Techniques and Applications. *Front. Phys.* **10**, 307 (2022).
3. Organic semiconductors open up new possibilities in electronics. https://hellofuture.orange.com/en/organic-semiconductors-open-up-new-possibilities-in-electronics/.
4. Yokota, T., Fukuda, K. & Someya, T. Recent Progress of Flexible Image Sensors for Biomedical Applications. *Adv. Mater.* **33**, 2004416 (2021).
5. Ostroverkhova, O. Organic Optoelectronic Materials: Mechanisms and Applications. *Chem. Rev.* **116**, 13279–13412 (2016).
6. Three ways organic electronics is changing technology as we know it. https://theconversation.com/three-ways-organic-electronics-is-changing-technology-as-we-know-it-63287.
7. Sun, L., Fukuda, K. & Someya, T. Recent progress in solution-processed flexible organic photovoltaics. *npj Flex. Electron.* **6**, 1–14 (2022).
8. Valeur, B. *Molecular Fluorescence. Principles and Applications*. (Wiley-VCH Verlag GmbH & Co. KGaA, 2002).
9. Köhler, A. & Bässler, H. Triplet states in organic semiconductors. *Mater. Sci. Eng. R Reports* **66**, 71–109 (2009).
10. Baldo, M. A. *et al.* Highly efficient phosphorescent emission from organic electroluminescent devices. *Nature* **395**, 151–154 (1998).
11. Lamansky, S. *et al.* Highly phosphorescent bis-cyclometalated iridium complexes: Synthesis, photophysical characterization, and use in organic light emitting diodes. *J. Am. Chem. Soc.* **123**, 4304–4312 (2001).
12. Guo, S. *et al.* Recent Progress in Pure Organic Room Temperature Phosphorescence of Small Molecular Host-Guest Systems. *ACS Mater. Lett.* **3**, 379–397 (2021).
13. Adachi, C. & Sandanayaka, A. S. D. The Leap from Organic Light-Emitting Diodes to Organic Semiconductor Laser Diodes. *CCS Chem.* **2**, 1203–1216 (2020).
14. Wu, D. *et al.* Fluorescent chemosensors: the past, present and future. *Chem. Soc. Rev.* **46**, 7105–7123 (2017).

15. Oyama, Y. *et al.* Design Strategy for Robust Organic Semiconductor Laser Dyes. *ACS Mater. Lett.* **2**, 161–167 (2020).
16. Hong, G. *et al.* A Brief History of OLEDs—Emitter Development and Industry Milestones. *Adv. Mater.* **33**, 2005630 (2021).
17. Lim, H. *et al.* Breaking the Efficiency Limit of Deep-Blue Fluorescent OLEDs Based on Anthracene Derivatives. *Adv. Mater.* **34**, 2100161 (2022).
18. Fang, F. *et al.* Thermally Activated Delayed Fluorescence Material: An Emerging Class of Metal-Free Luminophores for Biomedical Applications. *Adv. Sci.* **8**, 2102970 (2021).
19. Bryden, M. A. & Zysman-Colman, E. Organic thermally activated delayed fluorescence (TADF) compounds used in photocatalysis. *Chem. Soc. Rev.* **50**, 7587–7680 (2021).
20. Yan, X. *et al.* Recent Advances on Host–Guest Material Systems toward Organic Room Temperature Phosphorescence. *Small* **18**, 2104073 (2022).
21. Misra, R. & Bhattacharyya, S. P. *Intramolecular Charge Transfer*. (Wiley-VCH Verlag GmbH & Co. KGaA, 2018).
22. Grabowski, Z. R. & Rotkiewicz, K. Structural Changes Accompanying Intramolecular Electron Transfer: Focus on Twisted Intramolecular Charge-Transfer States and Structures. *Chem. Rev* **103**, 3899–4031 (2003).
23. Braun, D., Rettig, W., Delmond, S., Létard, J.-F. & Lapouyade, R. Amide Derivatives of DMABN: A New Class of Dual Fluorescent Compounds. *J. Phys. Chem. A* **101**, 6836–6841 (1997).
24. Bureš, F. Fundamental aspects of property tuning in push-pull molecules. *RSC Adv.* **4**, 58826–58851 (2014).
25. Liang, X. & Zhang, Q. Recent progress on intramolecular charge-transfer compounds as photoelectric active materials. *Sci. China Mater.* **60**, 1093–1101 (2017).
26. Kumar, R., Aggarwal, H. & Srivastava, A. Of Twists and Curves: Electronics, Photophysics, and Upcoming Applications of Non-Planar Conjugated Organic Molecules. *Chem. – A Eur. J.* **26**, 10653–10675 (2020).
27. Uoyama, H., Goushi, K., Shizu, K., Nomura, H. & Adachi, C. Highly efficient organic light-emitting diodes from delayed fluorescence. *Nature* **492**, 234–238 (2012).
28. Adachi, C., Xie, G., Reineke, S. & Zysman-Colman, E. Editorial: Recent Advances in Thermally Activated Delayed Fluorescence Materials. *Front. Chem.* **8**, 1140 (2020).

29. Xie, F. M., Zhou, J. X., Li, Y. Q. & Tang, J. X. Effects of the relative position and number of donors and acceptors on the properties of TADF materials. *J. Mater. Chem. C* **8**, 9476–9494 (2020).
30. Data, P. & Takeda, Y. Recent Advancements in and the Future of Organic Emitters: TADF- and RTP-Active Multifunctional Organic Materials. *Chem. – An Asian J.* **14**, 1613–1636 (2019).
31. Huang, T., Jiang, W. & Duan, L. Recent progress in solution processable TADF materials for organic light-emitting diodes. *J. Mater. Chem. C* **6**, 5577–5596 (2018).
32. Duan, Y. C. *et al.* Fluorescence, Phosphorescence, or Delayed Fluorescence? - A Theoretical Exploration on the Reason Why a Series of Similar Organic Molecules Exhibit Different Luminescence Types. *J. Phys. Chem. C* **122**, 23091–23101 (2018).
33. Jabłoństski, A. Efficiency of anti-stokes fluorescence in dyes. *Nature* **131**, 839–840 (1933).
34. Lakowicz, J. R. *Principles of Fluorescence Spectroscopy*. (Springer, 2006).
35. Kasha, M. Characterization of electronic transitions in complex molecules. *Discuss. Faraday Soc.* **9**, 14–19 (1950).
36. Itoh, T. Fluorescence and phosphorescence from higher excited states of organic molecules. *Chem. Rev.* **112**, 4541–4568 (2012).
37. Koziar, J. C. & Cowan, D. O. Photochemical Heavy-Atom Effects. *Acc. Chem. Res.* **11**, 334–341 (1978).
38. Lees, A. J. Luminescence Properties of Organometallic Complexes. *Chem. Rev.* **87**, 711–743 (1987).
39. Reichardt, C., Vogt, R. A. & Crespo-Hernández, C. E. On the origin of ultrafast nonradiative transitions in nitro-polycyclic aromatic hydrocarbons: Excited-state dynamics in 1-nitronaphthalene. *J. Chem. Phys.* **131**, 224518 (2009).
40. Minns, R. S., Parker, D. S. N., Penfold, T. J., Worth, G. A. & Fielding, H. H. Competing ultrafast intersystem crossing and internal conversion in the " channel 3" region of benzene. *Phys. Chem. Chem. Phys.* **12**, 15607–15615 (2010).
41. Dias, F. B., Penfold, T. J. & Monkman, A. P. Photophysics of thermally activated delayed fluorescence molecules. *Methods Appl. Fluoresc.* **5**, 012001 (2017).
42. Dias, F. B. Kinetics of thermal-assisted delayed fluorescence in blue organic emitters with large singlettriplet energy gap. *Philos. Trans. R. Soc. A Math. Phys. Eng. Sci.* **373**, (2015).
43. El-Sayed, M. A. Spin-orbit coupling and the radiationless processes in

nitrogen heterocyclics. *J. Chem. Phys.* **38**, 2834–2838 (1963).
44. Noda, H. *et al.* Critical role of intermediate electronic states for spin-flip processes in charge-transfer-type organic molecules with multiple donors and acceptors. *Nat. Mater.* **18**, 1084–1090 (2019).
45. Xu, Y., Xu, P., Hu, D. & Ma, Y. Recent progress in hot exciton materials for organic light-emitting diodes. *Chem. Soc. Rev.* **50**, 1030–1069 (2021).
46. Maeda, H., Maeda, T. & Mizuno, K. Absorption and fluorescence spectroscopic properties of 1- and 1,4-silyl-substituted naphthalene derivatives. *Molecules* **17**, 5108–5125 (2012).
47. Zhang, F. *et al.* Self-assembly, optical and electrical properties of perylene diimide dyes bearing unsymmetrical substituents at bay position. *Sci. Rep.* **8**, 8208 (2018).
48. Maciejewski, A. & Steer, R. P. Spectral and photophysical properties of 9,10-diphenylanthracene in perfluoro-n-hexane: the influence of solute—solvent interactions. *J. Photochem.* **35**, 59–69 (1986).
49. Grabowski, Z. R., Rotkiewicz, K. & Siemiarczuk, A. Dual fluorescence of donor-acceptor molecules and the Twisted Intramolecular Charge Transfer (TICT) states. *J. Lumin.* **18**–**19**, 420–424 (1979).
50. Skardziute, L. *et al.* Synthesis and optical properties of the isomeric pyrimidine and carbazole derivatives: Effects of polar substituents and linking topology. *Dye. Pigment.* **118**, 118–128 (2015).
51. Eberle, B., Hübner, O., Ziesak, A., Kaifer, E. & Himmel, H. J. What Makes a Strong Organic Electron Donor (or Acceptor)? *Chem. – A Eur. J.* **21**, 8578–8590 (2015).
52. Juršėnas, S. *Organiniai puslaidininkiai*. (Biznio mašinų kompanija, 2008).
53. Skaisgiris, R. *et al.* Origin of dual emission in σ-bridged donor-acceptor TADF compounds. *J. Mater. Chem. C* **7**, 12601–12609 (2019).
54. Woon, K.-L. *et al.* Intramolecular Dimerization Quenching of Delayed Emission in Asymmetric D–D′–A TADF Emitters. *J. Phys. Chem. C* **123**, 12400–12410 (2019).
55. Aydemir, M. *et al.* Photophysics of an Asymmetric Donor–Acceptor–Donor′ TADF Molecule and Reinterpretation of Aggregation-Induced TADF Emission in These Materials. *J. Phys. Chem. C* **121**, 17764–17772 (2017).
56. Li, W. *et al.* Employing ~100% Excitons in OLEDs by Utilizing a Fluorescent Molecule with Hybridized Local and Charge-Transfer

Excited State. *Adv. Funct. Mater.* **24**, 1609–1614 (2014).
57. Shizu, K. & Kaji, H. Comprehensive understanding of multiple resonance thermally activated delayed fluorescence through quantum chemistry calculations. *Commun. Chem.* **5**, 53 (2022).
58. Kochman, M. A., Durbeej, B. & Kubas, A. Simulation and Analysis of the Transient Absorption Spectrum of 4-(N,N-Dimethylamino)benzonitrile (DMABN) in Acetonitrile. *J. Phys. Chem. A* **125**, 8635–8648 (2021).
59. Park, M., Kim, C. H. & Joo, T. Multifaceted ultrafast intramolecular charge transfer dynamics of 4-(dimethylamino)benzonitrile (DMABN). *J. Phys. Chem. A* **117**, 370–377 (2013).
60. Zhong, C. The driving forces for twisted or planar intramolecular charge transfer. *Phys. Chem. Chem. Phys.* **17**, 9248–9257 (2015).
61. Nandi, A., Ghosh, R. & Palit, D. K. Excited state relaxation pathways of 4-dimethylamino-β-nitrostyrene: Effect of solvent polarity and donor-acceptor conjugation. *J. Photochem. Photobiol. A Chem.* **321**, 171–179 (2016).
62. Zheng, S. *et al.* Structural effects on the pH-dependent fluorescence of naphthalenic derivatives and consequences for sensing/switching. *Photochem. Photobiol. Sci.* **11**, 1675–1681 (2012).
63. Wang, C. *et al.* Quantitative Design of Bright Fluorophores and AIEgens by the Accurate Prediction of Twisted Intramolecular Charge Transfer (TICT). *Angew. Chemie* **132**, 10246–10258 (2020).
64. Guido, C. A., Mennucci, B., Jacquemin, D. & Adamo, C. Planar vs. twisted intramolecular charge transfer mechanism in Nile Red: new hints from theory. *Phys. Chem. Chem. Phys.* **12**, 8016–8023 (2010).
65. Gómez, I., Castro, P. J. & Reguero, M. Insight into the Mechanisms of Luminescence of Aminobenzonitrile and Dimethylaminobenzonitrile in Polar Solvents. An ab Initio Study. *J. Phys. Chem. A* **119**, 1983–1995 (2015).
66. Chi, W. *et al.* A Photoexcitation-Induced Twisted Intramolecular Charge Shuttle. *Angew. Chemie Int. Ed.* **58**, 7073–7077 (2019).
67. Wang, C. *et al.* Twisted intramolecular charge transfer (TICT) and twists beyond TICT: From mechanisms to rational designs of bright and sensitive fluorophores. *Chem. Soc. Rev.* **50**, 12656–12678 (2021).
68. Marcus, R. A. On the Theory of Oxidation-Reduction Reactions Involving Electron Transfer. I. *J. Chem. Phys.* **24**, 966 (1956).
69. Escudero, D. Revising Intramolecular Photoinduced Electron Transfer (PET) from First-Principles. *Acc. Chem. Res.* **49**, 1816–1824 (2016).
70. Natali, M., Campagna, S. & Scandola, F. Photoinduced electron

transfer across molecular bridges: electron- and hole-transfer superexchange pathways. *Chem. Soc. Rev.* **43**, 4005–4018 (2014).
71. Santoro, A. *et al.* Photoinduced Electron Transfer in Organized Assemblies—Case Studies. *Molecules* **27**, 2713 (2022).
72. de Silva, A. P., Fox, D. B., Moody, T. S. & Weir, S. M. The development of molecular fluorescent switches. *TRENDS Biotechnol.* **19**, 29–34 (2001).
73. de Silva, A. P., Moody, T. S. & Wright, G. D. Fluorescent PET (photoinduced electron transfer) sensors as potent analytical tools. *Analyst* **134**, 2385–93 (2009).
74. Valeur, B. Design principles of fluorescent molecular sensors for cation recognition. *Coord. Chem. Rev.* **205**, 3–40 (2000).
75. Daly, B., Ling, J. & de Silva, A. P. Current developments in fluorescent PET (photoinduced electron transfer) sensors and switches. *Chem. Soc. Rev.* **44**, 4203–4211 (2015).
76. Carter, K. P., Young, A. M. & Palmer, A. E. Fluorescent sensors for measuring metal ions in living systems. *Chem. Rev.* **114**, 4564–4601 (2014).
77. Magri, D. C. Logical sensing with fluorescent molecular logic gates based on photoinduced electron transfer. *Coord. Chem. Rev.* **426**, 213598 (2021).
78. Xiao, H., Li, P. & Tang, B. Recent progresses in fluorescent probes for detection of polarity. *Coord. Chem. Rev.* **427**, 213582 (2021).
79. Li, L., Wang, J., Xu, S., Li, C. & Dong, B. Recent Progress in Fluorescent Probes For Metal Ion Detection. *Front. Chem.* **10**, 398 (2022).
80. Tian, X., Murfin, L. C., Wu, L., Lewis, S. E. & James, T. D. Fluorescent small organic probes for biosensing. *Chem. Sci.* **12**, 3406–3426 (2021).
81. Park, S. H., Kwon, N., Lee, J. H., Yoon, J. & Shin, I. Synthetic ratiometric fluorescent probes for detection of ions. *Chem. Soc. Rev.* **49**, 143–179 (2020).
82. Du, K. *et al.* A highly selective ratiometric fluorescent probe for the cascade detection of Zn2+ and H2PO4− and its application in living cell imaging. *RSC Adv.* **7**, 40615–40620 (2017).
83. Zhang, S., Zhao, M., Zhu, W., Xu, Y. & Qian, X. A highly sensitive, selective ratiometric fluorescent probe for cobalt(II) and its applications for biological imaging. *Dalt. Trans.* **44**, 9740–9743 (2015).
84. Huang, Y., Zhang, Y., Huo, F., Wen, Y. & Yin, C. Design strategy and

bioimaging of small organic molecule multicolor fluorescent probes. *Sci. China Chem.* **63**, 1742–1755 (2020).

85. de Silva, A. P. *et al.* Signaling Recognition Events with Fluorescent Sensors and Switches. *Chem. Rev.* **97**, 1515–1566 (1997).
86. Sasaki, S., Drummen, G. P. C. & Konishi, G. Recent advances in twisted intramolecular charge transfer (TICT) fluorescence and related phenomena in materials chemistry. *J. Mater. Chem. C* **4**, 2731–2743 (2016).
87. Han, J. & Burgess, K. Fluorescent indicators for intracellular pH. *Chem. Rev.* **110**, 2709–2728 (2010).
88. Sun, W., Li, M., Fan, J. & Peng, X. Activity-Based Sensing and Theranostic Probes Based on Photoinduced Electron Transfer. *Acc. Chem. Res.* **52**, 2818–2831 (2019).
89. Magri, D. C., Johnson, A. D. & Spiteri, J. C. Fluorescent Photoinduced Electron Transfer (PET) Logic Gates for Acidity (pH) and Redox Potential (pE). *J. Fluoresc.* **27**, 551–559 (2017).
90. Schubert, J., Schulze, A., Prodromou, C. & Neuweiler, H. Two-colour single-molecule photoinduced electron transfer fluorescence imaging microscopy of chaperone dynamics. *Nat. Commun.* **12**, 6964 (2021).
91. Adachi, C. Third-generation organic electroluminescence materials. *Jpn. J. Appl. Phys.* **53**, 060101 (2014).
92. Eng, J. & Penfold, T. J. Understanding and Designing Thermally Activated Delayed Fluorescence Emitters: Beyond the Energy Gap Approximation. *Chem. Rec.* **20**, 831–856 (2020).
93. Olivier, Y., Moral, M., Muccioli, L. & Sancho-García, J.-C. Dynamic nature of excited states of donor–acceptor TADF materials for OLEDs: how theory can reveal structure–property relationships. *J. Mater. Chem. C* **5**, 5718–5729 (2017).
94. Ward, J. S. *et al.* The interplay of thermally activated delayed fluorescence (TADF) and room temperature organic phosphorescence in sterically-constrained donor–acceptor charge-transfer molecules. *Chem. Commun.* **52**, 2612–2615 (2016).
95. Gibson, J., Monkman, A. P. & Penfold, T. J. The Importance of Vibronic Coupling for Efficient Reverse Intersystem Crossing in Thermally Activated Delayed Fluorescence Molecules. *ChemPhysChem* **17**, 2956–2961 (2016).
96. Marian, C. M. Spin-orbit coupling and intersystem crossing in molecules. *Wiley Interdiscip. Rev. Comput. Mol. Sci.* **2**, 187–203 (2012).
97. Penfold, T. J., Gindensperger, E., Daniel, C. & Marian, C. M. Spin-

Vibronic Mechanism for Intersystem Crossing. *Chem. Rev.* **118**, 6975–7025 (2018).
98. Marian, C. M. Mechanism of the Triplet-to-Singlet Upconversion in the Assistant Dopant ACRXTN. *J. Phys. Chem. C* **120**, 3715–3721 (2016).
99. Tian, X., Sun, H., Zhang, Q. & Adachi, C. Theoretical predication for transition energies of thermally activated delayed fluorescence molecules. *Chinese Chem. Lett.* **27**, 1445–1452 (2016).
100. Dias, F. B. *et al.* Triplet harvesting with 100% efficiency by way of thermally activated delayed fluorescence in charge transfer OLED emitters. *Adv. Mater.* **25**, 3707–3714 (2013).
101. Hirata, S. *et al.* Highly efficient blue electroluminescence based on thermally activated delayed fluorescence. *Nat. Mater.* **14**, 330–336 (2015).
102. Gibson, J. & Penfold, T. J. Nonadiabatic coupling reduces the activation energy in thermally activated delayed fluorescence. *Phys. Chem. Chem. Phys.* **19**, 8428–8434 (2017).
103. Lyskov, I. & Marian, C. M. Climbing up the ladder: Intermediate triplet states promote the reverse intersystem crossing in the efficient TADF emitter ACRSA. *J. Phys. Chem. C* **121**, 21145–21153 (2017).
104. Andrea, D. K. *et al.* Thermally Activated Delayed Fluorescence: Polarity, Rigidity, and Disorder in Condensed Phases. *J. Am. Chem. Soc.* **144**, 15211–15222 (2022).
105. Dhali, R., Phan Huu, D. K. A., Terenziani, F., Sissa, C. & Painelli, A. Thermally activated delayed fluorescence: A critical assessment of environmental effects on the singlet–triplet energy gap. *J. Chem. Phys.* **154**, 134112 (2021).
106. Fu, C. *et al.* Highly efficient deep-blue OLEDs based on hybridized local and charge-transfer emitters bearing pyrene as the structural unit. *Chem. Commun.* **55**, 6317–6320 (2019).
107. Pan, Y. *et al.* Theoretical investigation of high-efficiency organic electroluminescent material: HLCT state and hot exciton process. *RSC Adv.* **7**, 19576–19583 (2017).
108. Hatakeyama, T. *et al.* Ultrapure Blue Thermally Activated Delayed Fluorescence Molecules: Efficient HOMO–LUMO Separation by the Multiple Resonance Effect. *Adv. Mater.* **28**, 2777–2781 (2016).
109. Hasan, M. *et al.* Exciton–Exciton Annihilation in Thermally Activated Delayed Fluorescence Emitter. *Adv. Funct. Mater.* **30**, 2000580 (2020).
110. Lin, T.-A. *et al.* Sky-Blue Organic Light Emitting Diode with 37%

External Quantum Efficiency Using Thermally Activated Delayed Fluorescence from Spiroacridine-Triazine Hybrid. *Adv. Mater.* **28**, 6976–6983 (2016).

111. Gong, X. *et al.* High-efficiency red thermally activated delayed fluorescence emitters based on benzothiophene-fused spiro-acridine donor. *Chem. Eng. J.* **405**, 126663 (2021).
112. Kuang, Z. *et al.* Conformational Relaxation and Thermally Activated Delayed Fluorescence in Anthraquinone-Based Intramolecular Charge-Transfer Compound. *J. Phys. Chem. C* **122**, 3727–3737 (2018).
113. Liu, Y., Li, C., Ren, Z., Yan, S. & Bryce, M. R. All-organic thermally activated delayed fluorescence materials for organic light-emitting diodes. *Nat. Rev. Mater.* **3**, 18020 (2018).
114. Gan, N. *et al.* Recent Advances in Polymer-Based Metal-Free Room-Temperature Phosphorescent Materials. *Adv. Funct. Mater.* **28**, 1802657 (2018).
115. Xu, S. *et al.* Excited State Modulation for Organic Afterglow: Materials and Applications. *Adv. Mater.* **28**, 9920–9940 (2016).
116. Lin, Z., Kabe, R., Wang, K. & Adachi, C. Influence of energy gap between charge-transfer and locally excited states on organic long persistence luminescence. *Nat. Commun.* **11**, 191 (2020).
117. Ma, H. *et al.* Room-Temperature Phosphorescence in Metal-Free Organic Materials. *Ann. Phys.* **531**, 1800482 (2019).
118. Ma, H., Peng, Q., An, Z., Huang, W. & Shuai, Z. Efficient and Long-Lived Room-Temperature Organic Phosphorescence: Theoretical Descriptors for Molecular Designs. *J. Am. Chem. Soc.* **141**, 1010–1015 (2019).
119. Kenry, Chen, C. & Liu, B. Enhancing the performance of pure organic room-temperature phosphorescent luminophores. *Nat. Commun.* **10**, 2111 (2019).
120. Gu, L. *et al.* Colour-tunable ultra-long organic phosphorescence of a single-component molecular crystal. *Nat. Photonics* **13**, 406–411 (2019).
121. Jia, W., Wang, Q., Shi, H., An, Z. & Huang, W. Manipulating the Ultralong Organic Phosphorescence of Small Molecular Crystals. *Chem. – A Eur. J.* **26**, 4437–4448 (2020).
122. Ma, H. *et al.* Hydrogen Bonding-Induced Morphology Dependence of Long-Lived Organic Room-Temperature Phosphorescence: A Computational Study. *J. Phys. Chem. Lett.* **10**, 6948–6954 (2019).
123. Zhao, W., He, Z. & Tang, B. Z. Room-temperature phosphorescence

from organic aggregates. *Nat. Rev. Mater.* **5**, 869–885 (2020).
124. An, Z. *et al.* Stabilizing triplet excited states for ultralong organic phosphorescence. *Nat. Mater.* **14**, 685–690 (2015).
125. Ma, X. K. & Liu, Y. Supramolecular Purely Organic Room-Temperature Phosphorescence. *Acc. Chem. Res.* **54**, 3403–3414 (2021).
126. Forni, A., Lucenti, E., Botta, C. & Cariati, E. Metal free room temperature phosphorescence from molecular self-interactions in the solid state. *J. Mater. Chem. C* **6**, 4603–4626 (2018).
127. Louis, M. *et al.* Blue-Light-Absorbing Thin Films Showing Ultralong Room-Temperature Phosphorescence. *Adv. Mater.* **31**, 1807887 (2019).
128. Kropp, J. L. & Dawson, W. R. Radiationlese deactivation of triplet coronene in plastics. *J. Phys. Chem.* **71**, 4499–4506 (1967).
129. Jin, J. *et al.* Thermally activated triplet exciton release for highly efficient tri-mode organic afterglow. *Nat. Commun.* **11**, 842 (2020).
130. Wang, X. *et al.* TADF-Type Organic Afterglow. *Angew. Chemie Int. Ed.* **60**, 17138–17147 (2021).
131. Yang, Y. *et al.* Efficient and Color-Tunable Dual-Mode Afterglow from Large-Area and Flexible Polymer-Based Transparent Films for Anti-Counterfeiting and Information Encryption. *Angew. Chemie Int. Ed.* **61**, e202201820 (2022).
132. Zhang, Y. *et al.* Large-Area, Flexible, Transparent, and Long-Lived Polymer-Based Phosphorescence Films. *J. Am. Chem. Soc.* **143**, 13675–13685 (2021).
133. Ma, Z. *et al.* Converting molecular luminescence to ultralong room-temperature phosphorescence via the excited state modulation of sulfone-containing heteroaromatics. *Chem. Sci.* **12**, 14808–14814 (2021).
134. Fu, Y. *et al.* Boosting external quantum efficiency to 38.6% of sky-blue delayed fluorescence molecules by optimizing horizontal dipole orientation. *Sci. Adv.* **7**, eabj2504 (2021).
135. Wang, J. *et al.* Triarylboron-cored multi-donors TADF emitter with high horizontal dipole orientation ratio achieving high performance OLEDs with near 39% external quantum efficiency and small efficiency Roll-off. *Chem. Eng. J.* **450**, 137805 (2022).
136. Zhang, Y. *et al.* Multi-Resonance Deep-Red Emitters with Shallow Potential-Energy Surfaces to Surpass Energy-Gap Law**. *Angew. Chemie Int. Ed.* **60**, 20498–20503 (2021).
137. Chan, C. Y. *et al.* Stable pure-blue hyperfluorescence organic light-

emitting diodes with high-efficiency and narrow emission. *Nat. Photonics* **15**, 203–207 (2021).
138. Kyulux says it is on track to commercialize green Hyperfluorescence materials in 2023, red and blue in 2024 | OLED Info. https://www.oled-info.com/kyulux-says-it-track-commercialize-green-hyperfluorescence-materials-2023-red.
139. Chen, W. & Song, F. Thermally activated delayed fluorescence molecules and their new applications aside from OLEDs. *Chinese Chem. Lett.* **30**, 1717–1730 (2019).
140. Ma, W. *et al.* Thermally activated delayed fluorescence (TADF) organic molecules for efficient X-ray scintillation and imaging. *Nat. Mater.* **21**, 210–216 (2022).
141. Fang, F. *et al.* Near-Infrared Thermally Activated Delayed Fluorescence Nanoparticle: A Metal-Free Photosensitizer for Two-Photon-Activated Photodynamic Therapy at the Cell and Small Animal Levels. *Small* **18**, 2106215 (2022).
142. Zhen, X. *et al.* Ultralong Phosphorescence of Water-Soluble Organic Nanoparticles for In Vivo Afterglow Imaging. *Adv. Mater.* **29**, 1606665 (2017).
143. Jiang, Y. *et al.* A generic approach towards afterglow luminescent nanoparticles for ultrasensitive in vivo imaging. *Nat. Commun.* **10**, 1–10 (2019).
144. Gao, R., Mei, X., Yan, D., Liang, R. & Wei, M. Nano-photosensitizer based on layered double hydroxide and isophthalic acid for singlet oxygenation and photodynamic therapy. *Nat. Commun.* **9**, 2798 (2018).
145. Lei, Y. *et al.* Wide-Range Color-Tunable Organic Phosphorescence Materials for Printable and Writable Security Inks. *Angew. Chemie Int. Ed.* **59**, 16054–16060 (2020).
146. Ding, L. & Wang, X. D. Luminescent Oxygen-Sensitive Ink to Produce Highly Secured Anticounterfeiting Labels by Inkjet Printing. *J. Am. Chem. Soc.* **142**, 13558–13564 (2020).
147. Wang, Z. *et al.* Color-Tunable Polymeric Long-Persistent Luminescence Based on Polyphosphazenes. *Adv. Mater.* **32**, 1907355 (2020).
148. Hirata, S. *et al.* Reversible Thermal Recording Media Using Time-Dependent Persistent Room Temperature Phosphorescence. *Adv. Opt. Mater.* **1**, 438–442 (2013).
149. Zhou, Y. *et al.* Long-Lived Room-Temperature Phosphorescence for Visual and Quantitative Detection of Oxygen. *Angew. Chemie* **131**,

12230–12234 (2019).
150. Gmelch, M., Thomas, H., Fries, F. & Reineke, S. Programmable transparent organic luminescent tags. *Sci. Adv.* **5**, eaau7310 (2019).
151. Suzuki, K. *et al.* Reevaluation of absolute luminescence quantum yields of standard solutions using a spectrometer with an integrating sphere and a back-thinned CCD detector. *Phys. Chem. Chem. Phys.* **11**, 9850 (2009).
152. Leyre, S. *et al.* Absolute determination of photoluminescence quantum efficiency using an integrating sphere setup. *Rev. Sci. Instrum.* **85**, 123115 (2014).
153. Edinburgh Instruments, FLS980 Series Reference Guide. https://www.edinst.com/wp-content/uploads/2016/02/FLS980-Series-Reference-Guide-Integrating-Sphere.pdf.
154. Frisch, M. J.; Trucks, G. W.; Schlegel, H. B.; Scuseria, G. E.; Robb, M. A.; Cheeseman, J. R.; Scalmani, G.; Barone, V.; Petersson, G. A.; Nakatsuji, H.; Li, X.; Caricato, M.; Marenich, A. V.; Bloino, J.; Janesko, B. G.; Gomper, J. B. . F. Gaussian 16, Revision C.01. *Gaussian, Inc., Wallingford CT* (2016).
155. Neese, F. The ORCA program system. *Wiley Interdiscip. Rev. Comput. Mol. Sci.* **2**, 73–78 (2012).
156. Neese, F. Software update: The ORCA program system—Version 5.0. *Wiley Interdiscip. Rev. Comput. Mol. Sci.* **12**, e1606 (2022).
157. Lu, T. & Chen, F. Multiwfn: A multifunctional wavefunction analyzer. *J. Comput. Chem.* **33**, 580–592 (2012).
158. Jacquemin, D. *et al.* Absorption and emission spectra of 1,8-naphthalimide fluorophores: A PCM-TD-DFT investigation. *Chem. Phys.* **372**, 61–66 (2010).
159. Marinova, N. V., Georgiev, N. I. & Bojinov, V. B. Facile synthesis, sensor activity and logic behaviour of 4-aryloxy substituted 1,8-naphthalimide. *J. Photochem. Photobiol. A Chem.* **254**, 54–61 (2013).
160. Oelgemöller, M. & Kramer, W. H. Synthetic photochemistry of naphthalimides and related compounds. *J. Photochem. Photobiol. C Photochem. Rev.* **11**, 210–244 (2010).
161. Gudeika, D. *et al.* New derivatives of triphenylamine and naphthalimide as ambipolar organic semiconductors: Experimental and theoretical approach. *Dye. Pigment.* **106**, 58–70 (2014).
162. Bojinov, V. B., Georgiev, N. I. & Marinova, N. V. Design and synthesis of highly photostable fluorescence sensing 1,8-naphthalimide-based dyes containing s-triazine UV absorber and HALS units. *Sensors Actuators, B Chem.* **148**, 6–16 (2010).

163. Gudeika, D. *et al.* Structure properties relationship of donor-acceptor derivatives of triphenylamine and 1,8-naphthalimide. *J. Phys. Chem. C* **116**, 14811–14819 (2012).
164. Xu, S. Y. *et al.* Synthesis and evaluation of a boronate-tagged 1,8-naphthalimide probe for fluoride recognition. *Org. Biomol. Chem.* **13**, 4143–4148 (2015).
165. Gopikrishna, P., Meher, N. & Iyer, P. K. Functional 1,8-Naphthalimide AIE/AIEEgens: Recent Advances and Prospects. *ACS Appl. Mater. Interfaces* **10**, 12081–12111 (2018).
166. Geraghty, C., Wynne, C. & Elmes, R. B. P. 1,8-Naphthalimide based fluorescent sensors for enzymes. *Coord. Chem. Rev.* **437**, 213713 (2021).
167. Duke, R. M., Veale, E. B., Pfeffer, F. M., Kruger, P. E. & Gunnlaugsson, T. Colorimetric and fluorescent anion sensors: An overview of recent developments in the use of 1,8-naphthalimide-based chemosensors. *Chem. Soc. Rev.* **39**, 3936–3953 (2010).
168. Yu, H., Guo, Y., Zhu, W., Havener, K. & Zheng, X. Recent advances in 1,8-naphthalimide-based small-molecule fluorescent probes for organelles imaging and tracking in living cells. *Coord. Chem. Rev.* **444**, 214019 (2021).
169. Gudeika, D. *et al.* Electron-transporting naphthalimide-substituted derivatives of fluorene. *Dye. Pigment.* **99**, 895–902 (2013).
170. Liu, K. *et al.* Electrooxidative para-selective C–H/N–H cross-coupling with hydrogen evolution to synthesize triarylamine derivatives. *Nat. Commun.* **10**, 639 (2019).
171. Xu, W., Chan, K. M. & Kool, E. T. Fluorescent nucleobases as tools for studying DNA and RNA. *Nat. Chem.* **9**, 1043–1055 (2017).
172. Novosjolova, I., Bizdena, E. & Turks, M. Synthesis and applications of azolylpurine and azolylpurine nucleoside derivatives. *European J. Org. Chem.* **2015**, 3629–3649 (2015).
173. Zilbershtein-Shklanovsky, L., Weitman, M., Major, D. T. & Fischer, B. Rules for the design of highly fluorescent nucleoside probes: 8-(substituted cinnamyl)-adenosine analogues. *J. Org. Chem.* **78**, 11999–12008 (2013).
174. Yang, Y. *et al.* Blue-violet electroluminescence from a highly fluorescent purine. *Chem. Mater.* **22**, 3580–3582 (2010).
175. Yang, Y. *et al.* Ultraviolet-violet electroluminescence from highly fluorescent purines. *J. Mater. Chem. C* **1**, 2867–2874 (2013).
176. Wang, Z. *et al.* Purine-based thermally activated delayed fluorescence emitters for efficient organic light-emitting diodes. *Dye. Pigment.* **180**,

108437 (2020).
177. Sun, K. M., McLaughlin, C. K., Lantero, D. R. & Manderville, R. A. Biomarkers for phenol carcinogen exposure act as pH-sensing fluorescent probes. *J. Am. Chem. Soc.* **129**, 1894–1895 (2007).
178. Venkatesh, V., Shukla, A., Sivakumar, S. & Verma, S. Purine-stabilized green fluorescent gold nanoclusters for cell nuclei imaging applications. *ACS Appl. Mater. Interfaces* **6**, 2185–2191 (2014).
179. Li, J. *et al.* Nucleoside-Based Ultrasensitive Fluorescent Probe for the Dual-Mode Imaging of Microviscosity in Living Cells. *Anal. Chem.* **88**, 5554–5560 (2016).
180. Šišuļins, A. *et al.* Synthesis and fluorescent properties of N(9)-alkylated 2-amino-6-triazolylpurines and 7-deazapurines. *Beilstein J. Org. Chem.* **15**, 474–489 (2019).
181. Collier, G. S. *et al.* Linking design and properties of purine-based donor-acceptor chromophores as optoelectronic materials. *J. Mater. Chem. C* **5**, 6891–6898 (2017).
182. Wex, B. & Kaafarani, B. R. Perspective on carbazole-based organic compounds as emitters and hosts in TADF applications. *J. Mater. Chem. C* **5**, 8622–8653 (2017).
183. Hosokai, T. *et al.* Evidence and mechanism of efficient thermally activated delayed fluorescence promoted by delocalized excited states. *Sci. Adv.* **3**, e1603282 (2017).
184. Noda, H., Nakanotani, H. & Adachi, C. Excited state engineering for efficient reverse intersystem crossing. *Sci. Adv.* **4**, eaao6910 (2018).
185. Zhang, D., Cai, M., Zhang, Y., Zhang, D. & Duan, L. Sterically shielded blue thermally activated delayed fluorescence emitters with improved efficiency and stability. *Mater. Horizons* **3**, 145–151 (2016).
186. Youn Lee, S. *et al.* Luminous Butterflies: Efficient Exciton Harvesting by Benzophenone Derivatives for Full-Color Delayed Fluorescence OLEDs. *Angew. Chemie Int. Ed.* **53**, 6402–6406 (2014).
187. Li, Y., Xie, G., Gong, S., Wu, K. & Yang, C. Dendronized delayed fluorescence emitters for non-doped, solution-processed organic light-emitting diodes with high efficiency and low efficiency roll-off simultaneously: two parallel emissive channels. *Chem. Sci.* **7**, 5441–5447 (2016).
188. Lee, S. Y., Yasuda, T., Park, I. S. & Adachi, C. X-shaped benzoylbenzophenone derivatives with crossed donors and acceptors for highly efficient thermally activated delayed fluorescence. *Dalt. Trans.* **44**, 8356–8359 (2015).
189. Wang, F. *et al.* Twisted penta-Carbazole/Benzophenone Hybrid

Compound as Multifunctional Organic Host, Dopant or Non-doped Emitter for Highly Efficient Solution-Processed Delayed Fluorescence OLEDs. *Chinese J. Chem.* **36**, 241–246 (2018).

190. Lesher, G. Y., Froelich, E. J., Gruett, M. D., Bailey, J. H. & Brundage, R. P. 1,8-Naphthyridine Derivatives. A New Class of Chemotherapeutic Agents. *J. Med. Pharm. Chem.* **5**, 1063–1065 (1962).
191. Srivastava, S. K., Jha, A., Agarwal, S. K., Mukherjee, R. & Burman, A. C. Synthesis and Structure-Activity Relationships of Potent Antitumor Active Quinoline and Naphthyridine Derivatives. *Anticancer. Agents Med. Chem.* **7**, 685–709 (2008).
192. Chen, C. *et al.* Naphthyridine-based thermally activated delayed fluorescence emitters for multi-color organic light-emitting diodes with low efficiency roll-off. *J. Mater. Chem. C* **7**, 4673–4680 (2019).
193. Lee, Y., Woo, S. J., Kim, J. J. & Hong, J. I. Linear-shaped thermally activated delayed fluorescence emitter using 1,5-naphthyridine as an electron acceptor for efficient light extraction. *Org. Electron.* **78**, 105600 (2020).
194. Shen, Y. F. *et al.* Naphthyridine-based thermally activated delayed fluorescence emitters for highly efficient blue OLEDs. *Dye. Pigment.* **178**, 108324 (2020).
195. Ji, L., Griesbeck, S. & Marder, T. B. Recent developments in and perspectives on three-coordinate boron materials: a bright future. *Chem. Sci.* **8**, 846–863 (2017).
196. Hoffend, C. *et al.* Effects of boron doping on the structural and optoelectronic properties of 9,10-diarylanthracenes. *Dalt. Trans.* **42**, 13826–13837 (2013).
197. Reus, C., Weidlich, S., Bolte, M., Lerner, H. W. & Wagner, M. C-functionalized, air- and water-stable 9,10-dihydro-9,10-diboraanthracenes: Efficient blue to red emitting luminophores. *J. Am. Chem. Soc.* **135**, 12892–12907 (2013).
198. Wu, T. L. *et al.* Diboron compound-based organic light-emitting diodes with high efficiency and reduced efficiency roll-off. *Nat. Photonics* **12**, 235–240 (2018).
199. Hsieh, C. M. *et al.* Diboron-Based Delayed Fluorescent Emitters with Orange-to-Red Emission and Superior Organic Light-Emitting Diode Efficiency. *ACS Appl. Mater. Interfaces* **12**, 23199–23206 (2020).

CURRICULUM VITAE

Justina Jovaišaitė

Birth date 02/05/1991

Email jovaisaite.justina@gmail.com,
justina.jovaisaite@ff.vu.lt

Education

2016 – 2020 & 2022 – 2023 ** Maternity leave in 2020-2022*

PhD in Physics
Vilnius University, Faculty of Physics, Institute of Photonics and Nanotechnology
Research topic: "Control of singlet and triplet states in organic intramolecular charge transfer compounds"
Supervisor prof. Saulius Juršėnas

2014 – 2016

Master's degree in Materials Technology
Vilnius University, Faculty of Physics, Institute of Photonics and Nanotechnology
Studies: Materials and Technology of Optoelectronics
Thesis: "Fluorescence sensors based on nitrogen heterocycles materials"
Supervisor prof. Saulius Juršėnas

2010 – 2014

Bachelor's degree in Physics
Vilnius University, Faculty of Physics, Institute of Photonics and Nanotechnology
Studies*:* Physics of Modern Technologies and Management
Thesis: "Fluorescence sensing of metal ions by using pyrrole-pyrimidine derivatives"
Supervisor prof. Saulius Juršėnas

Research/Work experience

2018 – present

Junior Research Fellow
Vilnius University, Institute of Photonics and Nanotechnology

2016 – 2018

Engineer
Vilnius University, Institute of Photonics and Nanotechnology

Participation in scientific projects

2022 – present	**Junior Research Fellow** "Molecular Electronics in functionalized Purines: fundamental Study and applications (MEPS)", The Research Council of Lithuania. Project no. S-LLT-22-3. Project supervisor prof. S. Juršėnas.
2018 – 2022	**Junior Research Fellow** "Development of advanced optoelectronic materials via smart molecular engineering", SMART, The Research Council of Lithuania. Project no. 09.3.3-LMT-K-718-01-0026. Project supervisor prof. S. Juršėnas.
2018 – 2022	**Junior Research Fellow** "Triplet state engineering in organic optoelectronics compounds", Global Grant, The Research Council of Lithuania. Project no.09.3.-LMT-K-712-01-0084. Project supervisor dr. K. Kazlauskas.

Internship and Practice

04/2018 – 06/2018	**Internship, supported by the Research Council of Lithuania** **Université de Bordeaux, Laboratoire Ondes et Matière d'Aquitaine (LOMA), France** Project topic: "Internship in LOMA laboratory, France, to study ultrafast excited state processes in bis-triazolyl-purine derivatives". Project no. 09.3.3-LMT-K-712-07-0004) Supervisor dr. Gediminas Jonušauskas
11/2017 – 04/2018	***Erasmus*+ internship** **Université de Bordeaux, Laboratoire Ondes et Matière d'Aquitaine (LOMA), France** Research topic: "Solvent and metal ion effect studies on the photophysics of purine,

	pyrimidine, pyrrole-pyrimidine and additional materials by steady-state and transient absorption spectroscopy." Supervisor dr. Gediminas Jonušauskas
09/2015 – 12/2015	***Erasmus*+ internship** **Centre National de la Recherche Scientifique (CNRS), Laboratoire Francis Perrin, CEA/Saclay, France** Research topic: "Solvent effects on the photophysics of 5-methylcytidine, studied by steady-state and time-resolved fluorescence spectroscopy (femtosecond fluorescence upconversion)" Supervisor dr. Akos Banyasz
09/2013 – 05/2016	**Practice according to scholarship of Jurgis Viščakas** **Vilnius University, Department of Physics** Research topic: "Metal ion sensing by pyrrole-pyrimidine, pyrimidine and purine derivatives Supervisors dr. Lina Skardžiūtė and prof. Saulius Juršėnas
02/2013 – 05/2013	**Students' scientific research of Physics 2013** **Vilnius University, Department of Physics** Research topic: "Research of charge transfer in multifunctional pyrrole-pyrimidines" Supervisor prof. Saulius Juršėnas
11/2011 – 05/2012	**Students' scientific research of Physics 2011** **Vilnius University, Department of Physics** Research topic: "Alkyl chain length effect on the fluorescence properties of triphenylamine derivatives" Supervisor dr. Karolis Kazlauskas

COPIES OF PUBLICATIONS

Paper I

TICT compounds by design: comparison of two naphthalimide-π-dimethylaniline conjugates of different lengths and ground state geometries

J. Jovaišaitė, P. Baronas, G. Jonusauskas, D. Gudeika, A. Gruodis, J. V. Gražulevičius and S. Juršėnas

Phys. Chem. Chem. Phys., **25**, 2411-2419 (2023)

DOI: 10.1039/d2cp04250a

https://doi.org/10.1039/D2CP04250A

PCCP

ROYAL SOCIETY OF CHEMISTRY

PAPER

View Article Online
View Journal

Check for updates

Cite this: DOI: 10.1039/d2cp04250a

TICT compounds by design: comparison of two naphthalimide-π-dimethylaniline conjugates of different lengths and ground state geometries†

Justina Jovaišaitė,[a] Paulius Baronas,[a] Gediminas Jonusauskas,[b] Dalius Gudeika,[c] Alytis Gruodis,[d] Juozas V. Gražulevičius[c] and Saulius Juršėnas[a]

Two new twisted intramolecular charge transfer (TICT) donor-π-acceptor compounds were designed by combining a well-known electron acceptor naphthalimide unit with a classic electron donor dimethylaniline through two types of different rigid linkers. The combined steady-state and time-resolved spectroscopy of molecules in solvents of different polarities in comparison to solid-state solvation experiments of doped polymer matrixes of different polarities allowed distinguishing between solvation and conformation determined processes. The photophysical measurements revealed that non-polar solutions possess high fluorescence quantum yields of up to 70% which is a property of pre-twisted/planar molecules in the excited charge transfer (CT) states. The increase of polarity allows tuning the Stokes shift through all the visible wavelength range up to 8601 cm^{-1} which is accompanied by a three orders of magnitude drop of fluorescence quantum yields. This is a result of the emerged TICT states as dimethylaniline twists to a perpendicular position against the naphthalimide core. The TICT reaction of molecules enables an additional non-radiative excitation decay channel, which is not present if the twisting is forbidden in a rigid polymer matrix. Transient absorption spectroscopy was employed to visualize the excited state dynamics and to obtain the excited state reaction constants, revealing that TICT may occur from both the Franck-Condon region and the solvated pre-twisted/planar CT states. Both molecules undergo the same photophysical processes, however, a longer linker and thus a higher excited state dipole moment determines the faster excited state reactions.

Received 12th September 2022,
Accepted 7th December 2022

DOI: 10.1039/d2cp04250a

rsc.li/pccp

Published on 07 December 2022. Downloaded on 1/17/2023 9:01:23 AM.

Introduction

Organic π-conjugated molecules with electron donating (D) and electron accepting (A) characters represent so-called push-pull systems with an intramolecular charge transfer (CT) character which is essential to realize tuneable structural and functional properties for organic optoelectronic applications. The main strategy to design specific features of CT compounds comprises the appropriate selection of D and A moieties connected through π-conjugated linkers and the substitution position as well as the realization of planar/twisted and rigid/flexible molecular scaffolds. The conformational differences resulting in a perpendicular configuration of D and A fragments in the excited state may be further classified as a twisted intramolecular charge transfer (TICT) state, first proposed by Grabowski *et al.*[1] TICT states undergo full charge separation as twisting around the single bond leads to the deconjugation of electron donor and acceptor excited states, and are desirable for electrostatic force driven molecular motors, fluorescent molecular rotors, switches, probes, bioimaging, and lighting or even energy harvesting techniques.[2–4] Depending on the targeted application, both suppression and enhancement of TICT states could be required.[5]

In terms of molecular orbitals, the excited state geometry can be predicted considering several factors: (i) the HOMO–LUMO energy gaps between planar and twisted geometries; (ii) the difference in the hole-electron interactions; and (iii) the geometry relaxation of the excited state.[6] The first factor, mostly contributing to the formation of TICT, states that TICT is only possible if the twisted geometry has a smaller HOMO–LUMO

[a] Institute of Photonics and Nanotechnology, Vilnius University, Saulėtekio Ave. 3, LT-10257 Vilnius, Lithuania. E-mail: justina.jovaisaite@ff.vu.lt
[b] Laboratoire Ondes et Matière d'Aquitaine, Bordeaux University, UMR CNRS 5798, 351 cours de la Libération, 33405 Talence, France
[c] Department of Polymer Chemistry and Technology, Kaunas University of Technology, Radvilėnų rd. 19, LT-50254 Kaunas, Lithuania
[d] Institute of Chemical Physics, Vilnius University, Saulėtekio Ave. 3, LT-10257 Vilnius, Lithuania

† Electronic supplementary information (ESI) available. See DOI: https://doi.org/10.1039/d2cp04250a

Published on 07 December 2022. Downloaded on 1/17/2023 9:01:23 AM.

gap than that of a planar geometry, which can be favoured by strong HOMO–D and LUMO–A interactions.[6] Intuitively, TICT can be predicted by selecting an electron donor with a low ionization potential and an electron acceptor with a high electron affinity and an appropriate conjugation length between these two groups.[6] If TICT is favourable in a molecular system, it is more likely to occur in non-viscous, polar solvents due to the unrestricted molecular motions and better stabilization of polar charge transfer states.[7]

1,8-Naphthalimides (NIs), one of the well-known electron acceptors, are considered among the most important building blocks of efficient fluorescent materials.[8] Due to the relative simplicity of synthetic operations for targeted modification,[9,10] tuneable photophysical properties,[11] photostability,[12] thermostability[11,13] and biocompatibility,[14] NI materials have received tremendous attention from the scientific community and became a highly adaptable scaffold with a huge diversity of proposed real life applications.[15] These include studies demonstrating NI compounds as materials for optoelectronic devices (OLEDs, organic solar cells, logic gates),[16–21] as well as bio[22,23] and chemosensors[24–26] or even as fluorescent cell imaging agents.[27–30] Having in mind a redox potential of the 1,8-naphthalimide core (~ -1.8 V, *vs.* Ag/Ag^+),[31] many of the strategies for the mentioned applications cover the simple design of adding an electron donating substituent to the NI core at its 4th position to create donor–acceptor (D–A) type compounds with a CT character. One of the classic electron-donating substituents is *N*,*N*-dimethylaniline (DMA) with a redox potential of at least 0.65 V (*vs.* Ag/AgCl),[32] which may serve as a perfect charge donor with a high driving force for the intramolecular charge transfer upon combination with the NI core through selected linkers.

Thus, in this work, we present a comprehensive study of two new A-π-D fluorophores with electron acceptor NI and electron donor DMA fragments connected through two types of linkers at the 4th position of the NI core: single bond (**NA1**) or acetylene-like junction (**NA2**) (Fig. 1). Diverse pre-requisites (pre-twisted or planar ground state geometries as well as different conjugation lengths and different molecular dipolar moments in the excited state) were compared by steady-state and time-resolved spectroscopic methods; the transient absorption spectroscopy provided the main insights and allowed visualizing the dynamics of CT and TICT reactions, governed by environmental parameters (polarity and rigidity) and molecular properties. The supplementary studies of both compounds in rigid polymer matrices made it possible to clearly differentiate the spectral effects produced by dynamic solvation from those observed in the excited charge transfer states.

Results and discussion

DFT modelling, intramolecular charge transfer

Optimized ground state geometries and charge density distributions in the HOMO and LUMO states of compounds **NA1** and **NA2** in cyclohexane (CyHex) are depicted in Fig. 1. Both molecules reveal a CT nature of the electronic transition. The

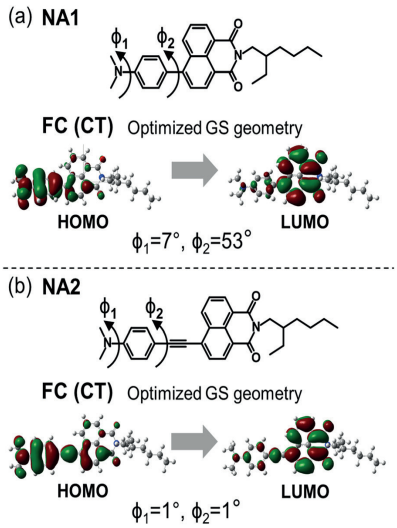

Fig. 1 Molecular structures and optimized ground state geometries with calculated electron density distributions for HOMO and LUMO molecular orbitals of compounds **NA1** (a) and **NA2** (b) in cyclohexane.

HOMO state comprises charge redistribution between NI and DMA moieties, while the charge density in the LUMO state is localized mainly on the NI core. The studied compounds show different twist angles between NI and DMA moieties. Compound **NA1** with phenyl ring as a π-linker has a pre-twisted geometry in a ground state: the twist angle between dimethylamine and benzene (ϕ_1) is 7°, while between NI and DMA (ϕ_2) is 53°. Compound **NA2** with the phenyl-acetylene junction possesses a planar ground state geometry. The energies of upward transitions of singlet states as well as a short comment on the excited state optimization are provided in the ESI† (Table S1).

CT and TICT states probed by steady-state and time-resolved fluorescence spectroscopy

Normalized absorption and fluorescence spectra of **NA1** and **NA2** in a range of aprotic solvents are depicted in Fig. 2. Photophysical data obtained by steady-state and time-resolved fluorescence experiments are summarized in Table 1.

As already predicted from molecular structures (A-π-D), both molecules exhibit photophysical properties characteristic to CT states. The absorption spectra are comprised of higher energy bands, typical of dimethylaniline (285–313 nm),[33] 1,8-naphthalimide (350 nm)[8,34] fragment absorption and the CT state absorption at 407–448 nm in various solutions, also observed for similar D–A naphthalimide derivatives.[11,34,35] The structureless absorption band of **NA1** and a clear vibronic structure of **NA2** in CyHex confirm the pre-twisted and planar ground state geometries, respectively. Upon increasing the polarity of the solvent, a slight red-shift and a gradual

This journal is © the Owner Societies 2022

Published on 07 December 2022. Downloaded on 1/17/2023 9:01:23 AM.

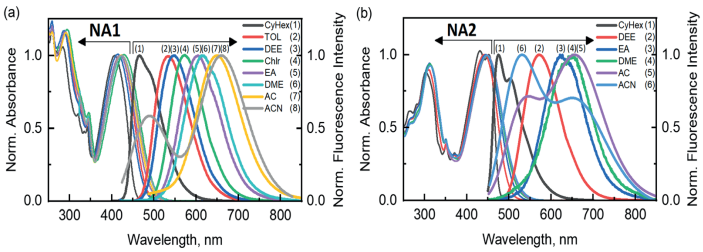

Fig. 2 Normalized absorption and fluorescence spectra of compounds **NA1** (a) and **NA2** (b) in different solvents: cyclohexane (CyHex), toluene (TOL), diethyl ether (DEE), chloroform (Chlr), ethyl acetate (EA), dimethoxyethane (DME), acetone (AC) and acetonitrile (ACN). Samples were excited at 420 nm. The legend denotes solvent name abbreviations. The plotted emission spectra of **NA1** in acetonitrile and **NA2** in acetone and acetonitrile are Gaussian fits of experimental data, see Fig. S2 (ESI†) for original spectra.

Table 1 Steady-state absorption, fluorescence and time-resolved fluorescence data of compounds **NA1** and **NA2** in solvents of different polarizabilities and polymer matrixes of different polarities, obtained by exciting samples at 420 nm

	Solvent	ε	$\Delta f'$[a]	λ_{ABS},[b] nm	λ_{FL},[c] nm	$\Delta\nu$,[d] cm^{-1}	Φ_{FL},[e] %	τ,[f] ns	τ_r,[g] ns	τ_n,[h] ns
NA1	Cyclohexane (CyHex)	2.02	0.100	407	465	3255	73	3.45	4.70	12.96
	Diethyl ether (DEE)	4.33	0.256	414	547	6083	39	6.25	15.99	10.26
	Ethyl acetate (EA)	6.02	0.292	420	605	7397	6.5	2.96	45.24	3.17
	Dimethoxyethane (DME)	7.2	0.309	423	616	7539	3.0	0.84	28.14	0.86
	Acetone (AC)	20.7	0.374	423	651	8456	0.45	0.17	37.18	0.17
	Acetonitrile (ACN)	37.5	0.393	424	490, 661	3430, 8601	0.1 (0.03/0.07)[j]	0.01/0.07[k]	21.18/98.22	0.01/0.07
	1% wt in polystyrene (PS)	2.45[i]	—	428	519	4190	76	6	7.83	24.79
	1% wt in PMMA (PMMA)	3.41[i]	—	428	544	5274	56	8	14.29	18.18
	1% wt in PMMA, 20% wt of CA (PMMA/CA)	8.31[i]	—	431	578	6170	41	9.5	23.17	16.1
NA2	Cyclohexane (CyHex)	2.02	0.100	452	475	1203	71	2.41	3.38	8.42
	Diethyl ether (DEE)	4.33	0.256	443	572	5302	26	4.05	15.63	5.47
	Ethyl acetate (EA)	6.02	0.292	445	631	6711	0.71	0.50	70.32	0.50
	Dimethoxyethane (DME)	7.2	0.309	449	652	6958	0.27	0.25	92.94	0.25
	Acetone (AC)	20.7	0.374	448	538, 662	3991, 7448	0.06 (0.02/0.04)[j]	<0.002/0.04[l]		
	Acetonitrile (ACN)	37.5	0.393	448	529, 667	3688, 7579	0.03 (0.02/0.01)[j]	<0.002/0.04[l]		
	1% wt in polystyrene (PS)	2.45[i]	—	459	546	3578	68	5	6.94	14.75
	1% wt in PMMA (PMMA)	3.41[i]	—	452	578	4961	44	6	13.64	10.71
	1% wt in PMMA, 20% wt of CA (PMMA/CA)	8.31[i]	—	456	610	5818	33	5.5	16.67	8.21

[a] Solvent-dependent parameter according to Weller's equation, $\Delta f = \frac{\varepsilon - 1}{2\varepsilon + 1} - \frac{n^2 - 1}{4n^2 + 2}$. Here, ε is a static dielectric constant and n is a refractive index of the solvent. [b] Wavelength of the lowest energy absorption maxima. [c] Wavelength of the fluorescence spectra maxima. Excitation wavelength was set to 420 nm. [d] Stokes shift. [e] Fluorescence quantum yields. [f] Fluorescence lifetimes. [g] $\tau_{rad} = \frac{\tau}{QY}$. [h] $\tau_{nonrad} = \frac{\tau}{1 - QY}$. [i] The dielectric constant values were taken from ref. 37. [j] The fluorescence quantum yield values in parenthesis correspond to the blue and red side fluorescence bands. [k] Two fluorescence lifetimes were recorded at maxima of dual fluorescence peaks (517 nm/663 nm). [l] The fluorescence decay transients of **NA2** in AC and ACN could be fitted bi-exponentially. Here only longer lifetime values are given as the fast components are below the equipment's temporal resolution.

broadening of absorption spectra are observed for both molecules. The absorption spectral changes in the extended solvents list, presented in Table S3 and Fig. S3 (ESI†), mainly suggest that absorption solvatochromism of the pre-twisted **NA1** is mostly related to slightly different ground state geometries. In terms of planar **NA2**, its dipole moments in ground state (as well as in the excited Franck–Condon state) are roughly the same and thus, only a minor absorption spectral red-shift of a few nanometres is observed[36] (see a more detailed discussion in the ESI†).

The CT character of NI compounds ensures the significant dependence of fluorescence properties on solvent polarizability. In CyHex, both compounds already exhibit a large Stokes shift of 3255 cm^{-1} (**NA1**) and 1203 cm^{-1} (**NA2**), respectively, pointing towards the fluorescence from CT states even in a non-polar environment. The smaller Stokes shift and more pronounced vibronic shape of fluorescence spectra of **NA2** show the planar excited state geometry in a non-polar solvent. In the case of **NA1**, the fluorescence spectrum in CyHex also possesses a vibronic shape. This may be related to the partial planarization of the molecule's geometry after photoexcitation in a non-polar environment. The planarization of **NA1** is also supported by the excited state optimization calculations, which show the decrease of the dihedral angle between NI and DMA moieties to *ca.* 30° (see Table S1, ESI†).

Even the small increase of the solvent's dielectric constant up to ε = 4.33 (diethyl ether, DEE) determines the pronounced

Published on 07 December 2022. Downloaded on 1/17/2023 9:01:23 AM.

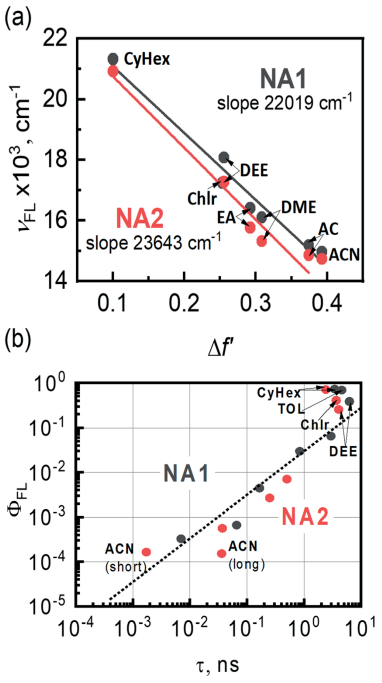

Fig. 3 Weller's polarity plots of compounds **NA1** (black dots) and **NA2** (red dots) (a). The black and red lines represent the best linear fits. Only red bands of fluorescence spectra are included for **NA1** in ACN and **NA2** in AC and ACN. Fluorescence quantum yields (Φ_{FL}) *versus* fluorescence lifetimes (τ) for **NA1** (black dots) and **NA2** (red dots) (b). The dotted line represents a slope equal to 1 in a log–log scale.

Stokes shift of 6083-5302 cm^{-1} which becomes as large as 8601–7579 cm^{-1} in most polar tested environment with ε = 37.5 (acetonitrile, ACN) for **NA1–NA2**, respectively. The dynamics of absorption and fluorescence spectra of **NA1** and **NA2** already suggests the increase of molecules' dipole moment upon excitation.[35] The excited state dipole moments (μ_e) of compounds were evaluated by a modified Lippert-Mataga approach, called Weller's equation[38] (see Fig. 3a and section Weller's polarity plot in the ESI†), that accounts for fluorescence solvatochromic effects only. The estimated μ_e is 20 D for **NA1** and 22.5 D for **NA2**. The obtained excited state values are twice as high as the calculated ground state dipole moments (see Table S2, ESI†) and indicate a strong charge transfer character of compounds. Thus, not only different geometries but also different μ_e are the molecular prerequisites for the excited state dynamics.

The pronounced fluorescence spectral shift is accompanied by significant changes in fluorescence quantum yields (Φ_{FL}) and lifetimes (τ) (Table 1). The high value of Φ_{FL} in CyHex of *ca.* 70% drops to 39% (**NA1**) and 26% (**NA2**) in DEE. At the same time, the slight increase in solvents polarity prolongs fluorescence lifetimes by a factor of two: from 3.4 ns (CyHex) to 6.3 ns (DEE) for **NA1** and from 2.4 ns to 4.1 ns for **NA2**. A further increase of solvent dielectric constant leads to a further Φ_{FL} drop (down to 6.5% for **NA1** and to 0.7% for **NA2** in EA) and, interestingly, a decrease of fluorescence lifetimes (τ = 3 ns and τ = 0.5 ns for **NA1** and **NA2** in EA). Thus, from a certain dielectric constant of the solvent (ε = 6.02), the opposite trend of fluorescence lifetime behaviour is observed, where non-radiative excitation decay starts to dominate. The most polar environment (AC and ACN) determines almost forbidden (QY < 1%) dual fluorescence with extremely short τ values of tens of picoseconds (τ = 70 ps for **NA1** and τ = 40 ps for **NA2**, ACN). One has to note that the dual fluorescence in AC and ACN is of very low intensity, and thus, the impact of the emission from two different states (*e.g.*, determined by different geometries) as well as the impact of the impurities may have been observed.

The fluorescence quantum yields *versus* fluorescence lifetimes, shown in Fig. 3b, nicely illustrate the discussed trends. A negative slope of $\Phi_{FL}(\tau)$ is observed in CyHex, DEE, toluene (TOL), and chloroform (Chlr), while for the rest of the tested more polar solvents (ε > 6) a positive slope close to 1 is determined. These two distinct tendencies of Φ_{FL} *versus* τ as well as a significant Stokes shift accompanied by the drop in both fluorescence quantum yields as well as their lifetimes cannot be explained by the excited charge transfer states itself. We suggest that the observed photophysical properties of NI compounds arise from the competition between pre-twisted or planar CT states and TICT, that become dominant in solvents with ε > 6. The fluorescence in most polar solvents, however, can be observed due to the conformational disorder of twist angles near 90° at room temperature. In order to distinguish between solvation and twisting determined processes/properties in solvents, we further employed solid-state solvation experiments in rigid polymer matrixes with different dielectric constants, where molecular motions would be highly restricted.

Three different rigid systems were employed to obtain the set of polymer samples of different dielectric constants that were doped with **NA1** and **NA2** compounds: 1 wt% polystyrene (PS) (ε = 2.45), 1 wt% poly(methyl methacrylate) (PMMA) (ε = 3.41) and 1 wt% PMMA with 20 wt% of camphoric anhydrite (PMMA/CA) (ε = 8.31).[37] The CA was selected as a co-dopant for polymeric samples due to its small size and high ground state dipole moment in order to realize the solid-state solvation effect.[37,39] Upon the increase of polymer matrix polarity, the gradual red-shift of fluorescence spectra was observed (Fig. S4, ESI† and Table 1). Contrary to the obtained results in solutions, only a slight decrease of Φ_{FL} (from 76% in PS to 41% in PMMA/CA for **NA1** and from 68% to 33% for **NA2**) along with slightly prolonged fluorescence lifetimes (6 ns to 9.5 ns for **NA1** and 5 ns to 6 ns for **NA2**) were observed in a rigid environment. Thus, the obtained results in polymeric films confirm that the efficient non-radiative decay channel is enabled only in polar solvents and is mainly related to geometry changes. One has to note that the decrease of fluorescence lifetimes in solvents is not a TICT property itself but should be considered as an outcome of an efficient non-radiative decay channel that is enabled by the twisted geometry, whether

 This journal is © the Owner Societies 2022

Published on 07 December 2022. Downloaded on 1/17/2023 9:01:23 AM.

through an efficient coupling with a dense manifold of polar solvent vibrational states[40,41] or, alternatively, through the intersection of the excited singlet state potential surface with triplet states.

So far, it is evident that the excited state relaxation dynamics of studied naphthalimide compounds highly depends on the solvent-fluorophore interaction as well as the viscosity of the environment. The more efficient non-radiative excitation decay channel of **NA2** and a more pronounced decrease of fluorescence quantum yields upon an increase of solvents' polarity correlate well with a higher excited state dipole moment μ_e. However, no influence of the pre-twisted geometry of **NA1** was observed. In order to get deeper insights into excited CT/TICT state dynamics, we further employed transient absorption spectroscopy experiments.

Transient absorption spectroscopy: the solvation dynamics and TICT reaction rates

The obtained picosecond time scale transient absorption (TA) maps and spectra in solvents of different polarity (CyHex, TOL, EA and ACN) (Fig. 4) illustrate the competition between pre-twisted/planar and twisted geometries upon excitation at the CT absorption band, confirming the results obtained by steady-state and time-resolved fluorescence spectroscopy.

The initially recorded spectra of **NA1** (**NA2**) in CyHex are already of charge transfer nature and comprise the excited state

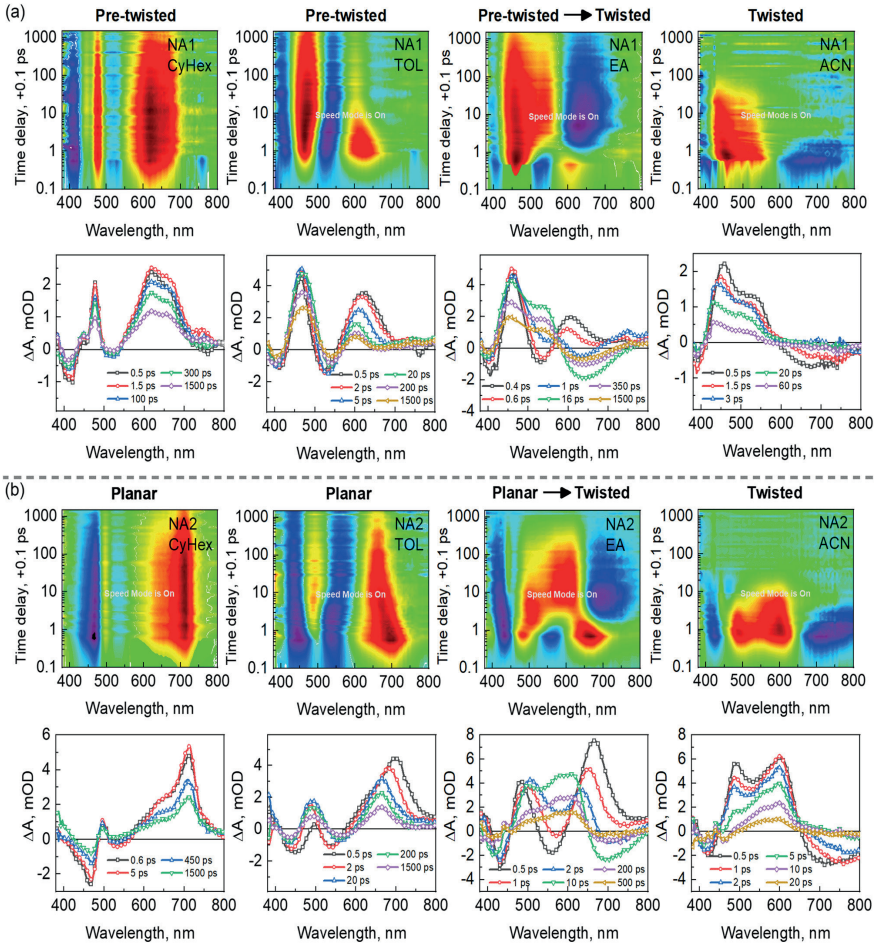

Fig. 4 Time-resolved transient absorption maps of **NA1** (a) and **NA2** (b) in cyclohexane (CyHex), toluene (TOL), ethyl acetate (EA) and acetonitrile (ACN), and its corresponding spectra at a given time delay. Samples were excited at 420 nm.

Published on 07 December 2022. Downloaded on 1/17/2023 9:01:23 AM.

absorption (ESA) observed at 460 nm (500 nm), similar to 1,8-naphthalimide S_1 state absorption spectra,[42] also, at 620 nm (650) and at 660 nm (710 nm). ESA of both compounds significantly overlaps with signals of ground state bleaching (GSB) at *ca.* 400 nm (450 nm) and signals of negative nature, related to stimulated emission (SE) that appear at *ca.* 500 nm (520 nm). No pronounced dynamic solvation was observed in a non-polar environment, as expected. In slightly more polar TOL, the dynamic solvation with a time constant of 2.6 ps[43] takes place, which is nicely illustrated by the spectral shifts for both compounds: signals of SE shift to the red side of spectra, while ESA observed at around 600 nm undergoes the blue-shift. The TA spectral shape observed in a non-polar environment is attributed to partially twisted or planar CT states, as also discussed in the previous section.

The most interesting, though, complex, excited state relaxation dynamics is observed in more polar EA. The initial TA spectra are similar to those observed in less polar solvents. Clearly, spectral shifts occur in time and are characteristic of dynamic solvation with an EA re-orientation time constant of 0.86 ps.[43] Besides, the new spectral component starts to form even earlier than the dynamic solvation is completed and only at the time delay of 16 ps for **NA1** and 10 ps for **NA2** it is completely formed and has a lifetime similar to those observed in time-resolved fluorescence measurements.

One could argue whether the observed changes in TA maps in EA are attributed to geometry changes (planar *vs.* twisted, where full charge separation takes place) or are mainly related to solvation (*i.e.*, the negative band shifts to the red and so the positive band at 500 nm could be observed, which was not possible due to spectral band overlap before solvation took place). Thus, the TA experiments were repeated for samples in PMMA and PMMA/CA. At different time delays of 1 ps and 100 ps, the slight spectral shifts are only observed (Fig. 5a and c). The comparison of results in EA and PMMA/CA (Fig. 5b and d) clearly demonstrates that transient absorption spectra of

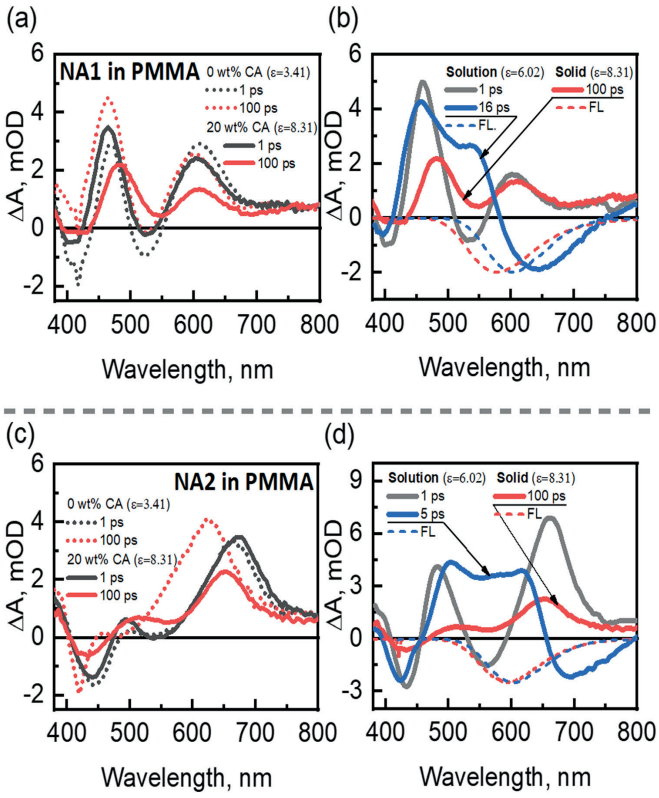

Fig. 5 Transient absorption spectra in 1 wt% PMMA (0 wt% CA) (dotted lines) and 1 wt% PMMA with 20 wt% CA (20 wt% CA) (solid lines) at 1 ps (black) and 100 ps (red) time delays of **NA1** (a) and **NA2** (c). The transient absorption spectra in ethyl acetate (solution) at 1 ps (grey lines) and at 16 ps or 5 ps (blue solid lines) in comparison with TA spectra in 1 wt% PMMA with 20 wt% CA (solid) at 100 ps time delay (red solid line) of **NA1** (b) and **NA2** (d). The dashed red and blue lines in (b) and (d) represent inverted normalized fluorescence spectra respective to solvents or films. Samples were excited at 420 nm.

 This journal is © the Owner Societies 2022

Published on 07 December 2022. Downloaded on 1/17/2023 9:01:23 AM.

NA1 and **NA2** in polar polymer resemble those obtained for a solution at early time delay (1 ps) rather than the one after dynamic solvation along with TICT reaction is completed. Consequently, the "new" spectral shapes at 16 ps for **NA1** and 10 ps for **NA2** are attributed to the excited TICT states. However, even if TICT should determine the complete charge separation, the observed spectra in EA (and ACN) are not formally bi-radical TA spectra as stimulated emission exists and has the same lifetime as ESA components. As mentioned previously, the emission from TICT states may be allowed due to the disorder of naphthalimide-dimethylaniline twist angles near 90°. The dynamic solvation in most polar ACN solvents happens in 0.26 ps,[43] thus, due to the temporal resolution of the experiment, the initial shape of TA spectra for both **NA1** and **NA2** is already an outcome of dynamic solvation and TICT reaction (Fig. 4).

To evaluate the pathways that lead to the formation of twisted charge transfer states, global analysis (GA) together with a target analysis of transient absorption data was employed.[44,45] GA was performed for **NA1** and **NA2** in EA by applying the sequential model including 3 (**NA1**) or 4 (**NA2**) compartments (Fig. S5, ESI†). The GA was applied up to 16 or 10 ps time delay in order to simplify the model and to account only for the early time-scale excited state dynamics. The obtained evolution associated spectra (EAS) highly resemble the particular TA spectra obtained in other environments (non-polar or polar solvents, or solid state). The EAS of the first compartment are similar to non-solvated TA spectra obtained in CyHex or TOL, while the EAS of 3rd (or 4th compartments in case of **NA2**) are analogous to TA spectra in most polar ACN, corresponding to the TICT state (Fig. 4). The intermediate states of the 2nd compartment for both compounds remind the solvated state as it was seen in polar polymer samples (Fig. 5). However, in terms of EAS, they are clearly affected by an additional process.

As it was already shown in a work of Park *et al.* that the TICT state can be reached through several pathways for a classic DMABN compound (*e.g.*, from locally excited or from partially twisted states),[46] the applied sequential model was updated by including a parallel process, which presumably could correspond to a different channel for the TICT state to be formed. Again, 3 or 4 compartments were included for a reasonable fit for **NA1** and **NA2** molecules, respectively (Fig. 6 and Fig. S6, ESI†). The obtained decay associated spectra were similar to EAS, as recently discussed. Thus, we associate the included compartments to the excited singlet charge transfer state in a Frack–Condon region (S_{FC}) of a ground state geometry, the intermediate state that corresponds to the solvated CT state (S_{CT}) (*i.e.*, the excited state that forms after the dynamic solvation) and TICT states (S_{TICT}). In the case of **NA2**, the 4th compartment represents a possible formation of the second oriented solvent shell around the elongated dipole in the **NA2** TICT state. It is quite possible that the molecular structure of **NA2** may accept a few additional solvent molecules in the space between D and A since the distance separating these is almost 2.4 Å longer than in **NA1**. An evolution of the transient spectra

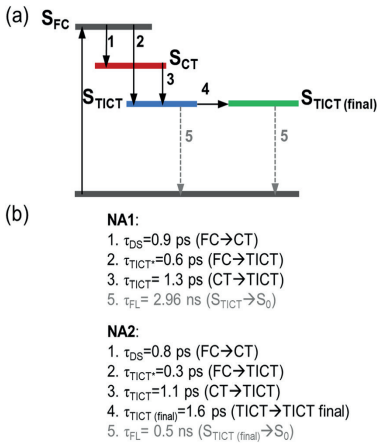

Fig. 6 The simplified model employed to perform the Global Analysis for the TA measurements of **NA1** and **NA2** in ethyl acetate (a). Model includes the excited Franck–Condon state (S_{FC}), the excited solvated charge transfer state (S_{CT}), the excited twisted intramolecular charge transfer state (S_{TICT}) and the final TICT state for **NA2** ($S_{TICT\ (final)}$). The punctured arrows are included for clarity to demonstrate the completion of the excited state reactions, *i.e.*, the relaxation of excited twisted molecules to the ground state. The obtained reaction rates for **NA1** and **NA2** are given in (b). The values of fluorescence lifetimes (τ_{FL}) were taken from time-resolved fluorescence experiments.

of **NA1** in EA contains an isosbestic point at 570 nm contrary to **NA2** where the isosbestic point disappears after 2 ps of spectral evolution (Fig. 4). The global and target analysis shows that the solvated excited state (S_{CT}) is reached within 0.8–0.9 ps that matches the EA re-orientation time constant. The TICT state (S_{TICT}) may be formed directly from the Franck–Condon region with τ_{TICT^*} = 0.6 ps (or 0.3 ps for **NA2**) or from the solvated CT state with τ_{TICT} = 1.3 ps (1.1 ps), meaning that molecules have two different pathways to reach perpendicular geometry, and TICT, in fact, may occur earlier than dynamic solvation is completed.

Thus, the TA results in non-polar CyHex and TOL represent excitation relaxation in CT states of partially twisted or planar geometries, while the results in middle polar EA show the competition between CT and TICT, and finally, the TA spectra in ACN correspond to the dominant TICT. These findings nicely match the earlier discussed results obtained by steady-state and time-resolved fluorescence experiments, suggesting the twisting starts to occur in solvents of middle polarity. As is seen from Fig. 4, the increased reaction rates of TICT in a more polar environment cause more pronounced fluorescence quenching. The dynamic solvation determines whether twisting occurs; however, its reaction rate does not outcompete the reaction rate of TICT. We see that conjugation length and, yet, the higher polarity of molecules may cause the TICT reaction to occur slightly faster. Again, no signs of the influence of pre-twisted geometry are observed.

Published on 07 December 2022. Downloaded on 1/17/2023 9:01:23 AM.

Conclusions

To sum up, two naphthalimide-dimethylaniline A-π-D molecules were thoroughly studied in terms of their photophysical behaviours in solvents and polymer matrixes of different polarities. Both molecules demonstrate a charge transfer character whether in partially planar/planar or twisted excited state geometries, which significantly depends on the parameters of the environment. The molecules are pre-twisted or planar in non-polar solvents and thus, high fluorescence quantum yields of up to 70% were achieved. However, the increase of solvent polarity determines the competition between CT and TICT states. Once TICT state is dominant in solvents with $\varepsilon > 6$, the efficient non-radiative decay channel is enabled which determines up to three orders of magnitude drop in fluorescence quantum yields and the decreased fluorescence lifetimes. In contrast, in the polymer matrix of similar polarity, the fluorescence quantum yields remain comparatively high (*ca.* 30% – 40%) along with slightly increased fluorescence lifetimes due to more stabilized CT states. The transient absorption spectroscopy confirmed the results obtained by steady-state and time-resolved fluorescence measurements and revealed that different channels exist to reach TICT states: whether from the CT states in the Franck–Condon region or from the solvated CT states. In case TICT is formed directly from the FC region, its reaction rate outcompetes the dynamic solvation. The pre-twisted geometry of the compound has no influence in terms of excited state reaction rates. On the other hand, the higher excited state dipole moment determines the faster excited state processes.

Conflicts of interest

There are no conflicts to declare.

Acknowledgements

We thank dr. Rokas Skaisgiris for the contribution at the early stages of the project. We also thank dr. Karolis Šarka for the insights on theoretical modelling. Computations were performed on resources at the High Performance Computing Centre "HPC Saulėtekis" in Vilnius University, Faculty of Physics.

References

1 Z. R. Grabowski, K. Rotkiewicz and A. Siemiarczuk, *J. Lumin.*, 1979, **18–19**, 420–424.
2 E. Y. Chernikova, D. V. Berdnikova, Y. V. Fedorov, O. A. Fedorova, F. Maurel and G. Jonusauskas, *Phys. Chem. Chem. Phys.*, 2017, **19**, 25834–25839.
3 S. Sasaki, G. P. C. Drummen and G. Konishi, *J. Mater. Chem. C*, 2016, **4**, 2731–2743.
4 S. C. Lee, J. Heo, H. C. Woo, J. A. Lee, Y. H. Seo, C. L. Lee, S. Kim and O. P. Kwon, *Chem. – Eur. J.*, 2018, **24**, 13706–13718.
5 C. Wang, W. Chi, Q. Qiao, D. Tan, Z. Xu and X. Liu, *Chem. Soc. Rev.*, 2021, **50**, 12656–12678.
6 C. Zhong, *Phys. Chem. Chem. Phys.*, 2015, **17**, 9248–9257.
7 A. Nandi, R. Ghosh and D. K. Palit, *J. Photochem. Photobiol., A*, 2016, **321**, 171–179.
8 D. Jacquemin, E. A. Perpète, G. Scalmani, I. Ciofini, C. Peltier and C. Adamo, *Chem. Phys.*, 2010, **372**, 61–66.
9 N. V. Marinova, N. I. Georgiev and V. B. Bojinov, *J. Photochem. Photobiol., A*, 2013, **254**, 54–61.
10 M. Oelgemöller and W. H. Kramer, *J. Photochem. Photobiol., C*, 2010, **11**, 210–244.
11 D. Gudeika, J. V. Grazulevicius, G. Sini, A. Bucinskas, V. Jankauskas, A. Miasojedovas and S. Jursenas, *Dyes Pigm.*, 2014, **106**, 58–70.
12 V. B. Bojinov, N. I. Georgiev and N. V. Marinova, *Sens. Actuators, B*, 2010, **148**, 6–16.
13 D. Gudeika, A. Michaleviciute, J. V. Grazulevicius, R. Lygaitis, S. Grigalevicius, V. Jankauskas, A. Miasojedovas, S. Jursenas and G. Sini, *J. Phys. Chem. C*, 2012, **116**, 14811–14819.
14 S. Y. Xu, X. Sun, H. Ge, R. L. Arrowsmith, J. S. Fossey, S. I. Pascu, Y. B. Jiang and T. D. James, *Org. Biomol. Chem.*, 2015, **13**, 4143–4148.
15 P. Gopikrishna, N. Meher and P. K. Iyer, *ACS Appl. Mater. Interfaces*, 2018, **10**, 12081–12111.
16 W. Zeng, H. Y. Lai, W. K. Lee, M. Jiao, Y. J. Shiu, C. Zhong, S. Gong, T. Zhou, G. Xie, M. Sarma, K. T. Wong, C. C. Wu and C. Yang, *Adv. Mater.*, 2018, **30**, 1704961.
17 W. Chai and R. Jin, *J. Mol. Struct.*, 2016, **1103**, 177–182.
18 D. Gudeika, *Synth. Met.*, 2020, **262**, 116328.
19 W. Zhang, Y. Xu, M. Hanif, S. Zhang, J. Zhou, D. Hu, Z. Xie and Y. Ma, *J. Phys. Chem. C*, 2017, **121**, 23218–23223.
20 B. Wang, Y. Zheng, T. Wang, D. Ma and Q. Wang, *Org. Electron.*, 2021, **88**, 106012.
21 C. J. Christopherson, D. M. Mayder, J. Poisson, N. R. Paisley, C. M. Tonge and Z. M. Hudson, *ACS Appl. Mater. Interfaces*, 2020, **12**, 20000–20011.
22 L. Zhou, L. Xie, C. Liu and Y. Xiao, *Chin. Chem. Lett.*, 2019, **30**, 1799–1808.
23 C. Geraghty, C. Wynne and R. B. P. Elmes, *Coord. Chem. Rev.*, 2021, **437**, 213713.
24 R. M. Duke, E. B. Veale, F. M. Pfeffer, P. E. Kruger and T. Gunnlaugsson, *Chem. Soc. Rev.*, 2010, **39**, 3936–3953.
25 H. Q. Dong, T. B. Wei, X. Q. Ma, Q. Y. Yang, Y. F. Zhang, Y. J. Sun, B. B. Shi, H. Yao, Y. M. Zhang and Q. Lin, *J. Mater. Chem. C*, 2020, **8**, 13501–13529.
26 J. W. Chen, C. M. Chen and C. C. Chang, *Org. Biomol. Chem.*, 2017, **15**, 7936–7943.
27 S. Banerjee, E. B. Veale, C. M. Phelan, S. A. Murphy, G. M. Tocci, L. J. Gillespie, D. O. Frimannsson, J. M. Kelly and T. Gunnlaugsson, *Chem. Soc. Rev.*, 2013, **42**, 1601–1618.
28 M. Poddar, V. Sharma, S. M. Mobin and R. Misra, *Chem. – Asian J.*, 2018, **13**, 2881–2890.
29 H.-H. Lin, Y.-C. Chan, J.-W. Chen and C.-C. Chang, *J. Mater. Chem.*, 2011, **21**, 3170.
30 H. Yu, Y. Guo, W. Zhu, K. Havener and X. Zheng, *Coord. Chem. Rev.*, 2021, **444**, 214019.
31 D. Gudeika, R. R. Reghu, J. V. Grazulevicius, G. Buika, J. Simokaitiene, A. Miasojedovas, S. Jursenas and V. Jankauskas, *Dyes Pigm.*, 2013, **99**, 895–902.

 This journal is © the Owner Societies 2022

Published on 07 December 2022. Downloaded on 1/17/2023 9:01:23 AM.

32 K. Liu, S. Tang, T. Wu, S. Wang, M. Zou, H. Cong and A. Lei, *Nat. Commun.*, 2019, **10**, 639.
33 I. Fdez. Galván, M. Elena Martín, A. Muñoz-Losa and M. A. Aguilar, *J. Chem. Theory Comput.*, 2009, **5**, 341–349.
34 D. Gudeika, A. Michaleviciute, J. V. Grazulevicius, R. Lygaitis, S. Grigalevicius, V. Jankauskas, A. Miasojedovas, S. Jursenas and G. Sini, *J. Phys. Chem. C*, 2012, **116**, 14811–14819.
35 D. Gudeika, R. R. Reghu, J. V. Grazulevicius, G. Buika, J. Simokaitiene, A. Miasojedovas, S. Jursenas and V. Jankauskas, *Dyes Pigm.*, 2013, **99**, 895–902.
36 H. El-Gezawy, W. Rettig and R. Lapouyade, *J. Phys. Chem. A*, 2006, **110**, 67–75.
37 T. Serevičius, R. Skaisgiris, J. Dodonova, I. Fiodorova, K. Genevičius, S. Tumkevičius, K. Kazlauskas and S. Juršėnas, *J. Phys. Chem. Lett.*, 2022, **13**, 1839–1844.
38 H. Beens, H. Knibbe and A. Weller, *J. Chem. Phys.*, 2004, **47**, 1183.
39 B. L. Cotts, D. G. McCarthy, R. Noriega, S. B. Penwell, M. Delor, D. D. Devore, S. Mukhopadhyay, T. S. De Vries and N. S. Ginsberg, *ACS Energy Lett.*, 2017, **2**, 1526–1533.
40 P. A. Panchenko, A. N. Arkhipova, O. A. Fedorova, Y. V. Fedorov, M. A. Zakharko, D. E. Arkhipov and G. Jonusauskas, *Phys. Chem. Chem. Phys.*, 2017, **19**, 1244–1256.
41 X. Sun, B. M. Chapin, P. Metola, B. Collins, B. Wang, T. D. James and E. V. Anslyn, *Nat. Chem.*, 2019, **11**, 768–778.
42 A. Samanta and G. Saroja, *J. Photochem. Photobiol., A*, 1994, **84**, 19–26.
43 M. L. Horng, J. A. Gardecki and M. Maroncelli, *J. Phys. Chem. A*, 1997, **101**, 1030–1047.
44 Y. Braver, A. Gelzinis, J. Chmeliov and L. Valkunas, *Chem. Phys.*, 2019, **525**, 110403.
45 I. H. M. Van Stokkum, D. S. Larsen and R. Van Grondelle, *Biochim. Biophys. Acta, Bioenerg.*, 2004, **1657**, 82–104.
46 M. Park, C. H. Kim and T. Joo, *J. Phys. Chem. A*, 2013, **117**, 370–377.

Paper II

Proof of principle of a purine D–A–D’ ligand based ratiometric chemical sensor harnessing complexation induced intermolecular PET

J. Jovaisaite, D. Cirule, A. Jeminejs, I. Novosjolova, M. Turks, P. Baronas, R. Komskis, S. Tumkevicius, G. Jonusauskas and S. Jursenas

Phys. Chem. Chem. Phys., **22**, 26502-26508 (2020)

DOI: 10.1039/d0cp04091f

https://doi.org/10.1039/D0CP04091F

PCCP

PAPER

View Article Online
View Journal

Check for updates

Cite this: DOI: 10.1039/d0cp04091f

Proof of principle of a purine D–A–D′ ligand based ratiometric chemical sensor harnessing complexation induced intermolecular PET†

Justina Jovaisaite, *[a] Dace Cīrule,[b] Andris Jeminejs,[b] Irina Novosjolova,[b] Māris Turks,[b] Paulius Baronas,[a] Regimantas Komskis,[a] Sigitas Tumkevicius,[a] Gediminas Jonusauskas *[c] and Saulius Jursenas[a]

Received 2nd August 2020,
Accepted 24th October 2020

DOI: 10.1039/d0cp04091f

rsc.li/pccp

A comprehensive photophysical study of a series of purines, doubly decorated at C2 and C6 positions with identical fragments ranging from electron acceptor to donor groups of different strengths, is presented. The asymmetry of substitutions creates a unique molecular D–A–D′ structure possessing two independent electronic charge transfer (CT) systems attributed to each fragment and exhibiting dual-band fluorescence. Moreover, the inherent property of coordination of metal ions by purines was enriched due to a presence of nearby triazoles used as spacers for donor or acceptor fragments. New molecules present a bidentate coordination mode, which makes the assembly of several ligands with one metal cation possible. This property was exploited to create a new concept of a ratiometric chemical fluorescence sensor involving the photoinduced electron transfer between branches of different ligands as a mechanism of fluorescence modulation.

Published on 13 November 2020. Downloaded on 11/17/2020 11:40:54 AM.

Introduction

Organic π-conjugated systems with electron accepting cores coupled with electron donating functional groups are generally known as push–pull materials that have been of high interest for years due to their charge transfer (CT) character, tuneable optical properties and HOMO–LUMO gap, and non-linear optical response.[1] The donor–acceptor–donor′ (D–A–D′) type of push–pull compounds stands out with their uniqueness as two different electron donating parts are combined, allowing both to maintain the symmetry of molecules or to realize asymmetric structures. A wide variety of possible D–A–D′ chemical structures and configurations provides an opportunity to tune energy levels and molecular geometries that further assist in the development of organic solution based as well as soft and semiconducting materials. The latter strategy has already found its application in the development of organic solar cells,[2–5] as well as third generation organic light emitting diodes (OLEDs).[6–8] Furthermore, the D–A–D′ structure based intramolecular chemical sensors have been reported for multimodal detection of metal cations[9] or acids.[10]

The electron donating parts such as anisole and dimethylaniline are considered to be general for push–pull systems[1] and may be selected based on their strength. Purines, on the other hand, are known to be ambipolar;[11] however, using them as electron accepting units may provide several advantages.

Purines as nitrogen heterocycles are starting materials widely available in the natural product pool and are readily accessible for chemical modifications that can alter their photophysical properties dramatically. The electron donating functional groups may be coupled at the C2, C6 or C8 positions of the purine core. Some of the desired optical properties of the purine push–pull derivatives have been achieved due to the progress in synthetic methods and their integrity.[12,13] For instance, the azole-type substituents at the C2 and (or) at the C6 position of the purine core enabled reaching fluorescence quantum yields (QYs) of around 60%[14] (in the case of 7-deazapurines, similarly substituted compounds exhibit more than 70% of QYs[14–16]) while by complementing typical donor groups at C2 and C6 of the purine by a substituent at C8, fluorescence quantum yields of near unity were easily achieved.[17] In addition to high fluorescence quantum yields, more advantages of push–pull purine systems can be realized and successfully applied. The purine derivatives have already been demonstrated as emitters in OLEDs,[18–20] as pH[21] sensors

[a] Institute of Photonics and Nanotechnology, Faculty of Physics, Vilnius University, Sauletekis Av. 3, LT-10222 Vilnius, Lithuania. E-mail: justina.jovaisaite@ff.vu.lt
[b] Institute of Technology of Organic Chemistry, Faculty of Materials Science and Applied Chemistry, Riga Technical University, Valdena Str. 3, LV-1048 Riga, Latvia
[c] Laboratoire Ondes et Matière d'Aquitaine, Bordeaux University, UMR CNRS 5798, 351 Cours de la Libération, 33405 Talence, France. E-mail: gediminas.jonusauskas@u-bordeaux.fr

† Electronic supplementary information (ESI) available. See DOI: 10.1039/d0cp04091f

Published on 13 November 2020. Downloaded on 11/17/2020 11:40:54 AM.

or even as imaging tools for cell compartments[22] and their environment.[23] Additionally, the purine derivatives are natural-like molecules that can be more easily recognized by cells.[14]

During the last decade a few examples of purines bearing traditional complexing structures like crown ethers,[24] pincer forming substituents[25] and salicyl-imine side chains[22] have been reported and applied as metal ion sensors. Alternatively, derivatives containing an external C8-complexing arm which works in tandem with the purine N7 have been developed.[26,27] To the best of our knowledge, there are only a few recent examples of the purine-based metal ion sensors that make use of both C6-substitent and the purine N7.[28–30]

Herein, we present the design, synthesis and photophysical properties of four 2,6-bis-(1,2,3-triazol-1-yl)purine derivatives (see Synthesis and product characterization in the ESI†).[31] Our design extends the use of the metal ion complexation mode between a ligand attached to C6 and the N7 intrinsic for the purine ring. Moreover, with the 2,6-bis-substituted systems we demonstrate the utility of complex forming ligands at the purine C2 position for the first time. The investigated compounds bear an electron accepting methyl carboxylate (compound **1**) or an electron donating phenyl ring (**2**),[32,33] and 4-methoxyphenyl (**3**) or 4-*N*,*N*-dimethylaminophenyl (**4**) functional groups at the C4 position of each triazole ring (Fig. 1).

The combination of two chemically identical electron donating branches at the purine C2 and C6 positions (compounds **2**, **3** and **4**), allowed the creation of unique donor–acceptor–donor′ (D–A–D′) systems with two distinct electron transitions from each of the electron donating branches. The latter molecular design results in dual fluorescence in polar aprotic solvents that is altered by the strength of the electron donating properties of the substituents. The close proximity of D–A–D′ molecules upon complexation with metal ions enables the intermolecular interbranch photoinduced electron transfer (PET) with subsequent complete quenching of a blue side band of dual fluorescence. This allows demonstrating a new concept of a ratiometric fluorescence sensor.

Results and discussion

Independent CT states of D–A–D′ purines

The photophysical characterization of each compound was performed in aprotic solvents of different polarities (ethyl acetate (EA), dimethoxyethane (DME) and acetonitrile (ACN)) and summarized in Table 1 and Fig. S13, S14 in the ESI.† The representative absorption and fluorescence spectra in ACN are given in Fig. 2a and b.

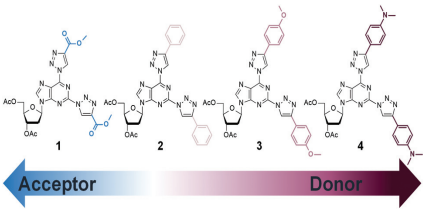

Fig. 1 Chemical structure of bis-triazolyl-purine nucleoside derivatives with electron accepting (**1**) and electron donating (**2**, **3**, **4**) substituents.

The absorption spectra in ACN of all studied derivatives have two intense UV-blue bands, which in the case of **1** have their maxima at around 250 nm and 300 nm, typical of other purine analogues, substituted at C2 and C6 or at C8 positions.[34,35] Once the conjugation is expanded by the addition of electron donating functional groups, the lowest absorption band gradually red shifts (from 298 nm (**1**) to 364 nm (**4**)).

As revealed by TD-DFT modelling (ESI,† Theoretical calculations, Tables S2–S5), the lowest energy transitions (for compounds **2**, **3** and **4**) are of the charge transfer (CT) nature related to both electron donating substituents and bis-triazolyl-purine as an electron acceptor. The schematic view of HOMO−1, HOMO, LUMO, LUMO+1 energies for each compound are given in the Fig. 2a inset (ESI,† Table S6). The analysis of molecular orbitals shows that HOMO−1 and HOMO correspond to substituents coupled at the purine C2 and C6 positions, respectively, and are energetically separated by *ca.* 130 meV. Intense higher-energy absorption bands (for compounds **2**, **3** and **4** peaking from 244 nm to 290 nm) consist of several transitions, including strong locally excited (LE) states in each of electron donating branches, the purine core itself and higher energy CT transitions.

More pronounced changes are observed in the fluorescence spectra (Fig. 2b). Compound **1** has the blue LE fluorescence peaking at 358 nm, which, as expected, does not depend on the polarity of the surrounding media (ESI,† Fig. S14a). However, in accordance with the CT nature of the lowest absorption states of **2**, **3** and **4**, the emission spectra in ACN are broadened and strongly bathochromically shifted (from 358 nm (**1**) to 653 nm (**4**)),

Table 1 Steady-state spectroscopic data for compounds **1–4** obtained in ethyl acetate (EA), dimethoxyethane (DME) and acetonitrile (ACN)

Compound	Solvent	λ_{abs}[a], nm	ε[b], M^{-1} cm^{-1}	λ_{fl}[c], nm	QY[d]
1	EA	297		357	0.10
	DME	298		357	0.07
	ACN	251, 298	26 103, 15 766	358	0.18
2	EA	306		386	0.01
	DME	306		408	0.02
	ACN	244, 306	47 681, 22 568	435	0.03
3	EA	323		441	0.18
	DME	256, 323		386, 443[e]	0.20
	ACN	257, 321	43 396, 14 819	393, 490[e]	0.17
4	EA	288, 363		436, 585[e]	0.05
	DME	289, 363		452, 603[e]	0.02
	ACN	290, 364	31 929, 6264	513, 653[e]	0.001

[a] Absorption maxima. [b] Molar extinction coefficients at wavelengths of absorption maxima. [c] Fluorescence maxima, obtained by excitation of compounds **1** and **2** at 300 nm, **3** at 320 nm and **4** at 360 nm. [d] Quantum yields were determined by the comparative method relative to 9,10-diphenyl anthracene in cyclohexane. [e] Dual fluorescence peak wavelengths were obtained by fitting emission spectra with the Gaussian peak function (ESI, Fig. S15).

This journal is © the Owner Societies 2020

Published on 13 November 2020. Downloaded on 11/17/2020 11:40:54 AM.

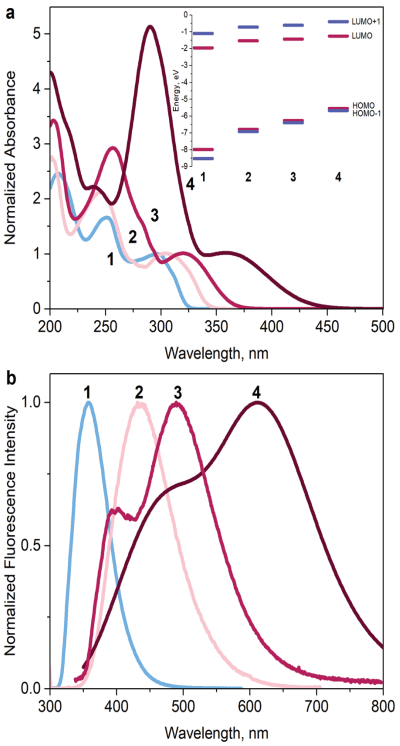

Fig. 2 (a) Absorption spectra normalized to maxima of red side absorption bands of compounds **1** to **4** in ACN. The inset is a representative scheme of HOMO, HOMO−1, LUMO and LUMO+1 energies, obtained using the BMK functional at the 6-31g(d,p) basis set level in a vacuum. (b) Normalized fluorescence spectra of **1** to **4** in ACN (10^{-5} M). The represented fluorescence spectrum of **4** is a two Gaussian peak function fit of the experimental spectrum (ESI†, Fig. S15).

along with positive solvatochromism in other solvents (ESI,† Fig. S14b–d) also observed in similarly modified 2,4-bis(triazolyl) pyrrolo[2,3-*d*]pyrimidines.[15] The most impressive emission feature is present in compounds **3** and **4**, as the incorporation of strong electron donors results in dual fluorescence. In the case of **3**, two CT emission bands are observed in DME and ACN, while for **4**, dual CT emission was recorded in all of the three tested solvents along with more explicit spectral separation between fluorescence bands. It is evident that the dual character of fluorescence is enhanced with increased electron donating ability of substituents as well as increased polarity (dielectric constant) of solvents.

Time-resolved fluorescence experiments in ACN show that both emitting states have their characteristic fluorescence decay transients and should be fitted separately (see Fig. 3 for **3** and **4** and the ESI,† Table S1 for lifetime values of all compounds). For instance, the blue side emission of compound **3** has a lifetime of 2.41 ns, while the red side – 4.4 ns.

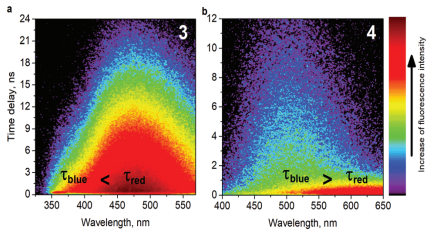

Fig. 3 Time-resolved fluorescence maps of compounds **3** (a) and **4** (b) in ACN (10^{-5} M).

More unusual behaviour is observed for compound **4** as the emission lifetime at the blue side of spectra (6 ns) is longer than the red one (2.71 ns). The latter behaviour (of compound **4** fluorescence decay) suggests that both CT states might be independent of each other.

Many examples of organic molecules exhibiting dual fluorescence can be found in the literature. Most commonly, for donor–acceptor systems two fluorescence bands are attributed to emission from the LE states, which occurs in the (near) Franck–Condon region, while the low-energy emission is mostly referred to the CT state, accompanied by excited-state structural relaxation and charge re-distribution.[36] The CT states can also be classified into several other states like the twisted internal charge transfer (TICT)[37–39] and planar internal charge transfer (PICT)[38] states that depend on the molecular configuration. However, to all in common, CT states are usually inaccessible by direct excitation, and thus can only be formed from the LE state and therefore exhibit fluorescence at longer wavelengths with longer fluorescence lifetimes.[36] Usually, fluorescence from the LE state does not depend on solvent polarity, while, on the contrary, because of molecule being more polar in the CT state, strongly red-shifted or broaden CT emission spectra are often observed.[37] In the present case, both the emitting states of **3** and **4** are solvent dependent, with the red side emitting species being more polar. Additionally, "pure" LE-like spectra of compound **1** are in the deep blue region, peaking at 357–358 nm. As the observed blue side fluorescence for **3** and **4** is already shifted to longer wavelengths by at least 30 nm, the origin of the dual emission of studied compounds is from two CT states.

Several unusual cases of the dual emission from two CT states have already been shown; however, each case is specific. For example, for the D–A–D′ systems (which can be successfully applied for the third generation organic light emitting diodes) two CT states of one molecule have been attributed to both intramolecular CT and intermolecular CT, caused by exciplex emission,[6] or to different conformers of the D–A–D′ system.[7] Additionally, it was shown that two transitions are possible from D and D′ fragments.[40] Furthermore, it was discovered that two independent CT emitting states can exist in one molecular system and can be attributed to D–A and A–D′ moieties and are controlled by conformations and stabilized by the polarity of the surroundings.[8]

Published on 13 November 2020. Downloaded on 11/17/2020 11:40:54 AM.

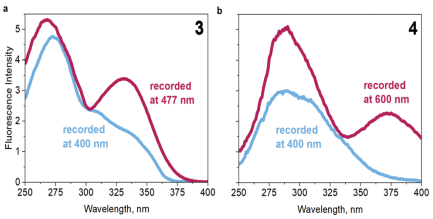

Fig. 4 Excitation spectra of **3** (a) and **4** (b) recorded in ACN (10^{-5} M) at different wavelengths – 400 nm and 477 nm for **3**; 400 nm and 600 nm for **4**.

To further prove the independent origin of the observed CT emission bands in the current work, excitation spectra were recorded for **3** and **4** (Fig. 4). States responsible for the blue and red side emissions have different excitation spectra. The red emission is related to the lowest absorption CT states (>325 nm (**3**), >360 nm (**4**)), while the blue emission corresponds to higher excited states (*ca.* 310 nm (**3**) and *ca.* 330 nm (**4**)). Thus the origin of the dual CT emission may be assigned to an interplay of charge transfer between one of the electron donating branches and bis-triazolyl-purine as an acceptor in separate molecules, which is a unique feature of asymmetric D–A–D′ systems.[7,8]

According to electron density distribution in HOMO – LUMO and HOMO−1 – LUMO (Fig. 5a and the ESI,† Table S4 for compound **3**, Tables S3 and S5 for **2** and **4**), we attribute the blue emission to transition within the C2 branch (for further simplification, we name it a "blue" branch), while the red side band of emission is caused by charge transfer in the C6 branch (a "red" branch). See Fig. 5b for the representative fluorescence spectra for both transitions.

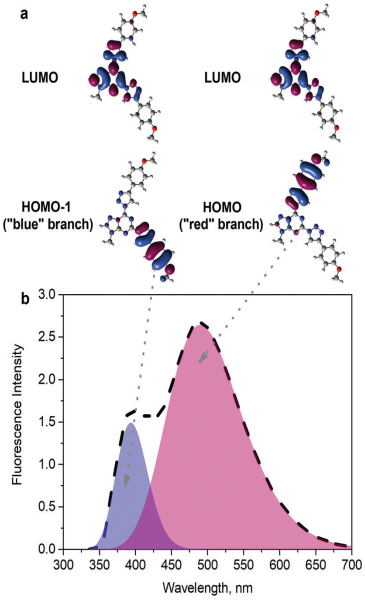

Fig. 5 (a) Spatial distribution of HOMO – LUMO and HOMO−1 – LUMO molecular orbitals of compound **3**, obtained using a BMK functional with a 6-31g(d,p) basis set in a vacuum. (b) The contribution of emission caused by distinct charge transfer to the fluorescence spectra of **3** in ACN. The dashed line represents the experimental spectrum. The filled blue and red emission spectra were obtained by spectral deconvolution, performed with the two Gaussian peak function.

Fluorescence ratiometric chemical sensor

In the current work, the uncommon molecular feature of the dual independent emission of the D–A–D′ asymmetric compound was exploited for the creation of a ratiometric chemical sensor, since the change of the intensity ratio between two fluorescence peaks in the presence of analytes is an operating principle of a self-calibrating sensor.[41–43] Here we combine the selective bonding and the dual nature of the fluorescence to create a fluorescence sensor based on a purine D–A–D′ system. We further selected compound **3** as the best candidate for cation sensor due to its highest fluorescence QYs (around 20%) along with a sufficient spectral separation between fluorescence bands in ACN.

Steady-state absorption and fluorescence titration experiments were performed using alkali (Na^+ and K^+), alkaline earth (Ca^{2+}) and transition (Fe^{2+}, Cu^+, Zn^{2+}) metal ions (ESI,† Fig. S16). The steady-state absorption spectra upon titration with cations remained almost unchanged. However, the main changes upon complexation with metal ions are observed in the fluorescence spectra, where the blue side emission is completely quenched (Fig. 6a and the ESI,† Fig. S16). The dependence of the fluorescence intensity at 400 nm on the equivalents of Zn^{2+} and Ca^{2+} upon titration is shown in Fig. 6a inset (see the ESI,† Fig. S17 for other salts), which implies another appealing fact that complexation at room temperature occurs between one metal ion and three to five purine molecules. The interaction of **3** with metal ions leads to only negligible changes of the "red" branch emission at 500 nm, most probably due to the specific site of coordination of each metal ions. It is worth noting that **3** was not sensitive to alkali metal ions (Na^+ and K^+).

The NMR titration experiments of compound **3**, performed using $Ca(ClO_4)_2{\cdot}4H_2O$ and $Zn(ClO_4)_2{\cdot}6H_2O$ in CD_3CN at 50 °C (ESI,† Fig. S22–S25), prove the complexation with the equivalence point reached at the purine : M^{2+} ratio of 3 : 1. Interestingly, changes of the chemical shift ($\Delta\delta$) during titration with Ca^{2+} and Zn^{2+} salts showed different patterns. With calcium perchlorate the largest $\Delta\delta$ values were observed for H–C5′ of both triazoles, whereas with zinc perchlorate the purine H-C8 and one of the triazoles H–C5′ underwent the largest shift. This indicates that Ca^{2+} is coordinated between both triazoles, while Zn^{2+} complexes between the triazole at C6 and N7 of the purine (Fig. 6b and c). The coordination and its pattern with Zn^{2+} ions was additionally proved by the NMR titration experiments with a model compound, bearing a sole triazole substituent at C6 (compound **6**, see Synthesis and product characterization in the ESI†). The latter molecule revealed an identical complexation pattern (chemical shift change) as compound **3** (ESI,† Fig. S26 and S27). In fact, compounds **2** and **4** also form the same

This journal is © the Owner Societies 2020

Published on 13 November 2020. Downloaded on 11/17/2020 11:40:54 AM.

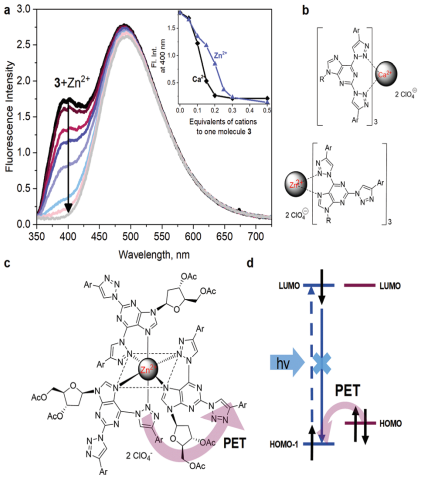

Fig. 6 (a) The fluorescence titration experiment of compound **3** (10^{-5} M) upon addition of Zn^{2+} metal ions from 0 to 0.5 equivalents in ACN; inset – the dependence of the fluorescence intensity at 400 nm on the equivalents of Ca^{2+} and Zn^{2+} metal ions. (b) The suggested complexation mode of compound **3** to Ca^{2+} and Zn^{2+} salts based on NMR titration results, where Ar = 4-methoxyphenyl; R = 3′,5′-di-*O*-acetyl-2′-deoxy-β-D-ribofuranosyl, and (c) the illustration of the purine – Zn^{2+} (3 : 1) octahedral complex. (d) The sensing mechanism of PET upon complexation with metal ions and excitation of the "blue" branch. The scheme represents PET occurring between two distinct molecules.

complexes with metal ions, confirming the generality of using bis-triazolyl purines as chemosensors (ESI,† Fig. S28–S31).

So far, it is evident that the complexation of **3** with metal ions causes an assembly ("aggregation") of several ligand molecules, along with complete quenching of the "blue" branch emission. In addition, metal ions do not induce changes of fluorescence lifetimes upon complexation (ESI,† Table S1). Therefore, three sensing mechanisms, related to intermolecular distances, should be considered – Förster resonance energy transfer (FRET), Dexter exchange energy transfer (EET) and PET. These processes should happen on a sub-picosecond time scale, similar to that reported for covalently bounded compounds.[44] Even if the essentials for FRET and EET are realized in our system (a close proximity between energy donor and acceptor and spectral overlap between acceptor absorption and donor emission[45,46]), these mechanisms were ruled out as no increase of the red fluorescence band intensity together with no changes of emission lifetimes were observed.

Thus, we suggest that upon interaction with cations, molecules pack closely with each other and in the case of the "blue" branch being excited, the intermolecular interbranch PET takes place. Importantly, estimated energies of HOMO and HOMO−1 are favorable for the latter process. This is an exceptional property of the D–A–D′ based system, determined by chemically identical, though assymetrically linked donor moieties. Fig. 6d summarizes the following suggested mechanism: the electron is transferred from the HOMO level of the unexcited molecule ("red" branch) to the HOMO−1 of the excited one ("blue" branch), thus the blue side emission is quenched.

To get a deeper insight into the mechanism of PET, we employed the transient absorption spectroscopy experiments. Two representative metal ions of Ca^{2+} and Zn^{2+} (0.5 equivalents of each) and compound **3** diluted in ACN were used in experiments, performed by excitation at 320 nm (both branches were excited) and 350 nm (only the "red" branch was excited). The results are presented in Fig. 7 and the ESI,† Fig. S18 and S19.

To all samples in common, there are two main regions of the excited state absorption (ESA) that will be further referred to as region I (with spectral components named as **a** at 395 nm, **b** at 425 and **c** at 465 nm) and region II (*ca.* 600 nm). Starting from a few tens of picoseconds, the transient absorption spectra are the same for all samples and are similar to cation-radical absorption of anisole, peaking at 430 nm,[47] while the red side ESA at around 590 nm is analogous to the purine anion-radical absorption spectra.[48]

Once the samples are excited (at 320 nm or at 350 nm), the initial spectral feature at 465 nm (band **c**) evolves with an excitation pulse and may be attributed to the excited ligand of **3** or to the excited complexes of **3** with Ca^{2+} or Zn^{2+} in the ground state geometry. The relaxation of component **c** (ESI,† Fig. S20a) in a few hundred femtoseconds corresponds to the structural relaxation of the excited samples together with the rearrangement of surrounding solvent molecules. The transient absorption experiments on the compound **3** embedded in the PMMA matrix (frozen ground state geometry) show no spectral shifts of the band **c** even up to 10 ps delay (ESI,† Fig. S21).

If the samples are excited at 320 nm (both "blue" and "red" branches), two distinct peaks at *ca.* 395 nm (band **a**) and *ca.* 425 nm (band **b**) and the region II grow with the same time

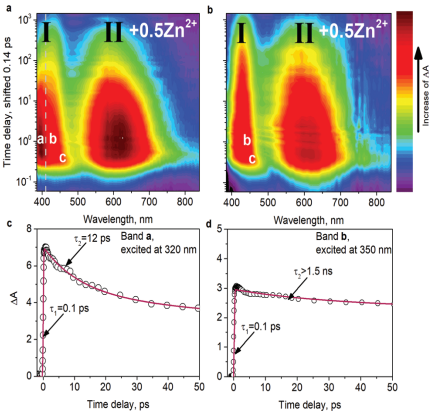

Fig. 7 Transient absorption maps of compound **3** with 0.5 equivalent of Zn^{2+} cations in ACN, obtained by excitation of the sample at (a) 320 nm and (b) 350 nm. The respective excited state absorption transients, fitted at (c) 395 nm and (d) at 425 nm. A slight overlap with band **c** is observed in kinetics (d), which produces a short and weak component at the beginning of decay.

Published on 13 November 2020. Downloaded on 11/17/2020 11:40:54 AM.

constant of a few hundred femtoseconds corresponding to the lifetime of the band **c**. In the case of excitation at 350 nm (only the "red" branch), the band **a** is not present (Fig. 7b and the ESI,† Fig. S19).

During the relaxation of the band **c**, the formation of the radical pair with intermolecular electron transfer from the "red" chromophore ground state to the excited "blue" chromophore ground state occurs. The observed 12 ps decay of ESA, located at *ca.* 395 nm (band **a**) and 630–650 nm (region II), corresponds to the radical recombination time constant (Fig. 7a, c and the ESI,† Fig. S20b). It is worth noting that no signal increase with the time constant of 12 ps was observed in the entire experimental spectral range, indicating that neither FRET nor EET occurs in the present system.

Thus, the easily accessible modification of the purine ring allowed creation of a unique molecular structure with two chemically identical, though, asymmetrical electron donating branches linked through a triazole, which assists in the coordination with metal ions. This allowed us to realize the favorable conditions for the efficient PET – the energy difference between HOMO and HOMO−1 of each branche is small enough; in addition, the coordination with cations ensures the close proximity between those "non-communicating" branches. The further modification of triazoles as spacers and coordinating elements opens endless opportunities to selectively sense the desired analytes. On the other hand, the alteration of the electron donating moieties would provide possibilities for boosting sensitivity and combining the appropriate optical properties. The study in alcohols and water revealed a somewhat different behaviour of ligand **3** upon complexation; the upcoming article will be devoted to comprehensive investigations of photophysics and sensing mechanism of compounds **1–4** in protic environments.

Conclusions

In conclusion, we demonstrate the possibility of constructing a ratiometric fluorescence cation sensor based on the asymmetrically functionalized purine with electron donating groups. The observed dual-band fluorescence is produced by two non-communicating electronic transitions within the same ligand. PET occurs between D and D′ fragments of neighbouring ligands assembled upon complexation with metal ions and is responsible for the quenching of the blue fluorescence band. We believe that the reported strategy can be general for a wealth of D–A–D′ compounds across a wide spectral window and specific selectivity for chemical species, which can be further altered by the modification of spacers used for the coordination or electron donating substituents.

Conflicts of interest

There are no conflicts to declare.

Acknowledgements

This project has received funding from the European Social Fund (Project No. 09.3.3-LMT-K-718-01-0026) under a grant agreement from the Research Council of Lithuania (LMTLT) and from the Latvian Council of Science (Project No. LZP-2018/2-0037). The authors thank Kamile Tulaite for the help with sample preparation and optical measurements.

Notes and references

1 F. Bureš, *RSC Adv.*, 2014, **4**, 58826–58851.
2 S. Tang and J. Zhang, *J. Phys. Chem. A*, 2011, **115**, 5184–5191.
3 P. Gautam, R. Misra, S. A. Siddiqui and G. D. Sharma, *ACS Appl. Mater. Interfaces*, 2015, **7**, 10283–10292.
4 P. Sonar, S. P. Singh, P. Leclère, M. Surin, R. Lazzaroni, T. T. Lin, A. Dodabalapur and A. Sellinger, *J. Mater. Chem.*, 2009, **19**, 3228–3237.
5 Z. Chen, J. Yang, F. Wu, L. Chen and Y. Chen, *Chem. Res. Chin. Univ.*, 2017, **33**, 305–311.
6 R. Skaisgiris, T. Serevičius, K. Kazlauskas, Y. Geng, C. Adachi and S. Juršėnas, *J. Mater. Chem. C*, 2019, **7**(40), 12601–12609.
7 K.-L. Woon, C.-L. Yi, K.-C. Pan, M. K. Etherington, C.-C. Wu, K.-T. Wong and A. P. Monkman, *J. Phys. Chem. C*, 2019, **123**, 12400–12410.
8 M. Aydemir, S. Xu, C. Chen, M. R. Bryce, Z. Chi and A. P. Monkman, *J. Phys. Chem. C*, 2017, **121**, 17764–17772.
9 E. Tulyakova, S. Delbaere, Y. Fedorov, G. Jonusauskas, A. Moiseeva and O. Fedorova, *Chem. – Eur. J.*, 2011, **17**, 10752–10762.
10 P. Meti, J. W. Yang and Y. D. Gong, *Dyes Pigm.*, 2018, **156**, 233–242.
11 G. S. Collier, L. A. Brown, E. S. Boone, M. Kaushal, M. N. Ericson, M. G. Walter, B. K. Long and S. M. Kilbey, *J. Mater. Chem. C*, 2017, **5**, 6891–6898.
12 I. Novosjolova, E. Bizdena and M. Turks, *Eur. J. Org. Chem.*, 2015, 3629–3649.
13 L. Zilbershtein-Shklanovsky, M. Weitman, D. T. Major and B. Fischer, *J. Org. Chem.*, 2013, **78**, 11999–12008.
14 A. Šišuļins, J. Bucevičius, Y. T. Tseng, I. Novosjolova, K. Traskovskis, Ē. Bizdēna, H. T. Chang, S. Tumkevičius and M. Turks, *Beilstein J. Org. Chem.*, 2019, **15**, 474–489.
15 J. Bucevicius, L. Skardziute, J. Dodonova, K. Kazlauskas, G. Bagdziunas, S. Jursenas and S. Tumkevicius, *RSC Adv.*, 2015, **5**, 38610–38622.
16 J. Bucevicius, M. Turks and S. Tumkevicius, *Synlett*, 2018, 525–529.
17 R. S. Butler, A. K. Myers, P. Bellarmine, K. A. Abboud and R. K. Castellano, *J. Mater. Chem.*, 2007, **17**, 1863–1865.
18 Y. Yang, P. Cohn, A. L. Dyer, S. H. Eom, J. R. Reynolds, R. K. Castellano and J. Xue, *Chem. Mater.*, 2010, **22**, 3580–3582.
19 Y. Yang, P. Cohn, S. H. Eom, K. A. Abboud, R. K. Castellano and J. Xue, *J. Mater. Chem. C*, 2013, **1**, 2867–2874.

Published on 13 November 2020. Downloaded on 11/17/2020 11:40:54 AM.

20 Z. Wang, J. Yao, L. Zhan, S. Gong, D. Ma and C. Yang, *Dyes Pigm.*, 2020, 108437.
21 K. M. Sun, C. K. McLaughlin, D. R. Lantero and R. A. Manderville, *J. Am. Chem. Soc.*, 2007, **129**, 1894–1895.
22 V. Venkatesh, A. Shukla, S. Sivakumar and S. Verma, *ACS Appl. Mater. Interfaces*, 2014, **6**, 2185–2191.
23 J. Li, Y. Zhang, H. Zhang, X. Xuan, M. Xie, S. Xia, G. Qu and H. Guo, *Anal. Chem.*, 2016, **88**, 5554–5560.
24 S. H. Gao, M. S. Xie, H. X. Wang, H. Y. Niu, G. R. Qu and H. M. Guo, *Tetrahedron*, 2014, **70**, 4929–4933.
25 J.-P. Li, H.-X. Wang, H.-X. Wang, M.-S. Xie, G.-R. Qu, H.-Y. Niu and H.-M. Guo, *Eur. J. Org. Chem.*, 2014, 2225–2230.
26 A. Dumas and N. W. Luedtke, *Chem. – Eur. J.*, 2012, **18**, 245–254.
27 A. Omumi, C. K. McLaughlin, D. Ben-Israel and R. A. Manderville, *J. Phys. Chem. B*, 2012, **116**, 6158–6165.
28 Z. Dong, W. Chen, H. Li, Y. Dai, T. Zheng, H. Zhang, H. Xu and H. Lu, *Inorg. Chem. Commun.*, 2020, **116**, 107915.
29 G. Wu, Z. Wang, W. Zhang, W. Chen, X. Jin and H. Lu, *Inorg. Chem. Commun.*, 2019, **102**, 233–239.
30 H.-Y. Xu, W. Chen, W. Zhang, L. Ju and H. Lu, *New J. Chem.*, 2020, **44**, 15195–15201.
31 K. Ozols, D. Cīrule, I. Novosjolova, D. Stepanovs, E. Liepinsh, Ē. Bizdēna and M. Turks, *Tetrahedron Lett.*, 2016, **57**, 1174–1178.
32 D. Cīrule, K. Ozols, O. Platnieks, Ē. Bizdēna, I. Māliņa and M. Turks, *Tetrahedron*, 2016, **72**, 4177–4185.
33 A. Kovaļovs, I. Novosjolova, Ē. Bizdēna, I. Bižāne, L. Skardziute, K. Kazlauskas, S. Jursenas and M. Turks, *Tetrahedron Lett.*, 2013, **54**, 850–853.
34 C. Dyrager, K. Börjesson, P. Dinér, A. Elf, B. Albinsson, L. M. Wilhelmsson and M. Grøtli, *Eur. J. Org. Chem.*, 2009, 1515–1521.
35 R. S. Butler, P. Cohn, P. Tenzel, K. A. Abboud and R. K. Castellano, *J. Am. Chem. Soc.*, 2009, **131**, 623–633.
36 J. R. Lakowicz, *Principles of Fluorescence Spectroscopy*, Springer, 3rd edn, 2006.
37 S. Sasaki, G. P. C. Drummen and G. Konishi, *J. Mater. Chem. C*, 2016, **4**, 2731–2743.
38 Z. R. Grabowski and K. Rotkiewicz, *Chem. Rev.*, 2003, **103**, 3899–4031.
39 Z. R. Grabowski, K. Rotkiewicz and A. Siemiarczuk, *J. Lumin.*, 1979, **18–19**, 420–424.
40 A. Tomkeviciene, T. Matulaitis, M. Guzauskas, V. Andruleviciene, D. Volyniuk and J. V. Grazulevicius, *Org. Electron.*, 2019, **70**, 227–239.
41 Z. Liu, W. He, Z. Guo, M. Schmittel, P. Aneesa, A. Ajayaghosh, W. Guo, J. Kim, S. Park, J. Yoon and Z. Zeng, *Chem. Soc. Rev.*, 2013, **42**, 1568.
42 X. Zhang, Y. Xiao and X. Qian, *Angew. Chem., Int. Ed.*, 2008, **47**, 8025–8029.
43 J. F. Zhang, Y. Zhou, J. Yoon, Y. Kim, S. J. Kim and J. S. Kim, *Org. Lett.*, 2010, **12**, 3852–3855.
44 P. A. Panchenko, Y. V. Fedorov, O. A. Fedorova and G. Jonusauskas, *Phys. Chem. Chem. Phys.*, 2015, **17**, 22749–22757.
45 I. Medintz and N. Hildebrandt, *FRET – Förster Resonance Energy Transfer: From Theory to Applications*, 2013.
46 S. Faure, C. Stern, R. Guilard and P. D. Harvey, *J. Am. Chem. Soc.*, 2004, **126**, 1253–1261.
47 P. O'Neill, S. Steenken and D. Schulte-Frohlinde, *J. Phys. Chem.*, 1975, **79**, 2773–2779.
48 P. N. Moorthy and E. Hayon, *J. Am. Chem. Soc.*, 1975, **97**, 3345–3350.

Paper III

Suppression of benzophenone-induced triplet quenching for enhanced TADF performance

G. Kreiza, D. Banevičius, J. Jovaišaitė, K. Maleckaitė, D. Gudeika, D. Volyniuk, J. V. Gražulevičius, S. Juršėnas and K. Kazlauskas

J. Mater. Chem. C., **7**, 11522 (2019)

DOI: 10.1039/c9tc02408e

https://doi.org/10.1039/C9TC02408E

Journal of
Materials Chemistry C

PAPER

View Article Online
View Journal | View Issue

Check for updates

Cite this: J. Mater. Chem. C, 2019, 7, 11522

Suppression of benzophenone-induced triplet quenching for enhanced TADF performance†

Gediminas Kreiza,[a] Dovydas Banevičius,[a] Justina Jovaišaitė,[a] Karolina Maleckaitė,[a] Dalius Gudeika,[b] Dmytro Volyniuk,[b] Juozas V. Gražulevičius,[b] Saulius Juršėnas[a] and Karolis Kazlauskas *[a]

Received 7th May 2019,
Accepted 28th August 2019

DOI: 10.1039/c9tc02408e

rsc.li/materials-c

Efficient TADF relies on effective reverse intersystem crossing (rISC) from triplet to singlet manifold, and therefore the transition rate associated with this process must outcompete non-radiative decay rate of the triplets. Herein the issue of non-radiative triplet quenching in benzophenone-derived compounds frequently employed as blue TADF emitters in OLEDs is addressed and an effective way to suppress this quenching is proposed. TADF emitters designed for this study were based on phenone-derived electron-accepting units linked with multiple carbazolyl donors to deliver similar and large rISC rates ($k_{rISC} \sim 4 \times 10^6$ s^{-1}), yet significantly different non-radiative triplet quenching rates (k_{nr}^T). We found that substitution of a loose phenyl moiety by a methoxy group in benzophenone suppresses k_{nr}^T by one order of magnitude (from 3×10^6 s^{-1} down to 0.3×10^6 s^{-1}), while leaving rISC rate k_{rISC} almost unaffected. A 10 times enlarged ratio k_{rISC}/k_{nr}^T in **5tCzMeB** as compared to that in **5tCzBP** emitter suffices to retrieve the vast majority of triplet population *via* the rISC resulting in PL quantum yields of 0.99 and 0.58 in doped DPEPO and neat films, respectively. Sky-blue TADF OLEDs with doped and non-doped emissive layers based on **5tCzMeB** demonstrated impressive maximum external quantum efficiency (EQE) values of 24.6% and 13.4%, respectively, whereas at 100 cd m^{-2} the devices exhibited 16.5% and 7.7% EQEs, respectively.

Published on 29 August 2019. Downloaded on 11/6/2019 11:27:24 AM.

1. Introduction

Organic light-emitting diodes (OLEDs) represent one of the most attractive technologies for large-area ultrathin displays and lighting applications as they offer high luminous efficacy and contrast ratio in addition to mechanical flexibility, low weight, and cost- and power-efficiency.[1,2] Over the last decade thermally activated delayed fluorescence (TADF) has become a widely researched phenomenon that is exploited for fabrication of high-efficiency OLEDs.[3,4] Recent breakthroughs in TADF studies allowed harvesting of up to 100% triplet excitons through a reverse intersystem crossing (rISC) process in organic materials without employing precious metals, thus rivaling the efficiencies of state-of-the-art phosphorescent OLEDs.[5–7] Since then a variety of new TADF compounds were synthesized demonstrating an upper limit of external quantum efficiency (EQE = 20–30%) in OLEDs without using light extracting structures or horizontal dipole orientation.[6,8,9]

TADF compounds are typically designed by utilizing twisted electron-donating and accepting groups to ensure the spatially decoupled highest occupied and lowest unoccupied molecular orbitals, HOMO and LUMO, respectively, which subsequently results in a small singlet–triplet energy gap ΔE_{ST}.[10] The small ΔE_{ST} is crucial for achieving efficient thermally-assisted rISC from triplet to singlet manifold.[11] Usually, materials with large rISC rate (k_{rISC}), typically above 10^5 s^{-1}, are searched for when aiming for efficient TADF and overall photoluminescence quantum yield (Φ_{PL}).[4,12,13] However, Noda *et al.* demonstrated that these features can be also achieved in low rISC compounds with $k_{rISC} \sim 10^3$ s^{-1} if the competing relaxation pathway, *i.e.* triplet non-radiative decay from T_1 to the ground state S_0, is suppressed.[14] Thus, essentially, irrespective of the k_{rISC} value the ratio k_{rISC}/k_{nr}^T must be large to retrieve the majority of the triplets *via* rISC and sustain efficient TADF.

When designing TADF compounds for the current study we focused our attention on carbazole-based donors and phenone-derived acceptors, *i.e.* the units capable of delivering efficient rISC if linked properly. Apart from the great stability, ease of functionalization, excellent hole transport *etc.*,[15] carbazoles coupled with acceptors such as benzonitrile or phthalonitrile showed increased excited state delocalization resulting in enhanced k_{rISC}.[16] Moreover, k_{rISC} could be further improved by decorating carbazolyls with either phenyl or methyl groups at the 3rd and 6th positions,[13] whereas incorporating bulky *t*-butyl groups at these positions additionally benefited with a noticeable boost in the

[a] Institute of Photonics and Nanotechnology, Vilnius University, Saulėtekio av. 3, LT-10257 Vilnius, Lithuania. E-mail: karolis.kazlauskas@ff.vu.lt
[b] Department of Polymer Chemistry and Technology, Kaunas University of Technology, Radvilenu pl. 19, LT- 50254, Kaunas, Lithuania

† Electronic supplementary information (ESI) available. See DOI: 10.1039/c9tc02408e

This journal is © The Royal Society of Chemistry 2019

Published on 29 August 2019. Downloaded on 11/6/2019 11:27:24 AM.

device lifetime.[17] We chose benzophenone as an acceptor not only because it is a popular building block of blue TADF emitters,[18–21] but mainly because it was shown to be responsible for the non-radiative decay of long-lived excited states in TADF emitters.[19,21,22] This quality is most relevant to benzophenones with a loose phenyl moiety in the emitter structure. Importantly, the non-radiative decay facilitated by intramolecular rotations/vibrations[23] could not be completely suppressed even in the solid state preventing TADF emitters with high k_{rISC} ($>10^5$ s^{-1}) and small ΔE_{ST} (<100 meV) to attain unity PL quantum yields.[19,24] Resolving the issue of the non-radiative triplet quenching is thereby anticipated to improve TADF performance and consequently EQE of benzophenone-derived OLEDs.

To this end, two TADF emitters consisting of five electron-donating carbazolyl groups and benzophenone (**5tCzBP**) or methyl benzoate (**5tCzMeB**) electron-accepting units were investigated. The main emphasis was put on elucidating and suppressing TADF performance-hampering non-radiative decay of the triplet states imposed by the benzophenone acceptor. Carbazolyl moieties were intentionally substituted with *tert*-butyl groups at C-3 and C-6 positions to reduce concentration quenching, and enhance morphological stability and solubility of the compounds.[25] These engineered features enabled to assess and compare performance of both TADF emitters in doped and non-doped OLEDs fabricated by vacuum evaporation. Additionally, the compounds were tested in non-doped devices made by a solution process. The studies revealed that the replacement of the loose phenyl moiety in the benzophenone acceptor by a methoxy group suffices to reduce the non-radiative decay of the triplets to a level where k_{nr}^{T} is well below k_{rISC} in the solid films, and to fabricate sky-blue TADF OLEDs with doped and non-doped emissive layers demonstrating outstanding EQE values of 24.6% and 13.4%, respectively.

2. Experimental

2.1. Materials

All materials were purchased from commercial suppliers and used as received unless otherwise stated. **5tCzBP**, **5tCzMeB** and bis[2-(diphenylphosphino)phenyl] ether oxide (DPEPO) were additionally purified by using a temperature-gradient vacuum sublimation system DSU-20 (CreaPhys). 3,6-Di-*tert*-butyl-9*H*-carbazole was synthesized as described earlier.[26]

Synthesis of methyl 2,3,4,5,6-penta(3,6-di-*tert*-butyl-9*H*-carbazol-9-yl)benzoate (5tCzMeB). A mixture of methyl pentafluorobenzoate (0.5 g, 2.21 mmol) and 3,6-di-*tert*-butyl-9*H*-carbazole (3.36 g, 12.04 mmol) together with K_2CO_3 (4.58 g, 16.5 mmol) in 7 mL of dimethyl sulfoxide was stirred at 140 °C for 24 h under N_2 atmosphere. After cooling to room temperature, the mixture was poured into water, filtered, and purified by column chromatography over silica gel (eluent – ethylacetate/*n*-hexane, vol. ratio 1 : 2) to obtain a yellow solid (1.38 g, yield: 61%). ^{1}H NMR (400 MHz, $CDCl_3$, δ, ppm): 7.66 (d, J = 1.9 Hz, 5H), 7.25 (d, J = 1.9 Hz, 5H), 7.07–6.98 (m, 11H), 6.92 (d, J = 8.6 Hz, 4H), 6.63 (dd, J_1 = 8.6 Hz, J_2 = 1.9 Hz, 5H), 2.54 (s, 3H), 1.35 (s, 90H). ^{13}C NMR (75 MHz, $CDCl_3$, δ, ppm): 142.6, 142.5, 142.3, 138.5, 137.4, 137.3, 136.6, 135.7, 124.0, 123.8, 122.6, 122.0, 121.8, 115.4, 114.2, 110.2, 110.1, 109.7, 52.1, 34.2, 31.73. MS (APCI$^+$, 20 V), *m*/*z*: 1524 ([M + H]$^+$). Elemental analysis calcd (%) for $C_{108}H_{123}N_5O_2$: C, 85.16; H, 8.14; N, 4.60; O, 2.10; found: C, 85.20; H, 8.16; N, 4.64.

Synthesis of 2,3,4,5,6-penta(3,6-di-*tert*-butyl-9*H*-carbazol-9-yl)benzophenone (5tCzBP). A procedure similar to that used for **5tCzMeB** was followed with 2,3,4,5,6-pentafluorobenzophenone (0.5 g, 2.91 mmol). The residue was purified by column chromatography (eluent – ethylacetate/*n*-hexane, vol. ratio 1 : 1) to obtain **5tCzBP** as a yellow solid. Yield: 1.95 g, 68%. ^{1}H NMR (400 MHz, $CDCl_3$, δ, ppm): 7.93 (d, J = 1.8 Hz, 5H), 7.59 (d, J = 1.8 Hz, 5H), 6.97–6.94 (m, 16H), 6.86 (d, J = 8.3 Hz, 4H), 6.68 (dd, J_1 = 8.3 Hz, J_2 = 1.8 Hz, 5H), 1.38 (s, 90H). ^{13}C NMR (75 MHz, $CDCl_3$, δ, ppm): 143.7, 143.5, 142.5, 142.2, 137.4, 137.1, 136.3, 128.4, 128.3, 127.7, 126.6, 124.2, 123.8, 123.6, 122.9, 121.7, 116.2, 116.1, 115.4, 110.5, 110.2, 109.6, 34.5, 31.7. MS (APCI$^+$, 20 V), *m*/*z*: 1570 ([M + H]$^+$). Elemental analysis calcd (%) for $C_{113}H_{125}N_5O$: C, 86.49; H, 8.03; N, 4.46; O, 1.02; found: C, 86.51; H, 8.08; N, 4.44.

2.2. Sample preparation and spectroscopic characterization

For studying photophysical properties in dilute solutions, the investigated TADF compounds were dissolved in toluene (10^{-5} mol L^{-1}) and then degassed by using the freeze–pump–thaw method. Poly(methyl methacrylate) PMMA films doped by 1 wt% of the compounds were prepared by spin-coating chloroform solutions (20 mg mL^{-1}) of the PMMA and compound mixtures on quartz plates at 2000 rpm. Neat and doped (20 wt% in DPEPO host) films were deposited by thermal evaporation in vacuum (base pressure of $<10^{-6}$ Torr) at ~1.0 Å s^{-1} evaporation rate on quartz substrates to achieve a layer thickness of about 50 nm. Absorption spectra were measured by utilizing a UV-Vis-NIR spectrophotometer Lambda 950 (PerkinElmer). Steady state PL spectra were recorded on a back-thinned CCD spectrometer PMA-11 (Hamamatsu) by exciting samples with a xenon lamp coupled to a monochromator. Doped DPEPO films were excited at the absorption maximum of DPEPO (at 300 nm), whereas 350 nm excitation wavelength was used for the rest of the solutions and films. Φ_{PL} values of thin films in oxygen-free ambient conditions were determined by first performing measurements in air using an integrating sphere (Sphere Optics), and then estimating the increase of PL signal upon placing the samples in a vacuum chamber. A vacuum cryostat equipped with a turbo-molecular pump and capable of achieving 10^{-6} Torr pressure served as a vacuum chamber for PL measurements of the studied films. Time-resolved PL spectra were recorded on a time-gated iCCD camera New iStar DH340T (Andor) by exciting the samples with a tunable-wavelength optical amplifier (Ekspla) pumped by a nanosecond Nd^{3+}:YAG laser (pulse duration 5 ns, repetition rate 10 Hz). Excitation power dependencies of the neat films were measured in vacuum by using a continuous-wave laser diode (375 nm, PicoQuant) as an excitation source.

2.3. OLED fabrication and characterization

OLEDs were fabricated onto pre-patterned ITO glass substrates (Kintec company), which were cleaned by sonicating consecutively in detergent (Hellmanex II), distilled water, acetone and isopropyl alcohol, and treated with O_2 plasma afterwards. Vacuum-processed

Published on 29 August 2019. Downloaded on 11/6/2019 11:27:24 AM.

devices were fabricated in a vacuum chamber (base pressure of $<10^{-6}$ Torr) by depositing multiple organic layers at a rate of 0.7–1.2 Å s^{-1}. The doped emissive layer was obtained by co-evaporating materials from two different sources with different evaporation rates.

Solution-processed devices were prepared as follows: poly(3,4-ethylenedioxythiophene)-poly(styrenesulfonate) (PEDOT:PSS, Al 4083) was ultrasonicated and filtered through a hydrophilic filter (pore size 0.22 μm), and then spin-coated on top of glass/ITO substrates at 5000 rpm and annealed at 200 °C for 10 minutes. Samples were then moved into a nitrogen glove-box, where poly(9-vinylcarbazole) (PVK) was spin-coated at 2000 rpm from a chlorobenzene solution (7 mg mL^{-1}) and thermally annealed at 160 °C for 15 min. Subsequently an emissive layer was spin-coated at 2000 rpm from cyclohexane solutions (1.5 mg mL^{-1}) and annealed at 70 °C for 15 min. The samples from the glove-box were then transferred to an integrated high-vacuum chamber, where a layer of DPEPO followed by that of 2,2′,2″-(1,3,5-benzinetriyl)-tris(1-phenyl-1-*H*-benzimidazole) (TPBi) were evaporated.

Finally, for both vacuum- and solution-processed devices, samples were transferred from the organic to metal deposition chamber without breaking the vacuum for successive deposition of LiF and Al layers at a rate of 0.2 and 1.5 Å s^{-1}, respectively. The active area of the devices tested was 1×1 mm^2, as defined by the shadow mask for cathode deposition. Before exposing to air, devices were transported from vacuum into nitrogen ambient and encapsulated using UV-curable epoxy KATIOBOND LP655 (DELO). A calibrated LED characterization system (ORB Optronix) comprising an integrating sphere, a spectroradiometer GS-1290 (RadOMA) and a source meter 2601A (Keithley) was employed to evaluate current–voltage-luminance characteristics as well as external quantum efficiency of fabricated OLEDs.

3. Results and discussion

3.1. Synthesis and theoretical calculations

Both TADF compounds **5tCzMeB** and **5tCzBP** were prepared by a one-step synthesis as shown in Scheme 1. Methyl 2,3,4,5,6-penta-(3,6-di-*tert*-butyl-9*H*-carbazol-9-yl)benzoate and 2,3,4,5,6-penta(3,6-di-*tert*-butyl-9*H*-carbazol-9-yl)benzophenone were synthesized *via* nucleophilic cross-coupling reactions between 9*H*-carbazole and methyl pentafluorobenzoate or 2,3,4,5,6-pentafluorobenzophenone, respectively. Finally, the chemical structures of **5tCzMeB** and **5tCzBP** were characterized and verified by ^{1}H NMR and ^{13}C NMR spectroscopies, mass spectrometry and elemental analysis. The detailed information about the synthetic procedures and identification of molecular structures are provided in the Experimental section.

First, the potential of compounds **5tCzMeB** and **5tCzBP** as TADF emitters was evaluated by optimizing their molecular structures in vacuum by using density functional theory (DFT) with the B3LYP functional at 6-31G(d) basis set level embedded in the Gaussian 09W software.[27] It was determined that dihedral angles between the carbazole groups and central phenyl fragment varied from 63° to 73° for **5tCzMeB** and from 64° to 76° for **5tCzBP** due to the strong steric crowding. Optimized ground state

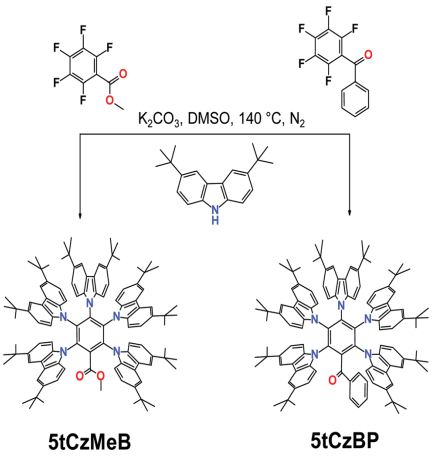

Scheme 1 Synthetic routes of **5tCzMeB** and **5tCzBP**.

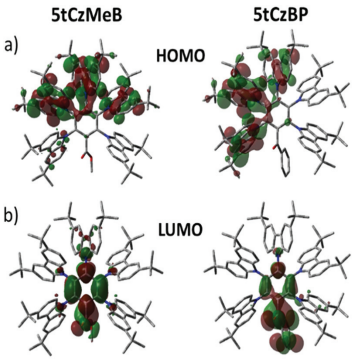

Fig. 1 HOMO (a) and LUMO (b) of **5tCzMeB** and **5tCzBP** calculated by TD-DFT with B3LYP/6-31G(d).

geometries were used to calculate absorption energies from S_0 to S_1 and T_1 states as well as distributions of the HOMO and LUMO by the time-dependent DFT method (see Fig. 1). Calculated data are summarized in Table S1, ESI.† Strong spatial separation of the HOMO and LUMO ensured small ΔE_{ST} for **5tCzMeB** (0.25 eV) and **5tCzBP** (0.05 eV), whereas the remaining small overlap between the molecular orbitals ensured moderate oscillator strengths (f) for the $S_0 \rightarrow S_1$ transition allowing to expect decent k_r values.

3.2. Photophysical properties

To gain insight into photophysical properties of the synthesized compounds, steady-state UV-Vis absorption and photoluminescence (PL) measurements were carried out (Fig. 2). While both compounds in dilute toluene solutions showed intense absorption at 340 nm, mostly assigned to local transitions, the main differences

 This journal is © The Royal Society of Chemistry 2019

Published on 29 August 2019. Downloaded on 11/6/2019 11:27:24 AM.

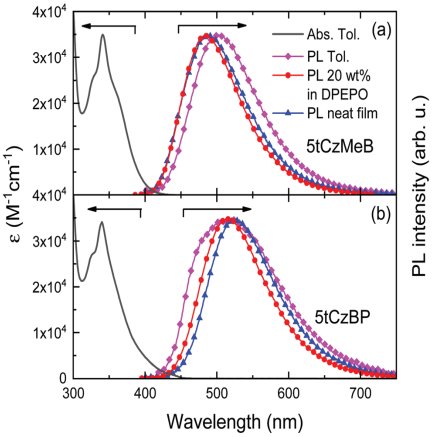

Fig. 2 Absorption and fluorescence spectra of **5tCzMeB** (a) and **5tCzBP** (b) in toluene solution (10^{-5} mol L^{-1}) as well as their fluorescence spectra in neat and DPEPO films at 20 wt% doping.

were observed at longer wavelengths where the weak and broad absorption tail was mainly governed by intramolecular charge transfer (ICT) between donor and acceptor groups. **5tCzBP** demonstrated a red-shifted absorption spectrum shoulder as compared to **5tCzMeB** associated with higher delocalization of the LUMO over the benzophenone moiety. These results were found to be consistent with PL measurements of toluene solutions, where bathochromically shifted fluorescence of **5tCzBP** (peaked at 524 nm) in respect to that of **5tCzMeB** (peaked at 498 nm) was obtained. Structureless PL spectra of both compounds clearly signified ICT transitions. The slightly broader PL band of **5tCzBP** could be attributed to the greater variety of excited state conformations due to the labile benzophenone moiety.[28,29] To determine ΔE_{ST} values, investigated compounds were dispersed in an inert PMMA host at low concentration (1 wt%), which allowed to neglect intermolecular interactions, meanwhile simulating the rigid environment of a device. Since S_1 and T_1 were identified as charge transfer (CT) states for both compounds, corresponding zero–zero transition energies (E_{0-0}) were deduced from the onset of broad fluorescence and phosphorescence spectra (see Fig. S1, ESI† and Table 1).[30] Relatively small ΔE_{ST} values of 0.08 eV and 0.10 eV were revealed for **5tCzMeB** and **5tCzBP**, respectively, indicating their potential for efficient TADF.

PL quantum yield (Φ_{PL}) measurements of toluene solutions in an oxygen-free environment resulted in moderate Φ_{PL} (0.43) for **5tCzMeB** and significantly lower Φ_{PL} (0.084) for **5tCzBP**, respectively. Due to the high T_1 energies of the investigated compounds (2.88 eV – **5tCzMeB**, 2.76 eV – **5tCzBP**), DPEPO (T_1 = 3.0 eV) was chosen as an active host material. To confirm energetic compatibility between the host and investigated compounds, HOMO and LUMO energies of the compounds were determined. HOMO levels were found by performing ionization potential measurements of the compound thin films (see Fig. S2, ESI†), meanwhile LUMO were deduced from the relationship LUMO = HOMO + E_g, where the energy gap (E_g) was determined from the onset of absorption spectra. Finally, we verified that compounds **5tCzMeB** (HOMO/LUMO = −5.9/−3.0 eV) and **5tCzBP** (HOMO/LUMO = −5.9/−3.1 eV) are compatible with the DPEPO host (HOMO/LUMO = −6.1/−2.0 eV).[31] To ensure efficient energy transfer from the host to guest molecules, while avoiding PL quenching, 20 wt% doping concentration of the synthesized emitters was selected. As compared to toluene solutions, **5tCzMeB** and **5tCzBP** demonstrated slightly blue-shifted fluorescence spectra in the DPEPO host (see Fig. 2) with peak wavelengths at 483 nm and 514 nm, respectively, due to reduced solvatochromic effect. When introduced into DPEPO host **5tCzMeB** expressed a 2-fold increase in emission efficiency (Φ_{PL} = 0.99), while **5tCzBP** enjoyed a 5-fold boost in Φ_{PL} (Φ_{PL} = 0.53) as compared to those of toluene solutions. The enhancement was previously reported for similar compounds bearing labile carbonyl groups and associated with suppression of intramolecular motion-induced non-radiative decay in rigid media.[19,32,33] Unlike in **5tCzMeB**, half of the excitation in **5tCzBP** decayed non-radiatively confirming the previously reported finding,[19,24] *i.e.* the inability to entirely restrict intramolecular torsions provoked by the benzophenone moiety in the solid state. PL spectra of the compounds' neat films resembled those of doped DPEPO films. Φ_{PL} values of the neat films were reduced only slightly, *i.e.* down to 0.58 (for **5tCzMeB**) and 0.28 (for **5tCzBP**) as compared to the values of doped DPEPO films. Φ_{PL} values of the neat film as well as solution of **5tCzBP** were found to be similar to the analogous benzophenone derivative without *t*-butyl groups.[22] The obtained weak concentration quenching of the compounds combined with their amorphous nature and excellent morphological stability

Table 1 Photophysical properties of the investigated TADF compounds in toluene, DPEPO host (at 20 wt% doping) and neat films

	Toluene/DPEPO/neat film			Toluene[a]								PMMA[b]		
Compound	PL_{max} (nm)	Φ_{PL}	Φ_{DF}/Φ_{PF}	τ_{PF} (ns)	k_r (10^6 s^{-1})	τ_{DF} (μs)	Φ_{rISC}	k_{rISC} (10^6 s^{-1})	Φ_{ISC}	k_{ISC} (10^8 s^{-1})	k_{nr}^T (10^6 s^{-1})	S_1 (eV)	T_1 (eV)	ΔE_{ST} (eV)
5tCzMeB	498/483/488	0.43/0.99/0.58	0.38/0.05, 0.94/0.05, 0.55/0.03	4.9	10.2	1.80	0.93	4.44	0.95	1.94	0.33	2.96	2.88	0.08
5tCzBP	524/514/525	0.084/0.53/0.28	0.043/0.041, 0.48/0.05, 0.25/0.03	12.2	3.3	0.29	0.53	3.81	0.96	0.79	3.32	2.86	2.76	0.10

[a] Determined in degassed toluene solutions (10^{-5} mol L^{-1}). [b] Estimated from the onset of fluorescence and phosphorescence spectra in dilute (1 wt%) PMMA films.

Published on 29 August 2019. Downloaded on 11/6/2019 11:27:24 AM.

(glass transition temperatures >190 °C, and thermal degradation temperatures >400 °C see Fig. S3 and S4, ESI†) rendered them promising for application in non-doped OLEDs.

To reveal the distinct features in excited state dynamics of the investigated compounds, time-resolved PL spectroscopy in toluene solutions, doped DPEPO and neat films was performed. The corresponding transients of spectrally integrated PL intensity are shown in Fig. 3. The photophysical parameters extracted from these measurements are provided in Table 1.

Measurements in degassed toluene solutions revealed double-exponential decay profiles with slow and fast components. The latter was assigned to prompt fluorescence (PF) with the lifetime (τ_{PF}) of 4.9 ns and 12.2 ns for **5tCzMeB** and **5tCzBP**, respectively. τ_{PF} were then used to determine radiative rates of the singlet state ($k_r = \Phi_{PF}/\tau_{PF}$) yielding a larger rate (1.02×10^7 s^{-1}) for compound **5tCzMeB** and a 3-fold smaller one (3.3×10^6 s^{-1}) for **5tCzBP**. Φ_{PF} was obtained by integrating the PF part of the PL decay curves while assuming that the total integral of PL transients corresponds to Φ_{PL}. Since the slower component of PL transients was significantly reduced upon exposure of the samples to air, it was naturally associated with oxygen-sensitive triplet species. Taking into account that no phosphorescence was observed at room temperature (only at low temperatures) and the PL spectra of the slow and prompt components were alike (an example for **5tCzMeB** is provided in Fig. 3c) the slow component could only be attributed either to triplet–triplet annihilation (TTA) or TADF. TTA was ruled out by measuring the PL intensity dependencies on the excitation power density, which clearly indicated intensity slope of ~1 for both compounds (Fig. S5, ESI†). Hence, the slower component of PL transients was assigned to TADF arising from the S_1 state populated through the rISC process. High k_{rISC} is generally considered to be a key parameter for achieving efficient TADF.[10,16,34]

k_{rISC} was determined by employing delayed fluorescence lifetimes (τ_{DF}), prompt and delayed fluorescence quantum efficiencies, Φ_{PF} and Φ_{DF}, respectively, and rISC efficiency (Φ_{rISC}).[10]

$$k_{rISC} = \frac{\Phi_{rISC}}{\tau_{DF}}\left(\frac{\Phi_{PF} + \Phi_{DF}}{\Phi_{PF}}\right) \quad (1)$$

$$\Phi_{rISC} = \frac{\Phi_{DF}}{\Phi_{PL}\Phi_{ISC}} \quad (2)$$

τ_{DF} was evaluated from the slower component of PL transients, while Φ_{PF} and Φ_{DF} were obtained from the corresponding integrals in the PL decay curves. Since Φ_{PF} and τ_{PF} were found to be similar in solution and rigid environment for both compounds (see Fig. 3), non-radiative deactivation of the singlets to the ground state was neglected, and thus, the main non-radiative losses were associated with a decay of long-lived triplet states characterized by k_{nr}^T. This implies that non-radiative decay of the S_1 state is governed solely by ISC to triplet states, thereby allowing us to express the quantum efficiency of the ISC process (Φ_{ISC}) as

$$\Phi_{ISC} = 1 - \Phi_{PF} \quad (3)$$

Even though similar k_{rISC} values 4.44×10^6 s^{-1} and 3.81×10^6 s^{-1} were obtained in accordance with eqn (1) for **5tCzMeB** and **5tCzBP**, respectively, Φ_{rISC} was estimated to be significantly higher for **5tCzMeB** (Φ_{rISC} = 0.93) than that for **5tCzBP** (Φ_{rISC} = 0.53). This result revealed that the triplets are quenched much more efficiently in **5tCzBP**. Indeed, the calculated non-radiative triplet quenching rate from eqn (4)

$$k_{nr}^T = k_{rISC}/\Phi_{rISC} - k_{rISC} \quad (4)$$

was one order magnitude larger in **5tCzBP** ($k_{nr}^T = 3.32 \times 10^6$ s^{-1}) as compared to that in **5tCzMeB** ($k_{nr}^T = 0.33 \times 10^6$ s^{-1}).

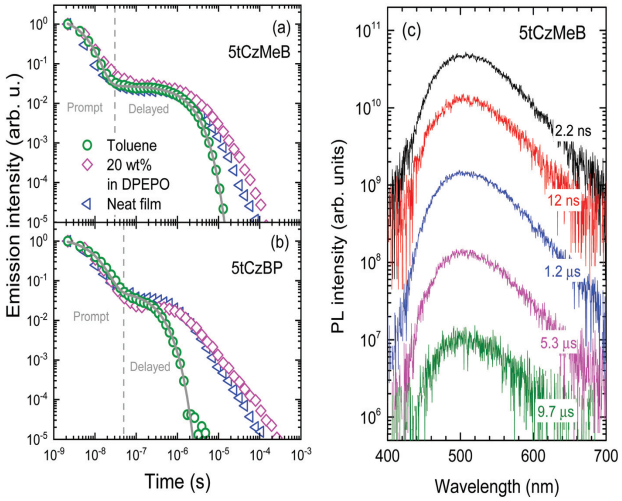

Fig. 3 Spectrally integrated PL transients of **5tCzMeB** (a) and **5tCzBP** (b) in degassed toluene solutions, 20 wt% DPEPO and neat films. Lines indicate double-exponential decay fits of PL transients in solutions. (c) Time-resolved PL spectra of **5tCzMeB** in degassed toluene solution. Delay time indicated.

 This journal is © The Royal Society of Chemistry 2019

Published on 29 August 2019. Downloaded on 11/6/2019 11:27:24 AM.

For a deeper insight into the causes of larger k_{nr}^{T} in **5tCzBP** we evaluated IR vibrational spectra of both compounds using the Hartree–Fock approach with the 3-21G basis set in the ground state geometry (see Fig. S6, ESI†). The comparison of both spectra revealed differences in low-frequency vibrational modes in otherwise identical spectra (Fig. S6a, ESI†). The differences (indicated by arrows) primarily originated from torsional/rotational displacement associated with the loose phenyl moiety of compound **5tCzBP**. These distinct low-frequency modes below 200 cm^{-1} likely facilitated non-radiative relaxation and thus larger k_{nr}^{T} in **5tCzBP**.

The provided energy diagrams in Fig. 4 nicely visualize energy transfer routes along with their rates pertinent to the studied TADF emitters.

Evidently, the fulfillment of the conditions $k_{ISC} > k_r$ and $k_{rISC} \geq k_{nr}^{T}$ ensured that spin cycling is repeated multiple times. The deduced rates infer that for both compounds over 95% of the generated singlets are converted into triplets *via* ISC, whereas the reverse process rISC is nearly as efficient (~93%) for **5tCzMeB** and only half as efficient (~53%) in the case of **5tCzBP**. The latter is caused by similar k_{rISC} and k_{nr}^{T} in **5tCzBP** forcing roughly half of the triplet population to decay non-radiatively. The corresponding DF contribution in **5tCzBP** is thereby relatively small $\Phi_{DF} = \Phi_{PF} = 0.04$ (see Table 1). Conversely, significantly suppressed non-radiative triplet quenching in **5tCzMeB** achieved upon substituting the loose phenyl moiety in the benzophenone by a methoxy group enabled to enlarge the ratio k_{rISC}/k_{nr}^{T} and retrieve the majority of the triplets. This resulted in considerably prolonged τ_{DF} and enhanced thermally-assisted DF contribution $\Phi_{DF} = 8 \times \Phi_{PF} = 0.38$ in solution. Taking into account near unity Φ_{PL} (0.99) obtained for **5tCzMeB** in the rigid DPEPO host, this substitution signified complete suppression of k_{nr}^{T} in the solid state, and hence 100% efficient rISC. In fact, such efficient rISC and large k_r (~10^7 s^{-1}) obtained for **5tCzMeB** is a perfect combination for a TADF material as well as TADF-OLED.[35] Other effective strategies for disabling k_{nr}^{T} in benzophenone-derived compounds rely on (i) the anchoring of both phenyl rings of benzophenone to donor fragments,[36] or (ii) replacing the loose phenyl ring by pyridine.[24,33] In both cases the modifications result in enhanced molecular rigidity; however they also redshift the PL spectrum as compared to the analogous unsubstituted benzophenone derivative thereby not permitting to preserve blue TADF emission.[24,36]

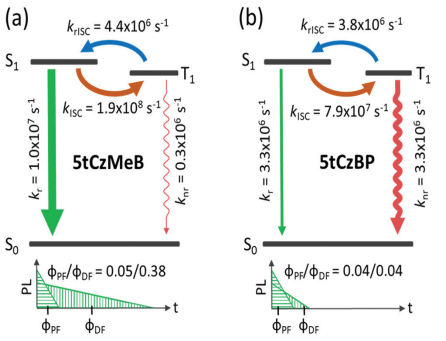

Fig. 4 Energy diagrams representing viable energy transfer routes along with their rates for compounds **5tCzMeB** (a) and **5tCzBP** (b) in solutions. Schematic representations of PF and DF contributions in PL transients for each compound are shown below.

It is noteworthy that τ_{DF} and Φ_{DF} in the doped DPEPO or neat films of both TADF compounds increased considerably, in particular for **5tCzBP** films, as compared to that in solution (see Fig. 3). The increase can be justified by suppression of intramolecular motions (as discussed above) and also by enhanced conformational disorder in the rigid media causing the multi-exponential decay profile of DF transients.[37,38] Although the multi-exponential nature of the decay precluded the determination of τ_{DF} and k_{rISC} values, the enlarged DF integral (and nearly identical PF contribution) in the rigid films of compounds **5tCzMeB** and **5tCzBP** as compared to their solutions implied higher or at least similar k_{rISC} values.

3.3. OLED performance

Electroluminescence (EL) properties of the TADF compounds **5tCzMeB** and **5tCzBP** were assessed by employing them in doped or neat (non-doped) emitting layers of OLEDs. While the doped TADF-OLEDs were fabricated by utilizing vacuum evaporation, the non-doped devices were made by using both the vacuum deposition and solution processing techniques. In terms of device performance, the doped OLEDs with TADF emitters serving as dopants are known to perform somewhat better as compared to the non-doped devices.[36,39–42] Despite this, non-doped OLEDs seem to be more attractive in respect of easier device fabrication and better reliability.[42] They also completely eliminate phase separation problems. Still, the main challenges for producing efficient non-doped emitting layers are mainly related to concentration quenching and exciton annihilation effects governed by strong intermolecular interactions.[42]

Vacuum-deposited doped devices were fabricated by employing 20 wt% doping concentration of **5tCzMeB** (Device 1) and **5tCzBP** (Device 1a) emitters in a DPEPO host. The following configuration, similar to that reported for high-triplet-energy TADF emitters, was adopted to fabricate these devices: ITO/NPB (30 nm)/TCTA (20 nm)/CzSi (10 nm)/emitter (20 wt%):DPEPO (20 nm)/DPEPO (10 nm)/TPBi (30 nm)/LiF (1 nm)/Al (100 nm).[8] Here, ITO and Al acted as the anode and cathode, respectively. Layers of *N*,*N*′-di(1-naphthyl)-*N*,*N*′-diphenyl-(1,1′-biphenyl)-4,4′-diamine (NPB) and 4,4′,4″-tris(carbazol-9-yl)triphenylamine (TCTA) were used for hole injection and transport, whereas LiF and TPBi were employed for electron injection and transport, respectively. 10 nm-thick layers of 9-(4-*tert*-butylphenyl)-3,6-bis(triphenylsilyl)-9*H*-carbazole (CzSi, $E(T_1)$ = 3.02 eV, HOMO/LUMO = −6.0/−2.5) and DPEPO were utilized for exciton confinement and charge carrier blocking. A schematic representation of layer thicknesses and energy level diagrams are provided in Fig. 5a. The main characteristics of the investigated devices are summarized in Table 2.

Device 1 based on **5tCzMeB** doped into the DPEPO host at 20 wt% demonstrated relatively low turn-on voltage (4.0 V) with electroluminescence maximum at 481 nm (see Fig. 5b) corresponding to sky-blue emission with Commission Internationale

Published on 29 August 2019. Downloaded on 11/6/2019 11:27:24 AM.

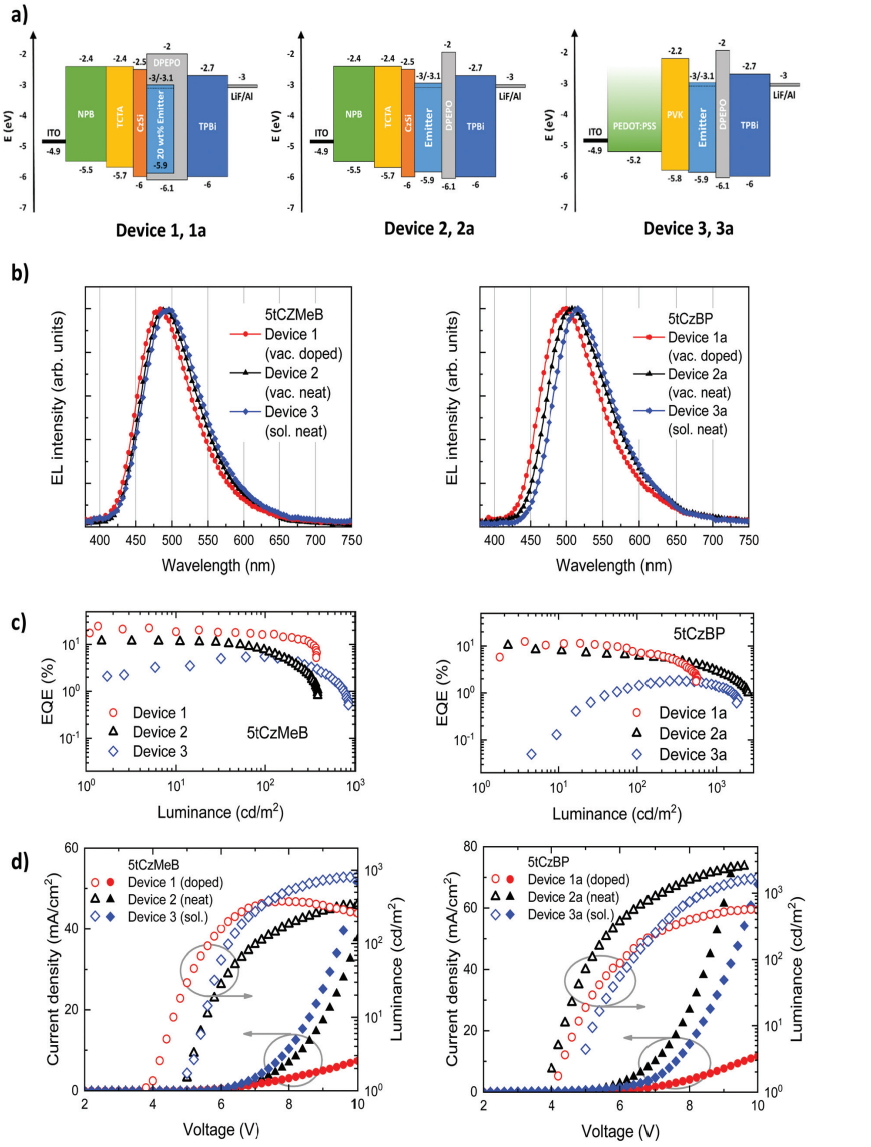

Fig. 5 (a) Structure and energy level diagrams of the fabricated devices. Devices 1, 2, 1a and 2a were vacuum-deposited using doped (20 wt%, DPEPO) or neat emitting layer based on **5tCzMeB** or **5tCzBP**; devices 3 and 3a were fabricated by solution processing using **5tCzMeB** or **5tCzBP** as neat emitting layer. (b) EL spectra of the investigated devices. (c) EQE *vs.* luminance curves. (d) Current density and luminance as a function of applied voltage of investigated OLEDs.

de L'Eclairage (CIE) coordinates of (0.19, 0.32). Due to the high Φ_{PL} (0.99) and efficient TADF, Device 1 exhibited extraordinarily high maximum EQE values reaching 24.6% at low current density and allowing to demonstrate rather high luminous efficacy (46.7 lm W^{-1}), whereas maximum EQE for the green-emitting (λ_{max} = 497 nm) doped OLED based on **5tCzBP** was only 12.5%, which is in good agreement with Φ_{PL} measurements (Φ_{PL} = 0.53) if light outcoupling efficiency of 20–30% is taken into account. We note that possibly even lower turn-on voltages as well as improved efficiencies particularly at higher current

This journal is © The Royal Society of Chemistry 2019

Table 2 Main characteristics of the investigated TADF-OLEDs based on **5tCzMeB** and **5tCzBP** emitters

				Maximum values				Values at 100 cd m^{-2}					
Device	Emitter	Form[a]	On[b] (V)	EQE (%)	CE[c] (cd A^{-1})	L[d] (cd m^{-2})	LE[e] (lm W^{-1})	Voltage (V)	EQE (%)	CE[c] (cd A^{-1})	LE[e] (lm W^{-1})	CIE (x, y)	λ_{max} (nm)
1	**5tCzMeB**	Doped (vac.)	4.0	24.6	59.4	378	46.7	5.6	16.5	33	18.2	0.19, 0.32	481
2		Neat (vac.)	4.8	13.4	35	380	27.5	7.0	7.7	3.6	1.6	0.20, 0.36	488
3		Neat (sol.)	4.8	5.5	12.5	847	6.5	6.2	5.5	12.5	6.4	0.21, 0.39	494
1a	**5tCzBP**	Doped (vac.)	4.1	12.5	34.9	568	27.3	6.2	7.5	18.0	9.5	0.23, 0.41	497
2a		Neat (vac.)	3.8	10.3	19.0	2544	14.9	5.2	6.0	17.0	10.3	0.26, 0.47	508
3a		Neat (sol.)	4.7	1.8	5.5	1884	2.4	6.4	1.4	4.5	2.2	0.28, 0.52	516

[a] Devices were fabricated by vacuum (vac.) or solution processing (sol.) using emitting layers based on neat or doped (20 wt% in DPEPO) films of the investigated compounds. [b] Turn-on voltage estimated at 1 cd m^{-2}. [c] Current efficiency. [d] Luminance. [e] Luminous efficacy.

densities of our devices could be achieved by doping injection or transport layers.[43,44]

Encouraged by the relatively weak concentration quenching (see Table 1) and good ambipolar charge carrier transport properties ($\mu \approx 10^{-3}$–10^{-4} cm^2 V^{-1} s^{-1}) determined in the neat films of the synthesized compounds (see Fig. S7, ESI†), non-doped OLEDs based on **5tCzMeB** (Device 2) and **5tCzBP** (Device 2a) were prepared. The non-doped devices employed a similar configuration as that used for doped devices: ITO/NPB (30 nm)/TCTA (20 nm)/CzSi (10 nm)/emitter (20 nm)/DPEPO (10 nm)/TPBi (30 nm)/LiF (1 nm)/Al (100 nm). Device 2 based on **5tCzMeB** neat film exhibited a maximum EQE of 13.4%, maximum luminous efficacy of 27.5 lm W^{-1} and slightly red-shifted EL peak (at 488 nm) as compared to the doped device 1. Meanwhile device 2a based on **5tCzBP** neat film demonstrated a maximum EQE of 10.3%, and luminous efficacy of 14.9 lm W^{-1} with green EL peaking at 508 nm (CIE coordinates (0.23, 0.41)). The obtained results confirmed the superiority of **5tCzMeB** over **5tCzBP** to be employed as an efficient emitter not only in the doped but also in non-doped OLEDs. Moreover, the results were found to be consistent with the photophysical measurements (see Φ_{PL} of the neat films in Table 1) implying that the main efficiency losses in non-doped devices occur due to the concentration quenching of PL in the neat films.

Since the compounds **5tCzMeB** and **5tCzBP** expressed excellent solubility in organic solvents due to the bulky *t*-butyl groups, they were also tested in solution-processed OLEDs. Wet processing is advantageous over the commonly utilized vacuum deposition technique because of the scalable manufacturing, simplified and low-cost fabrication as well as the possibility to produce large-area devices.[45] Devices based on the neat **5tCzMeB** (Device 3) and **5tCzBP** (Device 3a) emitting layers were prepared by using the following device structure ITO/PEDOT:PSS (60 nm)/PVK (20 nm)/emitter (20 nm)/DPEPO (10 nm)/TPBi (30 nm)/LiF (1 nm)/Al (100 nm). Here PEDOT:PSS was used for the hole injection, whereas PVK was utilized for hole transport and electron blocking. The PVK layer is one of the most popular alternatives for hole transport and electron blocking in highly efficient solution-processed OLEDs.[46,47] Emitting layers on top of PVK were spin-coated by using a relatively poor solvent – cyclohexane, which prevented the dissolution of bottom PVK films and allowed fabrication of OLEDs consisting of up to 3 solution-processed layers. Unfortunately, as compared to the vacuum-deposited devices, solution-processed OLEDs demonstrated significantly reduced maximum EQE values, corresponding to 5.5% for Device 3 and 1.8% for Device 3a, respectively. Such an efficiency decrease can be attributed to the lack of triplet exciton confinement, since PVK has a T_1 energy ($\sim$2.5 eV) significantly lower than that of **5tCzMeB** ($E(T_1)$ = 2.88 eV) or **5tCzBP** ($E(T_1)$ = 2.76 eV).[48] Efficient exciton confinement is extremely important in non-doped OLEDs due to the greater exciton diffusion and possible exciton quenching by carrier injection or transport materials. Hence, the development of new easy solution-processable hole transporting materials with high T_1 so as to suit blue-emitting OLEDs is highly important.[49]

I–V and *L–V* curves in semi-log scale highlighting the leakage current data of the devices are shown in Fig. S8, ESI.† Notably higher leakage currents were obtained for solution-processed devices ($<$0.1 mA cm^{-2} for **5tCzMeB** and $<$0.3 mA cm^{-2} for **5tCzBP**), whereas significantly lower ones were obtained for vacuum-deposited OLEDs ($<$0.001 mA cm^{-2} for **5tCzMeB** and $<$0.002 mA cm^{-2} for **5tCzBP**). The observed leakage currents are rather typical of vacuum-evaporated OLEDs,[50,51] yet in the case of solution-processed OLEDs they are somewhat higher as for the typical devices.[52,53]

Evidently, much lower current densities at the same driving voltages obtained for the doped devices 1 and 1a as compared to non-doped 2, 3, and 2a, 3a, can be attributed to the poor charge transporting ability of the DPEPO host. Electron and hole mobilities of DPEPO were found to be several orders of magnitude lower than those of the neat **5tCzMeB** and **5tCzBP** films.[54] Despite the lower currents, the doped OLEDs 1 and 1a experienced somewhat earlier (or at least similar) roll-off, which, to some extent, is caused by the accelerated device degradation with increasing current density. This can be explained by taking into account the fact that intrinsic emitter degradation is dominated by the exciton density[55] and that this density estimated per one emitting molecule in 20 wt%-doped emitting layers is larger as compared to that for the neat layers at the same current density. In fact, the roll-offs of non-doped devices 2, 3, and 2a, 3a, were also found to be fast. In comparison, devices based on TADF emitters with similarly fast TADF (τ_{DF} $<$ 10 μs) usually express significantly weaker efficiency roll-off enabling to attain luminances above 1000 cd m^{-2} without strongly reducing the maximum EQE.[8,40] Unfortunately, we found that the fast roll-offs of non-doped devices were also

Published on 29 August 2019. Downloaded on 11/6/2019 11:27:24 AM.

Published on 29 August 2019. Downloaded on 11/6/2019 11:27:24 AM.

affected by permanent device degradation. The accelerated degradation most likely resulted from the long injection current pulses (2 s) used by the measurement setup (ORB Optronix) employed for evaluation of current–voltage–luminance characteristics. The pulses were the shortest available in the setup software and could not be further reduced. Nevertheless, at a lower luminance <200 cd m^{-2}, *i.e.* in the degradation-free region, doped and non-doped OLEDs based on **5tCzMeB** and prepared by vacuum evaporation delivered excellent performance in terms of EQE, thus confirming effective suppression of non-radiative triplet quenching and ensuring efficient TADF.

4. Conclusions

In this work the issue of accelerated non-radiative triplet decay in benzophenone-derived TADF compounds frequently employed in blue OLEDs has been tackled. The enhanced triplet deactivation $T_1 \rightarrow S_0$ explicitly related to the loose phenyl moiety and intramolecular motions associated with it in the benzophenone acceptor was found to compete with the rISC process, thereby decreasing TADF efficiency even in compounds with high k_{rISC} ($>10^6$ s^{-1}). To address this problem and reduce the triplet quenching equivalent by rate to rISC ($k_{nr}^T \approx k_{rISC}$) in compound **5tCzBP** possessing benzophenone, the loose phenyl moiety in the acceptor was replaced by a methoxy group so as to result in methyl benzoate (compound **5tCzMeB**). The modification enabled to suppress the non-radiative triplet quenching by one order of magnitude thereby enhancing the k_{rISC}/k_{nr}^T ratio, yet maintaining an unchanged k_{rISC}. This benefited in complete harvesting of the triplets *via* the rISC resulting in almost unity Φ_{PL} in the doped DPEPO films and $\Phi_{PL} = 0.58$ in the neat films, which in the latter case was limited only by concentration quenching. The fabricated sky-blue TADF OLEDs based on **5tCzMeB** delivered outstanding maximal EQE values of 24.6% and 13.4% in the doped and non-doped devices, respectively, whereas at 100 cd m^{-2} the devices exhibited 16.5% and 7.7% EQEs, respectively. Hence, from the perspective of material design, the methyl benzoate acceptor seems to be much more appealing than the popular benzophenone as it can boost the TADF performance of a device while preserving its blue emission wavelength.

Conflicts of interest

There are no conflicts to declare.

Acknowledgements

The research was funded by the European Social Fund (project No. 09.3.3-LMT-K-712-01-0084) under grant agreement with the Research Council of Lithuania (LMTLT).

References

1 J. H. Burroughes, D. D. C. Bradley, A. R. Brown, R. N. Marks, K. Mackay, R. H. Friend, P. L. Burns and A. B. Holmes, *Nature*, 1990, **347**, 539–541.
2 R. H. Friend, R. W. Gymer, A. B. Holmes, J. H. Burroughes, R. N. Marks, C. Taliani, D. D. C. Bradley, D. A. Dos Santos, J. L. Brédas, M. Lögdlund and W. R. Salaneck, *Nature*, 1999, **397**, 121–128.
3 Z. Yang, Z. Mao, Z. Xie, Y. Zhang, S. Liu, J. Zhao, J. Xu, Z. Chi and M. P. Aldred, *Chem. Soc. Rev.*, 2017, **46**, 915–1016.
4 M. Y. Wong and E. Zysman-Colman, *Adv. Mater.*, 2017, **29**, 1605444.
5 F. B. Dias, K. N. Bourdakos, V. Jankus, K. C. Moss, K. T. Kamtekar, V. Bhalla, J. Santos, M. R. Bryce and A. P. Monkman, *Adv. Mater.*, 2013, **25**, 3707–3714.
6 H. Uoyama, K. Goushi, K. Shizu, H. Nomura and C. Adachi, *Nature*, 2012, **492**, 234–238.
7 C.-Y. Kuei, W.-L. Tsai, B. Tong, M. Jiao, W.-K. Lee, Y. Chi, C.-C. Wu, S.-H. Liu, G.-H. Lee and P.-T. Chou, *Adv. Mater.*, 2016, **28**, 2795–2800.
8 Q. Zhang, B. Li, S. Huang, H. Nomura, H. Tanaka and C. Adachi, *Nat. Photonics*, 2014, **8**, 326–332.
9 S. Hirata, Y. Sakai, K. Masui, H. Tanaka, S. Y. Lee, H. Nomura, N. Nakamura, M. Yasumatsu, H. Nakanotani, Q. Zhang, K. Shizu, H. Miyazaki and C. Adachi, *Nat. Mater.*, 2015, **14**, 330–336.
10 F. B. Dias, T. J. Penfold and A. P. Monkman, *Methods Appl. Fluoresc.*, 2017, **5**, 012001.
11 A. Endo, K. Sato, K. Yoshimura, T. Kai, A. Kawada, H. Miyazaki and C. Adachi, *Appl. Phys. Lett.*, 2011, **98**, 083302.
12 H. F. Higginbotham, C.-L. Yi, A. P. Monkman and K.-T. Wong, *J. Phys. Chem. C*, 2018, **122**, 7627–7634.
13 H. Noda, H. Nakanotani and C. Adachi, *Sci. Adv.*, 2018, **4**, 1–8.
14 H. Noda, H. Nakanotani and C. Adachi, *Chem. Lett.*, 2019, **48**, 126–129.
15 B. Wex and B. R. Kaafarani, *J. Mater. Chem. C*, 2017, **5**, 8622–8653.
16 T. Hosokai, H. Matsuzaki, H. Nakanotani, K. Tokumaru, T. Tsutsui, A. Furube, K. Nasu, H. Nomura, M. Yahiro and C. Adachi, *Sci. Adv.*, 2017, **3**, e1603282.
17 D. Zhang, M. Cai, Y. Zhang, D. Zhang and L. Duan, *Mater. Horiz.*, 2016, **3**, 145–151.
18 N. Aizawa, C.-J. Tsou, I. S. Park and T. Yasuda, *Polym. J.*, 2017, **49**, 197–202.
19 S. Y. Lee, T. Yasuda, Y. S. Yang, Q. Zhang and C. Adachi, *Angew. Chem., Int. Ed.*, 2014, **126**, 6520–6524.
20 Y. Li, G. Xie, S. Gong, K. Wu and C. Yang, *Chem. Sci.*, 2016, **7**, 5441–5447.
21 S. Y. Lee, T. Yasuda, I. S. Park and C. Adachi, *Dalton Trans.*, 2015, **44**, 8356–8359.
22 F. Wang, X. Cao, L. Mei, X. Zhang, J. Hu and Y. Tao, *Chin. J. Chem.*, 2018, **36**, 241–246.
23 W. Z. Yuan, X. Y. Shen, H. Zhao, J. W. Y. Lam, L. Tang, P. Lu, C. Wang, Y. Liu, Z. Wang, Q. Zheng, J. Z. Sun, Y. Ma and B. Z. Tang, *J. Phys. Chem. C*, 2010, **114**, 6090–6099.
24 P. Rajamalli, V. Thangaraji, N. Senthilkumar, C.-C. Ren-Wu, H.-W. Lin and C.-H. Cheng, *J. Mater. Chem. C*, 2017, **5**, 2919–2926.
25 J. Lee, N. Aizawa, M. Numata, C. Adachi and T. Yasuda, *Adv. Mater.*, 2017, **29**, 1604856.

 This journal is © The Royal Society of Chemistry 2019

Published on 29 August 2019. Downloaded on 11/6/2019 11:27:24 AM.

26 Y. Liu, M. Nishiura, Y. Wang and Z. Hou, *J. Am. Chem. Soc.*, 2006, **128**, 5592–5593.
27 M. J. Frisch, G. W. Trucks, H. B. Schlegel, G. E. Scuseria, M. A. Robb, J. R. Cheeseman, G. Scalmani, V. Barone, G. A. Petersson, H. Nakatsuji, X. Li, M. Caricato, A. Marenich, J. Bloino, B. G. Janesko, R. Gomperts, B. Mennucci, H. P. Hratchian, J. V. Ortiz, A. F. Izmaylov, J. L. Sonnenberg, D. Williams-Young, F. Ding, F. Lipparini, F. Egidi, J. Goings, B. Peng, A. Petrone, T. Henderson, D. Ranasinghe, V. G. Zakrzewski, J. Gao, N. Rega, G. Zheng, W. Liang, M. Hada, M. Ehara, K. Toyota, R. Fukuda, J. Hasegawa, M. Ishida, T. Nakajima, Y. Honda, O. Kitao, H. Nakai, T. Vreven, K. Throssell, J. A. J. Montgomery, J. E. Peralta, F. Ogliaro, M. Bearpark, J. J. Heyd, E. Brothers, K. N. Kudin, V. N. Staroverov, T. Keith, R. Kobayashi, J. Normand, K. Raghavachari, A. Rendell, J. C. Burant, S. S. Iyengar, J. Tomasi, M. Cossi, J. M. Millam, M. Klene, C. Adamo, R. Cammi, J. W. Ochterski, R. L. Martin, K. Morokuma, O. Farkas, J. B. Foresman and D. J. Fox, 2016.
28 Y. J. Cho, S. K. Jeon, S. S. Lee, E. Yu and J. Y. Lee, *Chem. Mater.*, 2016, **28**, 5400–5405.
29 Y. Im, M. Kim, Y. J. Cho, J.-A. Seo, K. S. Yook and J. Y. Lee, *Chem. Mater.*, 2017, **29**, 1946–1963.
30 Q. Zhang, J. Li, K. Shizu, S. Huang, S. Hirata, H. Miyazaki and C. Adachi, *J. Am. Chem. Soc.*, 2012, **134**, 14706–14709.
31 Q. Zhang, T. Komino, S. Huang, S. Matsunami, K. Goushi and C. Adachi, *Adv. Funct. Mater.*, 2012, **22**, 2327–2336.
32 M. Shimizu, M. Nakatani and K. Nishimura, *Sci. China: Chem.*, 2018, **61**, 925–931.
33 P. Rajamalli, N. Senthilkumar, P. Gandeepan, P.-Y. Huang, M.-J. Huang, C.-Z. Ren-Wu, C.-Y. Yang, M.-J. Chiu, L.-K. Chu, H.-W. Lin and C.-H. Cheng, *J. Am. Chem. Soc.*, 2016, **138**, 628–634.
34 J. Gibson, A. P. Monkman and T. J. Penfold, *ChemPhysChem*, 2016, **17**, 2956–2961.
35 B. Yurash, H. Nakanotani, Y. Olivier, D. Beljonne, C. Adachi and T. Nguyen, *Adv. Mater.*, 2019, 1804490.
36 Q. Zhang, D. Tsang, H. Kuwabara, Y. Hatae, B. Li, T. Takahashi, S. Y. Lee, T. Yasuda and C. Adachi, *Adv. Mater.*, 2015, **27**, 2096–2100.
37 T. Serevičius, R. Skaisgiris, J. Dodonova, L. Jagintavičius, J. Bucevičius, K. Kazlauskas, S. Juršėnas and S. Tumkevičius, *Chem. Commun.*, 2019, **55**, 1975–1978.
38 M. K. Etherington, F. Franchello, J. Gibson, T. Northey, J. Santos, J. S. Ward, H. F. Higginbotham, P. Data, A. Kurowska, P. L. Dos Santos, D. R. Graves, A. S. Batsanov, F. B. Dias, M. R. Bryce, T. J. Penfold and A. P. Monkman, *Nat. Commun.*, 2017, **8**, 14987.
39 T.-A. Lin, T. Chatterjee, W.-L. Tsai, W.-K. Lee, M.-J. Wu, M. Jiao, K.-C. Pan, C.-L. Yi, C.-L. Chung, K.-T. Wong and C.-C. Wu, *Adv. Mater.*, 2016, **28**, 7029.
40 T. L. Wu, M. J. Huang, C. C. Lin, P. Y. Huang, T. Y. Chou, R. W. Chen-Cheng, H. W. Lin, R. S. Liu and C. H. Cheng, *Nat. Photonics*, 2018, **12**, 235–240.
41 W. L. Tsai, M. H. Huang, W. K. Lee, Y. J. Hsu, K. C. Pan, Y. H. Huang, H. C. Ting, M. Sarma, Y. Y. Ho, H. C. Hu, C. C. Chen, M. T. Lee, K. T. Wong and C. C. Wu, *Chem. Commun.*, 2015, **51**, 13662–13665.
42 M. Godumala, S. Choi, M. J. Cho and D. H. Choi, *J. Mater. Chem. C*, 2019, **7**, 2172–2198.
43 M. Pfeiffer, X. Zhou, J. Huang, K. Leo and J. Blochwitz-Nimoth, *SID Symp. Dig. Tech. Pap.*, 2003, **34**, 1076.
44 R.-Q. Png, M. C. Y. Ang, M.-H. Teo, K.-K. Choo, C. G. Tang, D. Belaineh, L.-L. Chua and P. K. H. Ho, *Nat. Commun.*, 2016, **7**, 11948.
45 A. R. Duggal, C. M. Heller, J. J. Shiang, J. Liu and L. N. Lewis, *J. Disp. Technol.*, 2007, **3**, 184–192.
46 K. Albrecht, K. Matsuoka, D. Yokoyama, Y. Sakai, A. Nakayama, K. Fujita and K. Yamamoto, *Chem. Commun.*, 2017, **53**, 2439–2442.
47 H. J. Kim, C. Lee, M. Godumala, S. Choi, S. Y. Park, M. J. Cho, S. Park and D. H. Choi, *Polym. Chem.*, 2018, **9**, 1318–1326.
48 T. Ye, J. Chen and D. Ma, *Phys. Chem. Chem. Phys.*, 2010, **12**, 15410.
49 K. Tsai, M. Hung, Y. Mao and S. Chen, *Adv. Funct. Mater.*, 2019, **29**, 1901025.
50 Z. Wang, Y. Li, X. Cai, D. Chen, G. Xie, K. Liu, Y.-C. Wu, C.-C. Lo, A. Lien, Y. Cao and S.-J. Su, *ACS Appl. Mater. Interfaces*, 2016, **8**, 8627–8636.
51 F. B. Dias, J. Santos, D. R. Graves, P. Data, R. S. Nobuyasu, M. A. Fox, A. S. Batsanov, T. Palmeira, M. N. Berberan-Santos, M. R. Bryce and A. P. Monkman, *Adv. Sci.*, 2016, **3**, 1600080.
52 T.-H. Han, M.-R. Choi, C.-W. Jeon, Y.-H. Kim, S.-K. Kwon and T.-W. Lee, *Sci. Adv.*, 2016, **2**, e1601428.
53 F. Guo, A. Karl, Q.-F. Xue, K. C. Tam, K. Forberich and C. J. Brabec, *Light Sci. Appl.*, 2017, **6**, e17094.
54 J. Zhang, D. Ding, Y. Wei and H. Xu, *Chem. Sci.*, 2016, **7**, 2870–2882.
55 S. Winter, S. Reineke, K. Walzer and K. Leo, *International Society for Optics and Photonics*, ed. P. L. Heremans, M. Muccini and E. A. Meulenkamp, 2008, vol. 6999, p. 69992N.

Paper IV

Realization of deep-blue TADF in sterically controlled naphthyridines for vacuum- and solution-processed OLEDs

G. Kreiza, D. Banevičius, J. Jovaišaitė, S. Juršėnas, T. Javorskis, V. Vaitkevičius, E. Orentas and K. Kazlauskas

J. Mater. Chem. C., **8**, 8560 (2020)

DOI: 10.1039/d0tc01637c

https://doi.org/10.1039/D0TC01637C

Journal of Materials Chemistry C

ROYAL SOCIETY OF CHEMISTRY

PAPER

View Article Online
View Journal | View Issue

Check for updates

Cite this: J. Mater. Chem. C, 2020, 8, 8560

Realization of deep-blue TADF in sterically controlled naphthyridines for vacuum- and solution-processed OLEDs†

Gediminas Kreiza, [a] Dovydas Banevičius, [a] Justina Jovaišaitė, [a] Saulius Juršėnas,[a] Tomas Javorskis,[b] Vytenis Vaitkevičius,[b] Edvinas Orentas [b] and Karolis Kazlauskas *[a]

Received 31st March 2020,
Accepted 11th May 2020

DOI: 10.1039/d0tc01637c

rsc.li/materials-c

Published on 11 May 2020. Downloaded on 9/6/2020 10:35:59 AM.

Narrow-band deep-blue (emission peak < 460 nm) TADF emitters are in demand for commercial OLED display applications, yet the development of efficient emitters with low efficiency roll-off is very challenging. To address this issue, herein, we studied carbazole–naphthyridine (donor–acceptor)-based blue-emitting TADF compounds, which were designed by using both the H-bonding and sterically controlled charge-transfer (CT) interactions between D and A units. Methyl substitution employed at the first position of *t*-butyl-carbazole donors was found to affect CT strength and consequently the TADF properties of the studied compounds, enabling a significant reduction of delayed fluorescence lifetime (down to 3.1 μs) and enhancement of reverse intersystem crossing rate (up to 10^6 s^{-1}). The naphthyridines were demonstrated to hold great potential as deep-blue TADF emitters suitable for both vacuum- and solution-processed TADF OLEDs. The optimized devices with 7 wt% naphthyridine emitter in a weakly polar mCP host delivered external quantum efficiencies (EQEs) of up to ~17.6% and ~13.5% for vacuum- and solution-processed OLEDs, respectively. Unsubstituted naphthyridine exhibited deep-blue (λ_{max} < 460 nm) and narrow-band (FWHM = 66 nm) electroluminescence, whereas the more twisted methyl-substituted compound expressed broader band (FWHM > 80 nm) sky-blue (λ_{max} ≈ 480 nm) emission. The demonstrated emitters are among the best-performing conventional D–A-type blue/deep-blue TADF emitters in terms of EQE and efficiency roll-off properties of their devices.

1. Introduction

The basic design principles of high performance thermally activated delayed fluorescence (TADF) compounds routinely rely on the combination of spatially twisted donor (D) and acceptor (A) moieties.[1] This enables large separation of the highest occupied (HOMO) and lowest unoccupied (LUMO) molecular orbitals subsequently resulting in a small energy gap between the lowest excited singlet (S_1) and triplet (T_1) states. The twisted D–A compounds express charge-transfer (CT) character and are highly attractive for organic light emitting diode (OLED) applications due to the potentially fast and efficient reverse intersystem crossing (rISC).[2] It allows the utilization of both singlet and triplet excitons formed in the emitting layer of a device after electron and hole injection.[3] Although TADF-based OLEDs are frequently reported to reach 100% internal quantum efficiency,[4] their application in commercial displays is limited by their broadened (FWHM ~ 90 nm) and red-shifted fluorescence (FL) spectra due to the strong intramolecular CT and conformational disorder caused by variation in the twisting angle between D and A moieties.[5] Therefore, the development of efficient narrow-band (FWHM < 60 nm) TADF emitters is considered to be a challenging task, especially for the blue/deep-blue OLEDs.[6,7]

The reported approaches to achieve narrow blue TADF rely on rigid sterically hindered[8] or donor-interlocked molecular structures,[9] HOMO–LUMO separation by the multiple resonance effect[10] and weak CT compounds.[11] An additional involvement of H-bonding interactions between nitrogen heteroatoms in A and neighbouring C–H bonds in D units was also found to facilitate delivering narrow blue TADF emission.[12] It seems that the combination of both H-bonding and CT interactions in a controlled manner could be an attractive strategy to achieve high-performance blue OLEDs, and more importantly, to gain understanding of the TADF mechanism of D–A systems containing nitrogen heteroatoms in their building blocks.

[a] Institute of Photonics and Nanotechnology, Vilnius University, Saulėtekio av. 3, LT-10257 Vilnius, Lithuania. E-mail: karolis.kazlauskas@ff.vu.lt
[b] Department of Organic Chemistry, Vilnius University, Faculty of Chemistry and Geosciences, Naugarduko 24, Vilnius LT-03225, Lithuania

† Electronic supplementary information (ESI) available. CCDC 1991494 and 1992697. For ESI and crystallographic data in CIF or other electronic format see DOI: 10.1039/d0tc01637c

This journal is © The Royal Society of Chemistry 2020

Published on 11 May 2020. Downloaded on 9/6/2020 10:35:59 AM.

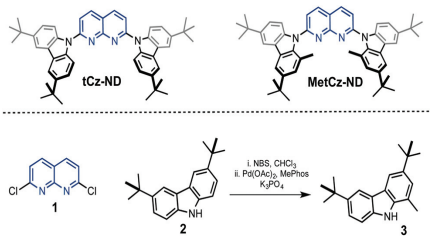

Fig. 1 Chemical structures of the synthesized 1,8-naphthyridine (ND) derivatives and precursors **1**–**3**.

Recently, a nitrogen heteroatom-containing naphthyridine acceptor was successfully utilized in the construction of TADF emitters.[13–16] The combination of naphthyridine with a variety of donors, *e.g.* those based on acridane, carbazole, phenoxazine and phenothiazine regularly employed for designing efficient TADF compounds, produced yellow/green/blue emitters with peak wavelength (λ_{max}) above 460 nm. Meanwhile, implementing them in efficient OLEDs produced surprisingly low external quantum efficiency (EQE) roll-offs.[15,16] Note, however, that for commercial applications like OLED displays, narrow-band deep-blue emitters with $\lambda_{max} < 460$ nm are required.[17] To reveal the potential of naphthyridine acceptors for the formation of deep-blue TADF emitters, we have designed a couple of 1,8-naphthyridine (ND)-based compounds with *tert*-butyl-carbazole (*t*Cz) serving as the donor (Fig. 1). Although one of the compounds, ***t*Cz-ND,** was recently reported,[16] its most intriguing photophysical properties and its possibilities to be employed in deep-blue OLEDs remained overlooked. Herein, ***t*Cz-ND** was also used for comparative analysis with the second compound **Met*t*Cz-ND** containing additional methyl (Me) moieties at the first position of the *t*Cz donors. Me substitution was employed to alter steric hindrance and, consequently, twisting of the D and A units. The modification permitted assessing the impact of intramolecular D–A interaction and CT strength on TADF properties of the studied compounds and on their performance in both solution- and vacuum-processed OLEDs.

2. Experimental section

2.1. Sample preparation and instrumentation

Absorption spectra of dilute toluene solutions (10^{-5} M) of the investigated naphthyridine derivatives were recorded using a Lambda 950 UV-vis-NIR spectrophotometer (PerkinElmer). 1,3-Bis(*N*-carbazolyl)benzene (mCP) films doped with 7 wt% contents of the compounds were prepared by spin-coating chloroform solutions (20 mg mL^{-1}) of mCP and compound mixtures on quartz substrates at 2000 rpm and annealing at 50 °C for 20 minutes to remove residual solvent. Steady state PL spectra were recorded using a PMA-12 back-thinned CCD spectrometer (Hamamatsu) by exciting samples with a xenon lamp coupled to a monochromator. Toluene solutions were degassed by the freeze–pump–thaw method. Fluorescence quantum yield (Φ_{FL}) was estimated in oxygen-free media by using the integrating sphere (Sphere Optics) and comparative methods for solutions, where quinine sulfate in 0.1 M H_2SO_4 served as the reference.[18] All samples were excited at 340 nm. FL transients were measured using an NT 242 nanosecond YAG:Nd^{3+} laser equipped with an optical parametric oscillator (Ekspla, excitation wavelength 340 nm, pulse duration 5 ns, and repetition rate 1 kHz) and an iStar DH340T time-gated intensified CCD camera (Andor) mounted on an SR-303i spectrograph (Shamrock). Measurements at low temperatures were performed in a 204N closed-cycle helium cryostat (Cryo Industries). Ionization potential (I_p) of the wet-casted films was estimated by photoelectron emission spectrometry in air.[19] The films for the measurements were prepared by dissolving materials in THF and by casting the solutions on polyester film coated with an Al conductive layer and ~0.5 μm-thick methylmethacrylate and methacrylic acid copolymer adhesive layers. Prior to experiments, the investigated compounds were purified using a DSU-20 vacuum sublimation system (CreaPhys).

2.2. OLED fabrication and characterization

OLEDs were fabricated on pre-patterned ITO/glass substrates (purchased from Kintec company). ITO layer thickness was 100 nm with a sheet resistance of 15–20 Ω □$^{-1}$. Prior to device fabrication, the substrates were cleaned by ultrasonication in a detergent (Hellmanex II) at 50 °C for 10 minutes; then, substrates were rinsed with running distilled water and blow-gunned ensuring no residual detergent is left. Afterwards, the substrates were sonicated consecutively in distilled water, acetone and isopropyl alcohol for 15 minutes (in each solvent). Immediately after the substrates were removed from the isopropanol bath, they were immersed in boiling hot distilled water and then dried. The substrates were then treated with O_2 plasma and transferred into a nitrogen-filled glovebox with an integrated vacuum evaporation chamber. The vacuum-processed devices were fabricated in a vacuum chamber (at a base pressure of $<10^{-6}$ Torr) by depositing multiple organic layers at a rate of 0.5–1.2 Å s^{-1}. The doped emissive layer was obtained by co-evaporating materials from two different evaporation sources at different evaporation rates for the desired doping concentration.

The solution-processed devices were fabricated by the following procedure. O_2 plasma-treated ITO/glass substrates were coated with a PEDOT:PSS (poly(3,4-ethylenedioxythiophene)-poly(styrenesulfonate)) layer by spin-coating from a water solution at 5000 rpm. Before the coating, PEDOT:PSS (Al 4083, purchased from Ossila) was ultrasonicated and filtered through a 0.45 μm PES filter. The spin-coating resulted in a 40 nm-thick film, which was annealed at 200 °C for 10 minutes to remove residual H_2O. Samples were then transferred into a nitrogen glovebox, where PVK (poly(9-vinylcarbazole)) was spin-coated at 2000 rpm from 6 mg mL^{-1} chlorobenzene solution, and annealed afterwards at 160 °C for 15 min resulting in a 15 nm-thick layer. Immediately after that, a 25 nm-thick emissive layer from a 2.5 mg mL^{-1} cyclohexane solution (emitter : host ratio of 7 : 93 by weight) was spin-coated on top at 1500 rpm. The samples were then left to dry for 30 minutes at room temperature before their transfer to an

Published on 11 May 2020. Downloaded on 9/6/2020 10:35:59 AM.

integrated vacuum chamber for further deposition of 5 nm-thick DPEPO (bis[2-(diphenylphosphino)phenyl] ether oxide) followed by a 50 nm-thick TmPyPB (1,3,5-tri(*m*-pyridin-3-ylphenyl)benzene) layer.

Finally, for both the solution- and vacuum-processed devices, the samples were transferred from the organic deposition chamber to a metal deposition chamber without breaking the vacuum, where (lithium fluoride) LiF and Al layers at the rates of 0.2 and 1.8 Å s^{-1}, respectively, were successively deposited. The active area of the final devices was 1 mm^2, 4 mm^2 or 16 mm^2 as defined by the cross-section of the patterned ITO anode and the shadow mask of cathode deposition. Before exposure to air, the devices were transferred from the vacuum chamber to a nitrogen atmosphere for encapsulation. The OLEDs were encapsulated using a UV-curable epoxy resin (DELO KATIOBOND LP655) and a cover glass on top.

A calibrated characterization set-up comprising an integrating sphere (Lab sphere), a photonic multichannel analyzer PMA-11 (Hamamatsu) and a source meter 2601A (Keithley) was employed to evaluate current–voltage–luminance characteristics and the EQE of the fabricated OLEDs.

3. Results and discussion

3.1. Synthesis

1,8-Naphthyridine derivatives ***t*Cz-ND** and **Met*Cz-ND** were synthesized in one step from a common precursor, 2,7-dichloro-1,8-naphthyridine **1**, and carbazole derivatives **2–3** possessing *tert*-butyl groups using Pd catalysed amination or nucleophilic aromatic substitution reactions, respectively (Fig. 1). The detailed information about the synthetic procedures and identification of molecular structures is provided in the ESI.† The methyl group-containing carbazole **3** was synthesized in high yield using a Suzuki coupling reaction between the corresponding 1-bromo-3,7-di-*tert*-butyl-9*H*-carbazole and methylboronic acid. The structures of ***t*Cz-ND** and **Met*Cz-ND** were unambiguously confirmed by X-ray analysis (see ESI†). The ND compounds were purified by vacuum sublimation prior to experiments and device fabrication. Thermogravimetry analysis (TGA) of ***t*Cz-ND** and **Met*Cz-ND** revealed high decomposition temperatures of 433 °C and 422 °C, respectively, implying high thermal stability of both compounds and thus suitability for practical applications (see Fig. S2, ESI†).

3.2. DFT calculations

To gain insight into the photophysical properties of the synthesized compounds, their excitation energies, oscillator strengths, D–A dihedral angles and HOMO and LUMO distributions were calculated by using DFT at the B3LYP/6-31G(d) level (see Table S2 in ESI† and Fig. 2).[20] The unmodified ***t*Cz-ND** demonstrated rather weak CT character due to the small dihedral angle (31°) between *t*Cz donor and ND acceptor. As expected, Me substituents in **Met*Cz-ND** imposed larger steric hindrance (dihedral angle 55°) resulting in considerably increased CT strength and thus reduced excitation energy, oscillator strength and ΔE_{ST}. Furthermore, analysis of molecular structures in optimized ground state geometries revealed proximity between the N atoms

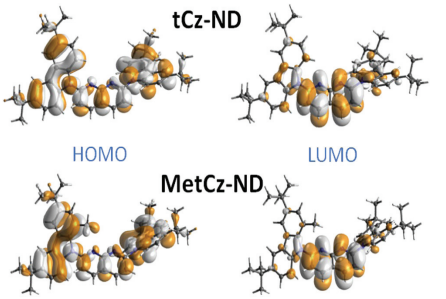

Fig. 2 HOMO and LUMO distributions in 1,8-naphthyridine derivatives calculated by TD-DFT.

of the ND acceptor and the nearest H atoms of neighbouring D groups in both compounds, similarly to previously reported di(pyridinyl)methanone-based TADF emitters.[12] C–H···N distances of 2.39 Å and 2.42 Å for ***t*Cz-ND** and **Met*Cz-ND**, respectively, were determined, suggesting an involvement of intramolecular H-bonding interactions expected to increase the rigidity of the investigated compounds and thus impact their photophysical properties.

3.3. Photophysical properties

Absorption spectra of the investigated ND derivatives in toluene solutions were found to be in good agreement with the DFT calculation results (see Fig. 3), *i.e.* ***t*Cz-ND** expressed intense

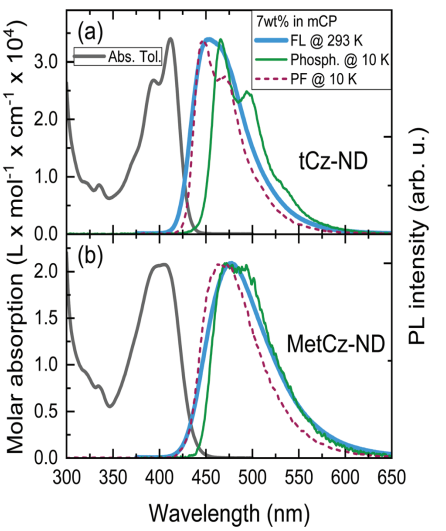

Fig. 3 Absorption (in toluene), fluorescence and phosphorescence spectra (in mCP, and an oxygen-free environment) of ***t*Cz-ND** (a) and **Met*Cz-ND** (b) at room temperature and 10 K. Prompt FL spectra at 10 K are also shown.

This journal is © The Royal Society of Chemistry 2020

Published on 11 May 2020. Downloaded on 9/6/2020 10:35:59 AM.

absorption with well-resolved vibronic structure, indicating weak CT character and a less-twisted molecular geometry, whereas **Met*t*Cz-ND** exhibited a less structured spectrum with 1.5-fold reduced oscillator strength likely due to enhanced CT and electron-vibronic coupling. Similarly, the FL spectrum of **Met*t*Cz-ND** in toluene was structureless and redshifted with respect to that of ***t*Cz-ND,** signifying enhanced CT character (Fig. S3, ESI†). This was additionally verified by estimating the spectral responses of ND compounds with increasing solvent polarity (Fig. S4, ESI†). The change of the polarity from non-polar (cyclohexane) to highly polar (acetonitrile) resulted in a strong red shift and broadening of the FL spectra, which were obviously more pronounced for **Met*t*Cz-ND** than for ***t*Cz-ND**. The photophysical properties of ND compounds are summarized in Table S3 (ESI†).

All the studied compounds demonstrated oxygen-sensitive FL in solutions with distinct prompt (PF) and delayed (DF) FL components, signifying the presence of TADF (Fig. 4). Moderately high FL quantum yield (Φ_{FL}) values of 0.53 and 0.64 obtained for ***t*Cz-ND** and **Met*t*Cz-ND**, respectively, in solutions were increased up to 0.76 and 0.86, respectively, by dispersing ND derivatives in a rigid mCP host at 7 wt% concentration. This concentration was found to be optimal for the devices delivering maximal EQE. The ND-doped mCP film processing method, *i.e.* vacuum or solution process, was found to have no impact on the Φ_{FL} values. The improved Φ_{FL} values of the compounds in mCP were accompanied by notably enhanced contributions of the DF components (Table 1 and Table S3, ESI†), implying reduced non-radiative decay from the triplet states most likely due to suppressed vibronic coupling to the ground state.[21] The vibronically-modulated prompt FL and phosphorescence spectra of ***t*Cz-ND** in mCP obtained at 10 K again confirmed the origin of the emissive states to be of a more localized (and less CT) nature. Conversely, the analogous spectra of **Met*t*Cz-ND** with redshifted structureless emission clearly indicated the CT-like origin of the states (Fig. 3).

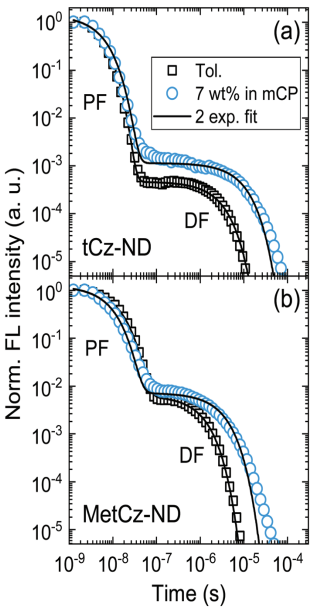

Fig. 4 FL decay transients of ***t*Cz-ND** (a) and **Met*t*Cz-ND** (b) in toluene (squares) and the mCP host at 7 wt% doping concentration (circles) in an oxygen-free environment. Solid lines represent double exponential fits. PF and DF components are indicated.

DF and PF lifetimes (τ_{DF} and τ_{PF}) in different media were obtained by fitting the transients with double exponential decay profiles (Fig. 4). Slight deviation of the experimental DF points from the fits in the mCP host at the latest times could arise due to the small conformational disorder of the molecular geometry in the solid film.[5] The determined lifetimes along with Φ_{FL} and DF/PF ratios were further used to calculate the rISC rate (k_{rISC}) according to the previously described procedures assuming that non-radiative decay occurs mainly from the triplet states (as discussed above).[21] The revealed k_{rISC} was found to be 3-fold larger for **Met*t*Cz-ND** (1.06×10^6 s^{-1} in mCP) as compared to that of the unmodified ***t*Cz-ND** (0.34×10^6 s^{-1} in mCP), which could be a result of the enhanced coupling between S_1 and T_1 due to the small ΔE_{ST} (0.09 eV) and stronger vibronic coupling because of the more labile molecular structure. On the other hand, less structurally twisted ***t*Cz-ND** showed the highest radiative decay rate ($k_r = 4.4 \times 10^7$), which, accompanied with a deep blue (λ_{max} = 452 nm) and narrow (FWHM = 66 nm) FL spectrum, makes ***t*Cz-ND** an excellent candidate for pure blue emitting TADF-OLEDs.

3.4. OLED performance

To evaluate the potential of naphthyridine compounds as blue TADF emitters for OLED applications, their electroluminescence (EL) properties were studied. The two ND compounds were compared in the same device architecture, where they were employed as dopants in the ND:mCP emissive layer at the same optimal doping concentration (7 wt%), identical to that used for FL studies (Fig. 3 and 4). Under such conditions, the obtained device characteristics including efficiency roll-off could be directly linked to the molecular properties of the ND compounds.

Table 1 Photophysical properties of the investigated naphthyridine-doped mCP films (7 wt%) prepared by the solution-process

Compd.	λ_{max} (nm)	Φ_{FL}	Φ_{DF}/Φ_{PF} [a]	τ_{PF} (ns)	τ_{DF} (μs)	k_r (10^7 s^{-1})	k_{ISC} (10^7 s^{-1})	k_{rISC} (10^6 s^{-1})	ΔE_{ST} [b] (eV)	HOMO/LUMO [c] (eV)
***t*Cz-ND**	452	0.76	0.53/0.23	5.2	8.8	4.4	14.8	0.34	0.18	5.6/2.7
Met*t*Cz-ND	478	0.86	0.61/0.25	8.3	3.1	3.0	9.0	1.06	0.09	5.6/2.7

[a] Estimated from the FL transient measurements. [b] ΔE_{ST} estimated from the onsets of FL (@293 K) and phosphorescence (@10 K) spectra. [c] HOMO obtained from ionization potential measured by photoelectron emission spectrometry; LUMO = HOMO − E_g.

Published on 11 May 2020. Downloaded on 9/6/2020 10:35:59 AM.

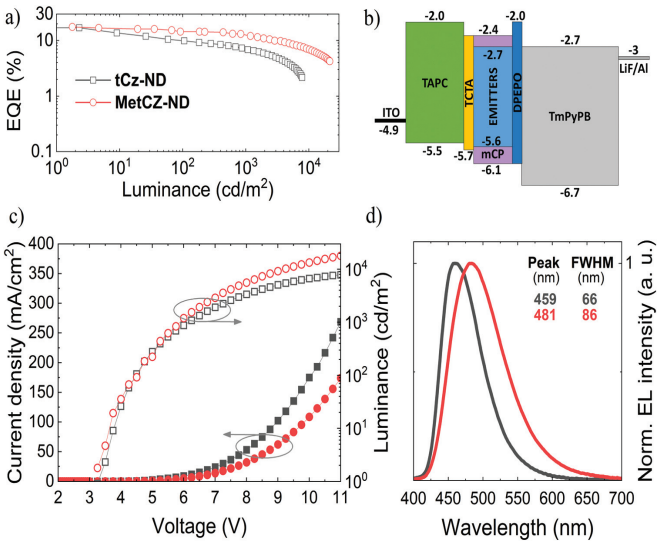

Fig. 5 Characteristics of vacuum-processed OLEDs based on the naphthyridine TADF emitters (7 wt% in mCP): (a) EQE *vs.* luminance, (b) energy level diagram, (c) current density and luminance *vs.* applied voltage, and (d) normalized electroluminescence spectra.

Table 2 Main parameters of vacuum- and solution-processed OLEDs based on the ND(7 wt%):mCP emissive layer

Tech.	Emitter	V_{on}[a] (V)	EQE[b] (%)	L_{max} (cd m^{-2})	CE_{max} (cd A^{-1})	LE_{max} (lm W^{-1})	λ_{max} (nm)	FWHM (nm)	CIE 1931 (x, y)
Vac.	***t*Cz-ND**	3.25	17.0/9.9/7.0	8424	22.17	19.88	459	66	(0.14, 0.16)
	Met*t*Cz-ND	3.25	17.6/14.4/12.5	21 459	31.98	23.60	481	88	(0.18, 0.32)
Sol.	***t*Cz-ND**	4.30	13.5/12.1/7.8	6840	17.26	10.24	452	66	(0.15, 0.14)
	Met*t*Cz-ND	3.40	11.7/7.5/11.0	23 028	23.84	11.76	479	80	(0.16, 0.29)

[a] Turn-on voltage at 1 cd m^{-2}. [b] Maximum EQE/EQE at 100 cd m^{-2}/EQE at 1000 cd m^{-2}.

The main characteristics of the vacuum-processed OLEDs are provided in Fig. 5, meanwhile the key parameters are summarized in Table 2. Vacuum-processed devices were fabricated using the following layer configuration: ITO(100 nm)/TAPC(30 nm)/TCTA(5 nm)/emitter(7 wt%): mCP(20 nm)/DPEPO(5 nm)/TmPyPB(50 nm)/LiF(0.8 nm)/Al(100 nm), where the emitter was either ***t*Cz-ND** or **Met*t*Cz-ND**. An energy level diagram of the devices is displayed in Fig. 5b. 4,4′-Cyclohexylidenebis[*N*,*N*-bis(4-methylphenyl)benzenamine] (TAPC) and 4,4′,4″-tris(carbazol-9-yl)triphenylamine (TCTA) acted as hole injection and transport layers, respectively, whereas LiF and TmPyPB were employed for electron injection and transport, respectively. A thin 5 nm layer of DPEPO possessing a large HOMO–LUMO gap and a high triplet energy (3.0 eV) was used to confine excitons within the emissive layer.

OLEDs based on ***t*Cz-ND** demonstrated a low turn-on voltage (V_{on}) of 3.25 V, EL peak at 459 nm and FWHM of 66 nm rendering deep-blue narrow-band emission with Commission Internationale de L'Eclairage (CIE) coordinates of (0.14, 0.16). With these parameters, our device surpassed the recently reported vacuum-processed OLED device based on the same naphthyridine compound.[16] Specifically, λ_{max} and FWHM of the current device were 10 nm smaller as compared to those of the previously reported device. This was mainly attributed to the proper device optimization carried out at 3 times lower emitter concentration (7 wt%) in the less polar mCP host (*versus* strongly polar DPEPO host). Moreover, as will be shown below, the ***t*Cz-ND** emitter was also confirmed to be suitable for fabrication of solution-processed deep-blue TADF OLEDs. The maximum EQE of ***t*Cz-ND**-based devices was 17% at low brightness and low current density (Fig. 5a). At the practically useful brightness of 100 cd m^{-2}, EQE decreased down to 9.9% with a further roll-off to 7% at 1000 cd m^{-2}. Maximum brightness achieved in this device was 8424 cd m^{-2}. A further increase of applied bias caused degradation of the device performance, most probably because of the exciton annihilation processes and loss of the current balance.

Although the **Met*t*Cz-ND**-based vacuum-processed OLEDs demonstrated similar turn-on characteristics with V_{on} = 3.25 V, EL of the devices was considerably redshifted with the EL peak at

 This journal is © The Royal Society of Chemistry 2020

Published on 11 May 2020. Downloaded on 9/6/2020 10:35:59 AM.

481 nm well matching the FL spectrum of the compound doped into mCP (Fig. 3). Additionally, the stronger CT character of **Met*t*Cz-ND** (as compared to that of ***t*Cz-ND**) also implied much broader EL emission of the device (FWHM = 86 nm) typical of conventional TADF emitters. The CIE coordinates of this device (0.18, 0.32) corresponded to sky-blue emission. Similar to ***t*Cz-ND** based OLEDs, the **Met*t*Cz-ND** based devices exhibited roughly the same maximum EQE of 17.6% at low brightness. However, in contrast to ***t*Cz-ND**, the latter demonstrated reduced efficiency roll-off. Explicitly, EQE was reduced only down to 14.4% and 12.5% at the brightness of 100 cd m^{-2} and 1000 cd m^{-2}, respectively. The device brightness maxed out at 21 459 cd m^{-2} still maintaining EQE above 4%.

The more rapid efficiency roll-off in the OLED based on ***t*Cz-ND** can be justified by the 3-fold longer τ_{DF} (8.8 μs) measured for this emitter as compared to that for **Met*t*Cz-ND**. Long triplet lifetimes are undesirable, since they increase the probability of triplet interaction causing detrimental annihilation effects. On the other hand, the fast rISC and short τ_{DF} (3.1 μs) of **Met*t*Cz-ND** significantly lowered the triplet population by rapid up-conversion to the singlet manifold resulting in only 29% loss of device efficiency at the brightness of 1000 cd m^{-2}. For comparison, the device based on ***t*Cz-ND** lost 60% of its initial efficiency at a similar brightness. It is worth noting that the maximum EQE values of ND-based OLEDs are in good agreement with the Φ_{FL} values obtained for the ND-doped mCP films, if ~20% light outcoupling efficiency of the devices (the case of random emitter orientation) is taken into account, *i.e.* EQE = 0.2 × Φ_{FL}.[22] This highlights the light outcoupling as the prime efficiency loss suggesting that the OLED structure is optimized at least for the low brightness regime. Compared to the performance of currently state-of-the-art narrow-band deep-blue (<460 nm) OLEDs based on conventional D–A-type TADF emitters, these ND-based (particularly ***t*Cz-ND**-based) OLEDs are among the best devices in terms of the EQE and efficiency roll-off properties (see Table S5 in the ESI†).[8,12,23–28] The results imply that sterically controlled CT interactions combined with H-bonding can indeed be promising in attaining narrow deep-blue TADF by employing ND acceptors.

Furthermore, both ND emitters were also tested in analogous solution-processed OLEDs in which TAPC and TCTA layers were replaced by solution-processable PEDOT:PSS and PVK (Fig. S5 in ESI† and Table 2). The performance of these OLEDs was found to be similar to that of the vacuum-processed devices at high current densities regardless of the inferior performance observed at low currents. The worsened performance in terms of the increased V_{on} and the reduced EQE can be attributed to the reduced homogeneity of the solution processed layers as compared to the vacuum evaporated ones and rather poor hole injection through PVK causing unbalanced electron and hole currents. Evidently, increasing the current density raises the EQE of the solution processed OLEDs almost up to the point of the vacuum-processed devices indicating that the injection regime close to optimal is achieved. Similar to the vacuum-evaporated OLEDs, the solution-processed devices based on ***t*Cz-ND** exhibited deep-blue (λ_{max} = 452 nm) and narrow-band (FWHM = 66 nm) emission with an EQE of up to 13.5%, which could be of potential interest to display manufacturers.[29] Although **Met*t*Cz-ND** showed a higher Φ_{FL} (86%) as compared to that of ***t*Cz-ND** (76%), the solution-processed device based on **Met*t*Cz-ND** exhibited a slightly lower maximum EQE (11.7%) than that of the ***t*Cz-ND**-based device. This can be explained by the different EQE *vs.* luminance dependences observed for the two studied compounds (see Fig. S5a, ESI†), which suggest that the current imbalance is more pronounced for the **Met*t*Cz-ND**-based device causing a delayed rise in EQE and thus slightly reduced maximum EQE. Summing up, the demonstrated performance shows the suitability of the investigated naphthyridines to be employed also as solution-processable deep-blue TADF emitters.

4. Conclusion

In conclusion, relying on H-bonding and sterically controlled CT interactions, blue/deep-blue TADF emitters based on D–A-type carbazole–naphthyridine compounds have been developed. The ND compounds were found to express a small singlet–triplet energy gap (down to 0.09 eV), high fluorescence quantum yield (up to 0.86) and rather short delayed fluorescence lifetimes (down to 3.1 μs) resulting in a high rISC rate (up to 10^6 s^{-1}) when dispersed in the mCP host. The TADF properties and emission wavelength and band-width of the ND derivatives were mainly governed by the CT strength of the D–A interaction, which could be controlled *via* methyl substituents introduced at the first linking position of *t*-butyl-carbazole donors. The less sterically hindered compound ***t*Cz-ND** exhibited more narrow and shorter wavelength blue TADF as compared to that of the more twisted methyl-substituted compound **Met*t*Cz-ND,** implying a trade-off between the reduced rISC and improved emissive properties (λ_{max} and FWHM). Importantly, the ND compounds were demonstrated to be suitable as TADF emitters for realization of vacuum- and solution-processed TADF OLEDs with low efficiency roll-off in sky-blue (CIE_{xy}: 0.18, 0.32) and deep-blue (CIE_{xy}: 0.14, 0.16) spectral ranges. The optimized devices with 7 wt% ND emitter in the weakly polar mCP host delivered up to ~17.6% and ~13.5% EQEs for the vacuum- and solution-processed OLEDs, respectively. The OLEDs based on unsubstituted ***t*Cz-ND** exhibited deep-blue (λ_{max} < 460 nm) and narrow-band (FWHM = 66 nm) electroluminescence, whereas those based on more twisted methyl-substituted **Met*t*Cz-ND** expressed broader band (FWHM > 80 nm) and sky-blue (λ_{max} ≈ 480 nm) emission. The demonstrated ND-based TADF OLEDs are among the best blue/deep-blue-emitting devices in terms of EQE and efficiency roll-off properties. This highlights the potential of carbazole–naphthyridine-derived materials to become the basis in future engineering of deep-blue TADF emitters.

Conflicts of interest

The authors declare no conflict of interests.

Published on 11 May 2020. Downloaded on 9/6/2020 10:35:59 AM.

Acknowledgements

The research was funded by the European Social Fund (project No 09.3.3-LMT-K-712-01-0084) under grant agreement with the Research Council of Lithuania (LMTLT). E. Kamarauskas is acknowledged for ionization potential measurements.

References

1 Y. Im, M. Kim, Y. J. Cho, J. A. Seo, K. S. Yook and J. Y. Lee, *Chem. Mater.*, 2017, **29**, 1946–1963.
2 F. B. Dias, T. J. Penfold and A. P. Monkman, *Methods Appl. Fluoresc.*, 2017, **5**, 012001.
3 H. Uoyama, K. Goushi, K. Shizu, H. Nomura and C. Adachi, *Nature*, 2012, **492**, 234–238.
4 Z. Yang, Z. Mao, Z. Xie, Y. Zhang, S. Liu, J. Zhao, J. Xu, Z. Chi and M. P. Aldred, *Chem. Soc. Rev.*, 2017, **46**, 915–1016.
5 T. Serevičius, R. Skaisgiris, J. Dodonova, K. Kazlauskas, S. Juršėnas and S. Tumkevičius, *Phys. Chem. Chem. Phys.*, 2019, **22**, 265–272.
6 T. J. Penfold, F. B. Dias and A. P. Monkman, *Chem. Commun.*, 2018, **54**, 3926–3935.
7 Y. Liu, C. Li, Z. Ren, S. Yan and M. R. Bryce, *Nat. Rev. Mater.*, 2018, **3**, 18020.
8 L.-S. Cui, H. Nomura, Y. Geng, J. U. Kim, H. Nakanotani and C. Adachi, *Angew. Chem., Int. Ed.*, 2017, **56**, 1571–1575.
9 Y. J. Cho, S. K. Jeon, S. S. Lee, E. Yu and J. Y. Lee, *Chem. Mater.*, 2016, **28**, 5400–5405.
10 T. Hatakeyama, K. Shiren, K. Nakajima, S. Nomura, S. Nakatsuka, K. Kinoshita, J. Ni, Y. Ono and T. Ikuta, *Adv. Mater.*, 2016, **28**, 2777–2781.
11 P. Pander, A. Swist, R. Motyka, J. Soloducho, F. B. Dias and P. Data, *J. Mater. Chem. C*, 2018, **6**, 5434–5443.
12 P. Rajamalli, N. Senthilkumar, P.-Y. Huang, C.-C. Ren-Wu, H.-W. Lin and C.-H. Cheng, *J. Am. Chem. Soc.*, 2017, **139**, 10948–10951.
13 X. Zhou, H. Yang, Z. Chen, S. Gong, Z. H. Lu and C. Yang, *J. Mater. Chem. C*, 2019, **7**, 6607–6615.
14 Y. Lee, S. J. Woo, J. J. Kim and J. I. Hong, *Org. Electron.*, 2020, **78**, 105600.
15 C. Chen, H. Y. Lu, Y. F. Wang, M. Li, Y. F. Shen and C. F. Chen, *J. Mater. Chem. C*, 2019, **7**, 4673–4680.
16 Y.-F. Shen, W.-L. Zhao, H.-Y. Lu, Y.-F. Wang, D.-W. Zhang, M. Li and C.-F. Chen, *Dyes Pigm.*, 2020, **178**, 108324.
17 M. Budzynski, T. Baumann and D. Ambrosek, in *Organic Light Emitting Materials and Devices XXII*, ed. F. So, C. Adachi and J.-J. Kim, SPIE, 2018, vol. 10736, p. 51.
18 M. J. Adams, J. G. Highfield and G. F. Kirkbright, *Anal. Chem.*, 1977, **49**, 1850–1852.
19 E. Miyamoto, Y. Yamaguchi and M. Yokoyama, *Electrophotography*, 1989, **28**, 364–370.
20 M. J. Frisch, G. W. Trucks, H. B. Schlegel, G. E. Scuseria, M. A. Robb, J. R. Cheeseman, G. Scalmani, V. Barone, G. A. Petersson, H. Nakatsuji, X. Li, M. Caricato, A. Marenich, J. Bloino, B. G. Janesko, R. Gomperts, B. Mennucci, H. P. Hratchian, J. V. Ortiz, A. F. Izmaylov, J. L. Sonnenberg, D. Williams-Young, F. Ding, F. Lipparini, F. Egidi, J. Goings, B. Peng, A. Petrone, T. Henderson, D. Ranasinghe, V. G. Zakrzewski, J. Gao, N. Rega, G. Zheng, W. Liang, M. Hada, M. Ehara, K. Toyota, R. Fukuda, J. Hasegawa, M. Ishida, T. Nakajima, Y. Honda, O. Kitao, H. Nakai, T. Vreven, K. Throssell, J. J. A. Montgomery, J. E. Peralta, F. Ogliaro, M. Bearpark, J. J. Heyd, E. Brothers, K. N. Kudin, V. N. Staroverov, T. Keith, R. Kobayashi, J. Normand, K. Raghavachari, A. Rendell, J. C. Burant, S. S. Iyengar, J. Tomasi, M. Cossi, J. M. Millam, M. Klene, C. Adamo, R. Cammi, J. W. Ochterski, R. L. Martin, K. Morokuma, O. Farkas, J. B. Foresman and D. J. Fox, *Gaussian 09, Revision D.01*, Gaussian, Inc., Wallingford CT, 2013.
21 G. Kreiza, D. Banevičius, J. Jovaišaitė, K. Maleckaitė, D. Gudeika, D. Volyniuk, J. V. Gražulevičius, S. Juršėnas and K. Kazlauskas, *J. Mater. Chem. C*, 2019, **7**, 11522–11531.
22 N. C. Greenham, R. H. Friend and D. D. C. Bradley, *Adv. Mater.*, 1994, **6**, 491–494.
23 T. Serevičius, R. Skaisgiris, I. Fiodorova, V. Steckis, J. Dodonova, D. Banevičius, K. Kazlauskas, S. Juršėnas and S. Tumkevičius, *Org. Electron.*, 2020, 105723.
24 P. Rajamalli, D. Chen, W. Li, I. D. W. Samuel, D. B. Cordes, A. M. Z. Slawin and E. Zysman-Colman, *J. Mater. Chem. C*, 2019, **7**, 6664–6671.
25 Y. Im, S. H. Han and J. Y. Lee, *J. Mater. Chem. C*, 2018, **6**, 5012–5017.
26 M. Kim, S. K. Jeon, S.-H. Hwang and J. Y. Lee, *Adv. Mater.*, 2016, **28**, 603.
27 C. Chan, L. Cui, J. U. Kim, H. Nakanotani and C. Adachi, *Adv. Funct. Mater.*, 2018, **28**, 1706023.
28 D. H. Ahn, S. W. Kim, H. Lee, I. J. Ko, D. Karthik, J. Y. Lee and J. H. Kwon, *Nat. Photonics*, 2019, **13**, 540–546.
29 J. H. Lee, C. H. Chen, P. H. Lee, H. Y. Lin, M. K. Leung, T. L. Chiu and C. F. Lin, *J. Mater. Chem. C*, 2019, **7**, 5874–5888.

 This journal is © The Royal Society of Chemistry 2020

Paper V

Diboraanthracene-Doped Polymer Systems for Colour-Tuneable Room-Temperature Organic Afterglow

J. Jovaišaitė, S. Kirschner, S. Raišys, G. Kreiza, P. Baronas, S. Juršėnas and M. Wagner

Angew. Chem. Int. Ed., **62**, e202215071 (2023)

DOI: 10.1002/anie.202215071

https://doi.org/10.1002/anie.202215071

Check for updates

How to cite: *Angew. Chem. Int. Ed.* **2023**, *62*, e202215071
International Edition: doi.org/10.1002/anie.202215071
German Edition: doi.org/10.1002/ange.202215071

Luminescence

Diboraanthracene-Doped Polymer Systems for Colour-Tuneable Room-Temperature Organic Afterglow

Justina Jovaišaitė, Sven Kirschner, Steponas Raišys, Gediminas Kreiza, Paulius Baronas, Saulius Juršėnas, and Matthias Wagner**

Abstract: Organic ultralong room temperature phosphorescence (RTP), or organic afterglow, is a unique phenomenon, gaining widespread attention due to its far-reaching application potential and fundamental interest. Here, two laterally expanded 9,10-dimesityl-dihydro-9,10-diboraanthracene (DBA) derivatives are demonstrated as excellent afterglow materials for red and blue-green light emission, which is traced back to persistent thermally activated delayed fluorescence and RTP. The lateral substitution of polycyclic DBA scaffold, together with weak transversal electron-donating mesityl groups, ensures the optimal molecular properties for (reverse) intersystem crossing and long-lived triplet states in a rigid poly(methyl methacrylate) matrix. The achieved afterglow emission quantum yields of up to 3 % and 15 %, afterglow lifetimes up to 0.8 s and 3.2 s and afterglow durations up to 5 s and 25 s (for red and blue-green emitters, respectively) are attributed to the properties of single molecules.

Introduction

Organic ultralong room temperature phosphorescence (RTP), often referred to as organic afterglow, is an exceptional phenomenon which exhibits a long emission lifetime, exceeding 100 ms.[1] Recently, it has attracted extensive scientific interest due to its promising widespread applications in multidisciplinary fields, such as data encryption,[2,3] anti-counterfeiting,[4] bioimaging,[5,6] and sensing.[6] Most of the aforementioned application fields require phosphorescence to be long-lasting and efficient, which are in principle conflicting design goals. This is because the increase of phosphorescence radiative rate enhances its quantum efficiency, thereby reducing its lifetime.[7] Thus, not only practical but also fundamental interest motivates the research efforts in this field. The strategies employed in order to achieve long (> 100 ms) and efficient (> 5 %) pure organic afterglow systems rely on the fulfilment of two main conditions: (i) promotion of the intersystem crossing (ISC) from S_1 to T_n for the efficient triplet generation; and (ii) suppression of the radiative and non-radiative decay of triplet state ($T_1 \rightarrow S_0$) to prolong its lifetime.[8] The first condition requires the small energy gap and sufficient spin-orbit coupling between S_1 and T_n states of different character,[9–11] while the second one implicates the locally excited (LE) character of T_1 and highly rigid environment, protected from oxygen and moisture.[8]

Thus far, many reported room temperature (RT) afterglow systems have been based on aggregation-induced emission,[12] including crystal engineering,[13,14] H-aggregation,[15] π-π stacking,[16] host-guest interaction[17] or even supramolecular assembly,[18] all of which facilitate the stabilization of triplet states and reduce the non-radiative quenching. However, the practical implementation of aggregated molecular states, especially crystals, may be hindered due to their brittleness and limited processability. Furthermore, the crystallization of the molecules greatly enhances triplet exciton migration, which may lead to capture at impurity or defect-related traps, causing the quenching of excited states. Thus, the focus has shifted towards polymer-based amorphous organic systems due to their appeal with regard to practical applications.[19,20] The most attractive approach in terms of fabrication is a simple physical blending of polymer and guest molecules, such that the appearance of noncovalent bonds would ensure a rigid environment for both reduced excitonic and vibrational quenching of triplet excitons, without affecting the excited states of molecules.[19,21] In this case, the chromophore itself must demonstrate the combination of long and efficient RTP; therefore, the same contradiction of long and efficient phosphorescence needs to be addressed.

In this work, we present two 9,10-dimesityl-9,10-diboraanthracene (DBA) compounds as a new class of organic RT emission afterglow materials. The mesityl groups not only render the materials air-and moisture-stable,[22,23] but

[*] J. Jovaišaitė, S. Raišys, G. Kreiza, P. Baronas, S. Juršėnas
Institute of Photonics and Nanotechnology, Vilnius University
Saulėtekis av. 3, 10257 Vilnius (Lithuania)
E-mail: justina.jovaisaite@ff.vu.lt

S. Kirschner, M. Wagner
Institut für Anorganische Chemie, Goethe-Universität Frankfurt
Max-von-Laue-Strasse 7, 60438 Frankfurt a. Main (Germany)
E-mail: matthias.wagner@chemie.uni-frankfurt.de

S. Kirschner
EaStCHEM School of Chemistry, The University of Edinburgh
David Brewster Road, Edinburgh EH9 3FJ (UK)

© 2022 The Authors. Angewandte Chemie International Edition published by Wiley-VCH GmbH. This is an open access article under the terms of the Creative Commons Attribution Non-Commercial NoDerivs License, which permits use and distribution in any medium, provided the original work is properly cited, the use is non-commercial and no modifications or adaptations are made.

© 2022 The Authors. Angewandte Chemie International Edition published by Wiley-VCH GmbH

15213773, 2023, 4, Downloaded from https://onlinelibrary.wiley.com/doi/10.1002/anie.202215071 by Vilnius University, Wiley Online Library on [17/01/2023]. See the Terms and Conditions (https://onlinelibrary.wiley.com/terms-and-conditions) on Wiley Online Library for rules of use; OA articles are governed by the applicable Creative Commons License

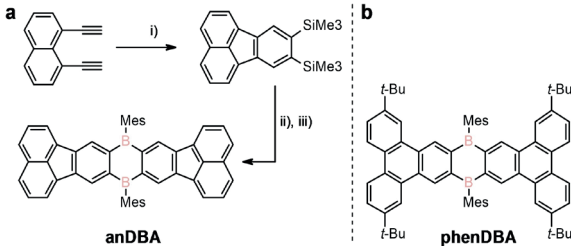

Scheme 1. Synthesis and Lewis structure of anDBA (a) and Lewis structure of phenDBA (b). Reagents and conditions: i) $Me_3SiC{\equiv}CSiMe_3$ (excess), $CpCo(CO)_2$ (10 mol%), reflux temperature, 10 h; ii) BBr_3 (3.5 eq.), 120 °C, 3 d; iii) MesMgBr (in tetrahydrofuran, 2.0 eq.), toluene, 0 °C to room temperature.

also work as weak electron donors to the central molecular systems. The lateral expansion of polycyclic DBA scaffold by acenaphthylene (anDBA) or phenanthrene (phenDBA) (Scheme 1) substructures tunes the singlet and triplet excited state energies, enabling extraordinary afterglow properties. This synthetic approach allows for the creation of a colour-tuneable (red and blue to green), ultralong (lifetimes up to 0.8 s and 3.2 s, afterglow duration up to 5 s and 25 s) and efficient (afterglow quantum efficiencies up to 3% and 15%) bicomponent organic RT afterglow systems by simply embedding compounds into a rigid poly(methyl methacrylate) (PMMA) matrix. Despite the present RTP of these compounds, the afterglow quantum yield is enhanced by an additional thermally activated delayed fluorescence (TADF) component, which is beneficial in terms of applicability since TADF and RTP exhibit the same long lifetime.[24,25] The pronounced TADF impact to afterglow spectra (especially in the case of phenDBA) also allows to tune the afterglow colour by simply changing the temperature. Even though the explicitly long phosphorescence lifetimes of coronene-h_{12} and coronene-d_{12} based systems in PMMA have already been shown by J. L. Kropp et al.,[26] the presented results in the current work are among the best of recently reported amorphous chromophore-polymer systems, based on simple physical blending.[20,24,25,27–30] The ultralong emission properties of these DBA compounds were further employed for a data-writing demonstration.

Results and Discussion

In order to access anDBA, it was necessary to synthesize 8,9-bis(trimethylsilyl)fluoranthene. This goal could be achieved by applying the Vollhardt-cyclization to 1,8-diethynyl naphthalene. Until now, this known compound could only be prepared under harsh Sonogashira conditions[31] or via HBr elimination from 1,8-bis(1,2-dibromoethyl)naphthalene.[32] In the course of our synthetic efforts, it was found that this versatile building block is accessible via Negishi-coupling of $Me_3SiC{\equiv}CZnCl{\cdot}LiCl$ with 1,8-diiodonaphthalene[33] within 2 h at room temperature in virtually quantitative yield. After desilylation, cyclization and Si/B-exchange, anDBA was obtained in 23% yield over five steps. The synthesis of phenDBA has already been published elsewhere.[34]

The UV/Vis spectra of anDBA and phenDBA (Figure 1 and Table S1 in Supporting Information) in *c*-hexane are comprised of absorption bands at ca. 330 nm with relatively high molar extinction coefficient values of $\varepsilon \approx 100000\ M^{-1}cm^{-1}$ for both compounds and structured bands at ca. 400–455 nm of lower intensity ($\varepsilon \approx 40000\ M^{-1}cm^{-1}$). The fluorescence spectra of both compounds also possess vibrationally resolved shapes. For anDBA, the 0 and 1st fluorescence vibronic bands located at 445 nm and 488 nm have a reduced intensity, leaving the 2nd at 520 nm to be the most intense (Figure S4, Supporting Information). According to the evaluated energy difference between bands of anDBA emission spectrum, the peak at 445 nm (2.78 eV) corresponds to a different emitting state than the rest of the observed fluorescence spectrum; however, its contribution to overall emission remains low. In

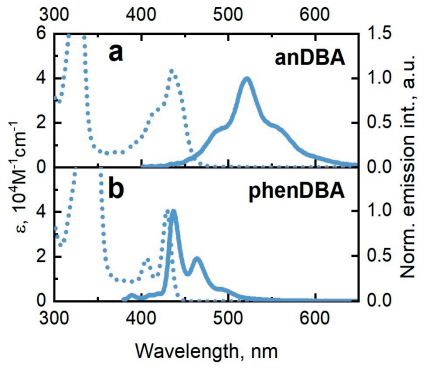

Figure 1. The absorption and fluorescence spectra of anDBA (a) and phenDBA (b) in *c*-hexane at ambient conditions. The concentration of the compounds for fluorescence measurements is 10^{-6} M, the excitation wavelength was set to 330 nm.

© 2022 The Authors. Angewandte Chemie International Edition published by Wiley-VCH GmbH

15213773, 2023, 4, Downloaded from https://onlinelibrary.wiley.com/doi/10.1002/anie.202215071 by Vilnius University, Wiley Online Library on [17/01/2023]. See the Terms and Conditions (https://onlinelibrary.wiley.com/terms-and-conditions) on Wiley Online Library for rules of use; OA articles are governed by the applicable Creative Commons License

15213773, 2023, 4, Downloaded from https://onlinelibrary.wiley.com/doi/10.1002/anie.202215071 by Vilnius University, Wiley Online Library on [17/01/2023]. See the Terms and Conditions (https://onlinelibrary.wiley.com/terms-and-conditions) on Wiley Online Library for rules of use; OA articles are governed by the applicable Creative Commons License

the case of phenDBA, a small Stokes shift and mirror image relationship between absorption and fluorescence spectra is observed. The fluorescence quantum yield (Φ_{FL}) of anDBA ($\Phi_{FL}=20\,\%$) is half as high as that of phenDBA ($\Phi_{FL}=47\,\%$), whereas the fluorescence lifetimes (τ) differ three-fold: 14 ns for anDBA and 5 ns for phenDBA (recorded at peak maximum in air saturated, *c*-hexane, see Table S1 in Supporting Information). The performed absorption and fluorescence spectra measurements in solvents of different polarity show no pronounced solvatochromism, revealing the dominant local excitonic (LE) transition for both compounds (Figure S5, Supporting Information). In addition, the degassing of the solutions resulted in a small increase of photoluminescence intensity (ca. 1.3 folds) (Table S1, Supporting Information), caused by the appearance of the weak delayed fluorescence, emphasizing that phosphorescence in solutions is quenched mainly by vibrational relaxation rather than by the oxygen.

The photophysical properties of anDBA and phenDBA compounds in organic solvents appear to be similar to those observed for other laterally expanded dibora-anthracenes.[34,35] However, the studied DBA compounds incorporated in a rigid polymer (PMMA) matrix disclosed the bicomponent delayed emission from the long-lived excited states. The excited state dynamics in a nanosecond to second timescale was revealed by time-resolved emission experiments. The emission decay profiles of 0.1 wt % PMMA encapsulated films and characteristic emission spectra at different time delays are shown in Figure 2a–d. At an early time scale from 0 to 100 ns the prompt fluorescence, peaking at 525 nm for anDBA and at 445–470 nm for phenDBA, is present, with fluorescence lifetimes ($\tau_{FL}=12.5$ ns for anDBA and $\tau_{FL}=8.5$ ns for phenDBA) similar to those observed in solutions. Excitingly, from 1 µs to several seconds, the delayed emission is observed with remarkably long mono-exponential ($\tau_A=0.42$ s) and bi-exponential ($\tau_{A1}=0.17$ s and $\tau_{A2}=0.93$ s) decays for anDBA and phenDBA, respectively, which is referred to as emission afterglow.

The afterglow emission spectra of both compounds are comprised of two bands each: a higher-energy band (at 525 nm for anDBA and 445–470 nm for phenDBA), which is nearly identical to prompt fluorescence spectrum, and a lower-energy band (at 614 nm for anDBA and 531 nm for phenDBA). The origin of the dual afterglow emission is revealed by time-resolved experiments at 30 K (Figure 2c, 2d and Figure S6, Supporting Information). After a significant time delay of 100 µs, the measured low-temperature delayed emission consists of the low-energy part, which is attributed to phosphorescence of compounds. Since the high-energy band, or in other words delayed fluorescence, is temperature dependent and is severely decreased at 30 K, it could originate via thermally activated delayed fluorescence (TADF) or due to triplet-triplet annihilation (TTA). In the case of TTA, the delayed fluorescence at low triplet exciton concentrations should exhibit a lifetime that is twice as short compared to phosphorescence.[36,37] However, the observed dual afterglow emission of DBA compounds has the same ultralong emission lifetimes (Figure S7, Supporting Information), which consequently eliminates TTA, leaving TADF as the most probable origin of delayed fluorescence.

The afterglow quantum yields (Φ_A) at RT obtained by peak-differentiation-imitating analysis for 0.1 wt % PMMA films are 3 % for the red afterglow of anDBA and 15 % for the blue to green afterglow of phenDBA (Table 1). The afterglow quantum yield is a sum of persistent TADF and RTP components ($\Phi_A=\Phi_{TADF}+\Phi_p$). According to the afterglow spectral composition, persistent TADF only slightly contributes to overall afterglow efficiency in the case of anDBA ($\Phi_{TADF}=0.4\,\%$), while in terms of phenDBA, it significantly promotes Φ_A ($\Phi_{TADF}=12\,\%$). The ultralong lifetimes of persistent TADF indicate a very slow reverse intersystem crossing (RISC), that is confirmed by estimated low RISC rate constants: $k_{RISC}=0.05\ s^{-1}$ for anDBA and $k_{RISC}=1.06\ s^{-1}$ for phenDBA.[38] On the other hand, the estimated ISC rates are considerably high: $k_{ISC}=6.0\times10^7\ s^{-1}$ for anDBA and $k_{ISC}=8.4\times10^7\ s^{-1}$ for phenDBA (see Evaluation of rate constants, Supporting Information). The ISC rates match well the non-radiative fluorescence rates obtained in solvents (Table S1, Supporting Information) and indicate the efficient ISC from the excited singlet to excited

Table 1: Emission quantum yields and lifetimes of anDBA and phenDBA, encapsulated in PMMA matrix at different concentrations, measured at room temperature.

wt % in PMMA	anDBA			phenDBA			
	Φ_{PL},[a] %	Φ_A,[b] %	τ_A,[c] s	Φ_{PL},[a] %	Φ_A,[b] %	τ_{A1},[d] s (%)	τ_{A2},[d] s (%)
0.1*[e]	28	3.1	0.42	44	15.1	0.17 (20)	0.93 (80)
1*[e]	20	2.8	0.42	49	11.7	0.39 (24)	1.19 (76)
0.1	30	3.2	0.59	47	11.8	0.21 (17)	1.33 (83)
1	21	2.6	0.70	50	10.3	0.47 (17)	2.60 (83)
5	10	2.3	0.74	47	10.8	0.98 (37)	2.72 (63)
10	11	2.9[f]	0.76	36	7.9[f]	1.00 (25)	3.19 (75)
20	8	1.9[f]	0.71	36	7.3[f]	0.83 (24)	3.06 (76)
40	5	_[g]	_[g]	29	9.2[f]	0.74 (23)	2.97 (77)

[a] Photoluminescence quantum yield including fluorescence and afterglow. [b] Afterglow quantum yield. [c] Afterglow lifetime. [d] Afterglow lifetime components of bi-exponential fit. Fractional contribution of each component is indicated in the parenthesis. [e] Samples that were not annealed prior to experiments. [f] Afterglow quantum yield errors of higher concentration samples may be increased due to aggregation determined processes. [g] The intensity of emission afterglow was too low to accurately record its efficiency and lifetime.

© 2022 The Authors. Angewandte Chemie International Edition published by Wiley-VCH GmbH

15213773, 2023, 4, Downloaded from https://onlinelibrary.wiley.com/doi/10.1002/anie.202215071 by Vilnius University, Wiley Online Library on [17/01/2023]. See the Terms and Conditions (https://onlinelibrary.wiley.com/terms-and-conditions) on Wiley Online Library for rules of use; OA articles are governed by the applicable Creative Commons License

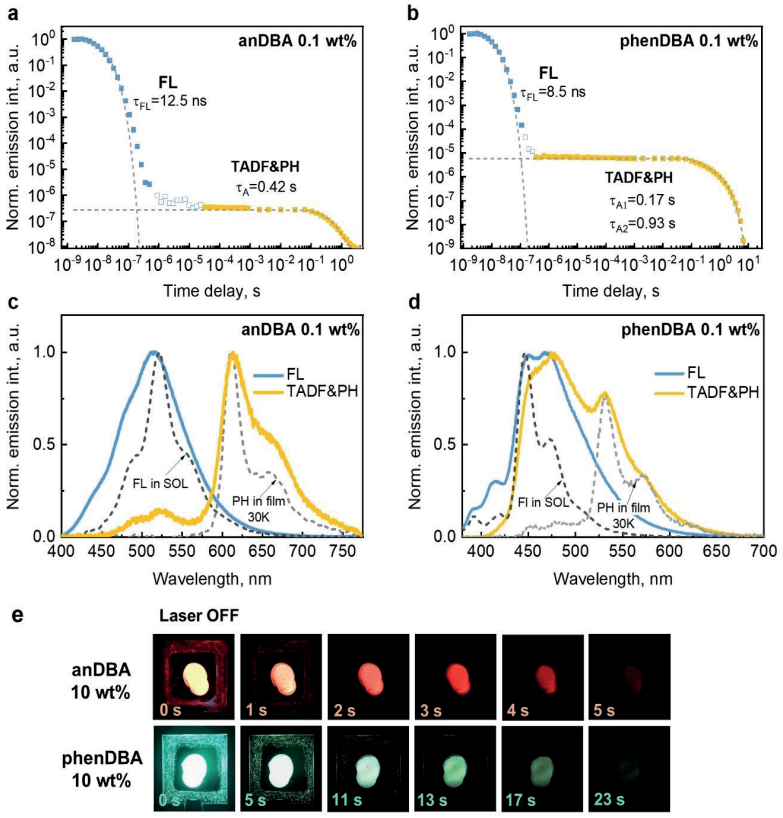

Figure 2. Emission decay transients (a, b) and its characteristic emission spectra (c, d) obtained at different time delays (the FL spectra, blue, at 0–100 ns and TADF&PH spectra, yellow, at 100 μs to few seconds) of anDBA and phenDBA, respectively, in 0.1 wt% encapsulated PMMA films. The excitation wavelength was set to 330 nm. The steady-state fluorescence spectra in *c*-hexane (FL in SOL) and phosphorescence spectra, measured with 100 μs delay and 800 μs optical window of 0.1 wt% PMMA films at 30 K (PH in film 30 K) are also displayed in (c, d) for reference. The photographs of anDBA and phenDBA in 10 wt% encapsulated PMMA films after excitation is turned off (e).

triplet states, which is one of the most important prerequisites for long and efficient afterglow emission.

Thus, despite conflicting in principle, the desired properties of a long and efficient afterglow were demonstrated. Importantly, τ_A can be prolonged even further by annealing the low-concentration PMMA films, since the heat treatment increases rigidity of the PMMA matrix (Table 1). However, the obvious signs of aggregation of the compounds were noted, as PMMA films become opaque once heat-treated. Consequently, we further performed concentration optimization experiments in order to discover the impact of aggregation and the limits of afterglow properties.

Upon increasing the concentration of samples from 0.1 wt% to 40 wt% in PMMA, the small red shift of fluorescence spectra and the redistribution of vibronic band intensity is observed (Figure S8, Supporting Information). The afterglow lifetimes are enhanced up to a certain concentration (10 wt%) and later start to shorten (Table 1, Figure S9, Supporting Information). Most likely, the intermediate to high concentration alters local environment rigidity (compounds act as hardening agents); however, further concentration increase enhances exciton diffusion to non-radiative deactivation sites such as impurities or structural defects. The longest emission afterglow, observed for 10 wt% PMMA samples, reaches up to $\tau_A = 0.76$ s and up to $\tau_{A1} = 1$ s, $\tau_{A2} = 3.19$ s, with considerably long afterglow durations (time until the afterglow is no longer visible to the naked eye) of 5 s and 25 s for anDBA and phenDBA,

© 2022 The Authors. Angewandte Chemie International Edition published by Wiley-VCH GmbH

15213773, 2023, 4, Downloaded from https://onlinelibrary.wiley.com/doi/10.1002/anie.202215071 by Vilnius University, Wiley Online Library on [17/01/2023]. See the Terms and Conditions (https://onlinelibrary.wiley.com/terms-and-conditions) on Wiley Online Library for rules of use; OA articles are governed by the applicable Creative Commons License

respectively (Table 1, Figure 2e and Movie S1). It has already been shown elsewhere that the morphology of samples may be critical to obtain long and efficient RTP (or afterglow).[39] However, it is debatable whether the emission afterglow in the current work is related to H-aggregation (or π-π stacking) as a typical mechanism of ultralong RTP.[12–16] Even though the increase of afterglow lifetimes was observed in films containing a higher concentration of the dopant, the absence of phosphorescence spectral shift in 10 wt % PMMA films, compared to 0.1 wt % (Figure S10, Supporting Information), rules out the possible stabilization of triplet states upon molecular aggregation. It is important to note that the slow evaporation of solvent due to selected preparation method (drop-casting) may cause the aggregation of chromophores, especially considering the large π-conjugated structures of studied compounds. Thus, the control measurements were repeated on the spin-coated thin film samples of 0.1 wt % in PMMA (see Figure S11, Supporting Information) in order to presumably avoid aggregation and to check the appearance of afterglow emission. Indeed, the obtained afterglow lifetimes (τ_A = 0.45 s for anDBA and τ_{A1} = 0.16 s, τ_{A2} = 1.35 s for phenDBA) are similar to those of drop-casted 0.1 wt % PMMA films. These results suggest that the ultralong afterglow arises due to properties of single molecules, in contrast to, for example, charge-separation based afterglow systems, where exciplexes need to be formed between a host and guest molecules in order to realize long afterglow durations, that may last up to hours.[40]

To comprehend the role of the excited state energy levels arrangement and other structure-related properties on bi-component emission afterglow of studied DBA compounds, the theoretical evaluation was further performed. The ground state and the selected excited state (S_1, S_2, S_3 and T_1) geometries as well as transition energies were calculated by using Tamm-Dancoff approximation (TDA)[41] to TD-DFT at the theory level of CAMB3LYP/6-31G(d), implemented in ORCA 5.0.3 software,[42,43] including linear response polarized continuum model (LR-PCM, solvent-toluene). Although the range-separated functionals tend to overestimate LE state energies, it was employed as a qualitative tool to evaluate the energetical arrangement and thus the energetical difference between states, as well as molecular orbital redistribution, especially as the upper triplet (as well as singlet) states appear to be of charge transfer (CT) nature (see below).[35,44] According to the obtained charge distribution in HONTO and LUNTO states (Figure 3 and Figures S13–S14, Supporting Information), acenaphthylene units determine more extended conjugation in the polycyclic scaffold of anDBA if compared to phenDBA, which is laterally expanded by phenanthrene units decorated with *tert*-butyl groups. The extended conjugation itself determines the lower energies of excited states of anDBA and thus, the red shifted fluorescence and phosphorescence spectra. The differences in conjugation

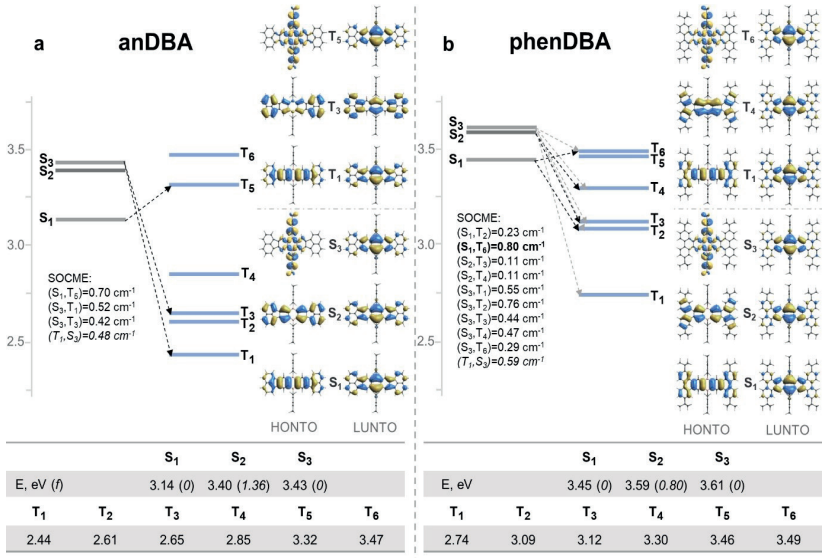

		S1	S2	S3		
E, eV (*f*)		3.14 (*0*)	3.40 (*1.36*)	3.43 (*0*)		
T1	T2	T3	T4	T5	T6	
2.44	2.61	2.65	2.85	3.32	3.47	

		S1	S2	S3		
E, eV		3.45 (*0*)	3.59 (*0.80*)	3.61 (*0*)		
T1	T2	T3	T4	T5	T6	
2.74	3.09	3.12	3.30	3.46	3.49	

Figure 3. The singlet-triplet energy diagram, the corresponding $S_0 \rightarrow S_n$ and $S_0 \rightarrow T_n$ energies in eV, oscillator strengths of $S_0 \rightarrow S_n$ transitions and natural transition orbital (NTO) distribution, obtained for optimized ground state geometries, for anDBA (a) and phenDBA (b). The arrows indicate spin-orbit coupling between states, which was obtained for optimized S_1, S_2 and S_3 and T_1 excited state geometries.

© 2022 The Authors. Angewandte Chemie International Edition published by Wiley-VCH GmbH

length may be defined by electron donoric properties of *tert*-butyl groups, causing a more localized charge distribution on the dibora core in LUNTO states of phenDBA.

The performed calculations revealed a multitude of nearby lying singlet and triplet states (Figure 3, Tables S2 and S4, Supporting Information). The calculated lowest excited singlet states S_1 in a ground state geometry were found to be forbidden "dark" states with oscillator strength (*f*) equal to zero for both compounds, mainly due to the lack of corresponding HONTO-LUNTO wavefunction overlap (see molecular orbital distribution in Figure 3 and in Figures S13–S14, Supporting Information), as was also observed elsewhere for a similar 6,13-dimesityl-6,13-dihydro-6,13-diborapentacene compound.[35] The first "bright" states, also observed as the lowest energy absorption bands in the absorption spectra, with significant oscillator strengths of $f=1.36$ for anDBA and $f=0.80$ for phenDBA are S_2 states, where charge is mainly located on the polycyclic core in the ground state and is redistributed to the dibora core upon excitation. Both S_1 and S_2 possess a LE character. Interestingly, almost degenerate states for locally excited S_2 are the S_3 states of charge transfer nature, where charge from mesityl groups is transferred to the dibora core. The optimization of the excited S_1, S_2 and S_3 geometries revealed that the lowest excited states, after molecular geometry relaxation, remain the forbidden S_1 states. However, in the case of phenDBA, the oscillator strength for S_1-S_0 transition acquires a non-zero oscillator strength value of 0.004. According to Figure 3, there are at least six excited triplet states that lie energetically close or below S_1-S_3 singlet states. The lowest triplet states T_1 are comprised of the same charge distribution in the HONTO and LUNTO states as S_1. Most of the triplet states that lay higher than T_1 also possess LE nature. However, the T_5 and T_6 for anDBA and phenDBA, respectively, are both of CT nature, with similar charge redistribution as for S_3 states.

The efficient emission afterglow and relatively short fluorescence lifetimes discussed in the previous section suggest an efficient intersystem crossing (ISC). The spin-orbit coupling (SOC) between singlet and triplet states were calculated for the optimized S_1, S_2, S_3 and T_1 excited state geometries for the respective $S_n \rightarrow T_n$ and $T_1 \rightarrow S_n$ transitions and are indicated for reference in Figure 3 and given in Tables S3 and S5, Supporting Information. In the case of anDBA, the highest SOC matrix element value (SOCME) was obtained for $S_1 \rightarrow T_5$ transition (SOCME $=0.70\ cm^{-1}$). Alternatively, significant SOCMEs were also obtained for $S_3 \rightarrow T_1$ ($0.52\ cm^{-1}$) or $S_3 \rightarrow T_3$ ($0.42\ cm^{-1}$) transitions, though the energy gap difference would be higher in the latter case. Nevertheless, it is obvious that CT states, whether singlet or triplet, play a crucial role in terms of ISC for anDBA. In the case of phenDBA, the possible multichannel ISC is estimated. The highest spin-orbit coupling is calculated for $S_1 \rightarrow T_6$ transition with SOCME $=0.80\ cm^{-1}$. In addition, the CT S_3 state efficiently couples with almost all triplet states. No spin-orbit coupling between S_1 and T_1 is obtained for either compound, as expected due to the same electronic character. The spin-orbit coupling was only considered for excited states up to S_3, as no significant changes of the excited state dynamics were observed by exciting anDBA or phenDBA samples at 330 nm or at 440 nm.

The immensely long lifetimes of the lowest excited triplet states, the existence of multiple intermediate triplet states and the relatively large SOCME values between S_n and T_n states also explain the presence of TADF, even though the significantly large $\Delta E(S_1\text{-}T_1)$ gaps (>500 meV (anDBA) and 440 meV (phenDBA)) are revealed experimentally from fluorescence and phosphorescence spectra and confirmed theoretically (Figure S6 and Tables S2 and S4, Supporting Information). According to the Arrhenius plots obtained from TADF spectral integral dependence on the reciprocal temperature, the activation energy (E_a) is equal to 160 meV for anDBA, while for phenDBA two E_a values were obtained: 115 meV at low temperatures and 57 meV at higher temperatures (Figure 4a–d). We suggest that the mismatch between $\Delta E(S_1\text{-}T_1)$ and E_a most likely indicates that TADF is enabled through intermediate triplet states, as it is quite frequently observed for other TADF-type emitters.[45–48] Furthermore, in case the activation

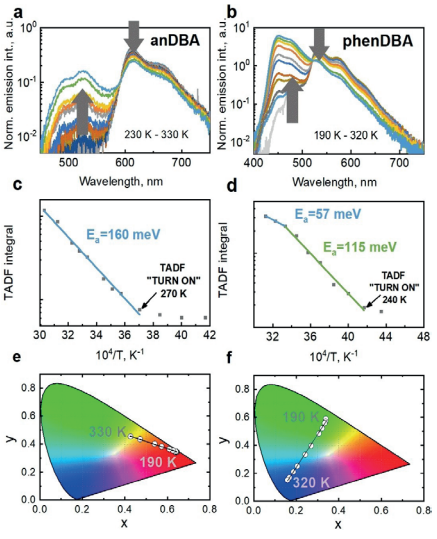

Figure 4. The afterglow spectra of anDBA (a) and phenDBA (b) in 1 wt% PMMA, measured after 100 μs delay and with 800 μs optical window, at different temperatures. The grey arrows in a and b represent the increase or decrease of afterglow intensity upon temperature increase (230–330 K for anDBA and 190–320 K for phenDBA). The respective Arrhenius plots, obtained by plotting TADF spectral integral versus reciprocal temperature, with activation energies, obtained from linear fits (blue and green lines), given in graphs for anDBA (c) and phenDBA (d). Samples of 1 wt% in PMMA were selected in order to facilitate measurement conditions by obtaining higher intensity of afterglow and also to avoid aggregation induced effects. The CIE chromaticity diagrams representing the dependence of afterglow colour on different temperatures for anDBA (e) and phenDBA (f).

© 2022 The Authors. Angewandte Chemie International Edition published by Wiley-VCH GmbH

15213773, 2023, 4, Downloaded from https://onlinelibrary.wiley.com/doi/10.1002/anie.202215071 by Vilnius University, Wiley Online Library on [17/01/2023]. See the Terms and Conditions (https://onlinelibrary.wiley.com/terms-and-conditions) on Wiley Online Library for rules of use; OA articles are governed by the applicable Creative Commons License

15213773, 2023, 4, Downloaded from https://onlinelibrary.wiley.com/doi/10.1002/anie.202215071 by Vilnius University, Wiley Online Library on [17/01/2023]. See the Terms and Conditions (https://onlinelibrary.wiley.com/terms-and-conditions) on Wiley Online Library for rules of use; OA articles are governed by the applicable Creative Commons License

energy reflects the adiabatic $\Delta E(S_1\text{-}T_1)$, the RISC between S_1 and T_1 would be highly restricted due to the same electronic nature of S_1 and T_1 and thus the absent SOC between these two states. The unusual dual activation energy of phenDBA may indicate different RISC channels.

The presence of persistent TADF component in the afterglow spectra and its intensity dependence on temperature results in the possibility to tune afterglow colour for studied compounds. The CIE (x, y) chromaticity coordinates change significantly: from (0.64, 0.34) at 190 K to (0.43, 0.45) at 330 K for anDBA and from (0.34, 0.59) at 190 K to (0.16, 0.15) at 320 K for phenDBA (see Figure 4e and 4f).

The estimated radiative phosphorescence rates $k_p = 0.06\ s^{-1}$ and $k_p = 0.04\ s^{-1}$ ($k_p = \Phi_p/\tau_A$) for anDBA and phenDBA, respectively, in 0.1 wt % PMMA at RT are sufficiently low. However, to observe the ultralong phosphorescence, the negligible non-radiative phosphorescence rates (k_{nr}) are also needed.[1] Indeed, the long-lived T_1 states are defined by the very low k_{nr} values: $k_{nr} = 2.3\ s^{-1}$ for anDBA and $k_{nr} = 1.2\ s^{-1}$ for phenDBA ($k_{nr} = [1\text{-}\Phi_p]/\tau_A$). This may be related to the weak electron-vibronic interaction caused by the localization of the excited states on the dibora core (in the excited T_1 geometry). Interestingly, the phosphorescence rates are significantly reduced (lifetimes prolonged) below TADF "turn-on" temperatures (270 K for anDBA and 240 K for phenDBA) (Figure S12, ESI), indicating that TADF actually acts as the main depopulation channel of the lowest excited triplet states at RT, while simultaneously increasing the afterglow quantum efficiency. The roughly estimated non-radiative phosphorescence rates at low temperatures (230 K, for 1 wt % PMMA films) are extremely small: $k_{nr} \approx 1\ s^{-1}$ for anDBA and $k_{nr} \approx 0.2\ s^{-1}$ for phenDBA. Thus, the rigidity of polymer matrix is sufficient to practically reach the limits of phosphorescence k_{nr}, which is also related to molecular properties, such as low vibronic coupling between the lowest excited triplet and ground states.[49]

Thus, we believe that the nature of such extraordinary triplet non-radiative decay rates deserves a separate study in order to better understand the design principles of single molecules for ultralong and efficient room temperature phosphorescence. In addition, the wide possibilities to adjust DBA structure by changing electron donating fragments or by incorporating different lateral substituents should help to fine-tune the energetical alignment for the desired properties, i.e. turning off TADF for even longer phosphorescence or, contrarily, enhancing long-lived delayed fluorescence for higher afterglow efficiencies.

The properties of the studied compounds were further tested for information recording. First, the transparent films were prepared by coating thin DBA layers of 0.2 wt % in PMMA on a glass and covering them with poly(vinyl alcohol) (PVA) layers that serve as an oxygen barrier. As the procedure is carried out in ambient conditions, only fluorescence is present upon excitation of films. Next, the samples were irradiated by 405 nm laser light (>5 mW power) through a selected mask for a certain time (≈1 min), until the intense phosphorescence was observed in an oxygen saturated environment. The selected information writing method is based on the control of molecular oxygen in chromophore-polymer film, as presented elsewhere.[50] Once excited, DBA compounds generate high triplet exciton concentration, which is quenched by molecular oxygen trapped in a polymer. Upon quenching, the singlet oxygen is generated, which mostly reacts with surrounding polymer and thus the depleted oxygen concentration leads to efficient phosphorescence in the irradiated area. The written information can be further read by changing the irradiation intensity to a low level (alternatively, a CW light source can be used), as only regions that were previously strongly irradiated are glowing. Consequently, two tags of different colours with encrypted information were prepared with visible red and cyan afterglow emission up to 2 s and 8 s, for anDBA and phenDBA, respectively (Figure 5 and Movie S2).

Conclusion

In summary, we have presented two laterally expanded 9,10-dimesityl-9,10-diboraanthracenes (DBA) by acenaphthylene and phenanthrene units with weak electron donating mesityl groups as a new class of purely organic room temperature afterglow materials. The ultralong and efficient emission afterglow is comprised of persistent TADF and RTP, with lifetimes of up to 0.8 s and 3.2 s, afterglow duration up to 5 s and 25 s, and maximum afterglow quantum efficiencies up to 3 % and 15 % for red and blue to green emitters, respectively. The afterglow emission originates from single molecules embedded into rigid polymer (PMMA) matrix, rather than from aggregated molecular states. On the other hand, the emission properties can be tuned upon annealing or increasing the compound concentration. The afterglow mechanism is a combination of i) the multiple available channels for an efficient ISC between excited singlet and triplet states of different nature; ii) the lowest excited LE triplet states (T_1) with very low radiative and non-radiative decay rates; and finally, iii) closely lying triplet and singlet states as well as long-lived population of T_1 that both create the possibility for reverse intersystem crossing, causing the appearance of TADF component through intermediate states. TADF is considered to be the main depopulation channel of the lowest excited triplet states at room temper-

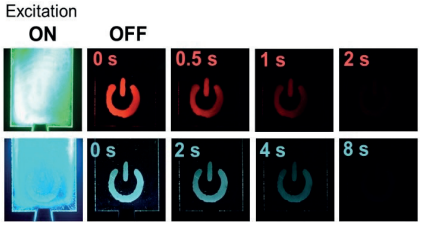

Figure 5. The afterglow images of recorded data on anDBA (top) and phenDBA (bottom) 0.2 wt % PMMA transparent layers.

© 2022 The Authors. Angewandte Chemie International Edition published by Wiley-VCH GmbH

15213773, 2023, 4, Downloaded from https://onlinelibrary.wiley.com/doi/10.1002/anie.202215071 by Vilnius University, Wiley Online Library on [17/01/2023]. See the Terms and Conditions (https://onlinelibrary.wiley.com/terms-and-conditions) on Wiley Online Library for rules of use; OA articles are governed by the applicable Creative Commons License

ature, while it significantly increases the afterglow efficiency. Besides, the presence of persistent TADF allows tuning the afterglow colour, which may be advantageous for temperature sensing. The ultralong-lived emission properties of studied molecules were successfully employed for data writing. The presented DBA compounds demonstrate the superior afterglow properties, especially compared to other amorphous chromophore-polymer systems. Our strategy allows for a wide range of synthetic possibilities to fine-tune the RT afterglow by incorporating stronger electron donors and/or by introducing different lateral substituents.

Acknowledgements

We wish to thank Klara R. Mertinkus, BSc., for synthetic support, Dr. Tomas Serevičius for the insightful discussions at the early stages of this project and Dr. Rokas Skaisgiris for the technical upgrade of equipment for spectroscopic measurements. We also thank Dr. Jan-Michael Mewes for the helpful discussion regarding theoretical calculations. The research was funded by the European Social Fund (Project No. 09.3.3-LMT-K-712-23-0053) under a grant agreement with the Research Council of Lithuania (LMTLT). Open Access funding enabled and organized by Projekt DEAL.

Conflict of Interest

The authors declare no conflict of interest.

Data Availability Statement

The data that support the findings of this study are available from the corresponding author upon reasonable request.

Keywords: Afterglow · Doped Polymer Films · Information Recording · Room Temperature Phosphorescence · Thermally Activated Delayed Fluorescence

[1] S. Xu, R. Chen, C. Zheng, W. Huang, S. Xu, R. Chen, C. Zheng, W. Huang, *Adv. Mater.* **2016**, *28*, 9920–9940.
[2] Y. Su, S. Z. F. Phua, Y. Li, X. Zhou, D. Jana, G. Liu, W. Q. Lim, W. K. Ong, C. Yang, Y. Zhao, *Sci. Adv.* **2018**, *4*, eaas9732.
[3] L. Gu, H. Wu, H. Ma, W. Ye, W. Jia, H. Wang, H. Chen, N. Zhang, D. Wang, C. Qian, Z. An, W. Huang, Y. Zhao, *Nat. Commun.* **2020**, *11*, 944.
[4] Y. Lei, W. Dai, J. Guan, S. Guo, F. Ren, Y. Zhou, J. Shi, B. Tong, Z. Cai, J. Zheng, Y. Dong, *Angew. Chem. Int. Ed.* **2020**, *59*, 16054–16060; *Angew. Chem.* **2020**, *132*, 16188–16194.
[5] F. Xiao, H. Gao, Y. Lei, W. Dai, M. Liu, X. Zheng, Z. Cai, X. Huang, H. Wu, D. Ding, *Nat. Commun.* **2022**, *13*, 186.
[6] X. Li, C. Yin, S. S. Liew, C.-S. Lee, K. Pu, X. Li, C.-S. Lee, C. Yin, S. S. Liew, K. Pu, *Adv. Funct. Mater.* **2021**, *31*, 2106154.
[7] S. Hirata, *Adv. Opt. Mater.* **2017**, *5*, 1700116.
[8] H. Ma, Q. Peng, Z. An, W. Huang, Z. Shuai, *J. Am. Chem. Soc.* **2019**, *141*, 1010–1015.
[9] M. A. El-Sayed, *J. Chem. Phys.* **1963**, *38*, 2834–2838.
[10] J. T. Buck, A. M. Boudreau, A. DeCarmine, R. W. Wilson, J. Hampsey, T. Mani, *Chem* **2019**, *5*, 138–155.
[11] C. M. Marian, *Wiley Interdiscip. Rev.: Comput. Mol. Sci.* **2012**, *2*, 187–203.
[12] W. Zhao, Z. He, B. Z. Tang, *Nat. Rev. Mater.* **2020**, *5*, 869–885.
[13] L. Gu, H. Shi, L. Bian, M. Gu, K. Ling, X. Wang, H. Ma, S. Cai, W. Ning, L. Fu, H. Wang, S. Wang, Y. Gao, W. Yao, F. Huo, Y. Tao, Z. An, X. Liu, W. Huang, *Nat. Photonics* **2019**, *13*, 406–411.
[14] W. Jia, Q. Wang, H. Shi, Z. An, W. Huang, *Chem. Eur. J.* **2020**, *26*, 4437–4448.
[15] Z. An, C. Zheng, Y. Tao, R. Chen, H. Shi, T. Chen, Z. Wang, H. Li, R. Deng, X. Liu, W. Huang, *Nat. Mater.* **2015**, *14*, 685–690.
[16] A. Forni, E. Lucenti, C. Botta, E. Cariati, *J. Mater. Chem. C* **2018**, *6*, 4603–4626.
[17] S. Guo, W. Dai, X. Chen, Y. Lei, J. Shi, B. Tong, Z. Cai, Y. Dong, *ACS Mater. Lett.* **2021**, *3*, 379–397.
[18] X. K. Ma, Y. Liu, *Acc. Chem. Res.* **2021**, *54*, 3403–3414.
[19] Y. Gong, J. Yang, M. Fang, Z. Li, *Cell Rep. Phys. Sci.* **2022**, *3*, 100663.
[20] Y. Zhang, Y. Su, H. Wu, Z. Wang, C. Wang, Y. Zheng, X. Zheng, L. Gao, Q. Zhou, Y. Yang, X. Chen, C. Yang, Y. Zhao, *J. Am. Chem. Soc.* **2021**, *143*, 13675–13685.
[21] J. Guo, C. Yang, Y. Zhao, *Acc. Chem. Res.* **2022**, *55*, 1160–1170.
[22] C. Hoffend, M. Diefenbach, E. Januszewski, M. Bolte, H. W. Lerner, M. C. Holthausen, M. Wagner, *Dalton Trans.* **2013**, *42*, 13826–13837.
[23] C. Reus, S. Weidlich, M. Bolte, H. W. Lerner, M. Wagner, *J. Am. Chem. Soc.* **2013**, *135*, 12892–12907.
[24] X. Wang, Y. Sun, G. Wang, J. Li, X. Li, K. Zhang, *Angew. Chem. Int. Ed.* **2021**, *60*, 17138–17147; *Angew. Chem.* **2021**, *133*, 17275–17284.
[25] M. Louis, H. Thomas, M. Gmelch, A. Haft, F. Fries, S. Reineke, *Adv. Mater.* **2019**, *31*, 1807887.
[26] J. L. Kropp, W. R. Dawson, *J. Phys. Chem.* **1967**, *71*, 4499–4506.
[27] Z. Ma, Z. Yang, L. Mu, L. Deng, L. Chen, B. Wang, X. Qiao, D. Hu, B. Yang, D. Ma, J. Peng, Y. Ma, *Chem. Sci.* **2021**, *12*, 14808–14814.
[28] M. Jian, Z. Song, X. Chen, J. Zhao, B. Xu, Z. Chi, *Chem. Eng. J.* **2022**, *429*, 132346.
[29] Y. Yang, Y. Liang, Y. Zheng, J. A. Li, S. Wu, H. Zhang, T. Huang, S. Luo, C. Liu, G. Shi, F. Sun, Z. Chi, B. Xu, *Angew. Chem. Int. Ed.* **2022**, *61*, e202201820; *Angew. Chem.* **2022**, *134*, e202201820.
[30] X. Yan, H. Peng, Y. Xiang, J. Wang, L. Yu, Y. Tao, H. Li, W. Huang, R. Chen, X. Yan, H. Peng, Y. Xiang, J. Wang, L. Yu, Y. Tao, H. Li, W. Huang, R. Chen, *Small* **2022**, *18*, 2104073.
[31] X. Liu, Q. Yi, Y. Han, Z. Liang, C. Shen, Z. Zhou, J. Sun, Y. Li, W. Du, R. Cao, *Angew. Chem. Int. Ed.* **2015**, *54*, 1846–1850; *Angew. Chem.* **2015**, *127*, 1866–1870.
[32] R. H. Mitchell, F. Sondheimer, *Tetrahedron* **1968**, *24*, 1397–1405.
[33] M. Weimar, G. Dürner, J. W. Bats, M. W. Göbel, *J. Org. Chem.* **2010**, *75*, 2718–2721.
[34] A. John, S. Kirschner, M. K. Fengel, M. Bolte, H. W. Lerner, M. Wagner, *Dalton Trans.* **2019**, *48*, 1871–1877.
[35] S. Kirschner, J.-M. Mewes, M. Bolte, H.-W. Lerner, A. Dreuw, M. Wagner, *Chem. Eur. J.* **2017**, *23*, 5104–5116.
[36] A. Köhler, H. Bässler, *Mater. Sci. Eng. R* **2009**, *66*, 71–109.
[37] A. Hayer, H. Bässler, B. Falk, S. Schrader, *J. Phys. Chem. A* **2002**, *106*, 11045–11053.
[38] Y. Tsuchiya, S. Diesing, F. Bencheikh, Y. Wada, P. L. dos Santos, H. Kaji, E. Zysman-Colman, I. D. W. Samuel, C. Adachi, *J. Phys. Chem. A* **2021**, *125*, 8074–8089.

© 2022 The Authors. Angewandte Chemie International Edition published by Wiley-VCH GmbH

[39] S. Reineke, M. A. Baldo, *Sci. Rep.* **2014**, *4*, 3797.
[40] Z. Lin, R. Kabe, N. Nishimura, K. Jinnai, C. Adachi, Z. Lin, R. Kabe, N. Nishimura, K. Jinnai, C. Adachi, *Adv. Mater.* **2018**, *30*, 1803713.
[41] S. Hirata, M. Head-Gordon, *Chem. Phys. Lett.* **1999**, *314*, 291–299.
[42] F. Neese, *Wiley Interdiscip. Rev.: Comput. Mol. Sci.* **2012**, *2*, 73–78.
[43] F. Neese, *Wiley Interdiscip. Rev.: Comput. Mol. Sci.* **2022**, *12*, e1606.
[44] J. Plötner, D. J. Tozer, A. Dreuw, *J. Chem. Theory Comput.* **2010**, *6*, 2315–2324.
[45] F. B. Dias, K. N. Bourdakos, V. Jankus, K. C. Moss, K. T. Kamtekar, V. Bhalla, J. Santos, M. R. Bryce, A. P. Monkman *Adv. Mater.* **2013**, *25*, 3707–3714.
[46] J. Gibson, T. J. Penfold, *Phys. Chem. Chem. Phys.* **2017**, *19*, 8428–8434.
[47] T. Serevičius, R. Skaisgiris, I. Fiodorova, G. Kreiza, D. Banevičius, K. Kazlauskas, S. Tumkevičius, S. Juršėnas, *J. Mater. Chem. C* **2021**, *9*, 836–841.
[48] H. Noda, X. K. Chen, H. Nakanotani, T. Hosokai, M. Miyajima, N. Notsuka, Y. Kashima, J. L. Brédas, C. Adachi, *Nat. Mater.* **2019**, *18*, 1084–1090.
[49] H. Ma, H. Yu, Q. Peng, Z. An, D. Wang, Z. Shuai, *J. Phys. Chem. Lett.* **2019**, *10*, 6948–6954.
[50] M. Gmelch, H. Thomas, F. Fries, S. Reineke, *Sci. Adv.* **2019**, *5*, eaau7310.

Manuscript received: October 13, 2022
Accepted manuscript online: November 22, 2022
Version of record online: December 14, 2022

© 2022 The Authors. Angewandte Chemie International Edition published by Wiley-VCH GmbH

15213773, 2023, 4, Downloaded from https://onlinelibrary.wiley.com/doi/10.1002/anie.202215071 by Vilnius University, Wiley Online Library on [17/01/2023]. See the Terms and Conditions (https://onlinelibrary.wiley.com/terms-and-conditions) on Wiley Online Library for rules of use; OA articles are governed by the applicable Creative Commons License

NOTES

Vilniaus universiteto leidykla
Saulėtekio al. 9, III rūmai, LT-10222 Vilnius
El. p. info@leidykla.vu.lt, www.leidykla.vu.lt
bookshop.vu.lt, journals.vu.lt
Tiražas 25 egz.